The Pennsylvania State University
The Graduate School

LARGE-EDDY SIMULATION OF TURBULENT FLAMES WITH RADIATION HEAT TRANSFER

A Dissertation in
Mechanical Engineering
by
Ankur Gupta

Submitted in Partial Fulfillment
of the Requirements
for the Degree of

Doctor of Philosophy

December 2011

The dissertation of Ankur Gupta was reviewed and approved* by the following:

Daniel C. Haworth
Professor of Mechanical Engineering
Dissertation Co-Advisor, Co-Chair of Committee

Michael F. Modest
Professor of Mechanical Engineering
Dissertation Co-advisor, Co-Chair of Committee

Stephen R. Turns
Professor of Mechanical Engineering

Philip J. Morris
Professor of Aerospace Engineering

Karen A. Thole
Professor of Mechanical Engineering
Head of the Department of Mechanical and Nuclear Engineering

*Signatures are on file in the Graduate School.

Abstract

Most practical combustion devices involve turbulent flow and operate at high temperatures. Reliable predictive models for these devices must not only represent each individual physical process (combustion, turbulence and radiation) with high accuracy, but also must capture the highly nonlinear interactions among these processes. In this work, a comprehensive computational tool is developed for numerical modeling of turbulent combustion systems with accurate representation of turbulence, chemistry, turbulence–chemistry interaction (TCI), radiation, and turbulence–radiation interaction (TRI). A hybrid finite-volume (FV)/particle-Monte-Carlo procedure is employed wherein a compressible FV Large-Eddy simulation (LES) formulation with a composition filtered-density function (FDF) method is used to model turbulence–chemistry interactions (TCI) and emission TRI. Nongray radiation and absorption TRI is modeled through a photon Monte Carlo (PMC) method where stochastic schemes are developed for treating thermal radiation in a turbulent flow field characterized by the notional particles of the Lagrangian-FDF method. LES/FDF/PMC computations are computationally highly expensive, and a novel "computational time-map"-based domain-decomposition technique is implemented in this study for effective parallelization

of the computational code. A nonpremixed methane/air flame is simulated to demonstrate the accuracy of the code developed here.

Since LES is inherently time-dependent, the PMC solution at each time step needs to be reasonably reflective of the instantaneous fields to preserve the transient nature of LES, which might require considering large number of photon bundles. Investigations are made in this work for a wide range of flames to estimate the statistical uncertainties in the PMC solution for various number of photon bundles for an instantaneous LES/FDF snapshot. The time-averaged solution is also compared for different bundle sizes.

The effect of thermal radiation appears as a source term in the energy equation, which consists of filtered emission and filtered absorption terms in the LES context. In LES, since only large scales are explicitly resolved, the contribution of subfilter-scale (SFS) fluctuations to filtered emission and absorption terms (referred to as SFS emission TRI and SFS absorption TRI, respectively) need to be modeled. The importance of SFS TRI is assessed here for a wide range of flames.

A state-of-the-art, advanced LES-based numerical tool for comprehensive modeling of turbulent reacting flows, encompassing all key processes in detail, has become available for the first time as a result of this work. An effective parallelization scheme is implemented in the code that scales well irrespective of the computational cost for chemistry calculations. Stochastic PMC schemes are devised that are consistent with the notional particle representation of the FDF method. It is estimated that approximately three-to-four photon bundles per grid-cell are sufficient to ensure accurate time-averaged solutions for a wide range of flames (ranging from small, optically thin to relatively-large, optically thick). SFS emission TRI

is found to be more important than resolved emission TRI for all flames for a grid resolution that is representative of engineering meshes, whereas SFS absorption TRI is found to be negligible for all flames.

Table of Contents

List of Figures ix

List of Tables xv

List of Symbols xvii

Acknowledgments xxii

Chapter 1 Introduction 1
- 1.1 Objectives . . . 5
- 1.2 Outline of Forthcoming Chapters . . . 6

Chapter 2 Chemically Reacting Turbulent Flows 7
- 2.1 Instantaneous Conservation Equations . . . 8
- 2.2 Treatment of Chemical Kinetics . . . 9
- 2.3 Turbulent Combustion Modeling . . . 11
  - 2.3.1 Direct Numerical Simulation (DNS) . . . 12
  - 2.3.2 RAS and LES Modeling Approaches . . . 13
    - 2.3.2.1 Reynolds-Averaged Simulation (RAS) . . . 13
    - 2.3.2.2 Large-Eddy Simulation (LES) . . . 15
- 2.4 Governing Equations for LES . . . 17
  - 2.4.1 Filtered Viscous Transport Terms . . . 19
  - 2.4.2 SFS Stress Tensor Closure . . . 20
    - 2.4.2.1 Interplay Between SFS Model and Numerical Error, and Convergence of Filtered Equations . . . 21
    - 2.4.2.2 Dynamic Modeling . . . 21
  - 2.4.3 Subfilter Closures for Turbulent Transport of Enthalpy and Species . . . 22
  - 2.4.4 Closures for the Filtered Chemical Source Term ($\widetilde{S_\alpha}$) . . . 23
- 2.5 Transported FDF Methods . . . 26

2.5.1 Background of FDF Methods 27
2.5.2 The Transported Composition FDF Method 30
2.5.2.1 Composition FDF Formulation for Variable Density Flows 31
2.5.2.2 Exact Transport Equation for the Composition FDF 32
2.5.2.3 Modeling in Composition FDF Methods 34
2.5.2.4 Modeled Transport Equation for Composition FDF 36
2.6 Solution to Modeled Composition FDF Transport Equation 37
2.6.1 Stochastic Differential Equations (SDEs) for Lagrangian Monte Carlo FDF Methods 40

Chapter 3 Thermal Radiation and TRI 42
3.1 Thermal Radiation 42
3.1.1 The Radiative Transfer Equation (RTE) 43
3.2 RTE Solution Methods 44
3.2.1 Monte Carlo Method 45
3.3 Spectral Treatment of Radiation 46
3.3.1 Spectral Radiation Properties of Combustion Gases 46
3.3.2 Spectral Models 47
3.3.2.1 Spectral Photon Monte Carlo Method 49
3.4 Turbulence–Radiation Interactions (TRI) 51
3.4.1 Optically Thin Fluctuation Approximation (OTFA) 54
3.4.2 Assessing Resolved and SFS Emission TRI in LES 56
3.5 Earlier Investigations of TRI 58

Chapter 4 Numerical Algorithms 63
4.1 Hybrid Lagrangian-Particle/Eulerian-Mesh Method 63
4.1.1 Coupling of Particle Monte Carlo with FV Solver 64
4.1.2 Parallelized Particle Monte Carlo Code for Domain-Decomposed Computations 65
4.1.2.1 Parallelized Particle Tracking 66
4.1.2.2 Parallelization of Chemistry Computations for Improved Load-Balancing 68
4.1.3 Particle Number Density Control 68
4.1.4 Estimation of FV Field at Particle Locations 69
4.1.5 Extraction of Cell-Based Quantities from Particle Values . . 70
4.1.6 Equivalent Enthalpy Approach for Robust Time-Accurate Coupling 70
4.2 PMC-Based Radiation Treatment for Hybrid FV/PDF Simulations 72
4.2.1 A Stochastic PMC Scheme 73

4.2.1.1 Motivation . . . 73
4.2.1.2 Model Formulation . . . 77
4.2.1.3 Coupling PMC with FV/PDF Routines . . . 79
4.3 Underlying Finite-Volume Solver . . . 80
4.4 Parallelization Strategies . . . 80
4.4.1 Local-Computation-Time-Map-Based Domain-Decomposition + Deferred Ray Tracking Scheme . . . 81
4.5 Modular Code Structure . . . 88
4.6 Summary of Key Equations for RAS/PDF and LES/FDF Simulations 89

Chapter 5 Development and Validation Studies 95
5.1 Variable-Density LES Solver: A Co-axial Annular Jet . . . 97
5.2 OpenFOAM/PDF Coupling: Lid-driven Cavity . . . 99
5.3 OpenFOAM-RAS/PDF Module: Sandia Flame D . . . 103
5.4 Comparison of Stochastic PMC Scheme with Previous Schemes . . 108
5.5 LES/FDF Module . . . 112
5.5.1 Computational Grid . . . 113
5.5.2 Turbulent Inflow . . . 115
5.5.3 Assessment of Mass Consistency and Density Feedback . . . 117
5.5.4 Results . . . 118
5.6 Parallelization Studies . . . 123
5.7 Summary . . . 127

Chapter 6 Treating Thermal Radiation in LES of Reacting Flows 130
6.1 PMC Requirements in LES . . . 131
6.2 TRI at Subfilter-Scale Level . . . 147
6.3 Summary . . . 163

Chapter 7 Summary and Conclusion 164
7.1 Recommendations for Future Work . . . 167

Bibliography 169

List of Figures

3.1 Spectral absorption coefficient for carbon dioxide in a small portion of the $4.3\mu m$ narrow band at $1000K$. 48

4.1 Particle tracking algorithm for parallel FV/PDF simulations. 67
4.2 Computational time map for RAS/PDF/PMC of a modified Sandia flame. The plot represents average CPU time spent (in s) per time-step for chemistry calculations. 83
4.3 Computational time map for RAS/PDF/PMC of a modified Sandia flame. The plot represents average CPU time spent (in s) per time-step for PMC calculations. 83
4.4 Computational time map for RAS/PDF/PMC of a modified Sandia flame. The plot represents average CPU time spent (in s) per time-step for chemistry and PMC calculations. 85
4.5 Default cell ordering in the FV mesh of a modified Sandia flame. The plot represents indices of cells. 86
4.6 Reordered cell indices in a modified Sandia flame. 86
4.7 Clustering of cells for the reordered cell indices. 86
4.8 Double layer approach for cell reordering. The plot represents two layers for reordering of cells 87
4.9 Reordered cell indices for a double layer in a modified Sandia flame. 88
4.10 Clustering of cells for a double layer reordered cell indices in a modified Sandia flame. 88
4.11 Comparison of processor cell counts for single-layer and double-layer reordering. 89
4.12 Schematic illustration of the LES/FDF/PMC/MOM-based computational module. 90

5.1 Instantaneous axial velocity component on a cutting plane for the annular jet flow. 98
5.2 Computed and measured mean axial velocity profiles for the annular jet flow. 99

5.3 Computed and measured rms axial velocity profiles for the annular jet flow. 100
5.4 The steady-state velocity field for the lid-driven cavity configuration. Arrows are used to depict the direction of the local velocity vectors. 101
5.5 Time evolution of instantaneous rms mass density deviation (ρ'_{rms}) over the computational domain for the lid-driven cavity. Results are compared with data obtained by Zhang and Haworth [139]. 103
5.6 Schematic of the piloted-jet burner and a flame image [190]. 104
5.7 Computational mesh for RAS/PDF simulation of Sandia Flame D. 105
5.8 Computed Favre-mean temperatures at three axial locations ($x/D_{jet} =$ 15, $x/D_{jet} = 30$, and $x/D_{jet} = 45$) for Sandia Flame D. 107
5.9 Computed mean temperature field for the scaled-up Sandia Flame D. 109
5.10 Computed Favre-mean temperatures at different axial locations ($x/D_{jet} =$ 15, $x/D_{jet} = 30$, and $x/D_{jet} = 45$) for scaled-up Sandia Flame D. . 110
5.11 Ratio of standard deviation and mean absorption at different axial locations ($x/D_{jet} = 15$, $x/D_{jet} = 30$, and $x/D_{jet} = 45$) for scaled-up Sandia Flame D. 110
5.12 Ratio of filter width to turbulence length scale in the computational domain for LES of Sandia Flame D. 114
5.13 Ratio of filter width to turbulence length scale plotted over only those regions in the computational domain where the temperature is above 292 K and the rms axial velocity is greater than 0.5 m/s. . 114
5.14 Instantaneous x-, y-, and z-velocities (in m/s) at the inlet constructed using the turbulence synthesis approach. The inner-most circle (as seen in the middle contour plot) is the fuel jet and the surrounding annulus is hot pilot. 117
5.15 Comparison of radial profiles of mean density at three axial locations for different density representations. 118
5.16 Computed instantaneous temperatures on a plane along the jet centerline for Sandia Flame D. 119
5.17 Radial profiles of mean temperature at three axial locations ($x/D_{jet} =$ 15, $x/D_{jet} = 30$, and $x/D_{jet} = 45$) for Sandia Flame D. 121
5.18 Radial profiles of rms temperature at three axial locations ($x/D_{jet} =$ 15, $x/D_{jet} = 30$, and $x/D_{jet} = 45$) for Sandia Flame D. 121
5.19 Radial profiles of mean axial velocity at three axial locations ($x/D_{jet} =$ 15, $x/D_{jet} = 30$, and $x/D_{jet} = 45$) for Sandia Flame D. 122
5.20 Radial profiles of mean mass-fraction of CO_2 at two axial locations ($x/D_{jet} = 15$ and $x/D_{jet} = 30$) for Sandia Flame D. 123
5.21 Radial profiles of rms mass-fraction of CO_2 at two axial locations ($x/D_{jet} = 15$ and $x/D_{jet} = 30$) for Sandia Flame D. 123

5.22 Radial profiles of mean mass-fraction of OH at two axial locations ($x/D_{jet} = 15$ and $x/D_{jet} = 30$) for Sandia Flame D. 124
5.23 Radial profiles of rms mass-fraction of OH at two axial locations ($x/D_{jet} = 15$ and $x/D_{jet} = 30$) for Sandia Flame D. 124
5.24 Speed-up for a 16-processor run for RAS/PDF/PMC of scaled-up Sandia Flame D. 125
5.25 Computational time-map for LES/FDF/PMC of Sandia Flame D. The plot represents average CPU time spent (in s) per time-step for chemistry calculations. 126
5.26 Computational time-map for LES/FDF/PMC of Sandia Flame D. The plot represents average CPU time spent (in s) per time-step for PMC calculations. 127
5.27 Computational time-map for LES/FDF/PMC of Sandia Flame D. The plot represents average CPU time spent (in s) per time-step for chemistry and PMC calculations. 128
5.28 Decomposed domain using a double-layer clustering approach for a 16-processor simulation of LES/FDF/PMC of Sandia Flame D. . . 129
5.29 Decomposed domain using a double-layer clustering approach for a 32-processor simulation of LES/FDF/PMC of Sandia Flame D. . . 129
5.30 Scalability (strong scaling limit) for LES/FDF/PMC of Sandia Flame D. 129

6.1 Soot volume fraction as a function of the mixture-fraction; state-relationship for soot employed in this study. 133
6.2 Computed instantaneous resolved temperatures on a plane along the jet centerline for flame (iv) [scaled-up Sandia Flame D with soot]. 134
6.3 Computed instantaneous resolved soot volume-fractions (from state-relationship) on a plane along the jet centerline for flame (iv) [scaled-up Sandia Flame D with soot]. 134
6.4 Radial profiles of the ratio of standard deviation in the volumetric absorption and its exact value at three axial locations ($x/D_{jet} = 15$, $x/D_{jet} = 30$, and $x/D_{jet} = 45$) for LES/FDF snapshot of scaled-up Sandia Flame D. 136
6.5 Radial profiles of exact volumetric absorption at three axial locations ($x/D_{jet} = 15$, $x/D_{jet} = 30$, and $x/D_{jet} = 45$) for LES/FDF snapshot of scaled-up Sandia Flame D. 136
6.6 Radial profiles of the ratio of standard deviation in the volumetric absorption to its exact value at three axial locations ($x/D_{jet} = 15$, $x/D_{jet} = 30$, and $x/D_{jet} = 45$) for LES/FDF snapshot of scaled-up Sandia Flame D with artificial soot. 138

6.7 Radial profiles of exact volumetric absorption at three axial locations ($x/D_{jet} = 15$, $x/D_{jet} = 30$, and $x/D_{jet} = 45$) for LES/FDF snapshot of scaled-up Sandia Flame D with artificial soot. 138
6.8 Radial profiles of the ratio of standard deviation in the volumetric absorption to its exact value at three axial locations ($x/D_{jet} = 15$, $x/D_{jet} = 30$, and $x/D_{jet} = 45$) for LES/FDF snapshot of Sandia Flame D. 140
6.9 Radial profiles of exact volumetric absorption at three axial locations ($x/D_{jet} = 15$, $x/D_{jet} = 30$, and $x/D_{jet} = 45$) for LES/FDF snapshot of Sandia Flame D. 140
6.10 Radial profiles of the ratio of standard deviation in the volumetric absorption to its exact value at three axial locations ($x/D_{jet} = 15$, $x/D_{jet} = 30$, and $x/D_{jet} = 45$) for LES/FDF snapshot of Sandia Flame D with artificial soot. 142
6.11 Radial profiles of exact volumetric absorption at three axial locations ($x/D_{jet} = 15$, $x/D_{jet} = 30$, and $x/D_{jet} = 45$) for LES/FDF snapshot of Sandia Flame D with artificial soot. 142
6.12 The variation in resolved temperature with time at two locations in scaled-up Sandia Flame D with artificial soot for different number of photon bundles in the PMC analysis. 144
6.13 Comparison of radial profiles of mean temperature at three axial locations ($x/D_{jet} = 15$, $x/D_{jet} = 30$, and $x/D_{jet} = 45$) for scaled-up Sandia Flame D with artificial soot for different numbers of photon bundles. 145
6.14 Comparison of radial profiles of mean radiative heat source at three axial locations ($x/D_{jet} = 15$, $x/D_{jet} = 30$, and $x/D_{jet} = 45$) for scaled-up Sandia Flame D with artificial soot for different numbers of photon bundles. 145
6.15 Comparison of radial profiles of mean temperature at three axial locations ($x/D_{jet} = 15$, $x/D_{jet} = 30$, and $x/D_{jet} = 45$) for scaled-up Sandia Flame D for different numbers of photon bundles. 146
6.16 Comparison of radial profiles of mean radiative heat source at three axial locations ($x/D_{jet} = 15$, $x/D_{jet} = 30$, and $x/D_{jet} = 45$) for scaled-up Sandia Flame D for different numbers of photon bundles. 146
6.17 Radial profiles of instantaneous volumetric absorption at three axial locations ($x/D_{jet} = 15$, $x/D_{jet} = 30$, and $x/D_{jet} = 45$) for a LES/FDF snapshot of scaled-up Sandia Flame D for different treatments of SFS absorption TRI. 148

6.18 Radial profiles of instantaneous volumetric absorption at three axial locations (x/D_{jet} = 15, x/D_{jet} = 30, and x/D_{jet} = 45) for a LES/FDF snapshot of scaled-up Sandia Flame D with artificial soot for different treatments of SFS absorption TRI. 149
6.19 Radial profiles of instantaneous volumetric emission at three axial locations (x/D_{jet} = 15, x/D_{jet} = 30, and x/D_{jet} = 45) for a LES/FDF snapshot of scaled-up Sandia Flame D for different treatments of SFS emission TRI. 150
6.20 Radial profiles of instantaneous volumetric emission at three axial locations (x/D_{jet} = 15, x/D_{jet} = 30, and x/D_{jet} = 45) for a LES/FDF snapshot of scaled-up Sandia Flame D with artificial soot for different treatments of emission SFS TRI. 150
6.21 Radial profiles of mean radiative heat source at two axial locations (x/D_{jet} = 15 and x/D_{jet} = 30) for scaled-up Sandia Flame D for different treatments of SFS emission TRI. 151
6.22 Radial profiles of mean radiative heat source at two axial locations (x/D_{jet} = 15 and x/D_{jet} = 30) for scaled-up Sandia Flame D with artificial soot for different treatments of SFS emission TRI. 151
6.23 Radial profiles of mean temperature at two axial locations (x/D_{jet} = 15 and x/D_{jet} = 30) for scaled-up Sandia Flame D for different treatments of SFS emission TRI. 153
6.24 Radial profiles of mean temperature at two axial locations (x/D_{jet} = 15 and x/D_{jet} = 30) for scaled-up Sandia Flame D with artificial soot for different treatments of SFS emission TRI. 153
6.25 Mean emission reordered as a function of the unresolved turbulence kinetic energy for scaled-up Sandia Flame D with and without the consideration of SFS emission TRI. 154
6.26 Comparison between resolved and SFS components for various contributions to TRI at x/D_{jet} = 15 axial location for scaled-up Sandia Flame D with artificial soot. Correlations plotted in this figure are summarized in Table 3.2. 155
6.27 Comparison between resolved and SFS components for various contributions to TRI at x/D_{jet} = 30 axial location for scaled-up Sandia Flame D with artificial soot. Correlations plotted in this figure are same as Fig. 6.26 and are also summarized in Table 3.2. 157
6.28 Comparison between resolved and SFS components for various contributions to TRI at x/D_{jet} = 45 axial location for scaled-up Sandia Flame D with artificial soot. Correlations plotted in this figure are same as Fig. 6.26 and are also summarized in Table 3.2. 159

6.29 Radial profiles of instantaneous volumetric absorption at three axial locations ($x/D_{jet} = 15$, $x/D_{jet} = 30$, and $x/D_{jet} = 45$) for a LES/FDF snapshot of Sandia Flame D for different treatments of SFS absorption TRI. 160
6.30 Radial profiles of instantaneous volumetric absorption at three axial locations ($x/D_{jet} = 15$, $x/D_{jet} = 30$, and $x/D_{jet} = 45$) for a LES/FDF snapshot of Sandia Flame D with artificial soot for different treatments of SFS absorption TRI. 160
6.31 Radial profiles of instantaneous volumetric emission at three axial locations ($x/D_{jet} = 15$, $x/D_{jet} = 30$, and $x/D_{jet} = 45$) for a LES/FDF snapshot of Sandia Flame D for different treatments of SFS emission TRI. 162

List of Tables

2.1 Comparison of commonly used turbulence models. 16
2.2 Unclosed terms that require modeling in the set of filtered equations for LES. 19

3.1 Radiative versus conductive/convective modes of heat transfer. . . . 42
3.2 TRI correlations for resolved-scale, SFS, and all (resolved+SFS) fluctuations. 58

4.1 A comparison of different PDF/PMC schemes. 79
4.2 Parallelization characteristics of the various components of the coupled FV/PDF/PMC code. 82
4.3 Values of model coefficients for a standard $k-\epsilon$ model. 92

5.1 Inlet boundary conditions for Sandia Flame D [191]. 105
5.2 Assessment of a global metric (summation of standard deviation over the entire computational domain divided by the total absorption) for various PDF/PMC schemes. 111

6.1 The aggregate absorption and radiative heat source expressed as a fraction of the total absorption and total radiative heat source, respectively, in the computational domain for flame (iii). The aggregation is conducted over FV cells where $\frac{\sigma}{Q_{\text{exact}}}$ is within a specified cutoff; here Q_{exact} refers to the exact volumetric absorption (or exact radiative heat source) for the LES/FDF snapshot, and σ corresponds to the standard deviation in the exact quantity. 137
6.2 The aggregated absorption and radiative heat source expressed as a fraction of the total absorption and total radiative heat source, respectively, in the computational domain for flame (iv). 139
6.3 The aggregated absorption and radiative heat source expressed as a fraction of the total absorption and total radiative heat source, respectively, in the computational domain for flame (i). 141

6.4 The aggregated absorption and radiative heat source expressed as a fraction of the total absorption and total radiative heat source, respectively, in the computational domain for flame (ii). 143
6.5 Total radiative emission in the computational domain for different treatments of SFS emission TRI. Here, "TRI-3" denotes emission with SFS TRI and "TRI-1" refers to emission without SFS TRI. "TRI-0" refers to emission based on mean temperature and mean mass fractions (no TRI). 154
6.6 Total absorption in the computational domain in the absence of absorption SFS TRI expressed as a fraction of the total absorption in the presence of SFS TRI. 161
6.7 Total radiative emission in the computational domain for different treatments of SFS TRI. Here, "TRI-3" denotes emission with SFS TRI and "TRI-1" refers to emission without SFS TRI. "TRI-0" refers to emission based on mean temperature and mean mass fractions (no TRI). 161

List of Symbols

Physical Constants

R_u	Universal gas constant
σ	Stefan-Boltzmann constant

Variables

c_P	Specific heat
C_α	Mixing model constant
D_α	Molecular diffusivity of species α
D_{jet}	Fuel jet diameter
D_{pilot}	Pilot diameter
E_{emm}	Total emission from a finite-volume cell
F	Mass density function or filtered mass density function
F_{mix}	Flux in the composition space due to molecular mixing
F^*_{mix}	Change in species composition due to mixing
f	One-point, one-time joint-composition probability density function
f_v	Soot volume-fraction
dh	Grid spacing
g_j	Body force component in the j^{th} direction
G	filter kernel; Also used for incident radiation
h	Absolute enthalpy
h_{eq}	Equivalent enthalpy
$I_{b\eta}$	Planck function
I	Radiative intensity
I_η	Spectral radiative intensity
J^h_i	Molecular flux of enthalpy in i^{th} direction
J^α_i	Molecular flux of species α in i^{th} direction

k	Turbulent kinetic energy or subfilter-scale turbulent kinetic energy
l	Turbulent eddy length scale
l_T	Turbulence integral length scale
M_α	Chemical species symbol
m	Fluid mass
N_s	Number of chemical species
N_p	Number of particles
n_r	Number of radiating species
N	Number of processors
p	Pressure
p_i	Partial pressure of species i
Pr_T	Turbulent Prandtl number or subfilter-scale Prandtl number
Q	An arbitrary physical quantity
Q_{emm}	Total emission
$\underline{q}_{rad}$	Radiative heat flux
Re	Reynolds number
r	Radial direction coordinate
R_η	Random number
$s.d.$	Standard deviation
$S_{\text{radiation}}$	Volumetric radiative source
S_α	Chemical production rate of species α per unit mass
Sc_T	Turbulent Schmidt number or subfilter-scale Schmidt number
S_{ij}	Rate-of-strain tensor
$\hat{s}, \hat{s}_i$	Unit direction vectors
t	Time
T_{ij}	Subfilter-scale stress tensor
T	Temperature
u_i, U_i	Velocity component in the i^{th} direction
$\underline{W}$	Isotropic vector Wiener process
W_i	Molecular weight of species i
x_i	i^{th} spatial cartesian coordinate
Y_α	Mass-fraction of species α

Greek-Letter Variables

ρ	Mass density
τ_{ij}	Viscous stress tensor
μ	Dynamic viscosity
δ_{ij}	Kronecker delta function

$\nu_{l\alpha}$	Stoichiometric coefficients in the elementary reactions
ϵ	Eddy dissipation rate
ω	Specific dissipation rate
Δ	Filter width
ν_T	Eddy viscosity
$\underline{\phi}$	Scalar composition vector consisting of mass-fraction and enthalpy
$\overline{\kappa}$	Absorption coefficient
κ_η	Spectral absorption coefficient
$\kappa_{p\eta}$	Pressure-based spectral absorption coefficient
κ_P	Planck-mean absorption coefficient
ς	Fine-grained density
δ	Delta function
$\underline{\psi}$	Composition space vector
$\overline{\alpha}$	Index in composition space
Γ	Molecular diffusivity
$\Gamma_t, \Gamma_{\text{eff}}$	Apparent diffusivity
$\sigma_\alpha, \sigma_\phi$	Subfilter-scale turbulent Prandtl or Schmidt number
Ω_m	Mixing frequency
τ	A turbulence timescale
η	Wavenumber
Ω	Solid angle
$\sigma_{s\eta}$	Spectral scattering coefficient
β_η	Spectral extinction coefficient
$\Phi_\eta\left(\hat{s}_i, \hat{s}\right)$	Scattering phase function
χ_i	Mole fraction of species i
λ	Wavelength
ξ	Mixture fraction

Subscripts

$i, j,$ or k	A cartesian vector or tensor component
rad	Radiation
abs	Radiative absorption
emm	Radiative emission
t or T	Turbulent
η	A spectral value (wavenumber)
α or β	A composition component

Operators

$\bar{}$	Mean quantity in RAS context; spatially filtered quantity in LES
$\tilde{}$	Favre-mean in RAS; Favre-filtered quantity in LES

Abbreviations

CD	Coalescence-Dispersion (mixing model)
CDS	Constant-density sphere
CFD	Computational fluid dynamics
CMC	Conditional-moment closure
CPU	Central processing unit
DNS	Direct numerical simulation
DOM	Discrete ordinates method
EMST	Euclidean minimum spanning tree
FDF	Filtered-density function
FDM	Finite-difference method
FEM	Finite-element method
FMDF	Filtered mass-density function
FV	Finite-volume
FVM	Finite-volume method
IC	Internal combustion
IEM	Interaction-by-exchange-with-the-mean (mixing model)
LBL	Line-by-line
LES	Large-eddy simulation
LMSE	Linear mean-square estimation (mixing model)
MCRT	Monte Carlo ray tracing
MILES	Monotone integrated large-eddy simulation
MDF	Mass-density function
MOM	Method of moments
ODE	Ordinary differential equation
OTFA	Optically thin fluctuation approximation
PDF	Probability density function
PMC	Photon Monte Carlo
PPM	Point particle model
RANS	Reynolds-averaged Navier-Stokes
RAS	Reynolds-averaged simulation
RSM	Reynolds-stress transport model
RTE	Radiative transfer equation

SDE	Stochastic differential equation
SFDF	Composition FDF
SFMDF	Composition FMDF
SFS	Subfilter-scale
SHM	Spherical harmonics method
TA	Time accurate
TCI	Turbulence–chemistry interaction
TRI	Turbulence–radiation interaction
TVD	Total variation diminishing
VFDF	Velocity FDF
VSFDF	Velocity-composition FDF
VSFMDF	Velocity-composition FMDF

Acknowledgments

There are so many people who have helped me complete this work in many different ways and without whom this thesis would not have been possible. I would like to express my sincere gratitude to my advisors Dr. Daniel Haworth and Dr. Michael Modest for their guidance, support and encouragement. Their profound commitment to scholarly research has been an indispensable source of inspiration and guidance throughout. I would like to extend many thanks to my committee members Dr. Stephen Turns and Dr. Phillip Morris for their feedback. I also thank Ginny Smith and Jenny Houser for all their help during my years at Penn State. I would like to acknowledge NASA (award NNX07AB40A) and NSF (grant CTS-0121573) for supporting this research work. The computational analysis conducted here was supported in part through instrumentation funded by the NSF through grant OCI-0821527.

I would also like to thank all my past and present lab members for the many helpful discussions we have had. My heartfelt appreciation towards my family and all my friends for their support, affection and patience during my years at Penn State. Last but not the least, a very special thank you to my parents Mrs Manju and Dr. Devendra Kumar Gupta, my brother Arpan and my wife Vibha for their unconditional love and support.

Chapter 1

Introduction

Most of our energy requirements for transportation and other applications are fulfilled via the burning of hydrocarbon fuels. This is accompanied by the release of combustion products such as carbon dioxide, water vapor, and pollutants like soot and NOx into the atmosphere. In recent times, there has been growing environmental concern about rising pollutant levels, calling for strict control on the level of pollutant emissions that arise from the burning of these hydrocarbon fuels [1–4]. This has motivated research efforts into the development of fuel burning devices with efficient combustion and with low pollutant emissions, aiming to reduce the amount of pollutants emitted without sacrificing system performance.

Combustion systems including gas-turbine combustors, furnaces, and rocket engines involve turbulent flow and operate at high temperatures where thermal radiation is an important mode of heat transfer. These systems are very complex and, therefore, have heavily relied on experimentation for their development. Experimental techniques suffer from high operating costs, scaling problems, and measurement difficulties compared to numerical methods; the latter have the potential to be less expensive and provide faster results. Numerical approaches can also be used to perform parametric studies that are difficult to realize experimentally. Thus, computational modeling has been receiving increasing attention in the design and optimization of turbulent combustion systems.

In turbulent combustion systems, chemistry, turbulence, and thermal radiation interact with each other in interesting and highly nonlinear ways. Their individual treatment is already quite challenging and complex for the purpose of

numerical modeling, let alone their interactions, which further increase the modeling difficulties. The predictive capabilities of computational modeling of turbulent combustion depend on the adequate representation of these physical and chemical processes in a numerical model. These processes and their interactions are exactly accounted for in a Direct Numerical Simulation (DNS), where all relevant continuum length and time scales are resolved. In other words, the underlying physical and chemical behavior of a system is completely captured in a numerical simulation via DNS. However, DNS is extremely expensive computationally, and with the current state of computing resources, it cannot be carried out for practical turbulent combustion systems. The range of scales represented in a numerical simulation needs to be reduced to make it feasible. Reynolds-Averaged Simulations (RAS) and Large-Eddy Simulation (LES) are two such reduction (modeling) techniques. In RAS, the mean flow is computed and the effects of all the turbulence scales are modeled, whereas in LES, the large, energy-carrying scales are explicitly resolved with the effects of the unresolved subfilter scales modeled.

LES is expected to be more accurate and general than RAS, since the large, energy-containing, flow-dependent scales are captured explicitly and only the (presumably) more universal small-scale dynamics require modeling. LES is also expected to capture phenomena that are difficult to accommodate in Reynolds-averaged approaches, such as large-scale unsteadiness and complicated flow patterns which are characteristic features of modern combustion devices. The accuracy required for predictions of pollutants, for example, may not be realizable using RAS. The need for predictive accuracy in the numerical modeling of turbulent reacting flows, therefore, has led to a significant interest in LES in recent years. There is a wide and rapidly growing body of evidence that demonstrates quantitative advantages of LES in modeling studies of laboratory flames [5–7] and in applications to gas-turbine combustors [8–11], IC engines [12–14], and other combustion systems. LES, therefore, promises to be an accurate and computationally feasible tool for investigations of chemically reacting, turbulent flows.

In LES, the range of scales considered is made tractable by filtering the exact, instantaneous form of governing equations. The resulting set of filtered equations contains unclosed terms which are manifestations of turbulence–chemistry interactions (TCI) and turbulence–radiation interactions (TRI), among other things.

The importance of considering TCI in numerical computations has long been recognized [15–17], and TCI has been an active area of research for the past several decades. The development in the modeling of turbulent reacting flows has mostly been done using RAS, and many of the developments made in RAS have been adopted in LES-based modeling of turbulent reacting flows. Filtered-density function (FDF) methods [6, 7, 18–23] have emerged as an attractive approach for treating TCI in the LES formalism.

Turbulence, chemistry, and TCI are already quite formidable to deal with and, therefore, thermal radiation often has been ignored or treated using simple models in turbulent reacting flows. Even where radiation has been considered, TRI has usually been ignored, even though the importance of TRI has long been recognized [24–31]. Studies have shown that the effects of TRI can be as significant as those of TCI. TRI is known to result in higher heat loss due to increased radiative emission [27–33], reduced temperatures and, consequently, significant changes in key pollutant species (particularly NOx and soot). Modest and coworkers [34, 35] observed approximately 30% increase in the radiative heat flux with TRI in their studies of nonpremixed turbulent jet flames. Mehta [36] demonstrated the necessity for considering thermal radiation along with TRI for accurate predictions in nonpremixed sooting flames.

The above studies have clearly established the importance of considering thermal radiation and TRI in accurate modeling of chemically reacting flows, especially in the presence of soot. LES explicitly captures some portion of the contribution of resolved scales to TRI. The unclosed subfilter-scale emission TRI, a one-point statistic based on local subfilter-scale fluctuations in species compositions and temperature, can be exactly represented by FDF methods. Wang et al. [37] developed a Photon Monte Carlo (PMC) method that models absorption TRI in the RAS/PDF context, which has subsequently been used to close absorption TRI in RAS/PDF studies of turbulent flames [38, 39]. A similar method can be used to treat subfilter-scale absorption TRI. PMC directly accounts for the various phenomena embedded in the radiative transfer equation (such as emission, absorption, and scattering) and has the distinct advantage that spectral radiative properties can be accurately represented. To date, studies by Frankel et al. [40] and Gupta et al. [41] are the only LES-based works reported in the literature that account for thermal radiation in

turbulent reacting flows. Those two studies, however, considered idealized configurations. Frankel et al. [40] account for emission TRI through a composition FDF method and neglected absorption TRI by assuming the optically thin fluctuation approximation (OTFA). Both SFS emission and absorption TRI were neglected by Gupta et al. [41] in their analysis. Some *a priori* studies [42–44] have been reported in the literature where the importance of SFS TRI is assessed for isotropic, homogenous media and non-isothermal turbulent planar jet flow. There have been no studies for assessing SFS TRI in turbulent reacting flows, where temperature and radiative properties fluctuate significantly due to turbulent structures. Fundamental studies need to be carried out to analyze the importance of SFS emission and absorption TRI in turbulent reacting flows.

The PMC method proposed by Wang et al. [37] provides a closure for absorption TRI, and assigns physical attributes (e.g., point mass or constant density sphere) to the notional particles that are used in Lagrangian PDF methods. The notional particles in these methods are purely stochastic however, and have no additional physical meaning. The schemes proposed in their work could also lead to situations where rays pass through finite-volume cells without getting attenuated due to the presence of void spaces between particles, which is not physical. This suggests that new PMC schemes need to be formulated for radiation treatment in Lagrangian PDF methods that are consistent with the notional particle representation, and that only utilize information that is available within the PDF framework.

Another area of concern in the use of PMC, which is specific to the radiation treatment in LES, is to obtain a time-dependent solution at every time-step. LES is inherently time-dependent and, therefore, the radiation solution also needs to be reasonably resolved in time to preserve the transient nature of LES, which means that both the spectral and the directional behavior of thermal radiation needs to be adequately resolved in the computational domain. Given that the radiative properties vary strongly in wavenumber space and emission needs to be accounted for in all possible directions, along with three-dimensional domains and fine grid requirements in LES (leading to large cell count), a very large number of photon bundles may be required to ensure reasonable time-resolution and low levels of stochastic uncertainty in the PMC solution and, consequently, accurate prediction of means and higher moments. This needs to be investigated to determine

the optimal number of photon bundles required for accurate predictions in LES computations.

1.1 Objectives

LES has shown great promise in becoming a predictive tool in the development of next-generation turbulent combustion devices. For high-fidelity predictions, LES of a turbulent reacting flow requires additional models to accurately account for (1) turbulence-chemistry interactions, (2) thermal radiation, and (3) turbulence-radiation interactions in a coupled manner. The development of such a comprehensive model for LES of turbulent combustion – which can accurately account for TCI (via FDF), thermal radiation (via PMC), and TRI (via FDF and PMC) – in canonical as well as laboratory configurations is the main aim of this work. The LES/FDF/PMC computational module is exercised to investigate the statistical uncertainty associated with various photon bundle sizes, and prediction of means for various flame configurations. The computational module is also applied to nonsooting and (artificial) sooting flames to investigate subfilter-scale TRI.

The main objectives of this study are summarized below:

1. Develop PMC schemes that are consistent with the notional particle representation in RAS/PDF and LES/FDF simulations.

2. Develop an LES/FDF/PMC based computational module for LES modeling of turbulent reacting flows. A finite-volume compressible LES solver is coupled with an FDF code (to account for TCI) and a spectral PMC code (for thermal radiation and TRI).

3. Establish the predictive accuracy of the LES/FDF/PMC approach for a non-premixed turbulent flame.

4. Implement effective parallelization of the LES/FDF/PMC code.

5. Analyze the requirement on the number of photon bundles for PMC solution in LES computations.

6. Investigate subfilter-scale TRI for both nonsooting and sooting flames.

1.2 Outline of Forthcoming Chapters

- Chapter 2 summarizes the instantaneous governing equations of turbulent reacting flows and the corresponding filtered equations for LES. Modeling of various unclosed terms, such as the subfilter-stress tensor and the filtered chemical source term, in the filtered equations are briefly reviewed. Background of the FDF methods is presented along with the underlying exact equations and modeling approximations.

- Chapter 3 discusses radiation modeling and gives an up-to-date review of the literature on modeling of TRI.

- Details of the numerical implementation of the composition FDF method and its coupling with the finite-volume solver are provided in Chapter 4. Theoretical background and the numerical details of the newly proposed PMC scheme are discussed. Parallelization strategies are explained for RAS/PDF/PMC and LES/FDF/PMC simulations.

- Chapter 5 presents validation studies for the various components of the comprehensive LES/FDF/PMC module. The computational module is also used to model a nonpremixed nonsooting flame.

- Chapter 6 investigates the stochastic uncertainty in the PMC solution for instantaneous LES/FDF snapshots, and accuracy in the time-averaged solution for various flame configurations. Subfilter-scale contributions to TRI are also reported for various flames.

- Chapter 7 summarizes the thesis and proposes topics that are important for future research in this area.

Chapter 2

Chemically Reacting Turbulent Flows

Most practical combustion systems involve turbulent flows. Examples include stationary and automotive reciprocating-piston engines, stationary and aircraft gas-turbine combustors, industrial burners, and chemical production/processing reactors. In such systems, chemistry and turbulence interact in highly nonlinear ways. Accurate treatment of turbulence and chemistry individually is quite complex and challenging, let alone their interaction which further increases the complexity of the combustion system under consideration. In principle, the instantaneous form of the governing equations for mass, momentum, species and energy along with a realistic chemistry mechanism exactly represent the underlying physics of various phenomena at work, and can be solved to yield the exact time-evolution of a turbulent combustion system. The instantaneous equations are presented in Section 2.1. Brief discussion on the treatment of gas-phase chemistry in turbulent reacting flows is provided in Section 2.2.

The instantaneous equations for turbulent reacting flows are, however, intractable in most practical cases; they require simplifications, such as averaging or spatial filtering, which are discussed in detail in Section 2.3. Spatial filtering of the instantaneous equations is adopted in this work. The filtered equations and modeling of unclosed terms are presented in Section 2.4. Turbulence–chemistry interactions are manifested in the filtered chemical source term, and transported FDF methods are used here to accurately account for them. Background on the

transported FDF method and underlying governing equations and physical models are presented in Section 2.5.

2.1 Instantaneous Conservation Equations

The basic set of governing equations includes the local balance equations for mass, momentum, species, and energy. Using Cartesian tensor notation, the governing equations are [15]:

- Mass

$$\frac{\partial \rho}{\partial t} + \frac{\partial}{\partial x_i}\left[\rho u_i\right] = 0 \tag{2.1}$$

  where ρ is the mixture density and u_i is a velocity component.

- Momentum $(j = 1, 2, 3)$

$$\frac{\partial}{\partial t}\left[\rho u_j\right] + \frac{\partial}{\partial x_i}\left[\rho u_i u_j\right] = \frac{\partial \tau_{ij}}{\partial x_i} - \frac{\partial p}{\partial x_j} + \rho g_j \tag{2.2}$$

  where τ_{ij} is the viscous stress tensor, p is the pressure and g_j is the body force.

- Chemical species (for N_s species, $\alpha = 1, 2, \ldots, N_s$)

$$\frac{\partial \rho Y_\alpha}{\partial t} + \frac{\partial \rho Y_\alpha u_i}{\partial x_i} = -\frac{\partial J_i^\alpha}{\partial x_i} + \rho S_\alpha \tag{2.3}$$

  where Y_α denotes the mass fraction of species α, J_i^α is the molecular diffusive flux of species α and S_α is the chemical production rate of species α per unit mass.

- Absolute enthalpy

$$\frac{\partial \rho h}{\partial t} + \frac{\partial \rho h u_i}{\partial x_i} = -\frac{\partial J_i^h}{\partial x_i} + \frac{Dp}{Dt} + \tau_{ij}\frac{\partial u_j}{\partial x_i} + \rho S_{\text{radiation}} \tag{2.4}$$

  where h is the absolute enthalpy, J_i^h denotes the molecular transport of enthalpy and $S_{\text{radiation}}$ is the volumetric radiative source term. Here absolute

enthalpy is chosen as the energy variable. Other commonly used energy variables include temperature and total internal energy.

The above set of equations is not closed; models are required for the viscous stress tensor, molecular transport of species and enthalpy, the chemical source term, and the radiative source term. The viscous stress tensor is given by the following equation:

$$\tau_{ij} = \mu \left(\frac{\partial u_i}{\partial x_j} + \frac{\partial u_j}{\partial x_i} \right) - \frac{2}{3} \mu \delta_{ij} \left(\frac{\partial u_k}{\partial x_k} \right) \tag{2.5}$$

where μ is the dynamic viscosity of the fluid and δ_{ij} is the Kronecker delta function. The molecular diffusive flux J_i^α is generally modeled based on Fick's law of diffusion and is given by

$$J_i^\alpha = -D_\alpha \frac{\partial Y_\alpha}{\partial x_i} \tag{2.6}$$

where D_α is the molecular diffusivity of species α. The molecular transport of enthalpy is usually modeled by Fourier's law.

The chemical source term S_α in the species conservation equation is generally based on a chemistry mechanism that expresses the details of transformation of species eventually leading to the oxidation of fuel into combustion products. More information on chemical mechanisms is presented in Section 2.2. The radiation source term $S_{\text{radiation}}$ is modeled in different ways by considering either a gray mixture or a nongray mixture. Details of radiation source term modeling are provided in Chapter 3.

2.2 Treatment of Chemical Kinetics

In combustion systems, the chemical conversion of fuel and oxidizer to combustion products does not happen in one single step; rather, it involves a large number of intermediate species and elementary reactions. For instance, detailed investigations show that water is not produced by a single collision between the three original reacting molecules (two molecules of hydrogen and one molecule of oxygen). Instead, many reactive intermediates including H, O, and OH are formed.

A set of elementary chemical reactions that describes the oxidation of hydrogen is referred to as chemical mechanism for combustion of hydrogen. Even for a fuel as simple as H_2, a reasonable level of description of the chemistry at a molecular level requires a 9-species, 11-reaction mechanism [45]. The combustion of a simple fuel like methane in air requires 325 reactions and 56 species [46] for a comprehensive chemical description, including nitrogen chemistry. A generalized form for an arbitrary elementary chemical mechanism with L reversible reactions and N_s species is expressed below:

$$\sum_{\alpha=1}^{N_s} \nu'_{l\alpha} M_\alpha \rightleftharpoons \sum_{\alpha=1}^{N_s} \nu''_{l\alpha} M_\alpha \quad (l = 1, 2, ..., L) \ . \tag{2.7}$$

Here M_α denotes a chemical species symbol, and $\nu'_{l\alpha}$ and $\nu''_{l\alpha}$ are the stoichiometric coefficients in the elementary reactions. The rate expressions for elementary reactions are usually specified using the modified Arrhenius form. The reaction rates thus are dependent on species concentrations and temperature. The net rate of change of a species can be calculated by summing up the contributions from all the reactions involving that species, leading to a system of ordinary differential equations (ODEs) with a size that is equal to the total number of species. Each of the elementary chemical reactions considered has a characteristic time scale (based on its rate expression), leading to a wide range of time scales in the chemical mechanism. The presence of disparate time scales makes the system of ODE's stiff, and demands that direct time integration of the set of ODE's be performed with integration sub-time-steps dictated by the smallest time scales in the reaction mechanism.

For large chemical mechanisms with disparate time scales, time integration typically dominates the computational effort. In a numerical simulation where time-integration has to be performed at each grid point in the computational domain, even with a reduced chemical mechanism, the chemistry calculations can account for more than 90% of the total computational time; therefore, detailed chemical mechanisms are usually avoided in time-dependent, three-dimensional numerical simulations. This inability to account for the detailed chemistry in numerical studies because of excessive computational cost has led to the development of various techniques that aim to make it possible to incorporate realistic chemistry in the

numerical simulation of practical combustion systems. Two such techniques are: (1) chemistry reduction, and (2) storage/retrieval schemes. Detailed information about these techniques can be found in [47–52].

Apart from the techniques mentioned above, the use of single-step or two-step global chemistry mechanisms in computational studies has also been reported [23, 53, 54]. In global mechanisms, the reaction order, pre-exponential coefficient, and activation temperature are tuned to match experimental data for canonical configurations (for example, one-dimensional laminar premixed/nonpremixed flames). Global mechanisms crudely approximate detailed chemical reactions, often lack accuracy, and do not fully capture finite-rate chemistry effects.

2.3 Turbulent Combustion Modeling

At moderate-to-high Reynolds numbers, turbulent flows contain a wide range of length and time scales. Turbulent flows are characterized by their unsteady, three-dimensional, fluctuating flow fields. The structure and description of turbulence still remains one of most challenging fundamental fields in classical physics. The flow description gets more complex in the presence of chemical reactions, and the range of length and time scales becomes wider. Turbulence and combustion are intimately coupled and interact with each other. Chemical reactions lead to significant density changes due to the release of heat, which in turn affects the dynamics of the flowfield. The large-scale motions of turbulence effectively augment the molecular diffusive rates of species and heat, and may enhance or quench the chemical reaction.

The conservation equations (Eqs. (2.1) – (2.4)) and detailed chemistry have been applied to laminar flames (for example [55]) with great success, highlighting that the present knowledge of chemical kinetics and molecular transport processes is adequate to make good predictions from first principles in limited cases. However, turbulent reactive flows, characterized by a broad spectrum of length and time scales, are very difficult to model and measure due to complex interactions between turbulence and other closely linked processes.

A variety of numerical methods have been developed to model and simulate turbulent combustion processes. Three categories can be distinguished: Direct

Numerical Simulation (DNS), Large Eddy Simulation (LES) and Reynolds Averaged Simulation (RAS).

2.3.1 Direct Numerical Simulation (DNS)

DNS appears to be a very straight-forward approach to model a turbulent reacting flow. In DNS, the instantaneous conservation equations are solved exactly: a complete time-dependent, three-dimensional simulation is performed that resolves all length and time scales in the flow. However, even in the absence of chemical reactions, DNS can only be carried out for relatively low-Reynolds-number turbulent flows, and even there, the computational requirements are high [56]. In a turbulent flow, the ratio of the largest to smallest length scales is proportional to $Re^{3/4}$, where Re is a turbulence Reynolds number [56]. Therefore, the number of grid points required to resolve all scales would be proportional to $Re^{9/4}$ for a three-dimensional simulation. At the same time, the computational timestep must decrease with increasing Re, as the temporal resolution is governed by the smallest, energy-dissipating scales. Furthermore, the presence of chemical reactions not only widens the range of length and time scales in the flow, but also results in an enormous computational load because of the expensive finite-rate chemistry calculations.

Advances in computing power have allowed progressively higher Reynolds numbers to be simulated [57, 58] and have allowed consideration of chemically reacting turbulent flows [59, 60], though at an enormous computational cost. For example, a DNS study of a three-dimensional, turbulent, temporally-evolving, planar CO/H_2 jet flame [60] with detailed chemistry at a Reynolds number of 9000 and with 500 million grid points required about 1 million CPU hours. In general, DNS remains inaccessible for turbulent chemically reacting flows of engineering interest, and several simplifications such as constant density, low Mach number, constant molecular transport properties, infinitely-fast or simplified multi-step chemistry are generally introduced.

A major limitation of DNS is that most of the computational effort is spent on solving the smallest dissipative scales, which do not contribute directly to the mean flow and contain negligible turbulent kinetic energy. Owing to its excessive com-

putational cost, DNS remains a research tool generally applied to simple canonical configurations or used to calibrate models based on other approaches [61–63].

2.3.2 RAS and LES Modeling Approaches

The necessity to represent the dynamics of all relevant length scales while being limited to explicitly resolving a limited range of scales in computations of practical flows has led to the development of turbulence modeling techniques. These approaches reduce the dynamic range of scales that is implicit in the instantaneous equations at high Reynolds numbers by averaging (Reynolds-averaged simulation) or spatial filtering (large-eddy simulation). The effects of unresolved scales then are modeled.

2.3.2.1 Reynolds-Averaged Simulation (RAS)

Generally, one is not interested in the full three dimensional time-dependent flow evolution in engineering applications. In statistically stationary flows, for example, one is primarily interested in time-averaged mean quantities. That is the rationale behind RAS methods, where transport equations for mean quantities are solved, with effects of all turbulent fluctuations about the local mean being modeled. In RAS one averages the instantaneous mass, momentum, species and energy equations to obtain equations for the mean fields. This introduces a term involving correlations of velocity fluctuations that plays the role of an apparent turbulent stress (denoted as the "Reynolds stress") in the mean momentum equation. The Reynolds stress can be modeled in terms of mean quantities or can be obtained by solving the Reynolds-stress transport equations derived from the Navier-Stokes equations [64–69]. However, the transport equations for the Reynolds stresses themselves contain unknown higher-order turbulence moments. Therefore, modeling needs to be done either for the Reynolds stress itself (algebraic models) or for the higher-order moments that appear in the Reynolds-stress transport equations. The available RAS turbulence models include zero-equation mixing-length models, one-equation models, two-equation k-ϵ models, and two-equation k-ω models, among others. Reynolds-stress transport models (RSM) require up to six additional modeled transport equations (one for each component of Reynolds stress).

RSM models are more expensive computationally than the more widely used two-equation models.

For complex flows, zero-equation and one-equation models usually are too simplistic to be reliable. Two-equation models are found to be reasonably accurate in many cases, but perform poorly in the simulation of complex vortical-shear layer interactions, post-separated flows, and mixing layers [70–75]. The more complicated RSM approach is computationally expensive, and it is not clear if the improvement in accuracy is worth the added computational cost.

The two-equation models have been widely used to close the turbulent transport terms in the mean momentum equations. Two-equation models usually are based on a gradient transport hypothesis, i.e., the assumption that the Reynolds stresses are proportional to the gradients in the mean velocity field. Loosely speaking, this is consistent with the idea that the Reynolds stresses are analogous to the viscous stresses in the kinetic theory of gases, with the former representing the stress due to the ensemble average of velocity fluctuations and the latter representing the stress due to the thermal velocities of molecules at a given point in a fluid. Thus, using a gradient transport hypothesis, Reynolds stresses can be thought of in terms of an apparent turbulent viscosity. The closures for turbulent transport terms in the mean species and energy equations are also generally based on a gradient transport hypothesis. Other approaches include solving transport equations for higher turbulence moments.

Another term (arguably the most important in turbulent combustion) that needs to be modeled is the mean chemical source term in the mean species equations. Available closures for the mean chemical source term include the Arrhenius model, flamelet models, conditional moment closure models, and probability density function models, among others. Details of these models (in the LES context) are provided in Section 2.4.4.

The increasing focus on the efficient production of energy from hydrocarbons and strict regulation of pollutant emissions has placed emphasis on developing high-fidelity design tools. These tools demand a reasonably accurate prediction of the time-evolution of combustion systems; that typically cannot be achieved using RAS where only the mean flow is accounted for. An alternative is LES, where the largest scales of motion are resolved explicitly.

2.3.2.2 Large-Eddy Simulation (LES)

LES is an intermediate approach between DNS and mean-flow-based RAS methods. The technique of LES emerged from the research of meteorologists in the 1960s. In LES, the larger three-dimensional unsteady turbulent motions are directly represented, whereas the effects of the smaller-scale motions are modeled. In other words, the LES technique is based on separation of the scales into two categories: only the scales of motion that carry appreciable energy (i.e., the large scales) are computed in LES while the effects of the small scales are taken into account through subfilter-scale (SFS) models [56]. The rationale behind LES is that the small scales tend to be more homogeneous and isotropic, and less affected by the boundary conditions than the large scales; therefore, it is expected that it should be possible to parameterize the effects of small scales using simpler and more universal models compared to RAS.

LES is expected to be more accurate and general than RAS, since the large, energy-containing, flow-dependent scales are captured explicitly and only the (presumably) more universal small-scale dynamics require modeling. Furthermore, since the resolved scales are responsible for a significant proportion of the Reynolds stresses, modeling errors should be smaller. LES is also expected to capture phenomena that are difficult to accommodate in Reynolds-averaged approaches, such as large-scale unsteadiness and combustion instabilities. Combustion instabilities generally manifest themselves as large-scale coherent structures resulting from an interaction between the hydrodynamic flow field, chemical heat release and acoustic waves. These instabilities can lead to system-wide variation of the properties, noise, unexpected heat transfer rates and even the destruction of the combustion device. It is possible to predict such instabilities using LES, and LES can be used to evaluate active and passive control measures in the combustion devices [76, 77]. A comparison of the three commonly used numerical methods for turbulence (namely, DNS, LES, and RAS) is presented in Table 2.1.

Accurate predictions of scalar mixing and turbulent scalar dissipation rates are of crucial importance in the numerical simulation of chemical reactions. Since mixing behavior is controlled by the large scales of motion in a turbulent flow, LES with its explicit capturing of the large-scale dynamics holds promise compared to RAS approaches. There is a wide and rapidly growing body of evidence that

Method	DNS	LES	RAS
Models needed	None	Effect of small scales on large scale; presumably universal	Effect of all scales on mean flow
Quantities computed	Instantaneous fields	Filtered instantaneous fields	Mean flow
Grid requirement	Fine	Intermediate	Coarse
Computational Requirements	Enormous; Almost impossible for practical applications	Significant	Economical
Accuracy	Most accurate	Accurate	Limited accuracy
Usage	Academia; Mostly for model development and validation	Academia; At acceptance stage in industry	Widely used in industry

Table 2.1. Comparison of commonly used turbulence models.

demonstrates quantitative advantages of LES in modeling studies of laboratory flames [5–7] and in applications to gas-turbine combustors [8–11], IC engines [12–14], and other combustion systems.

To separate the large from the small scales in LES, spatial filtering is used. The filtered (resolved or large-scale) variable corresponding to an arbitrary field $f(\underline{x}, t)$, is denoted by an overbar, and is defined as:

$$\overline{f} = \overline{f}\,(\underline{x}, t) = \int_D f\,(\underline{r}, t)\, G\,(\underline{x} - \underline{r}; \Delta)\, d\underline{r}\ . \tag{2.8}$$

Here D is the entire domain, G is the filter function, and Δ is the characteristic filter width; this corresponds to the wavelength of the smallest scale that is retained by the filtering operation. The filtering operation damps out fluctuations smaller than the filter width. Some of the standard filters include box and Gaussian filters in physical space and cut-off filters in spectral space.

A mass-weighted, Favre filtering is introduced in variable-density flows:

$$\tilde{f}\,(\underline{x}, t) = \overline{\rho f}/\overline{\rho} = \int_D \rho\,(\underline{r}, t)\, f\,(\underline{r}, t)\, G\,(\underline{x} - \underline{r}; \Delta)\, d\underline{r}/\overline{\rho}\ . \tag{2.9}$$

2.4 Governing Equations for LES

The governing equations in LES are derived by spatial filtering of the instantaneous mass, momentum, species, and energy equations. The filtering operation, which leads to the resolution of only those scales greater than the filter size, considerably reduces the degrees of freedom in the governing equations, but leads to a number of unclosed terms in the governing equations. The unclosed terms arise due to the filtering of the nonlinear terms. Favre-filtered representation of key variables is generally preferred since it reduces the number of unclosed variables.

The resulting filtered equations are given by (using Cartesian tensor notation) [15]:

- Mass

$$\frac{\partial \bar{\rho}}{\partial t} + \frac{\partial}{\partial x_i}\left[\bar{\rho}\widetilde{u_i}\right] = 0 \tag{2.10}$$

- Momentum ($j = 1, 2, 3$)

$$\frac{\partial}{\partial t}\left[\bar{\rho}\widetilde{u_j}\right] + \frac{\partial}{\partial x_i}\left[\bar{\rho}\widetilde{u_i}\widetilde{u_j}\right] = -\frac{\partial}{\partial x_i}\left[\bar{\rho}\left(\widetilde{u_i u_j} - \widetilde{u_i}\widetilde{u_j}\right)\right] + \frac{\partial \overline{\tau_{ij}}}{\partial x_i} - \frac{\partial \bar{p}}{\partial x_j} + \overline{\rho g_j} \tag{2.11}$$

- Chemical species (for N_s species, $\alpha = 1, 2, \ldots, N_s$)

$$\frac{\partial \bar{\rho}\widetilde{Y_\alpha}}{\partial t} + \frac{\partial \bar{\rho}\widetilde{Y_\alpha}\widetilde{u_i}}{\partial x_i} = -\frac{\partial \bar{\rho}\left(\widetilde{Y_\alpha u_i} - \widetilde{Y_\alpha}\widetilde{u_i}\right)}{\partial x_i} - \frac{\partial \overline{J_i^\alpha}}{\partial x_i} + \bar{\rho}\widetilde{S_\alpha} \tag{2.12}$$

- Absolute enthalpy

$$\frac{\partial \bar{\rho}\widetilde{h}}{\partial t} + \frac{\partial \bar{\rho}\widetilde{h}\widetilde{u_i}}{\partial x_i} = -\frac{\partial \bar{\rho}\left(\widetilde{hu_i} - \widetilde{h}\widetilde{u_i}\right)}{\partial x_i} - \frac{\partial \overline{J_i^h}}{\partial x_i} + \frac{D\bar{p}}{Dt} + \overline{\tau_{ij}\frac{\partial u_j}{\partial x_i}} + \overline{\rho S_{\text{radiation}}} \tag{2.13}$$

The above form of the filtered equations requires that the filtering operator $\bar{}$ commutes with spatial and temporal differentiation. The filtered equations contain a number of unclosed terms that need to be modeled. The terms that require modeling can be grouped based on their similar physical interpretation into the following categories:

- $\overline{\tau_{ij}}$, $\overline{J_i^\alpha}$, and $\overline{J_i^h}$: The first term is the filtered viscous stress tensor, representing the force due to the action of the molecular viscosity on the fluid flow. The latter two terms represent the molecular diffusive fluxes of species α and enthalpy, respectively. Details of modeling of these terms are provided in Section 2.4.1.

- $\bar{\rho}\left(\widetilde{u_i u_j} - \widetilde{u}_i \widetilde{u}_j\right)$: This term represents the effect of the subfilter-scale (unresolved) velocity fluctuations on the resolved scales, and is known as the subfilter-scale stress (SFS) tensor. The SFS stress tensor must be modeled in terms of resolved quantities to close the set of filtered governing equations. More details on the modeling of this term is presented in Section 2.4.2.

- $\left(\widetilde{Y_\alpha u_i} - \widetilde{Y}_\alpha \widetilde{u}_i\right)$ and $\left(\widetilde{h u_i} - \widetilde{h}\widetilde{u}_i\right)$: These unclosed terms are interpreted as the unresolved (subfilter) fluxes of species α and enthalpy, respectively, and are modeled in terms of resolved fields using a gradient transport hypothesis for the closure. Modeling details are provided in Section 2.4.3.

- $\overline{\tau_{ij}\frac{\partial u_j}{\partial x_i}}$: The filtered viscous dissipation term is usually neglected for high Reynolds Number, low Mach number flows.

- $\widetilde{S_\alpha}$: The modeling of the filtered chemical source term is of utmost importance in LES of turbulent reacting flows. The filtered chemical source term arises from the highly nonlinear interactions between species mass fractions, temperature and pressure. It often is dominated by subfilter-scale processes, thus making it imperative to account for the subfilter dynamics through a closure model. The various approaches to model the filtered chemical source term are explained in Section 2.4.4.

- $\overline{\rho S_{\text{radiation}}}$: The filtered radiative source term is similar in nature to the filtered chemical source term in the sense that it involves nonlinear interactions between temperature, species mass-fraction-dependent absorption coefficient, and incident radiation. Common methods being used for the modeling of this term are described in Chapter 3.

The various unclosed terms listed above are summarized in Table 2.2. Details about their modeling are provided in the following subsections.

Term	Remark	Modeling Approximation
$\overline{\tau_{ij}}$, $\overline{J_i^\alpha}$, $\overline{J_i^h}$	Filtered molecular transport terms	Computed from filtered quantities; Subfilter fluctuations neglected
$\bar{\rho}\left(\widetilde{u_i u_j} - \widetilde{u}_i\widetilde{u}_j\right)$	Effect of SFS velocity fluctuations on resolved scales	Most commonly, eddy-viscosity models
$\left(\widetilde{Y_\alpha u_i} - \widetilde{Y_\alpha}\widetilde{u_i}\right)$	Subfilter-scale flux of species α	Gradient Transport
$\left(\widetilde{hu_i} - \widetilde{h}\widetilde{u_i}\right)$	Subfilter-scale enthalpy flux	Gradient Transport
$\overline{\tau_{ij}\frac{\partial u_j}{\partial x_i}}$	Filtered viscous dissipation	Neglected (usually for high Re, Low Ma flows)
$\widetilde{S_\alpha}$	Filtered chemical source term for species α	Chemistry modeling (Details in Section 2.4.4)
$\overline{\rho S_{\text{radiation}}}$	Filtered radiative source term	Radiation modeling (Details in Sections 3.2 and 3.4)

Table 2.2. Unclosed terms that require modeling in the set of filtered equations for LES.

2.4.1 Filtered Viscous Transport Terms

The filtered molecular transport terms usually neglect the nonlinearities in the molecular transport expressions (Eqs. (2.5) and (2.6)). This approximation is justified from the work of Verman et al. [78] who conducted *a priori* tests for the filtered diffusion terms using DNS data of a mixing layer.

The filtered viscous stress tensor for a Newtonian flow is commonly expressed as follows:

$$\overline{\tau_{ij}} = \mu(\widetilde{T})\left(\frac{\partial \widetilde{u}_i}{\partial x_j} + \frac{\partial \widetilde{u}_j}{\partial x_i}\right) - \frac{2}{3}\mu(\widetilde{T})\delta_{ij}\left(\frac{\partial \widetilde{u}_k}{\partial x_k}\right) \tag{2.14}$$

where $\mu(\widetilde{T})$ is the dynamic viscosity of the gaseous mixture at the filtered temperature. Sutherland's law [79] is generally used for the temperature dependence of viscosity.

The filtered diffusive fluxes of species and enthalpy are based on Fick's law of diffusion and Fourier's law of conduction, respectively. Furthermore, Lewis

numbers are assumed to be unity with equal molecular diffusivities for all species:

$$\overline{J}_i^{\alpha} = -\rho D(\widetilde{T}) \frac{\partial \widetilde{Y}_{\alpha}}{\partial x_i} \tag{2.15}$$

$$\overline{J}_i^{h} = -\rho D(\widetilde{T}) \frac{\partial \widetilde{h}}{\partial x_i} \tag{2.16}$$

where D is the molecular diffusivity for all species at the filtered temperature.

2.4.2 SFS Stress Tensor Closure

The filtering of the instantaneous Navier-Stokes equation leads to an extra term on the right-hand side: the divergence of T_{ij}, where T_{ij} is given by:

$$T_{ij} = \bar{\rho} \left(\widetilde{u_i u_j} - \widetilde{u}_i \widetilde{u}_j \right) \ . \tag{2.17}$$

This term T_{ij}, also known as the SFS stress tensor, denotes the effect of subfilter-scale (unresolved) velocity fluctuations on the resolved scales, and needs to be modeled to close the filtered Navier-Stokes equation. Several SFS models have been proposed in the literature; these models have mostly been proposed for incompressible flows, and were modified later to account for the SFS stresses in variable-density flows. SFS models in variable-density flows can be broadly classified into three categories: eddy-viscosity models, similarity models, and mixed models that combine eddy viscosity and similarity expressions. The Smagorinsky model [80, 81], which is an eddy-viscosity type model, is the most commonly used SFS model and is widely reported in the literature.

Other available approaches include probability density function based closure [20, 82], two-point closure methods, SFS stress-tensor-transport equation methods [83] and SFS kinetic-energy transport equation methods [84, 85]. Both the eddy-viscosity and the similarity models relate the SFS stress tensor to the resolved quantities at the same instant in time t and in a neighborhood about $\underline{x}$. In contrast, transport-equation SFS models incorporate history and nonlocal effects by solving modeled transport equations for the SFS stress tensor. In this sense they are analogous to RSM in the RAS context.

Another approach to SFS tensor modeling is the Monotone Integrated LES

(MILES) method [86]. This is based on the observation that the high-resolution numerical methods that are typically used for LES (e.g., nonlinear, second-order monotone schemes) give rise to numerical errors whose character is similar to that desired in an SFS model. Thus, the instantaneous Navier-Stokes equations are solved using meshes that are too coarse to resolve the small scales, and the SFS model is implicit in the numerical method.

2.4.2.1 Interplay Between SFS Model and Numerical Error, and Convergence of Filtered Equations

With grid refinement (progressive reduction of grid spacing dh), LES with an explicit SFS model with fixed filter width Δ should converge to the exact solution of the modeled filtered equations. Full convergence may require a large value of Δ/dh. In usual practice, however, Δ/dh remains fixed at a value close to unity. In that case, the subfilter physical model changes with the refinement of the grid and this leads inevitably to an interaction between the modeled physics and the numerical error, which is difficult to unravel. The numerical error competes with the SFS model in dissipating the turbulent kinetic energy, and it has been suggested that the use of dissipative (upwind-based) schemes should be avoided in discretizing the advective term in the filtered equations. Also, with an implicit filter in place (grid spacing acting as a filter), LES solutions may approach the exact solution of the instantaneous conservation equations (i.e., DNS solution) with the refinement of grid.

2.4.2.2 Dynamic Modeling

An approach to dynamically determine local values for subfilter-scale model coefficients based on information contained in the resolved scales was proposed by Germano [87]. This approach is not limited to the Smagorinsky model, although much of the analysis and development has been done in that context. The dynamic procedure is extendable to compute the coefficients in similarity models and mixed models [88–90]. The most common dynamic procedures require averaging in directions of statistical homogeneity, making them inapplicable to complex unsteady flows with no directions of homogeneity. A Lagrangian dynamic procedure [91],

where averaging is done along fluid particle trajectories, is more broadly applicable and has been applied to complex flows including in-cylinder flows in reciprocating engines [92].

2.4.3 Subfilter Closures for Turbulent Transport of Enthalpy and Species

The filtered equations for enthalpy and species contain additional terms due to the nonlinearities present in the advection terms in the instantaneous equations. These unclosed terms ($\widetilde{Y_\alpha u_i} - \widetilde{Y}_\alpha \widetilde{u}_i$ and $\widetilde{hu_i} - \widetilde{h}\widetilde{u}_i$) represent the unresolved (subfilter-scale) fluxes of species and enthalpy, and need to be modeled in terms of resolved quantities. The most common closure for these quantities is through an eddy-diffusion model. The model employs a gradient transport hypothesis and proposes that the unresolved turbulent flux is proportional to the gradient in the filtered component of the quantity of interest. The eddy-diffusivity, which is the proportionality coefficient, is calculated using the eddy-viscosity (ν_T; from SFS stress closure) and the subfilter-scale turbulent Prandtl and Schmidt numbers:

$$\bar{\rho}\left(\widetilde{Y_\alpha u_i} - \widetilde{Y}_\alpha \widetilde{u}_i\right) = -\frac{\bar{\rho}\nu_T}{Sc_T}\frac{\partial \widetilde{Y}_\alpha}{\partial x_j} \tag{2.18}$$

$$\bar{\rho}\left(\widetilde{hu_i} - \widetilde{h}\widetilde{u}_i\right) = -\frac{\bar{\rho}\nu_T}{Pr_T}\frac{\partial \widetilde{h}}{\partial x_j} \ . \tag{2.19}$$

Fixed constant values are used usually for turbulent Prandtl and Schmidt numbers. However, they can be computed dynamically following the procedure suggested by Piomelli et al. [90] for the dynamic evaluation of turbulent Prandtl number. Speziale et al. [93] proposed a mixed model to close the subfilter enthalpy transport term, which is similar in nature to the mixed model described in SFS stress closures. Again, the model coefficients in the mixed model can be computed dynamically [90] for better accuracy.

2.4.4 Closures for the Filtered Chemical Source Term ($\widetilde{S_\alpha}$)

The modeling of the filtered chemical source term is of principal interest in turbulent combustion modeling. The instantaneous chemical source term is highly nonlinear with an exponential temperature dependence, and involves complex interaction between the various fluctuating quantities (species mass-fractions, temperature, pressure). The filtered chemical source term is usually significantly different from the chemical source term based on the filtered quantities, and such differences are referred to in the turbulent combustion literature as manifestations of turbulence–chemistry interactions. Neglecting these interactions, or using an overly simplistic treatment, can alter the flame structure both locally and globally, and will lead to inaccurate predictions of temperature and pollutant species.

Apart from the presence of the severe nonlinearities, modeling of the filtered chemical source term is complicated by the fact that the information in the resolved scales cannot be used in any straightforward way to model the filtered chemical source term. This is because the resolved component of the filtered chemical source term in LES of high-Reynolds-number flows is generally small. In nonpremixed systems, fuel and oxidizer have to mix at the molecular level for the chemical reaction to take place. Turbulent mixing reduces the scalar variance, but it is only the molecular diffusion that ultimately allows for the chemical reactions to occur. In the same manner, in premixed systems, fuel and oxidizer are already mixed at a molecular level but at low temperatures. The large-scale turbulent motions in the combustion system mix the unburned low-temperature reactants with the high-temperature products; however it is ultimately the molecular diffusion of heat that heats unburned reactants to sufficiently high temperatures that the chemical reaction occurs. The phenomenon of molecular mixing, which governs the rate of chemical reactions as explained above, takes place at the smallest dissipative scales; this implies that essentially no portion of the filtered chemical source term can be resolved in LES.

The absence of a resolved component of the filtered chemical source term suggests that the entire chemical source term has to modeled in LES, which is similar to the situation in RAS approaches. This can also be understood from the viewpoint that since chemical reactions take place at the smallest scales, and neither

LES nor RAS explicitly resolve the scales of interest (the former approach only resolving the large scales and the latter approach modeling the effects of all the turbulent scales), essentially the entire chemical source term has to be modeled in both the LES and RAS approaches. For this reason, the closures for the chemical source term in LES are usually adapted from those developed in the RAS framework. The modeling of mean chemical source terms in RAS has been an active area of research for several decades. Many models have been proposed ranging from physical-argument-based-models (Arrhenius model, eddy break-up model and its variants, etc,), models that approximate the flame structure (flamelet models), to models that employ statistical techniques to account for the turbulent fluctuations (conditional moment closure method, transported probability density function method, linear eddy model). Veynante and Vervisch [15] have presented an extensive review of the closures used in RAS for the modeling of turbulent combustion. Other good reviews can be found in [16, 17]. LES of turbulent combustion has been an active research field for approximately 10 years, during which most of the chemistry closure models developed for RAS have been adapted to work as LES chemistry closures. Various reviews [94–97] provide the details of the filtered chemical source term models that have been used for LES of turbulent combustion.

Generally speaking, models for turbulent combustion can be divided into two categories based on the assumed time scales for chemistry relative to other physical time scales, leading to: (1) the slow/fast chemistry models; and (2) finite-rate chemistry models.

In the fast/slow chemistry models, the interaction between chemistry and turbulence is essentially ignored, assuming that the chemical time scales are either very short or very long compared to the turbulent fluctuations' time scales. Thus, either turbulent mixing or the slow chemistry is the rate-determining process. The Arrhenius model, wherein the functional form of the instantaneous rate equation is used to model the filtered chemical source term simply by replacing the instantaneous quantities with the filtered quantities, provides a reasonable approximation to the filtered chemical source term in the slow chemistry limit. This is because when the chemistry is very slow relative to the turbulent mixing, all the quantities would be well micro-mixed at the molecular level before the start of the chemical reactions.

The eddy break-up model [98] and its variants (eddy dissipation model [15]), on the other hand, assume that the chemistry is fast compared to the turbulent mixing. In that case, turbulent transport of species and enthalpy is the rate-controlling process. These models are based on the concept of an equilibrium turbulence energy cascade in nonreacting flows.

Steady flamelet models and their variants, with decoupled chemical kinetics and turbulence hydrodynamics, assume that local structure of a turbulent flame corresponds to that of a laminar flame. This assumption requires that the spatial gradients normal to the flame-front must be dominant. When such conditions exist, there is a tight local coupling between chemical kinetics and molecular transport.

The above models generally are not sufficient in combustion systems where the effects of the finite-rate chemistry are important. For example, the reactions might be slow, and local extinction and possible reignition might occur. It is essential to capture the turbulence–chemistry interactions in such systems, and thus finite-rate models are required to account for the high nonlinearities present in the chemical source term. Pitsch and Steiner [99] have used an unsteady flamelet model for this purpose. In general, statistical techniques have shown great promise in treating the nonlinearities in the chemical source term. Various models have been proposed that use probability theory to estimate the filtered chemical source term. Conditional-moment-closure (CMC) models [100, 101] solve for the conditionally filtered first and higher moments of species mass-fractions and temperatures, where conditioning is usually done using a mixture-fraction variable in nonpremixed systems and a reaction progress variable in premixed systems. A good review of CMC models is available in [102].

Filtered density function models account for the effects of unresolved scalar fluctuations by considering the probability density function of the subfilter-scale quantities. FDF based models also employ a statistical approach, and can be further classified into presumed FDF models and transported FDF models. In presumed FDF models, the shape of the PDF is assumed (often a beta-function distribution) and is parameterized in terms of its lower moments, and modeled equations are solved for the parameters. This approach may not yield accurate results, as the functional form of the PDF is presumed with limited physical reasoning. In contrast, in transported FDF method one solves for the joint PDF of

subfilter-scale fluctuations of scalars, and is able to deal with arbitrary joint FDF shapes. The filtered chemical source term is in closed form and does not require any modeling assumption, which is the most compelling advantage of transported FDF methods. This has resulted in a huge interest in the development and application of transported FDF methods [6, 7, 18–23, 103]. In fact, any term that is solely dependent on the local scalars can be represented exactly in this method, no matter how nonlinear or complex it is. The transported FDF method is used in this work to close the filtered chemical source terms, and is discussed in more detail in Section 2.5. Another statistical approach, the linear eddy model [104], also has been used for LES of turbulent combustion. In that case, mechanistic stochastic models are employed to account for turbulence advection and mixing processes.

2.5 Transported FDF Methods

In reacting flows, turbulence and chemistry interact at the smallest (i.e., subfilter) scales. Little, if any, of the effects of turbulent fluctuations can be resolved in LES, and, therefore, the entire filtered chemical source term needs to be modeled. This situation is essentially same as for a RAS approach, and consequently the closure models proposed for filtered chemical source terms and applied in LES are essentially adaptations of closures developed for RAS formulations. Among the most promising closures available in RAS are the transported PDF methods, where the chemical source terms are exactly represented. The use of PDF methods was originally motivated by difficulties encountered in the closure of chemical source terms when using moment methods [105–107]. In PDF methods, one solves for the evolution of the joint probability density function of a set of variables that determine the local thermochemical state of a reacting system. A comprehensive description of PDF methodology has been given by Pope [108]. Other reviews are available in [109, 110], and a recent comprehensive review can be found in [111]. The predictive capability of PDF methods in RAS is well established [16, 56, 112], and this has generated interest and research activity in the application of PDF-based closures in LES of turbulent combustion [6, 7, 18–23]. In LES, the filtered-density function (FDF) is used as a statistical measure instead of the PDF. The physical

interpretation of a FDF is very different from a PDF. The FDF represents the instantaneous stochastic subfilter distribution of the quantity of interest, and is a fluctuating function that evolves with the flow, unlike a PDF which denotes a deterministic statistical property of system [113]. Nevertheless, for present purposes the FDF can be thought of as a PDF of the subfilter distribution. In the LES context, the terms "PDF" and "FDF" often have been used interchangeably in the literature. The PDF (to be precise, FDF) based closures in LES are denoted as FDF methods. The history of the development of FDF methods is presented in Section 2.5.1. The composition FDF method [19] is the most widely used FDF method, and is explained in detail in Section 2.5.2. Lagrangian Monte Carlo techniques [108] for the solution of modeled composition FDF transport equations are discussed in Section 2.6, along with the details of their numerical implementation.

2.5.1 Background of FDF Methods

The use of PDF-based approaches for SFS modeling was first suggested by Givi [114]. However, it was the formal definition of the FDF by Pope [115] that facilitated the implementation of FDF methods as SFS models in LES. An FDF represents the joint probability density function of subfilter-scale fluctuations, and includes a complete one-point subfilter statistical description of its variables.

Madnia and Givi [116] were the first to conduct a numerical study using LES/FDF; there the shape of the FDF was specified *a priori* (a presumed FDF method). The use of presumed FDF's continued in several subsequent studies. In most cases, the thermochemical state was parameterized by a single conserved scalar mixture fraction (a fast chemistry limit), and the mixture fraction FDF was taken to have a beta-function distribution. The beta distribution is parameterized by its first two moments; therefore, a transport equation is solved for the filtered conserved scalar, and an algebraic relation is normally used for the subfilter scalar variance. Solution of a modeled transport equation can also be used to obtain the subfilter scalar variance. The beta function promises to be a better model for the presumed FDF approach in LES than for the presumed PDF approach in RAS. This is because the FDF generally is narrower (smaller fluctuations). Moreover, intermittency, which is a significant source of error when using the beta function

in RAS, is less of a problem in the LES context since intermittency mostly occurs on the resolved scales. Several studies have investigated the validity of the beta function approximation for the FDF of mixture fraction for nonpremixed reacting flows of constant and variable density [117–119]. They concluded that the beta function distribution is a good approximation for the FDF of mixture fraction, and that this estimate is better in LES than in RAS models. However, Tong [120] and Tong et al. [121] reported that the FDF often substantially deviates from a beta function. Givi et al. [122] noted that the true shape of a probability distribution is strongly dependent on the actual physics of mixing in a given flow condition.

A more powerful technique, compared to assuming the shape of the FDF, is to determine the FDF directly via the solution of its transport equation. This class of methods is referred to as transported FDF methods. Transported FDF methods eliminate the need to specify the FDF shape *a priori*. The first application of transported FDF methods was reported by Colucci et al. [18]. They developed and solved a modeled transport equation for the marginal scalar FDF (SFDF) in constant-density flows, and demonstrated the importance of subfilter-scale fluctuations for accurate modeling of the filtered chemical reaction rates. Jaberi et al. [19] extended the SFDF approach to variable-density flows and formulated a marginal scalar filtered mass density function (SFMDF) method.

The above approaches considered only the joint PDF of the scalar subfilter-scale fluctuations and, therefore, conventional methods (normally a gradient transport approximation) were used to close terms that involve subfilter-scale velocity fluctuations. Scalar FDF methods also require the filtered velocity fields through the solution of filtered momentum equations, and information about the turbulent time and length scales. Gicquel et al. [82] developed and solved a transport equation for the marginal velocity FDF (VFDF) in constant density flows, and showed the advantages of the FDF approach over conventional methods in accounting for the effects of subfilter-scale velocity correlations. The development of the joint FDF of velocity and scalar fields for constant density flows (VSFDF) was carried out by Sheikhi et al. [20]. Givi et al. [103] presented a joint velocity and scalar filtered mass density function method for variable density flows (VSFMDF), and applied the method to conduct LES of relatively simple flows. This method, in addition to the chemistry closure, provides an exact closure for the terms involving subfil-

ter velocity fluctuations. However, although the velocity field is calculated, this method is still not stand-alone. Since the FDF is a one-point, one-time model, it contains no information on the time and length scales of unresolved turbulent motions. The subfilter turbulent dissipation field has to be provided externally to the process, to provide the necessary turbulence time-scale information. This external specification of time-scale information can be eliminated by considering turbulent frequency as a random variable in the FDF formulation. Such a method was reported by Sheikhi et al. [123] who considered a joint frequency–velocity–scalar FMDF to treat turbulent reacting flows.

The joint velocity–scalar FDF method is relatively new and is still in the development phase, and most applications of FDF methods to turbulent combustion [6, 7, 21–23] have been based on the marginal scalar FDF method, which is also known as the transported composition FDF method. Sheikhi et al. [7] conducted LES of Sandia Flame D [124, 125] using a variable-density marginal scalar FDF SFMDF closure, where they used a simple flamelet model to relate the instantaneous composition to the mixture fraction, and evolved the FDF of mixture fraction using a transported FDF approach. Raman et al. [6] applied a similar approach to a nonpremixed methane–hydrogen bluff-body stabilized flame [126]. James et al. [23] performed LES of the Sandia/Sydney swirl burners (SM1 and SMA1) and the Sandia/Darmstadt piloted jet diffusion flame (Flame D) using a simplified two-step chemistry and the transported composition FDF method. Raman and Pitsch [22] considered a 16-species reduced methane–air chemistry and performed LES of Sandia Flames D and E. They used a transported FDF method where the joint FDF of species compositions and energy scalar was considered. Frankel et al. [40] used a composition FDF method to account for turbulence–chemistry interactions and emission TRI, and neglected the unresolved absorption TRI by invoking the OTFA.

As discussed above, the joint frequency–velocity–scalar FDF method [123] is the most comprehensive LES/FDF model to date, but it is in the nascent stage. The joint velocity–scalar FDF method is potentially more accurate than composition FDF, but it remains immature. On the contrary, the SFMDF method or composition FDF method, has seen relatively more wide-spread usage and has proven to be quite effective in LES of turbulent flames [6, 7, 22, 23]. Hence, the transported

composition FDF in conjunction with the finite volume code OpenFOAM [127] is used in this study to account for the subfilter-scale turbulence–chemistry interactions and SFS emission TRI, as described in the following sections. As explained in Section 3.4, SFS absorption TRI is captured through the use of a photon Monte Carlo method [37, 128] as the RTE solver.

2.5.2 The Transported Composition FDF Method

The transported composition FDF method considers the subfilter-level fluctuations of composition variables in a probabilistic manner [19]. The composition variables include all the scalars necessary to determine the thermodynamic state of the reacting mixture (i.e., for low-Ma flows, species mass-fractions and mixture specific enthalpy or temperature). The subfilter-scale species mass fractions and the energy scalar are treated as random variables. Loosely speaking, the composition FDF quantifies the probability of having a particular gas composition (including temperature) in the subfilter fluctuations.

The most remarkable feature of the FDF method is that (as in RAS-based PDF methods) one-point nonlinear terms, such as chemical reactions, can be treated exactly no matter how complicated they are. As an extension, any term in the FDF equation, as long as it is a function of the local scalar variables only, can be treated exactly by composition FDF methods. Frankel et al. [40] used this fact to model the radiative emission including emission TRI. This is possible because radiative emission depends only on local quantities.

The exact treatment of local nonlinear terms in FDF methods is in contrast to conventional moment methods. In the latter approach, the filtered reaction rates can be determined only under special constraints of linearity or when the reactions are very fast or very slow compared to the turbulent time scales. Moreover, moment methods typically assume that only the lowest-order moments of a physical quantity Q are important and that higher moments can be neglected without significant loss of accuracy. However, in the FDF method, moments of all orders for any quantity Q, which is only a function of the scalar field $\underline{\phi}$ (here, species mass fraction and enthalpy), can be calculated directly from the FDF; the first moment is the filtered value of quantity Q. The quantity Q can include the absorption

coefficient κ, specific heat c_p, density ρ and any other quantities that depend only on $\underline{\phi}$.

The composition FDF is not a self-contained model. The filtered momentum equations must be solved for the velocity field $\underline{\widetilde{u}}$, and an SFS turbulence model (such as a Smagorinsky eddy-viscosity model) is required to determine both SFS diffusivity and the mixing rate used in the stochastic mixing model [129, 130]. As mentioned above, OpenFOAM (an open-source CFD code) [127] will be employed in this work to obtain the filtered velocity field.

2.5.2.1 Composition FDF Formulation for Variable Density Flows

For variable density flows, the filtered mass density function (FMDF) is considered instead of the filtered density function (FDF). Mathematically, the FMDF, denoted as $\mathcal{F}$, for a scalar composition vector $\underline{\phi}(\underline{x}, t)$ is defined as the mass-weighted spatially filtered value of the fine-grained density [19],

$$\mathcal{F}(\underline{\psi}; \underline{x}, t) \equiv \int_{-\infty}^{+\infty} \rho(\underline{x}', t)\ \varsigma[\underline{\psi}, \underline{\phi}(\underline{x}', t)]\ G(\underline{x}' - \underline{x})\ d\underline{x}'\ , \tag{2.20}$$

where the fine-grained density $\varsigma[\underline{\psi}, \underline{\phi}(\underline{x}, t)]$ is:

$$\varsigma[\underline{\psi}, \underline{\phi}(\underline{x}, t)] = \delta[\underline{\psi} - \underline{\phi}(\underline{x}, t)] \equiv \prod_{\alpha=1}^{\sigma} [\psi_\alpha - \phi_\alpha(\underline{x}, t)]\ . \tag{2.21}$$

In the above expressions, δ denotes the Dirac–delta function, G is the filter kernel, ρ is the density, σ is the size of scalar array, and $\underline{\psi}$ represents the composition space vector. The FMDF, $\mathcal{F}(\underline{\psi}; \underline{x}, t)$, is then the mass- and filter-kernel-weighted joint probability density of $\underline{\phi}$ having a certain composition $\underline{\psi}$ in a fluid in the vicinity of point $\underline{x}$ at time t. Integration of the FMDF over the entire composition space results in the filtered mass density at that point:

$$\int_{-\infty}^{+\infty} \mathcal{F}(\underline{\psi}; \underline{x}, t)\ d\underline{\psi} = \int_{-\infty}^{+\infty} \rho(\underline{x}, t)\ G(\underline{x}' - \underline{x})\ d\underline{x}' = \overline{\rho(\underline{x}, t)}\ . \tag{2.22}$$

Furthermore, the mass-weighted conditional filtered mean of a variable $Q(\underline{x}, t)$ is defined as:

$$\langle(\overline{Q(\underline{x},t)|\underline{\psi}}\rangle) \equiv \frac{\int_{-\infty}^{+\infty} \rho(\underline{x}',t)\ Q(\underline{x}',t)\ \varsigma[\underline{\psi},\underline{\phi}(\underline{x}',t)]\ G(\underline{x}'-\underline{x})\ d\underline{x}'}{\mathcal{F}(\underline{\psi};\underline{x},t)}\ . \tag{2.23}$$

The integration of the mass-weighted conditional filtered mean times the FMDF over the entire composition space results in the conventional filtered value of the product of mass density and the quantity Q:

$$\int_{-\infty}^{+\infty} \langle(\overline{Q(\underline{x},t)|\underline{\psi}}\rangle)\ \mathcal{F}(\underline{\psi};\underline{x},t)\ d\underline{\psi} = \overline{\rho(\underline{x},t)\ Q(\underline{x},t)} = \overline{\rho(\underline{x},t)}\ \widetilde{Q(\underline{x},t)}\ . \tag{2.24}$$

The expression for $\overline{Q(\underline{x},t)|\underline{\psi}}$ (Eq. 2.23) shows that if the variable Q is completely determined by the compositional vector $\underline{\phi}$ (i.e., $Q(\underline{x},t) = Q\left(\underline{\phi}(\underline{x},t)\right)$, then

$$\overline{Q(\underline{x},t)|\underline{\psi}} \equiv \widehat{Q}(\underline{\psi}) \tag{2.25}$$

Here the symbol $\widehat{\ }$ denotes that the variable Q can be determined from composition vector $\underline{\phi}$. Therefore, for any arbitrary variable $Q(\underline{x},t)$, which is only a function of the composition variable $\underline{\phi}$, Eq. (2.24) can be re-written as:

$$\int_{-\infty}^{+\infty} Q(\underline{\psi})\mathcal{F}(\underline{\psi};\underline{x},t)\ d\underline{\psi} = \overline{\rho(\underline{x},t)}\ \widetilde{Q(\underline{x},t)}\ . \tag{2.26}$$

This equation illustrates the most remarkable feature of the FDF method: any quantity $\widehat{Q}$ (i.e., $Q\left(\underline{\phi}(\underline{x},t)\right) = Q(\underline{x},t)$), regardless of its complexity, can be represented exactly in LES if the FMDF is known. The FMDF can be used not only to extract filtered quantities, but also higher moments of the fluctuations.

Following the usual practice in the literature, "FDF" will henceforth be used for "FMDF", unless noted otherwise.

2.5.2.2 Exact Transport Equation for the Composition FDF

The transport equation for the FDF $\mathcal{F}(\underline{\psi};\underline{\mathbf{x}},t)$ can be derived starting from the instantaneous conservation laws for the scalars. For a composition variable $\phi_\alpha(\underline{\mathbf{x}},t)$,

$$\rho \frac{D\phi_\alpha}{Dt} = -\frac{\partial J_i^\alpha}{\partial x_i} + \rho S_\alpha \ , \tag{2.27}$$

where D/Dt is the material derivative, $\underline{J}^\alpha$ is the molecular diffusive flux of ϕ_α, and S_α is the rate of creation of ϕ_α. Starting from Eq. (2.27), Colucci et al. [18] obtained a transport equation for the fine-grained density, $\varsigma[\underline{\psi}, \underline{\phi}(\underline{x}, t)]$. Jaberi et al. [19] obtained the following transport equation for FDF ($\mathcal{F}(\underline{\psi}; \underline{\mathbf{x}}, t)$) by spatially filtering the transport equation for fine-grained density and some algebraic manipulations:

$$\begin{aligned} &\tfrac{\partial \mathcal{F}}{\partial t} + \tfrac{\partial}{\partial x_i}[\widetilde{u}_i \ \mathcal{F}] + \tfrac{\partial}{\partial \psi_\alpha}[S_\alpha(\underline{\psi})\mathcal{F}] = \\ &-\tfrac{\partial}{\partial x_i}\left[\widetilde{u_i'|\underline{\psi}} \ \mathcal{F}\right] + \tfrac{\partial}{\partial \psi_\alpha}\left[\tfrac{1}{\overline{\rho}}\overline{\tfrac{\partial J_i^\alpha}{\partial x_i}|\underline{\psi}} \ \mathcal{F}\right] - \tfrac{\partial}{\partial \psi_\alpha}\left[\overline{S_{\alpha,\text{nonlocal}}|\underline{\psi}} \ \mathcal{F}\right] \ . \end{aligned} \tag{2.28}$$

This is an exact transport equation for the FDF. Here i and α represent directions in physical and composition space, respectively. The notation $\left(\overline{A|B}\right)$ denotes the conditional filtered value of term A, conditioned on the occurrence of event B. Similarly, the expression of the form $\left(\widetilde{A|B}\right)$ denotes the mass-weighted conditionally filtered value of term A. The first two terms on the left-hand side represent the transport of the FDF following the Favre filtered flow. The third term is the divergence of the flux of FDF in composition space due to source terms that depend only on the local composition (e.g., chemical reaction and radiative emission). These sources are represented exactly, no matter how nonlinear they are. The first two terms on the right-hand side emphasize the unclosed nature of SFS convection and mixing in composition FDF methodology, as indicated by the presence of the conditional filtered values. These terms require modeling. Modeling of these unclosed terms is discussed in the next section. The third term on the right-hand side is due to source terms that are not functions of local composition only (e.g., radiative absorption) and this term also requires modeling. Here a photon Monte Carlo method (Section 3.2.1) is used to model the effect of absorption.

2.5.2.3 Modeling in Composition FDF Methods

2.5.2.3.1 Subfilter-Scale Turbulent Transport

The first term on the right-hand side of Eq. (2.28) represents transport of the FDF in physical space by subfilter-scale velocity fluctuations. The composition FDF contains no information about the velocity fields, and hence this term needs to be modeled. A gradient-diffusion model is generally used. In that case, the unclosed flux of the FDF is proportional to the gradient of the FDF, with an apparent turbulent diffusivity that represents the effects of subfilter-scale motions:

$$\widetilde{u_i'|\underline{\psi}}\ \mathcal{F} \simeq -\overline{\rho}\ \Gamma_t \frac{\partial\left(\mathcal{F}/\overline{\rho}\right)}{\partial x_i}\ . \tag{2.29}$$

The apparent diffusivity (Γ_t) is calculated using the eddy-viscosity ν_T from a SFS stress closure, and the subfilter-scale turbulent Prandtl or Schmidt number (σ_ϕ):

$$\Gamma_t = \nu_T/\sigma_\phi\ . \tag{2.30}$$

2.5.2.3.2 Mixing Models

The second term on the right-hand side of Eq. (2.28) represents transport in the scalar (composition) space due to molecular transport: this is a "mixing" term. Spatial gradients that appear in the molecular mixing term require additional length-scale information that is not available in the one-point, one-time FDF formalism, and therefore this term needs to be modeled. This modeled term becomes very important when dealing with reactive flows, and has been one of the main limitations of probability-based methods (i.e., RAS/PDF and LES/FDF) for such flows. It is expected that the influence of the mixing model will be smaller for LES/FDF than in RAS/PDF simulations, since LES explicitly resolves the large-scale dynamics.

There are several constraints for a "good" mixing model, and these have been summarized in [16, 131]. Several mixing models have been proposed but none of them fully satisfies all of the constraints. One of the simplest models, proposed by Dopazo [132], is the interaction-by-exchange-with-the-mean, or the IEM

model [133]; this is also known as the LMSE (linear mean-square estimation) model. A known drawback of the IEM model is that it does not relax the PDF (in RAS/PDF simulations) to a Gaussian distribution in homogeneous isotropic turbulence, in contrast to experimental evidence. The conditional mixing term in the case of IEM can be written as,

$$\frac{\partial}{\partial \psi_\alpha}\left[-\frac{1}{\overline{\rho}}\overline{\frac{\partial J_i^\alpha}{\partial x_i}|\underline{\psi}}\,\mathcal{F}\right] \simeq \frac{\partial}{\partial x_i}\left[\overline{\rho}\,\Gamma\frac{\partial\left(\mathcal{F}/\overline{\rho}\right)}{\partial x_i}\right] + \frac{\partial}{\partial \psi_\alpha}\left[C_\phi \Omega_m(\psi_\alpha - \widetilde{\phi_\alpha})\mathcal{F}\right] \ , \quad (2.31)$$

where Γ is molecular diffusivity, C_ϕ is a model constant and Ω_m is the frequency of mixing within the subfilter scales. Note that the first term on the RHS in the above expression is actually not a part of the mixing model; it is added to make the model behave reasonably in regions where the flow is locally well resolved. Ω_m is given by

$$\Omega_m = \frac{\Gamma + \Gamma_t}{\Delta^2} \ , \quad (2.32)$$

where Δ is the local filter width.

An alternative to IEM is the coalescence-dispersion (CD) model, also known as the particle interaction model or stochastic mixing model or Curl's model. In this model, two notional particles* with distinct composition first "coalesce" and then "disperse" with identical compositions. Operationally, two particles p and q are selected at random in a control volume, and mix with a specified probability p_{mix} during one computational timestep dt. After mixing, the new scalar values on the two particles are the mass-weighted average of the values before mixing. The probability of a pair of particles mixing is given by

$$p_{\text{mix}} = C_\phi N \frac{\delta t}{\tau} \ , \quad (2.33)$$

where τ is a turbulence timescale for subfilter mixing ($\tau = \Omega_m^{-1}$), C_ϕ is the model constant, and N is the number of particles present in the control volume under consideration. A drawback of the CD model is that the new scalar values can only take a countable number of values. This can be overcome by using a modified CD

*Refer Section 2.6.1 for details on the context of these particles.

model proposed by Janicka et al. [134], so that the final scalar values can take any value between the bounds for that scalar. A second improvement to CD models is the age-biased CD model by Pope [135], in which the selection of particles for mixing is biased towards particles which have not mixed recently.

Both the IEM and CD models are nonlocal in reactive scalar space. In non-premixed combustion with fast chemistry, mixing based on IEM or CD can result in the transition of cold fuel and oxidizer particles across the reaction zone without the particles being subjected to chemical reaction. That violates the physical principle that mixing of adjacent material in physical space is equivalent to mixing of neighboring particles in reactive scalar space. The Euclidean Minimum Spanning Tree (EMST) model by Subramaniam and Pope [136, 137] addresses the above problem, and enforces locality in composition space. In the EMST model, the change in particle composition is determined by particle interactions along the edges of Euclidean minimum spanning trees constructed on ensembles of particles in the composition space.

Several mixing models have demonstrated success in simple configurations. However, the IEM and CD models (and variants) remain the most commonly employed due to their ability to handle realistic finite-rate chemistry more easily than others. In this work, a variant of the CD model is used.

2.5.2.4 Modeled Transport Equation for Composition FDF

The unclosed SFS convection and conditional mixing terms in the exact transport equation for $\mathcal{F}$ (Eq. 2.28) are treated using the gradient-diffusion model and a mixing model, respectively. The resulting modeled transport equation for the FDF, $\mathcal{F}(\underline{\psi};\underline{x},t)$ is

$$\frac{\partial \mathcal{F}}{\partial t} + \frac{\partial}{\partial x_i}\left[\widetilde{u}_i\ \mathcal{F}\right] + \frac{\partial}{\partial \psi_\alpha}[S_\alpha(\underline{\psi})\mathcal{F}] = \frac{\partial}{\partial x_i}\left[\overline{\rho}\left(\Gamma+\Gamma_t\right)\frac{\partial\left(\mathcal{F}/\overline{\rho}\right)}{\partial x_i}\right] + F_{\text{mix}} - \frac{\partial}{\partial \psi_\alpha}\left[\overline{S_{\alpha,\text{nonlocal}}|\underline{\psi}}\ \mathcal{F}\right] \ , \tag{2.34}$$

where F_{mix} is the flux in the composition space due to SFS molecular mixing and is obtained from a mixing model. For the IEM model, F_{mix} is:

$$F_{\text{mix}} = \frac{\partial}{\partial \psi_\alpha}\left[C_\phi \Omega_m (\psi_\alpha - \widetilde{\phi_\alpha})\mathcal{F}\right] \ . \tag{2.35}$$

The modeled transport equation for $\mathcal{F}$ is solved using a Lagrangian Monte Carlo method, as discussed in Section 2.6.

2.6 Solution to Modeled Composition FDF Transport Equation

The modeled composition FDF transport equation (Eq. 2.34) is similar in form to the modeled composition PDF transport equation encountered in RAS/PDF simulations [108]. Composition PDF methods in RAS have been an active research field for over two decades, and significant advances have been made in numerical solution algorithms for modeled composition PDF transport equations. These algorithms can be applied directly for LES/FDF methods. Here the key developments that have been made in solution techniques for composition PDFs are reviewed.

The modeled PDF (FDF) transport equation can be solved, in principle, by traditional finite-volume or finite-element methods. Janicka et al. [134] used this approach to solve for a composition PDF in a jet diffusion flame. In general, however, the PDF (FDF) transport equation has high dimensionality (up to $4+\sigma$ independent variables, where σ is the length of composition space vector), and is completely different from the traditional moment-closure model equations. The large number of independent variables makes it prohibitively expensive to use conventional grid-based methods, such as finite-volume methods (FVM), finite-difference methods (FDM), or finite-element methods (FEM) to solve Eq. (2.34), since the associated computational cost scales exponentially with the number of independent variables. Monte Carlo particle methods to the solution of the PDF

equation have been developed [108] as an alternative; in that case, there is only a linear growth in computational effort with the increase in number of independent variables. The key point in Monte Carlo methods is that the PDF (FDF) is represented by an ensemble of notional particles whose properties (compositions) evolve by deterministic or stochastic differential equations (SDEs) such that the particles follow the same PDF (FDF) as the solution of the modeled PDF (FDF) transport equation.

Monte Carlo methods have been applied both in the Eulerian sense (node-based particle) [110, 135] and the Lagrangian sense (particle-tracking) [108] to the solution of PDF equations. In the Eulerian node-based approach, a fixed number of particles is assigned to each cell in the grid. The particles do not individually represent physical mass, and therefore, do not have continuous locations; they are thus thought of as being located at cell-centers. The number of particles in each cell is constant, and transport processes such as diffusion and convection are modeled by exchanging particles in a given cell with particles from randomly selected neighboring cells. This method is relatively simple to implement, but has a major disadvantage that it introduces randomness in the implementation of both convection and turbulent diffusion, leading to a large statistical error. In contrast, in a Lagrangian particle-tracking method, notional particles are randomly distributed in the computational domain and are associated with the finite-volume cell that they occupy at a given instant of time. These particles represent a physical mass and their physical location is tracked throughout the flow field by solving for their evolution equations (SDEs). By its nature, the particle tracking method is grid-free; however, in general, a grid is required to extract the statistics of the scalars at discrete locations and for other purposes. The number of particles in a cell is not constant in this method, and fluctuates in time as particles move throughout the flow field. The Lagrangian particle-tracking method is more complicated and difficult to implement than the node-based Eulerian method, but brings a reduction in the statistical error since convection by the resolved velocity is not treated in a stochastic sense. Also, the Lagrangian method has lower numerical diffusion than the Eulerian method. A particle-tracking Monte Carlo method [138–140] will be used in this study to obtain the solution of the modeled composition FDF transport equation.

As discussed before, the composition FDF method is not self-contained; it requires information about the filtered velocity field for particle advection, turbulence length scales for SFS convection, and turbulence time-scales for SFS mixing from a flow solver. Therefore, a Lagrangian Monte Carlo method for the composition FDF needs to be coupled with a conventional grid-based flow solver, in a hybrid FV/particle composition FDF method. Details of the coupling procedure employed in this work are presented in Section 4.1.1. The solution algorithm used in this work is based on algorithms published by Pope and coworkers [108, 141, 142] and by Subramaniam and Haworth [138]. An algorithm developed by Zhang and Haworth [139] to ensure consistency between the values obtained by a FV solution and Monte Carlo solution is also used.

In stand-alone PDF (FDF) or hybrid FV/PDF (FDF) approaches, the mean (filtered) fields are extracted on the PDF (FDF) side by averaging over the particles. The extracted mean fields contain statistical noise which, when passed to the FV side, can lead to numerical instabilities. Therefore, coupling between the FV and particle representations in a hybrid RAS/PDF simulation usually involves simplifying assumptions for steady-state approaches, such as time-blending [139, 140] or loosely-coupled algorithms [142, 143], to minimize the statistical noise in the extracted fields. However, since LES is inherently transient, a time-accurate coupling is necessary, and no such steady-state simplifications can be made. An indirect feedback approach by Murodoglu et al. [142–144] reduces the statistical noise in the fields obtained from the PDF (FDF) side, and has been adopted in all of the LES/FDF studies conducted to date [6, 7, 22, 23, 103]. This approach will also be incorporated in this work, and is discussed in detail in Section 4.1.6.

The evaluation of mean (filtered) quantities and higher moments obtained from PDF (FDF) particle field is strongly tied with the numerics of particle tracing. Conventional particle tracing suffers from various weaknesses, which have been identified and described in detail by Li [145]. A large variation in cell size could result in too many or too few particles, and hence waste of computational time or large statistical errors, respectively. This imbalance in particle counts with the variation is cell size has been addressed by Subramaniam and Haworth [138], who proposed a scheme to control the particle number density in each cell of the computational domain. This scheme is used in this work, and is described in

Section 4.1.3. Li and Modest [146] targeted the limitation of using constant time steps, and developed a scheme where instead of using a single time step in the integration of SDEs for each particle, they used locally divided adaptive sub-time-steps governed by the local flowfield.

2.6.1 Stochastic Differential Equations (SDEs) for Lagrangian Monte Carlo FDF Methods

The development of stochastic simulation techniques for PDF equations is largely due to Pope and his coworkers. Since the modeled transport equation for the composition FDF is similar to that for the composition PDF, the Lagrangian Monte Carlo procedure outlined by Pope [108] for the solution of a modeled composition PDF transport equation is employed for the solution of a modeled transport equation for the composition FDF. The idea is to represent the FDF by a sufficiently large number of particles. Each particle can be interpreted as an independent realization of the flow, and evolves in time according to a set of stochastic differential equations which govern its transport. The particles move in physical space by convection due to the filtered flow velocity and diffusion due to molecular and subfilter diffusivities. The composition values of each particle undergo changes due to reaction and subfilter mixing. As shown by Pope [147], there is a one-to-one correspondence between the modeled transport equation for PDF, particle evolution equations obtained from the Lagrangian Monte Carlo procedure, and the modeled Eulerian governing equations for field means. Thus, for a modeled FDF equation (Eq. 2.34), the corresponding equations for particle location $\underline{\mathbf{x}}$ and composition $\underline{\phi}$ are the following stochastic equations:

$$d\underline{\mathbf{x}}^*(t) = \left[\widetilde{\underline{u}} + \nabla\left(\Gamma + \Gamma_T\right)/\overline{\rho}\right]_{\underline{\mathbf{x}}^*(t)} dt + \left[2\left(\Gamma + \Gamma_T\right)/\overline{\rho}\right]^{1/2}_{\underline{\mathbf{x}}^*(t)} d\underline{W} \ , \tag{2.36}$$

$$d\phi^*_\alpha(t) = S^*_{\alpha,\text{reaction}} dt + F^*_{\text{mix}} + \delta_{\alpha s}\frac{S^*_{\text{radiation}}}{\rho^*} dt, \alpha = 1, \ldots, s \ , \tag{2.37}$$

where F^*_{mix} is the change in species composition due to subfilter mixing, and $S^*_{\text{radiation}}$ is the radiative heat source calculated for the particle. In these equations, the number of species is varied from $\alpha = 1, \ldots, \sigma - 1$ and the σ^{th} scalar is the enthalpy; the radiation source term only affects the σ^{th} scalar. Variables with

an asterisk refer to the values of a Lagrangian particle, $\underline{W}$ is an isotropic vector Wiener process and Γ_T is the SFS turbulent diffusivity given in Eq. (2.30).

Pope [108, 148] argued that, according to the principle of stochastically equivalent systems, the solution of the above particle evolution equations yields the same statistics as those obtained directly from the solution of the modeled FDF transport equation. The FDF is then obtained approximately as the histogram of the particles' properties in sufficiently small neighborhoods in physical space, and the moments (filtered values and higher moments) of any quantity Q $\left(\text{where } \mathrm{Q}(\underline{\mathrm{x}},\mathrm{t}) \equiv \mathrm{Q}\left(\underline{\phi}(\underline{\mathrm{x}},\mathrm{t})\right)\right)$ are deduced statistically from the properties of these particles. The estimation of moments from particles' properties is described further in Section 4.1.5.

The particle SDEs listed above are solved in conjunction with a FV solver. Details of the numerical implementation of particle Monte Carlo scheme employed in this work are presented in Chapter 4.

Chapter 3

Thermal Radiation and TRI

3.1 Thermal Radiation

Radiative transfer of heat is quite different from the two other modes of heat transfer, conduction and convection, in many ways. In contrast to conduction and convection, radiative transfer of heat does not require the presence of a medium. Thermal radiation is treated conceptually in terms of electromagnetic waves, or of massless photons; the two representations are used interchangeably. As the presence of matter or a medium is not required for thermal radiation, radiative heat transfer is important in space and vacuum applications. For conduction and convection, heat transfer rates are roughly proportional to the temperature difference. By contrast, radiative transfer of heat is roughly proportional to the difference in the temperature to the fourth power. The key differences between radiative and conductive/convective transfer of heat are summarized in Table 3.1.

Radiation	Conduction and Convection
Dominates at high temperatures	Dominate at low temperatures
Does not require interaction with medium	Require medium to transfer energy
Roughly proportional to fourth power of temperature difference	Approximately linear dependence on temperature difference

Table 3.1. Radiative versus conductive/convective modes of heat transfer.

The fourth power temperature dependence makes thermal radiation increasingly significant with increasing temperature, thereby making thermal radiation an important mode of heat transfer in combustion applications. In spite of its significance at high temperatures, thermal radiation has often been neglected or accommodated using simple models in the numerical analysis of chemically reacting flows, while relatively more attention has been paid to the complex phenomena of turbulence, chemistry and turbulence–chemistry interactions. Thermal radiation is difficult to model accurately, and that partly explains the relative lack of attention to thermal radiation in reacting flows. However, in recent years, there has been an increase in the efforts to more accurately model thermal radiation in numerical studies of chemically reacting flows.

3.1.1 The Radiative Transfer Equation (RTE)

The radiative source term in the instantaneous energy equation can be expressed as the divergence of the radiative heat flux:

$$-S_{source} = \nabla \cdot \underline{q}_{rad} = \int_0^\infty \kappa_\eta \left(4\pi I_{b\eta} - \int_{4\pi} I_\eta d\Omega \right) d\eta = 4\kappa_P \sigma T^4 - \int_0^\infty \int_{4\pi} \kappa_\eta I_\eta d\Omega d\eta \tag{3.1}$$

Here η denotes wavenumber, κ_η is the spectral absorption coefficient, $I_{b\eta}$ is the Planck function (a known function of local temperature and wavenumber), Ω is solid angle, σ is the Stefan-Boltzmann constant, κ_P is the Planck-mean absorption coefficient, and I_η is the spectral radiative intensity that is obtained by solving the radiative transfer equation (RTE) [149].

The Planck-mean absorption coefficient is given by

$$\kappa_P = \frac{\int_0^\infty \kappa_\eta I_{b\eta} d\eta}{\int_0^\infty I_{b\eta} d\eta} = \frac{\pi}{\sigma T^4} \int_0^\infty \kappa_\eta I_{b\eta} d\eta \ . \tag{3.2}$$

For a gray medium, there is no wavenumber dependence and Eq. (3.1) reduces to

$$\nabla \cdot \vec{q}_{rad} = 4\kappa_P \sigma T^4 - \kappa_P G \ , \tag{3.3}$$

where $G \equiv \int_{4\pi} I d\Omega$ is the direction-integrated intensity, commonly known as inci-

dent radiation, which is obtained by solving the RTE [149]. The radiative source term consists of emission and absorption contributions, given by the first and second terms on the right-hand side of Eq. (3.3), respectively.

Radiative heat transfer is governed by an integro-differential equation with six independent variables: three spatial coordinates, two directional coordinates, and wavenumber for spectral dependence. The RTE is [149]:

$$\frac{dI_\eta}{ds} = \hat{s} \cdot \nabla I_\eta = \kappa_\eta I_{b\eta} - \beta_\eta I_\eta + \frac{\sigma_{s\eta}}{4\pi} \int_{4\pi} I_\eta \left(\hat{s}_i\right) \Phi_\eta \left(\hat{s}_i, \hat{s}\right) d\Omega_i \ . \tag{3.4}$$

Here $\hat{s}$ and $\hat{s}_i$ denote unit direction vectors, $\sigma_{s\eta}$ is the spectral scattering coefficient, $\beta_\eta = \kappa_\eta + \sigma_{s\eta}$ is the spectral extinction coefficient, and $\Phi_\eta \left(\hat{s}_i, \hat{s}\right)$ denotes the scattering phase function; the latter describes the probability that a ray from incident direction $\hat{s}_i$ is scattered into direction $\hat{s}$. The local value of I_η depends on nonlocal quantities, on direction $(\hat{s})$, and on wavenumber.

3.2 RTE Solution Methods

The integro-differential RTE has a structure that is quite different from the partial differential equations that express conservation of mass, momentum, energy, and species composition. The difficulty in solving the RTE is amplified in cases where spectral radiation properties of participating gases (e.g., H_2O and CO_2) need to be considered. The absorption coefficient of such gases includes hundreds of thousands of individual spectral lines, such that κ_η exhibits strong and irregular behavior with wavenumber. Coupling radiation with other modes of heat transfer further complicates the problem. Therefore, analytical solutions to the RTE are exceedingly difficult to obtain and explicit solutions exist for only a small number of simple configurations, such as one-dimensional plane-parallel media without scattering.

For realistic configurations, which may involve radiative equilibrium, multi-dimensional irregular geometry, anisotropic scattering or inhomogeneous media, a number of methods have been developed to obtain solutions to the RTE. The most common ones are: (1) the zonal method, (2) the spherical harmonics method (SHM), (3) the discrete ordinates method (DOM), and (4) the Monte Carlo method.

With the exception of the Monte Carlo method, all of the above methods approximate the directional distribution of intensity, reducing the daunting integro-differential equation to a set of partial differential equations or algebraic equations. The lowest order SHM ($P1$ approximation) and DOM method are the most popular, because they are relatively easy to implement and are reasonably accurate in many situations. The SHM and DOM differ in the way in which the directional dependence of radiative intensity is approximated. The solution to RTE can be further simplified in appropriate limiting conditions (e.g., cold-medium approximation, optically thin approximation, optically thick approximation).

The zonal, SHM and DOM are deterministic in nature, whereas the Monte Carlo method is a statistical method. The Monte Carlo method explicitly simulates the various thermal radiation phenomena (such as emission, absorption, reflection and scattering) accurately, and can be applied to the most complicated problems with relative ease. More information on the Monte Carlo methods is provided in Section 3.2.1. In this work, a Monte Carlo method is used.

3.2.1 Monte Carlo Method

Among radiative transfer models, Monte Carlo Ray Tracing (MCRT) can be applied to problems of arbitrary difficulty with relative ease [149]. The MCRT method directly simulates the underlying physical processes, i.e., emission, absorption, scattering and reflection, from which the RTE is derived. In the standard Monte Carlo method, a ray carrying a fixed amount of energy is emitted and its progress is then traced until it is absorbed at a certain point in the participating medium or on a wall, or until it escapes from the enclosure. However, this method is inefficient when the medium is optically thin or the walls are reflective [150]. To alleviate this problem, Modest applied the concept of energy partitioning, in which the energy carried by a ray is no longer absorbed all at once, but rather is attenuated gradually along its path until its depletion or until it leaves the enclosure [151, 152].

Wang et al. [153] extended the MCRT to account for continuous media represented by discrete particles. However, the particle representation in those MCRT schemes required assigning additional physical attributes to the notional particles

that are used in the PDF method. This is explained in more detail in Section 4.2. A set of MCRT schemes that is consistent with the notional particle representation of PDF methods is developed in this work, and is presented in Section 4.2.1.

3.3 Spectral Treatment of Radiation

Molecular gases including carbon dioxide and water vapor exhibit vibration–rotation bands formed as a result of hundreds of thousands of broadened and overlapping spectral lines. Therefore, the absorption coefficient of a molecular gas varies greatly and rapidly across the spectrum, and the assumption of a gray medium almost always fails when the medium contains absorbing–emitting gases. Nevertheless, traditionally radiation in combustion systems has been treated using gray models due to their simplicity and faster computation. It has only been in the last decade or so that spectral radiation has been considered, using models of varying levels of sophistication. All such studies have shown a strong influence of spectral radiation properties in combustion calculations [35, 154–159].

The origin of the vibration–rotation bands for molecular gases is briefly discussed in Section 3.3.1 below. Following that, the most common approaches to incorporate the spectral variation in radiation properties are presented in Section 3.3.2, alongwith an overview of the spectral PMC method used in this research in Section 3.3.2.1.

3.3.1 Spectral Radiation Properties of Combustion Gases

Radiative processes such as emission and absorption of a photon are associated with a change in the molecular energy level of a gas molecule that occurs due to one of the following radiative transitions: (a) Transitions between "nondissociated" atomic or molecular states, called bound–bound transitions; (b) transitions from "dissociated" to "nondissociated" or from "nondissociated" to "dissociated", called bound–free transitions; and (c) transitions between two different "free" states, called free–free transitions. Bound–free and free–free transitions usually occur at very high temperatures. Most engineering applications, such as boilers and gas turbine combustors, occur at moderate temperature levels, with little ionization

and dissociation, where bound–bound transitions are of most importance.

As per the quantum mechanics postulates, the energy levels for molecular rotation and vibration and that for atomic or molecular electronic orbit are quantized. That is, the energies associated with molecular rotation and vibration and electron orbits are not continuous and take discrete variations instead. The energy of a photon or an electro-magnetic wave is directly proportional to frequency, which necessitates that for bound–bound transitions, photons must have a certain frequency (or wavelength) for them to be captured or released, leading to discrete spectral lines for absorption and emission. The spectral lines are not truly monochromatic and span a tiny but finite range of wavenumbers as a result of natural line broadening, collision broadening, and Doppler broadening [149]. The absorption coefficient at a specific spectral location is a result of the overlap of nearby spectral lines which are broadened to overlap with each other.

The energy needed for changing the orbit of an electron is relatively large, and requires a high-frequency photon, leading to emission-absorption lines at short wavelengths between ultra-violet and near-infrared. Somewhat lesser energy is required for vibrational energy level changes, resulting in spectral lines in the infrared. The rotational energy level changes require the least amount of energy, and the corresponding spectral lines are found in the far infrared. The vibrational energy changes are usually accompanied by rotational transitions, leading to closely spaced groups of spectral lines that partly overlap due to line broadening. This leads to vibration–rotation bands in the infrared. The emissive power has its maximum in the infrared at combustion temperatures, highlighting the importance of vibration–rotation bands for combustion systems. The spectral absorption coefficient in a small portion of the $4.3\mu m$ narrow band of carbon dioxide at $1000K$ is shown in Fig. 3.1.

3.3.2 Spectral Models

The several approaches to account for spectral variation in radiation properties may be loosely grouped into the following categories: 1) line-by-line calculations (LBL); 2) band models; and 3) global models.

The most accurate approach for integration over the spectrum is the line-by-line

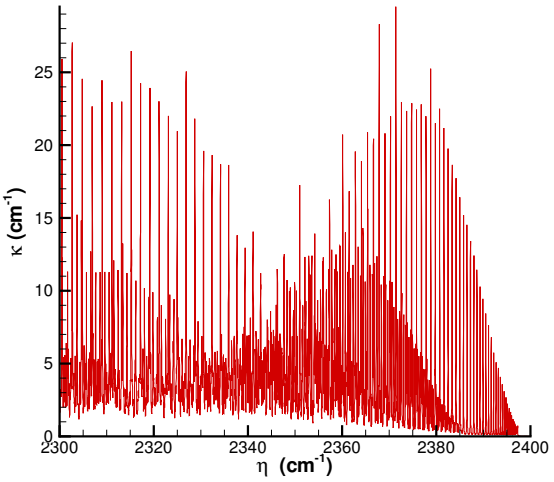

Figure 3.1. Spectral absorption coefficient for carbon dioxide in a small portion of the $4.3\mu m$ narrow band at $1000K$.

approach, which relies on very detailed knowledge of every single spectral line, usually taken from high-resolution spectroscopic databases [160–163]. The HITEMP database [161, 162] includes spectral data for CO_2 and H_2O, valid for temperatures up to 1000K. Another spectroscopic database, CDSD-1000 [163], became available recently, and contains more than three million lines for CO_2 and claims to be accurate up to 3000K. Line-by-line calculations are the most accurate, but they require vast amounts of computer resources. Because of the strong variation in the spectral radiative properties, the RTE needs to be solved at one million or more wavenumbers, followed by integration over the spectrum [149]. This is undesirable in the context of complex combustion codes, where radiation calculations form only a small part of the total computational effort. However, it has been observed that in the framework of Photon Monte Carlo [153], which in any case involves tracking of millions of rays, reduction in the computational time is not significant when LBL calculations are replaced with reordered distributions [37].

In band models, the spectrum is divided into narrow or wide bands, and radiative characteristics, appropriately averaged over each band, are calculated from the spectrum or statistical properties of the lines. Band models include the box models, the statistical narrow-band (SNB) model, the correlated-k (CK) model, the correlated-k fictitious gas (CKFG) model and the exponential wide-band (EWB) model [149]. Band models suffer from the following limitations: (1) They are dif-

ficult to apply to nonhomogeneous media; (2) statistical models (both narrow and wide band) cannot be applied for enclosures that have nonblack walls and/or in the presence of scattering particles; and (3) wide-band correlations have a typical correlational accuracy of 30%, and in some cases may be in error by as much as 70%.

In global models, the total radiative fluxes are calculated directly from spectrally integrated properties. These include early global models employing total emissivities and absorptivities of gas columns, the weighted-sum-of-gray-gases (WSGG) model [164], the spectral-line based weighted-sum-of-gray-gases (SLW) model [165, 166] and, more recently, the full-spectrum correlated-k (FSCK) distribution method [167], which has been shown to be superior to WSGG and SLW models. Within its limitations (gray walls, gray scattering properties, spectral absorption coefficient being correlated, i.e., all wavenumbers that have the same absorption coefficient value k at one state also have always the same absorption coefficient value k^* -different from k- at another state), the FSCK method is exact. However, the FSCK method can incur substantial inaccuracies in inhomogeneous media, especially in the presence of extreme temperature changes and/or changing mole fractions, because the assumptions of a correlated or scaled absorption coefficient are violated. To treat large temperature and partial pressure variations, sophisticated multi-group full-spectrum k distribution (MGFSK) and multi-scale full-spectrum k distribution (MSFSK) methods have been developed [168, 169].

The LBL spectral treatment is used in the current research in the context of a photon Monte Carlo method. The details of the method [37] are provided below.

3.3.2.1 Spectral Photon Monte Carlo Method

Following the development of Modest [149], the probability of a photon being emitted in a differential wavenumber interval $d\eta$ is proportional to the Planck function weighted by the spectral absorption coefficient, i.e.,

$$\text{Probability}\left(\eta \leq \eta^{'} \leq \eta + d\eta\right) \propto \kappa_\eta I_{b\eta} d\eta \ . \tag{3.5}$$

The emission process for such a nongray gas species i can be simulated statistically by mapping the emission wavenumber (η) to a random number ($R_{\eta,i}$)

distributed uniformly in $[0,1)$, as per the following expression [37]:

$$R_{\eta,i} = \frac{\int_0^{\eta} \kappa_{\eta,i} I_{b\eta} d\eta}{\int_0^{\infty} \kappa_{\eta,i} I_{b\eta} d\eta} = \frac{\int_0^{\eta} \kappa_{P\eta,i} I_{b\eta} d\eta}{\int_0^{\infty} \kappa_{P\eta,i} I_{b\eta} d\eta} = \frac{\pi}{\kappa_{P,i} \sigma T^4} \int_0^{\eta} \kappa_{P\eta,i} I_{b\eta} d\eta \ , \tag{3.6}$$

where $\kappa_{p\eta,i} = \kappa_{\eta,i}/p_i$ is the pressure-based spectral absorption coefficient, p_i is the partial pressure of species i, and $\kappa_{p,i}$ is the pressure-based Planck-mean absorption coefficient. The above relationship (Eq. 3.6) between the random number and the wavenumber is implicit and, therefore, it is more convenient to tabulate this relation in a database to invert random numbers into wavenumbers for emission of photon bundles.

For a gaseous mixture containing multiple emitting-absorbing species, as the absorption coefficients are additive, the emission wavenumber for the mixture and a uniform random number ($R_\eta \in [0,1)$) are related by [37]

$$R_\eta = \frac{\sum_i \chi_i \kappa_{P,i} R_{\eta,i}}{\sum_i \chi_i \kappa_{P,i}} \ , \tag{3.7}$$

where $\chi_i = p_i/p$ is the mole fraction of species i, p is the total pressure of the mixture, and $R_{\eta,i}$ are the species random numbers.

The above relationship between the mixture random number R_η and the corresponding wavenumber η is implicit and mapping must be done by trial and error. A database can be created with mappings of $R_{\eta,i} - \eta$ and $\kappa_{p\eta,i} - \eta$ to determine emission wavenumbers and absorption coefficients for the mixture. If the total pressure is fixed, both the species random number, as in Eq. (3.6), and the pressure-based absorption coefficient are functions of wavenumber, temperature, and species mole-fractions only, i.e.,

$$R_{\eta,i} = f_{R,i}\left(\eta, T, \chi_i\right), \quad \kappa_{P\eta,i} = f_{\kappa,i}\left(\eta, T, \chi_i\right), \quad i = 1, 2, ..., n_r \ , \tag{3.8}$$

where n_r is the number of radiating species. Both $R_{\eta,i}$ and $\kappa_{p\eta,i}$ are functions of temperature and wavenumber only, if self-broadening is neglected. Thus, a 3D interpolation scheme (or 2D if self-broadening is neglected) is sufficient for the database. A bisection search algorithm is employed to invert the relationship between $R_{\eta,i} - \eta$ to obtain the emission wavenumber [37]. Once η is known, the absorption coefficient can be obtained directly from $\kappa_{p\eta,i} - \eta$ tabulated values.

For sooting systems, the spectral absorption coefficient for soot is evaluated using the small-particle limit of Rayleigh theory for a cloud of nonuniform, spherical particles given by [149]

$$\kappa_\lambda = \frac{36\pi nk}{(n^2 - k^2 + 2^2 + 4n^2k^2)} \frac{f_v}{\lambda} \ , \tag{3.9}$$

where f_v is the soot volume-fraction, λ is the wavelength, and n and k are real and imaginary parts of the complex index of refraction for soot ($m = n - ik$) and are modeled using the correlations developed by Chang and Charalampopoulos [170]. For PMC analysis, the random number relation for soot is computed similarly to Eq. (3.6) as

$$R_{\eta,s} = \frac{\pi}{\kappa_{P,s}\sigma T^4} \int_0^\eta \kappa_{v\eta,s} I_{b\eta} d\eta \ , \tag{3.10}$$

where the subscript s denotes soot, $\kappa_{v\eta,s} = \kappa_{\eta,s}/f_v$ is the volume-fraction-based spectral absorption coefficient, f_v is the soot volume-fraction, and $\kappa_{p,s}$ is the Planck-mean of $\kappa_{v\eta,s}$. Thus, the random number relationship for mixtures involving soot is calculated similarly to Eq. (3.7) as

$$R_\eta = \frac{f_v\kappa_{P,s}R_{\eta,s} + \sum_i x_i\kappa_{P,i}R_{\eta,i}}{f_v\kappa_{P,s} + \sum_i x_i\kappa_{P,i}} \ , \tag{3.11}$$

where the subscript i denotes emitting-absorbing gas species involved in the mixture. In the current work, water vapor and carbon dioxide are considered as emitting-absorbing gas species and LBL random-number databases [37] are utilized to account for spectral radiation in PMC computations.

3.4 Turbulence–Radiation Interactions (TRI)

The prediction of the mean temperature field has been one of the prime objectives in numerical simulation of turbulent reacting flows. In RAS formulations, the mean temperature is obtained by solving an averaged form of the energy equation. The mean radiative source term in the mean energy equation consists of unclosed terms which arise due to the presence of nonlinear terms in the instantaneous radiative source term. The unclosed mean of the nonlinear terms is quite different from the

nonlinear terms evaluated from the mean quantities (similar to the chemical source term), and this difference is a manifestation of turbulence–radiation interactions.

The radiation source term for a gray case is considered here to explain the concept of TRI. In that case, TRI can be brought into evidence by taking the mean of Eq. (3.3):

$$\langle \nabla \cdot \vec{q}_{rad} \rangle = 4\sigma \langle \kappa_P T^4 \rangle - \langle \kappa_P G \rangle \ . \tag{3.12}$$

In the mean emission term, TRI appears as a correlation between the Planck-mean absorption coefficient and the fourth power of temperature: $\langle \kappa_P T^4 \rangle = \langle \kappa_P \rangle \langle T^4 \rangle + \langle \kappa_P' (T^4)' \rangle$, where a prime denotes a fluctuation about the local mean. The presence of TRI in the emission term is further manifested in the temperature self-correlation ($\langle T^4 \rangle \neq \langle T \rangle^4$). In the mean absorption term, TRI appears as a correlation between the Planck-mean absorption coefficient and the incident radiation: $\langle \kappa_P G \rangle = \langle \kappa_P \rangle \langle G \rangle + \langle \kappa_P' G' \rangle$.

In the case of spectral radiation in LES formulations, spatial filtering of the instantaneous radiative source term (Eq. 3.1) results in:

$$\overline{\nabla \cdot \vec{q}_{rad}} = \int_0^\infty \left(4\pi \overline{\kappa_\eta I_{b\eta}} - \int_{4\pi} \overline{\kappa_\eta I_\eta} d\Omega \right) d\eta \ . \tag{3.13}$$

The above expression contains unclosed terms due to the nonlinearities in the emission and the absorption rates. The unclosed terms can be expressed in terms of resolved scale and unresolved scale contributions as follows:

$$\overline{\kappa_\eta I_{b\eta}} = \widehat{\kappa}_\eta \widehat{I}_{b\eta} + \left(\overline{\kappa_\eta I_{b\eta}} - \widehat{\kappa}_\eta \widehat{I}_{b\eta} \right) \ , \tag{3.14}$$

$$\overline{\kappa_\eta I_\eta} = \widehat{\kappa}_\eta \widehat{I}_\eta + \left(\overline{\kappa_\eta I_\eta} - \widehat{\kappa}_\eta \widehat{I}_\eta \right) \ . \tag{3.15}$$

In the above expressions, quantities with $\widehat{\ }$ are evaluated using the Favre-filtered fields of temperature, species mass-fractions and pressure in the computational domain. That is, $\widehat{\kappa}_\eta \equiv \kappa_\eta(\widetilde{T}, \widetilde{P}, \underline{\widetilde{Y}})$ and $\widehat{I}_{b\eta} \equiv I_{b\eta}(\widetilde{T})$, and these quantities are solely dependent on the local values of $\widetilde{T}$, $\widetilde{P}$, and $\underline{\widetilde{Y}}$, while $\widehat{I}_\eta \equiv I_\eta[F(\widetilde{T}, \widetilde{P}, \underline{\widetilde{Y}})]$ is obtained by solving the RTE with radiation properties based on the filtered temperature, composition, and pressure fields. Since $\widetilde{T}$, $\widetilde{P}$, and $\underline{\widetilde{Y}}$ are known in LES, so are $\widehat{\kappa}_\eta$,

$\widehat{I}_{b\eta}$, and $\widehat{I}_{\eta}$, although the latter term requires an RTE solver. The quantities in parentheses in the above expressions (Eqs. 3.14 and 3.15) represent the contributions to the filtered radiative source term because of subfilter-scale fluctuations in T, P, and $\underline{Y}$ about their local spatially filtered values. In LES, it is appropriate to separate the contributions to the filtered radiative source term based on scales. The resolved-scales contributions to TRI are explicitly captured in LES (resolved-scale TRI), whereas contributions from interactions between resolved scales and subfilter-scales and contributions from correlations between subfilter-scale fluctuations (subfilter-scale TRI) must be modeled. The terms that require modeling are those in parentheses in the expressions above for the filtered emission and absorption terms. Thus, filtered emission and absorption terms each consist of a resolved-scale and an unresolved-scale contribution, and modeling of their unresolved parts is the motivation behind TRI modeling in LES.

The emission term is similar to the chemical source term, in the sense that both depend only on the local scalars. Hence radiative emission, including emission TRI, can be completely accounted for through a one-point/one-time composition FDF approach. There have been only a handful of studies to date investigating TRI in reacting flows using LES, and they have either neglected the subfilter-scale emission [41] or have employed a FDF method to account for subfilter-scale emission [40]. To date, no quantitative conclusions have been drawn about the importance of TRI at subfilter scales in turbulent reacting flows. A theoretical framework is developed in this research work and is presented in Section 3.4.2, to isolate the various contributions to resolved-scale TRI and subfilter-scale TRI in the mean filtered emission term.

The absorption term has nonlocal character; radiative intensity at a local point is the summation of the intensities of rays reaching this point from all other points throughout the computational domain. Therefore, the local intensity at a point depends on the properties of the entire medium. This nonlocal nature of the absorption term makes it highly difficult to model absorption TRI. In the limited LES studies of TRI to date [40, 41], the optically thin fluctuation assumption (OTFA) has been invoked, wherein the effects of subfilter-scale fluctuations are neglected in the absorption term. The OTFA is discussed in detail in the next section. The only methods of closing absorption-TRI that have been proposed in the literature are:

(1) to include intensity as one of the scalars in the transported composition-FDF method; or (2) to perform a coupled FDF/photon Monte Carlo (PMC) method wherein particles carrying scalars (composition, enthalpy, etc.) are assumed to represent an instantaneous realization of the flow and a Monte Carlo approach is used to solve for thermal radiation in such a particle field [37]. A PMC method to account for absorption TRI has been used in RAS/PDF formulations [38, 39].

In this work, a transported FDF/modified-PMC method is used to account for subfilter-scale emission and absorption TRI, and an assessment of the importance of subfilter-scale fluctuations on TRI (based on the theoretical framework of Section 3.4.2) in chemically reacting flows is made in Chapter 6.

3.4.1 Optically Thin Fluctuation Approximation (OTFA)

As discussed before, the nonlocal nature of the radiative intensity makes it highly difficult to model the unclosed absorption TRI terms in the mean (for RAS) or the filtered (in LES) radiative source term; hence the absorption coefficient–intensity correlation has generally been neglected in previous studies. This has been justified by Kabashnikov and Myasinkova [171], who argued that if the mean free path for radiation is much larger than the turbulent length scale, then the local incident radiative intensity should only be weakly correlated with the local absorption coefficient. Thus one can assume

$$\langle \kappa_\eta I_\eta \rangle \simeq \langle \kappa_\eta \rangle \langle I_\eta \rangle \,, \tag{3.16}$$

where $\langle \kappa_\eta \rangle$ is the mean absorption coefficient self-correlation, and angled brackets represent mean quantities. The rationale behind this assumption is that the instantaneous local incident intensity at a point is formed over paths traversing several turbulent eddies, and is therefore weakly correlated to the local radiative properties. Kabashnikov and Myasinkova provided several conditions for the validity of this thin-eddy approximation [171]. In general, however, the thin-eddy approximation will depend on the assumption that the optical thickness of the turbulent eddies is small,

$$\kappa_\eta l \ll 1 \,, \tag{3.17}$$

where l is the turbulent eddy length scale. The validity of this assumption will depend on the eddy-size distribution and radiative properties of the absorbing gases. In a RAS simulation of a combustion chamber, Hartick [172] showed that the thin-eddy approximation may not be valid over some highly absorbing spectral regions in the spectrum, but only has a slight effect on the integral radiative exchange. At the other extreme of the OTFA is the scenario where $\kappa_P l \gg 1$: the optical thickness is large compared to all hydrodynamic scales and chemical scales. In that case, the fluctuations in intensity are generated locally and are expected to be correlated strongly with those of the absorption coefficient. A diffusion approximation [149] can be used to model such cases. Using a diffusion approximation, Mehta [173] showed that absorption TRI may not be negligible over certain parts of the spectrum, though the overall contribution to radiative transfer may not be significant. The above studies suggest that the optically thin-eddy approximation may result in miscalculation of the re-absorption of radiative energy when the medium has fluctuating radiative properties, although the impact on the net radiative heat transfer may be small. In the case of turbulent sooting flames, the absorption coefficient is higher (than in nonsooting flames) over a large part of the spectrum, and hence it is expected that there may be significant correlation between the local incident radiative intensity and the local radiative properties. Wang [37] used an PDF/PMC approach to completely account for emission and absorption TRI in an artificial sooting flame, and showed that OTFA cannot be used for such flames.

In LES, some part of absorption TRI is explicitly captured as discussed in Section 3.4. The contribution to absorption TRI still needs to be modeled because of the effect of subfilter-scale fluctuations in temperature, species composition, and pressure on the local incident intensity and local absorption coefficient. The OTFA, when invoked in LES, neglects the effects of subfilter-scale fluctuations. It might be expected that OTFA should be more valid in LES than in RAS, since radiation is a large-scale phenomenon. However, the degree of approximation introduced with the use of OTFA is still unknown. Moreover, since absorption TRI is expected to be important in turbulent sooting flames, it is essential to quantify the approximation that is incurred with the use of OTFA in such flames.

3.4.2 Assessing Resolved and SFS Emission TRI in LES

In LES, both resolved and SFS fluctuations contribute to TRI. The contribution of resolved fluctuations to emission TRI can be assessed by computing the ratio of mean emission based on resolved scales and the emission based on time-averaged mean temperature and mean species fields. That is,

$$\text{Resolved TRI} \equiv \frac{\text{Mean emission based on resolved fields}}{\text{Emission based on means}} = \frac{\langle \kappa_P(\tilde{T}, \underline{\tilde{Y}})\tilde{T}^4 \rangle}{\kappa_P(\langle \tilde{T} \rangle, \langle \underline{\tilde{Y}} \rangle)\langle \tilde{T} \rangle^4} \tag{3.18}$$

Rearranging the above expression:

$$\text{Resolved TRI} = \left(\frac{\langle \kappa_P(\tilde{T}, \underline{\tilde{Y}})\tilde{T}^4 \rangle}{\langle \kappa_P(\tilde{T}, \underline{\tilde{Y}}) \rangle \langle \tilde{T}^4 \rangle} \right) * \left(\frac{\langle \kappa_P(\tilde{T}, \underline{\tilde{Y}}) \rangle}{\kappa_P(\langle \tilde{T} \rangle, \langle \underline{\tilde{Y}} \rangle)} \right) * \left(\frac{\langle \tilde{T}^4 \rangle}{\langle \tilde{T} \rangle^4} \right) \tag{3.19}$$

As seen in the above expression, the resolved-scale contribution to TRI can be split into various sub-contributions, which can be classified as:

- $\left(\frac{\langle \kappa_P(\tilde{T}, \underline{\tilde{Y}})\tilde{T}^4 \rangle}{\langle \kappa_P(\tilde{T}, \underline{\tilde{Y}}) \rangle \langle \tilde{T}^4 \rangle} \right)$: Correlation between κ_P and T^4 due to resolved fluctuations
- $\left(\frac{\langle \kappa_P(\tilde{T}, \underline{\tilde{Y}}) \rangle}{\kappa_P(\langle \tilde{T} \rangle, \langle \underline{\tilde{Y}} \rangle)} \right)$: κ_P self-correlation due to resolved fluctuations
- $\left(\frac{\langle \tilde{T}^4 \rangle}{\langle \tilde{T} \rangle^4} \right)$: Temperature self-correlation due to resolved fluctuations

Thus, the resolved-scale contribution to TRI can be expressed as:

$$\text{Resolved TRI} = \left(\kappa_P - T^4 \text{ Corr}\right) * \left(\kappa_P \text{ Self-Corr}\right) * \left(\text{Temp Self-Corr}\right) \tag{3.20}$$

The cummulative effect of both resolved and SFS fluctuations on TRI can be quantified as the ratio of mean filtered radiative emission (where the effects of all fluctuations are captured) and the mean emission based on mean quantities. That is,

$$\text{Total TRI} \equiv \frac{\text{Mean filtered emission}}{\text{Emission based on means}} = \frac{\widetilde{\langle \kappa_P T^4 \rangle}}{\kappa_P(\langle \tilde{T} \rangle, \langle \underline{\tilde{Y}} \rangle)\langle \tilde{T} \rangle^4} \tag{3.21}$$

Rearranging the above expression:

$$\text{Total TRI} = \left(\frac{\widetilde{\langle \kappa_P T^4 \rangle}}{\langle \widetilde{\kappa_P} \rangle \langle \widetilde{T^4} \rangle} \right) * \left(\frac{\langle \widetilde{\kappa_P} \rangle}{\kappa_P(\langle \tilde{T} \rangle, \langle \underline{\tilde{Y}} \rangle)} \right) * \left(\frac{\langle \widetilde{T^4} \rangle}{\langle \tilde{T} \rangle^4} \right) \tag{3.22}$$

Similar to the case for Eq. (3.19), the effects of both resolved and SFS fluctuations can be split into various sub-contributions as demonstrated in the above exprression.

The contribution of SFS fluctuations to emission TRI can be isolated by computing the ratio of mean filtered emission and mean emission based on filtered quantities (only resolved fluctuations). That is,

$$\text{SFS TRI} \equiv \frac{\text{Mean filtered emission}}{\text{Mean emission based on resolved fields}} = \frac{\widetilde{\langle \kappa_P T^4 \rangle}}{\langle \kappa_P(\tilde{T}, \underline{\tilde{Y}})\tilde{T}^4 \rangle} \tag{3.23}$$

From Eqs. (3.19) and (3.22), the SFS contribution to TRI can be expressed as:

$$\text{SFS TRI} = \left(\frac{\widetilde{\langle \kappa_P T^4 \rangle}}{\langle \widetilde{\kappa_P} \rangle \langle \widetilde{T^4} \rangle} * \frac{\langle \kappa_P(\tilde{T}, \underline{\tilde{Y}}) \rangle \langle \tilde{T}^4 \rangle}{\langle \kappa_P(\tilde{T}, \underline{\tilde{Y}})\tilde{T}^4 \rangle} \right) * \left(\frac{\langle \widetilde{\kappa_P} \rangle}{\langle \kappa_P(\tilde{T}, \underline{\tilde{Y}}) \rangle} \right) * \left(\frac{\langle \widetilde{T^4} \rangle}{\langle \tilde{T}^4 \rangle} \right) \tag{3.24}$$

Similar to Eqs. (3.19) and (3.22), the subfilter-scale contribution to TRI shown in Eq. (3.24) can be split into various sub-contributions, which can be classified as:

- $\left(\frac{\widetilde{\langle \kappa_P T^4 \rangle}}{\langle \widetilde{\kappa_P} \rangle \langle \widetilde{T^4} \rangle} * \frac{\langle \kappa_P(\tilde{T}, \underline{\tilde{Y}}) \rangle \langle \tilde{T}^4 \rangle}{\langle \kappa_P(\tilde{T}, \underline{\tilde{Y}})\tilde{T}^4 \rangle} \right)$: Correlation between κ_P and T^4 due to SFS fluctuations
- $\left(\frac{\langle \widetilde{\kappa_P} \rangle}{\langle \kappa_P(\tilde{T}, \underline{\tilde{Y}}) \rangle} \right)$ self-correlation due to SFS fluctuations
- $\left(\frac{\langle \widetilde{T^4} \rangle}{\langle \tilde{T}^4 \rangle} \right)$: Temperature self-correlation due to SFS fluctuations

	$\kappa_P - T^4$ correlation	κ_P self-correlation	temperature self-correlation	Over-all TRI
Resolved fluctuations	$\left(\frac{\langle\kappa_P(\tilde{T},\underline{\tilde{Y}})\tilde{T}^4\rangle}{\langle\kappa_P(\tilde{T},\underline{\tilde{Y}})\rangle\langle\tilde{T}^4\rangle}\right)$	$\left(\frac{\langle\kappa_P(\tilde{T},\underline{\tilde{Y}})\rangle}{\kappa_P(\langle\tilde{T}\rangle,\langle\underline{\tilde{Y}}\rangle)}\right)$	$\left(\frac{\langle\tilde{T}^4\rangle}{\langle\tilde{T}\rangle^4}\right)$	$\frac{\langle\kappa_P(\tilde{T},\underline{\tilde{Y}})\tilde{T}^4\rangle}{\kappa_P(\langle\tilde{T}\rangle,\langle\underline{\tilde{Y}}\rangle)\langle\tilde{T}\rangle^4}$
SFS fluctuations	$\left(\frac{\widetilde{\langle\kappa_P T^4\rangle}}{\langle\widetilde{\kappa_P}\rangle\langle\widetilde{T^4}\rangle} * \frac{\langle\kappa_P(\tilde{T},\underline{\tilde{Y}})\rangle\langle\tilde{T}^4\rangle}{\langle\kappa_P(\tilde{T},\underline{\tilde{Y}})\tilde{T}^4\rangle}\right)$	$\left(\frac{\langle\widetilde{\kappa_P}\rangle}{\langle\kappa_P(\tilde{T},\underline{\tilde{Y}})\rangle}\right)$	$\left(\frac{\langle\widetilde{T^4}\rangle}{\langle\tilde{T}^4\rangle}\right)$	$\frac{\widetilde{\langle\kappa_P T^4\rangle}}{\langle\kappa_P(\tilde{T},\underline{\tilde{Y}})\tilde{T}^4\rangle}$
All fluctuations	$\frac{\widetilde{\langle\kappa_P T^4\rangle}}{\langle\widetilde{\kappa_P}\rangle\langle\widetilde{T^4}\rangle}$	$\frac{\langle\widetilde{\kappa_P}\rangle}{\kappa_P(\langle\tilde{T}\rangle,\langle\underline{\tilde{Y}}\rangle)}$	$\frac{\langle\widetilde{T^4}\rangle}{\langle\tilde{T}\rangle^4}$	$\frac{\widetilde{\langle\kappa_P T^4\rangle}}{\kappa_P(\langle\tilde{T}\rangle,\langle\underline{\tilde{Y}}\rangle)\langle\tilde{T}\rangle^4}$

Table 3.2. TRI correlations for resolved-scale, SFS, and all (resolved+SFS) fluctuations.

From the analysis presented above, TRI due to resolved-scale fluctuations (Eq. (3.19)) and SFS fluctuations (Eq. (3.24)) consist of $\kappa_P - T^4$ correlation, κ_P self-correlation, and temperature self-correlation. These correlations for resolved-scale and SFS fluctuations are outlined in Table 3.2, and are compared in Section 6.2 for a turbulent reacting flow to assess the relative importance of SFS TRI.

3.5 Earlier Investigations of TRI

In RAS modeling of radiative heat transfer in a reacting flow field, turbulence–radiation interactions have often been simply ignored; in that case, the product of the mean quantities has been used to compute the radiative source term in the averaged energy equation, rather than the mean of the product. This has been the case until recently, despite the fact that importance of TRI has long been recognized [24–31, 174, 175]. Through the late 1990's and early 2000's, consideration of TRI in the simulation of thermal radiation in turbulent reacting flows has increased [33, 35, 156, 176]. An exhaustive review of the literature on TRI up to 2006 has been done by Coelho [177]; he surveyed various computational approaches to account for TRI and reviewed TRI studies based on those approaches.

In one of the earliest theoretical studies on TRI, Foster [174] found that the time-mean transmissivity of a medium based on the mean medium properties is in serious error when compared to the time-mean transmissivity based on assumed probability density distributions for the absorption coefficient. Becker [178] con-

ducted a theoretical analysis of a turbulent jet diffusion flame. Using a radiation model that accounted for emission from H_2O and CO_2, he found that the rms fluctuation of local emission per unit volume along the centerline ranged from 20% to 500% of the mean value. Cox [179] expanded the mean emissive power into a Taylor series, and showed that mean emission increases rapidly with increasing temperature fluctuations. Kabashnikov and Kmit [180] performed an analytical study on the effects of fluctuations in temperature and absorption coefficient on thermal radiation and introduced the OTFA.

The experimental studies by Faeth and Gore [27–31] have shown that with the inclusion of TRI, radiative emission from a flame may be 50% to 300% higher (depending on the type of fuel) than that expected with radiation but without TRI. Soufiani et al. [26] investigated the effects of TRI in a channel flow of nonreacting gases and found that the mean radiative flux predicted from the mean temperature field was accurate to within 10% of the mean flux predicted with the consideration of temperature fluctuations. This was attributed to the low level of turbulent temperature fluctuations in the absence of combustion. A fully coupled TRI analysis was conducted by Song and Viskanta [25] for an industrial methane flame in a furnace, where presumed probability density functions were used for the fluctuations in emission and species concentrations. They concluded that TRI is important when the flame occupies a large volume in the furnace. Hartick et al. [172] extended Song and Viskanta's analysis to a midsized enclosed diffusion flame, where they employed a two-dimensional PDF of mixture fraction and heat-release rate as the coupling model. They concluded that the coupling has only negligible influence on the spatial temperature, velocity, and mixture-fraction fields, but strongly affects the local nitrogen oxide production and total nitrogen oxide emission. Ripoll [181] proposed an averaged form of the $M1$ radiation model together with presumed PDFs for temperature, radiative flux, and the soot volume fraction to account for TRI. Coelho et al. [182] modeled Sandia Flame D [124] using the assumed Gaussian PDFs of Song and Viskanta [25] for TRI. They used a Reynolds-stress model for turbulence modeling, a laminar flamelet model for combustion, and the discrete-ordinates method as the radiation solver along with the SLW model for nongray radiation properties. Coelho [32] also investigated TRI in a nonluminous methane-air jet diffusion flame and compared the results obtained using the OTFA

with those obtained using the stochastic semicausal model [176]. He showed that the results obtained using the OTFA and the correlated k-distribution model for the radiative properties were in good agreement with those from the stochastic semicausal model for TRI and the statistical narrow-band model for the radiative properties. This is consistent with expectations for this small-scale, optically thin flame. Coelho also concluded that the consideration of turbulent fluctuations resulted in about 50% increase in the radiative heat loss.

The simplicity of using assumed PDFs to characterize fluctuating quantities has been the main motivation behind their use for studying TRI. The first study of TRI to abandon this simplification was that of Mazumder and Modest [156]. They used the velocity-composition joint PDF method to accurately account for TRI in modeling a methane-air diffusion flame in a bluff-body combustor. The optically-thin fluctuation approximation [180] was invoked, and thus, only the interaction between the absorption coefficient and the Planck function (emission TRI) was considered. Their study predicted an approximately 40% increase in the radiative heat loss from the flame due to TRI. Mazumder and Modest [175] used the same approach to model TRI in nonreacting turbulent flows and found TRI to be negligible in such situations. Li and Modest [35] used a joint composition PDF method to account for TRI in a piloted nonpremixed methane-air jet flame (Sandia Flame D) [124] and a family of larger flames extrapolated from Flame D. They examined correlations that quantify the interactions between various fluctuating quantities, and found that the correlation between the fluctuating absorption coefficient and the fluctuating Planck function is the most important.

Tessé et al. [33] were the first to conduct a full TRI study (i.e., without the OTFA) of a practical flame. They modeled a luminous turbulent ethylene jet diffusion flame using a $k-\epsilon$ turbulence model for flow together with the composition PDF method and detailed chemistry. Thermal radiation was treated using a photon Monte Carlo method and a narrow-band correlated-k approach for radiative properties. They found that the soot influences the global radiative heat loss more than the gaseous species, and with the consideration of TRI there was approximately a 30% increase in the radiative heat loss.

Wu et al. [183] carried out DNS of an idealized one-dimensional premixed turbulent flame to study TRI. They used a high-order photon Monte Carlo scheme

(of order commensurate with the underlying DNS code) to calculate the radiative heat source. The various contributions to TRI were isolated and quantified, and it was found that: the temperature self-correlation contribution was the dominant contribution to TRI only in the optically thin limit; the absorption coefficient–Planck function correlation and absorption coefficient–intensity correlation were not negligible even in the most optically thin case; and that the contributions from all three correlations were significant at intermediate values of optical thickness. Deshmukh et al. [184] applied the same approach to DNS of an idealized statistically homogeneous nonpremixed system with full consideration of TRI.

Frankel et al. [40] performed LES of an idealized nonpremixed jet flame using the optically thin eddy approximation and treating emission TRI through a filtered mass density function (FMDF) approach. Gupta et al. [41] conducted LES of an idealized chemically reacting nonpremixed turbulent planar channel flow with systematic variations in optical thickness. They considered only the resolved-scale contributions to TRI; various TRI correlations were isolated and quantified. They found that: emission TRI was important at all optical thicknesses, while absorption TRI increased with increasing optical thickness; and the temperature self-correlation made the most important contribution to emission TRI.

Wang and Modest [153, 185, 186] developed Monte Carlo emission and absorption schemes for media represented by discrete particles, thereby enabling them to account for absorption TRI in the context of composition PDF methods. Wang et al. [38, 187] used the above schemes together with the composition PDF method to model thermal radiation and TRI in both nonluminous and luminous flames. They employed a state-relationship-based model to account for soot. This was extended by Mehta et al. [188], who used a detailed soot model along with PDF and photon Monte Carlo methods, and demonstrated the necessity for considering TRI for accurate predictions in nonpremixed luminous flames.

Recently, Roger and coworkers [42–44] conducted filtered DNS and LES without SFS models for radiation to assess the contribution of unresolved scales to thermal radiation for homogeneous isotropic turbulence and non-isothermal turbulent plane jet flow. For isotropic turbulence, they found the SFS radiative absorption to be negligible; it was suggested to model SFS emission for coarse grids. However, the two important contributors to SFS emission, namely temperature self-correlation

and temperature-absorption coefficient correlation, showed opposite effects and, therefore, they concluded that it is better to neglect both correlations instead of modeling only one of them. The SFS modeling was recommended at higher optical thicknesses for turbulent plane jet flows.

Chapter 4

Numerical Algorithms

The comprehensive computational solver being developed in this work consists of several components including the finite-volume solver for LES, a Lagrangian Monte Carlo code to solve for the composition FDF, and photon Monte Carlo routines for thermal radiation. Details of the numerical implementation of the FDF method and its coupling with the FV-LES code is presented in Section 4.1. The PMC-based radiation treatment for hybrid FV/Lagrangian-particle simulations is discussed in Section 4.2, where a new stochastic scheme is presented for coupled PDF/PMC simulations. Section 4.3 briefly introduces the FV code that forms the backbone of the computational module. Parallelization strategies for the coupled LES/FDF/PMC (and RAS/PDF/PMC) code are outlined in Section 4.4.

4.1 Hybrid Lagrangian-Particle/Eulerian-Mesh Method

The mathematical formulation of the composition FDF method and the Lagrangian particle Monte Carlo method have been described in Chapter 2. The Monte Carlo method is coupled with a finite-volume solver to obtain information about the filtered velocity field and the subfilter length and time scales. Details of the coupling procedure are provided in Section 4.1.1. Coupling between a finite-volume solver and Monte Carlo code requires exchanging the filtered fields (in LES) to close the particle equations. The evaluation of FV fields at particle locations and

the extraction of filtered fields from particle values are described in Sections 4.1.4 and 4.1.5. The filtered fields extracted from the Monte Carlo code have statistical noise that may induce numerical instability in the flow solver. Therefore, an indirect feedback procedure is employed (Section 4.1.6). Other components in the numerical implementation of Monte Carlo particle methods, such as particle tracking (Section 4.1.2.1) and particle number density control (Section 4.1.3), are also explained. Parallelization of the Monte Carlo code is described in Section 4.1.2.

4.1.1 Coupling of Particle Monte Carlo with FV Solver

The composition FDF method is not a stand-alone method; it requires information on the filtered velocity field and turbulence scales to solve the particle SDEs (Eqs. 2.36 and 2.37), and those are obtained from a finite-volume flow solver. In this work, the Lagrangian Monte Carlo method is coupled with OpenFOAM [127], a pressure-based finite-volume CFD code (Section 4.3). OpenFOAM solves the set of filtered governing equations to obtain the hydrodynamic quantities (e.g., filtered velocity and pressure, the apparent subfilter-scale diffusivity for SFS transport, and turbulence time-scale for SFS mixing). These quantities are used in the Lagrangian Monte Carlo scheme to move the particles in physical and composition space (using Eqs. 2.36 and 2.37). Chemical reactions and turbulence–chemistry interactions are inherently accounted for as the particles move in composition space, and the updated particle compositions are used (see Section 4.1.5) to extract the filtered cell-based species mass-fractions and density that are fed to the finite-volume side. The density feedback from the particle Monte Carlo method is conducted in an indirect way, using an equivalent enthalpy procedure (Section 4.1.6).

The Lagrangian particle Monte Carlo code that is used in this work for hybrid LES/FDF simulations is derived from a previously developed particle Monte Carlo code [39, 138–140] for hybrid RAS/PDF simulations. The rationale for starting from an existing PDF code is that, although there are important mathematical and physical differences between PDF's and FDF's, from a practical point of view their implementations for three-dimensional time-dependent flows are similar. Key differences are in the specification of turbulent scales that drive the models for transport by velocity fluctuations and for molecular transport.

The coupling of the previously developed Fortran-90 PDF code with the OpenFOAM C++ code required several considerations, including identifying and accessing data that need to be passed, molding the data as required by the receiving unit, and casting C++ data that need to be passed to Fortran-90 subroutines into F90-recognizable format. The passing of C++ data to F90 subroutines was achieved through CHASM [189]. A validation study for the coupled OpenFOAM-RAS/PDF code is presented in the next chapter.

4.1.2 Parallelized Particle Monte Carlo Code for Domain-Decomposed Computations

Numerical simulation of laboratory flames within the framework of a coupled finite-volume–PDF code is computationally very expensive. This is especially the case for LES/FDF computations. Therefore, parallel computing is required to perform the desired calculations in a reasonable amount of time. OpenFOAM allows for parallel computing; it employs domain-decomposition to run cases in a parallel environment. Thus, it is highly desirable to parallelize the particle Monte Carlo code in a manner that will allow to run the coupled OpenFOAM/particle Monte Carlo code in parallel, which will lead to significant reduction in computational time. Since the Monte Carlo strategy used here is to maintain approximately the same number of particles in each FV cell, standard domain-decomposed-based parallelization by itself (i.e., without any extra measures) would be reasonably effective for the Monte Carlo code, except for chemistry computations.

Decomposing the computational domain across several processors for parallel runs requires particle tracking in the particle Monte Carlo code to be parallelized. Particle tracking is parallelized here to account for particles crossing the domain boundaries in domain-decomposed runs. Details of parallelized particle-tracking are provided in Section 4.1.2.1. With just this level of parallelization and no further load balancing for chemistry, a speed-up of approximately a factor of 12 was achieved for a RAS/PDF based parallel simulation of Sandia Flame D [125, 190] on 16 processors.

An extra layer of parallelization is added to the FV/PDF code to better balance chemistry calculations, if desired. A further speed-up of almost 30% was realized

in preliminary studies performed to check this implementation. This is discussed in detail in Section 4.1.2.2.

4.1.2.1 Parallelized Particle Tracking

The particle tracking scheme developed by Subramaniam and Haworth [138] has been modified in this work for parallelized particle tracking. In this modified scheme, for particle j in cell i on processor k, the minimum time to intersect with a face of cell i, $t^{(j)}_{min,i}$, is determined based on the velocity and location of particle j and the geometry of cell i. At the end of the time step δt, the particle remains inside cell i if $t^{(j)}_{min,i} > \delta t$. If $t^{(j)}_{min,i} < \delta t$, the particle is moved to the face intersection point. If that face lies on a domain–boundary that processor k shares with some neighboring processor l, then the particle's time step is decremented by $t^{(j)}_{min,i}$, the particle is stored in a special bin meant for particles leaving processor k and going to processor l, and the particle is rendered inactive for further tracking on processor k. For faces that are interior and are not on the domain-boundary, the particle's cell pointer is updated and its time step is decremented by $t^{(j)}_{min,i}$. Tracking continues until all active particles have zero time remaining. Then the particles stored in the processor boundary bins are passed to the neighboring processors, and tracking starts again until there are no remaining particles. This procedure of binning particles that are leaving the processor boundaries and tracking them on the neighboring processors continues until all bins on all processors are empty. The particle tracking algorithm for parallel FV/PDF runs is shown in Fig. 4.1.

This tracking scheme is suitable for three-dimensional unstructured stationary or deforming meshes with relatively large particle Courant numbers* (> 10) and large variations in the finite-volume cell size (up to factor of 10^6 variation in the cell volumes). Particles are tracked from cell to cell using trilinear basis functions [139, 191].

*Defined as the effective velocity of the particle times the time step size divided by the cell size.

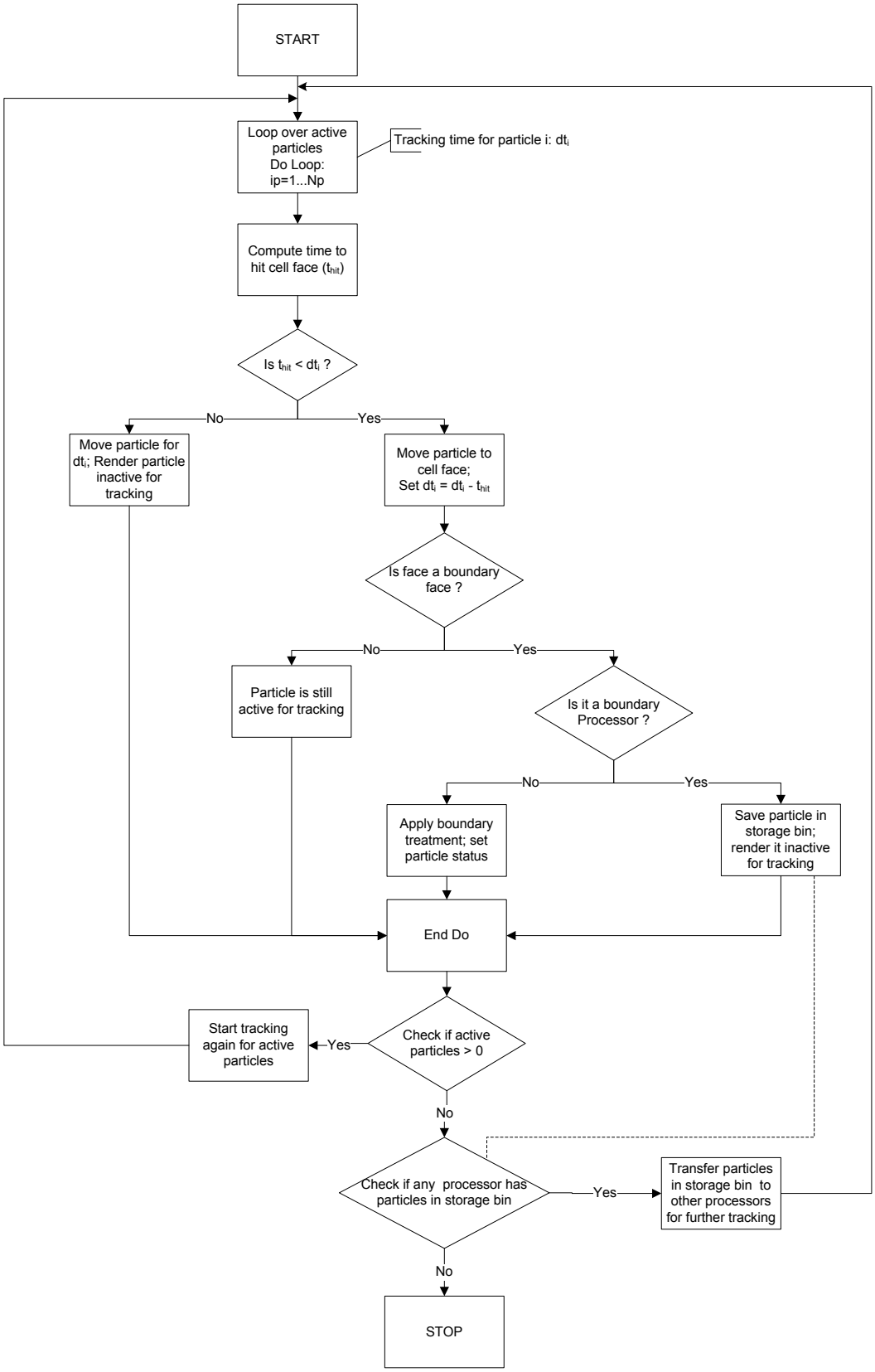

Figure 4.1. Particle tracking algorithm for parallel FV/PDF simulations.

4.1.2.2 Parallelization of Chemistry Computations for Improved Load-Balancing

The accurate representation of chemical kinetics requires a detailed chemical mechanism involving a large set of chemical reactions with disparate time scales. The presence of a large range of time scales makes the system of ordinary differential equations for chemistry computations stiff, and an implicit time-integration over the computational timestep is used to solve for chemistry. In a coupled finite-volume/particle Monte Carlo method, the time-integration is performed for each stochastic particle, and as a consequence chemistry computations typically account for 90% or more of the total computational time. Therefore, for domain-decomposed parallel computations, it is imperative to make sure that the computational load for the chemistry calculations is uniformly distributed over all processors. The simplest approach (each processor computes the chemistry for all the particles lying physically in its computational domain) is inadequate, because the location of particles in composition space dictates the computational effort for chemistry, and this varies widely from processor to processor. A straightforward and effective strategy is for each processor to distribute its particles to all other processors in a round-robin manner (sequentially assigning particles to processors) for the chemistry calculations.

The round-robin distribution of particles for chemistry calculations has been implemented for domain-decomposed parallel OpenFOAM/PDF computations. This approach essentially entails adding another layer of parallelization on top of the domain decomposition. With this approach, a speed-up of approximately a factor of 15 was achieved for a RAS/PDF simulation of Sandia Flame D on 16 processors.

4.1.3 Particle Number Density Control

A large variation in the finite-volume cell size and/or the movement of particles in physical space could result in large variations in the number of particles residing within each cell, thereby resulting in large statistical errors if the number of particles in a cell is too low or in a waste of computational resources if the number is too high. To maintain an acceptable distribution of particles as they move in physical space, particles are split (cloned) or recombined (annihilated) to

ensure that each cell contains approximately the same number of particles. Particles are cloned in cells where the number of particles drops below a prescribed minimum $\mathrm{Npc}_{\mathrm{min}}$, where the parent particle is split into two particles each having half the mass of the parent and the same properties as the parent particle. The highest-mass particles are cloned in each cell. This preserves the mean (filtered in LES) scalars at the cell level, and also the higher-order moments. If the number of particles exceeds a prescribed maximum $\mathrm{Npc}_{\mathrm{max}}$, a particle pair is selected at random, with preference given to low-mass particles. The particles in the pair are combined to give one particle such that the mass of the particles and cell-mean (i.e., filtered quantity in LES sense) particle properties are exactly conserved. This combination conserves the properties at the cell level, but induces artificial mixing at the higher-moments level.

4.1.4 Estimation of FV Field at Particle Locations

The Lagrangian Monte Carlo method is grid-free in principle, but it sits on top of a computational grid that is identical to the FV grid. This facilitates the (1) estimation of the FV values at particle locations, (2) extraction of cell-based quantities from particle values, and (3) computation of molecular mixing of particles.

The evolution equations (i.e., SDEs) for particles in the hybrid LES/Lagrangian Monte Carlo method require the specification of filtered quantities (e.g., filtered velocities) at particle locations. At each time-step, the cell-center values from a finite-volume code are interpolated to obtain the nodal values for the computational grid, which are then passed to the particle code. On the particle side, the global coordinates $\underline{x}$ are translated into cell local coordinates $\underline{\theta}$ by inverting the following relation [138]:

$$\underline{x}(\underline{\theta}) = \sum_{v} N_v(\underline{\theta})\underline{x}_v \ , \tag{4.1}$$

where v denotes vertices of a cell, N_v is the cell shape function and $\underline{x}_v$ are the global coordinates of cell vertices. The spatial variation of any dependent variable $B(\underline{x})$ in the interior of cell i is determined in terms of the vertex values $B_v^{(i)}$ [138] as

$$B^{(i)}(\underline{\theta}) = \sum_{v} b_v(\underline{\theta}) B_v^{(i)} \ , \tag{4.2}$$

where b_v is the cell interpolation function associated with each vertex. Linear functions are employed for shape and interpolation functions, because they ensure boundedness [138].

4.1.5 Extraction of Cell-Based Quantities from Particle Values

In a hybrid LES/FDF method, various filtered quantities (such as species mass-fractions, temperature, etc.) and the higher subfilter moments in a finite-volume cell are estimated from the particles' values by evaluating the mean of the quantity of interest over particles. Various approaches have been used to estimate the mean of particles' values in a FV cell from a notional particle field [191]. In this work, the straightforward method of taking mass-weighted ensemble averages over particles in a cell is employed. Thus, the filtered value of quantity ϕ in a finite-volume cell C can be calculated from

$$\underline{\widetilde{\phi}_C} = \frac{1}{M_{\text{total}}} \sum_{p \in C} m_p^* \underline{\phi}_p^*; \ \ M_{\text{total}} = \sum_{p \in C} m_p^* \ , \tag{4.3}$$

where M_{total} is the aggregated mass of all particles lying in cell C.

4.1.6 Equivalent Enthalpy Approach for Robust Time-Accurate Coupling

One of the essential features of coupled finite-volume/composition-PDF (i.e., RAS-based PDF approach) computations is that cell-based mean density and species mass-fractions are calculated based on particle values on the PDF side, and are fed to the finite-volume solver where conservation equations for mean mass, momentum, and energy are being solved. The mean density field calculated on the PDF side contains statistical noise, and this would result in numerical instability if passed directly to the finite-volume code. In RAS for statistically stationary flows, this difficulty is usually countered by performing time-blending [139, 140] or by

employing loosely coupled algorithms [142, 143]. In the time-blending approach, instead of passing the exact density and species field on the PDF side, values of quantities at the current timestep are heavily weighted with the values from the previous timestep before being fed to the FV solver. For a quantity ϕ that is passed as a feedback from the PDF side to the FV side, the time-blending procedure can be written as

$$\phi^{n+1} = k\phi^{n} + (1-k)\phi^{n+1}_{\mathrm{PDF}} \ , \tag{4.4}$$

where ϕ^{n+1} is the quantity fed to the FV side at the $(n+1)^{th}$ time-step, ϕ^{n} is the quantity from the n^{th} time-step, $\phi^{n+1}_{\mathrm{PDF}}$ is the simple mass-weighted particle value (Eq. 4.3) on the PDF side at the $(n+1)^{th}$ time-step, and k is the time-blending factor. As the blending factor increases toward unity, the fraction of the current time step that is fed back gets smaller and more time steps are included in the averaging process. The advantage of such a scheme is that no memory is required to store histories, while a disadvantage is that different time steps are not weighted equally in the average.

The above approach is valid only for statistically-stationary RAS/PDF simulations. Coupled LES/FDF simulations, on the other hand, require tighter coupling and time-accuracy. Special measures are required for stable, time-accurate feedback in coupled LES/FDF simulations. One technique that has been used successfully [143] is to solve for different forms of the energy equation on the finite-volume and PDF sides. On the PDF (or FDF) side, one continues to solve for the absolute specific enthalpy using stochastic particles, whereas a transport equation is solved for an equivalent sensible enthalpy variable [143] on the finite-volume side. The equivalent enthalpy used in this work is defined as

$$h_{eq} \equiv \frac{R_u T}{\gamma_o - 1} \sum_i Y_i / W_i \ , \tag{4.5}$$

where $\gamma_o = 1.4$, R_u is the universal gas constant, and Y_i and W_i are the mass-fraction and molecular weight of species i. It is important to recognize that a fixed value of γ_o does not imply any restrictive assumptions (e.g., constant specific-heats) in this formulation. The thermochemistry considered corresponds to that of a mixture of ideal-gases, and the treatment is quite general.

Instead of direct density feedback, the cell-averaged change in the equivalent enthalpy due to mixing and chemical reaction (and thermal radiation and other sources in absolute enthalpy) is calculated on the PDF (or FDF) side and is passed to the finite-volume side. Then, an elliptic equation is solved for equivalent enthalpy on the finite-volume side with feedback from PDF (or FDF) routine as a source term, which reduces the statistical noise. The elliptic transport equation for equivalent enthalpy can be derived from the modeled transport equation for the composition FDF (Eq. 2.34), since h_{eq} is a function of composition variables. The derived equation for filtered equivalent enthalpy (in the LES context) contains unclosed terms on the right-hand side, which can be interpreted as source terms due to chemical reaction and subfilter mixing (and other sources). The finite-volume cell-based source term ($\widetilde{S}_{h_{eq}}$) is estimated as the mass-weighted-average change in the equivalent enthalpy of particles lying within the cell due to chemical reaction and mixing (and other sources). The transport equation for filtered equivalent enthalpy is given by

$$\frac{\partial \overline{\rho}\widetilde{h}_{eq}}{\partial t} + \frac{\partial \overline{\rho}\widetilde{h}_{eq}\widetilde{u}_i}{\partial x_i} = \frac{\partial}{\partial x_i}\left[\overline{\rho}\left(\Gamma + \Gamma_t\right)\frac{\partial \widetilde{h}_{eq}}{\partial x_i}\right] + \overline{\rho}\widetilde{S}_{h_{eq}} \ . \tag{4.6}$$

To accommodate the above approach, the thermochemistry implementation in OpenFOAM has been modified to incorporate another energy variable (equivalent sensible enthalpy). The modified code has been tested for Sandia Flame D in a RAS/PDF framework. Further details are presented in Section 5.3.

4.2 PMC-Based Radiation Treatment for Hybrid FV/PDF Simulations

The PMC method, where different radiation processes such as emission, absorption, scattering and reflection are explicitly simulated by tracing representative photon bundles in the computational domain, is able to handle complex geometries, medium inhomogeneity and nongray radiative properties, in contrast to traditional radiation modeling methods. The importance of considering TRI for accurate modeling of turbulent reacting flows has already been established. Emission

TRI is dealt with exactly by virtue of the PDF method, and models have been developed to incorporate absorption TRI in hybrid FV/PDF simulations. The notional particle representation that stochastically mimics the evolution of the one-point, one-time joint scalar PDF provides information about scalar fluctuations in a turbulent flow field that has been utilized to develop models for absorption TRI. Wang and Modest [153] assumed that the notional particles are analogous to fluid parcels that represent an instantaneous snapshot of the turbulent flow field. Based on this assumption, they developed PMC algorithms for media represented by discrete particles, where particles were modeled as either point masses or as spherical particles, and rays were modeled as either lines or as cones with decaying influence function from the centerline. Three different interaction schemes between rays and particles were proposed in their work: line-sphere, cone-point and cone-sphere schemes. This approach requires physical attributes to be imparted to the notional particles that go beyond those that are required for the PDF method. Also, the schemes do not reduce naturally to a cell-based PMC formulation in the limit of no TRI. In this work, a new PMC scheme is proposed for treating radiation in media represented by a PDF particle field. This scheme deals with ray-particle interaction in a stochastic manner, without assigning any additional physical attributes to the notional particles beyond those that are implicit in the PDF formulation. Details of the scheme are presented below.

4.2.1 A Stochastic PMC Scheme

4.2.1.1 Motivation

In the Lagrangian formulation of transported PDF methods, a one-time, one-point joint-PDF of chemical species composition and enthalpy is considered, and a transport equation is solved for the mass density function (density times the joint-PDF) using a stochastically equivalent Lagrangian particle Monte Carlo procedure. The stochastic solution of the transported PDF equation is based on the idea that the collection of notional particles in a small region approximates the mass density function (MDF[†]) in that region. Here, the region corresponds to an infinitesimal

[†]This is the mass-weighted fine grain density in RAS/PDF that is analogous to FMDF (Eq. 2.20) of the LES/FDF formulation.

volume (a finite-volume cell) in which the MDF can be assumed to be uniform.

Notional particles evolve such that the PDF constructed from these particles is stochastically equivalent to the one-point, one-time PDF obtained from the solution of a modeled PDF transport equation. Each particle has a specified fluid mass assigned to it, and carries a distinct set of composition scalars. The particles evolve in physical and composition space through operations that represent the physical processes of advection, turbulent diffusion, chemical reaction, and mixing corresponding to the underlying modeled PDF transport equation. These particles are entities that are introduced to solve the modeled PDF transport equation, and should not be interpreted too literally as being fluid particles. The distribution of particle mass must remain consistent with the mean fluid mass at the finite-volume cell level.

Each particle in a FV cell (in general, a small region) can be thought of as an instantaneous realization of the flow quantities in the cell. That is, particles present inside a cell represent possible realizations of composition scalars in that cell in a fluctuating turbulent flow field.

Consider the mass density function (MDF), $\mathcal{F}(\underline{\psi}, \underline{x}; t)$. The MDF is expressed in terms of mass-density (ρ) and the one-point, one-time joint-composition PDF ($f(\underline{\psi}; \underline{x}, t)$) as

$$\mathcal{F}(\underline{\psi}, \underline{x}; t) = \rho(\underline{\psi}) f(\underline{\psi}; \underline{x}, t) \ . \tag{4.7}$$

In the above expression, $\underline{\psi}$ represents the composition space vector. The MDF can also be represented in terms of mean density and the one-point, one-time joint-composition Favre PDF:

$$\mathcal{F}(\underline{\psi}, \underline{x}; t) = \rho(\underline{\psi}) f(\underline{\psi}; \underline{x}, t) = \langle \rho(\underline{x}) \rangle \widetilde{f}(\underline{\psi}; \underline{x}, t) \ . \tag{4.8}$$

Now consider finite-volume cell ic (an infinitesimal volume) which contains N_p notional particles. Each particle carries a specified fluid mass and a composition vector, denoted by m_{ip} and $\underline{\psi}_{ip}$, respectively, where ip indicates the ip^{th} particle. Notional particles approximate the MDF in a discrete sense. Assuming the joint Favre PDF to be uniform inside cell ic, the joint Favre PDF for cell ic can be written in terms of the discrete MDF as follows:

$$\langle \rho(\underline{x}) \rangle \widetilde{f}(\underline{\psi}; \underline{x}, t) \approx \sum_{ip=1}^{N_p} m_{ip}\ \delta[\underline{\psi}(\underline{x}, t) - \underline{\psi}_{\ ip}]\ \delta[\underline{x} - \underline{x}_{ip}]\ . \tag{4.9}$$

Multiplying the above expression with a fine-grained PDF ($\delta[\underline{\psi}(\underline{x}, t) - \underline{\psi}_{\ k}]$) isolates the contribution of the k^{th} particle; then integrating over $\underline{\psi}$-space and over the cell yields,

$$\widetilde{f}(\underline{\psi}_{\ k}) \ \propto\ m_k\ . \tag{4.10}$$

This suggests that the mass that each notional particle carries is a weight factor that can be used in the estimation of Favre-averaged cell quantities. A Favre-averaged quantity is obtained by performing a weighted average over all notional particles in a cell. For quantity $Q(\underline{\psi}; \underline{x}, t)$:

$$\widetilde{Q(\underline{x}, t)} = \frac{\int\ Q(\underline{\psi})\ \widetilde{f}(\underline{\psi}; \underline{x}, t)\ d\underline{\psi}}{\int\ \widetilde{f}(\underline{\psi}; \underline{x}, t)\ d\underline{\psi}} \approx \frac{\sum_{ip=1}^{N_p} m_{ip} Q(\underline{\psi}_{\ ip})}{\sum_{ip=1}^{N_p} m_{ip}}\ . \tag{4.11}$$

From our previous discussion that the notional particles represent different realizations of a turbulent flow field inside a cell, the above expressions show that the particle mass can be considered as a measure of the contribution of that particle's realization when estimating Favre-averaged quantities at the cell level. Furthermore, the Favre probability of having the k_{th} particle's composition ($\underline{\psi}_k$) in cell ic is proportional to the particle mass m_k.

Re-stating Eq. (4.10) in terms of the one-point, one-time joint-composition PDF:

$$f(\underline{\psi}_k) \ \propto\ m_k / \rho(\underline{\psi}_k)\ . \tag{4.12}$$

This shows that for any cell ic, the probability of having a realization (as represented by particle ip) in cell ic in a fluctuating flow-field is proportional to $m_{ip}/\rho(\underline{\psi}_{\ ip})$. This is tested below, where Favre-average of a quantity Q is computed using Eq. (4.12) for $f(\underline{\psi}_{\ k})$ and the result thus obtained is verified to be the same as the previously computed expression for Favre-average in Eq. (4.11). For quantity $Q(\underline{\psi}; \underline{x}, t)$, the Favre-average can be expressed as

$$\widetilde{Q(\underline{x},t)} = \frac{\langle \rho(\underline{x},t)Q(\underline{x},t)\rangle}{\langle \rho(\underline{x},t)\rangle} = \frac{\int\ \rho(\underline{\psi})Q(\underline{\psi})\ f(\underline{\psi};\underline{x},t)\ d\underline{\psi}}{\int \rho(\underline{\psi})f(\underline{\psi};\underline{x},t)\ d\underline{\psi}}$$
$$\approx \frac{\sum_{ip=1}^{N_p} \rho(\underline{\psi}_{\ ip})Q(\underline{\psi}_{\ ip})f(\underline{\psi}_{\ ip})}{\sum_{ip=1}^{N_p} \rho(\underline{\psi}_{\ ip})f(\underline{\psi}_{\ ip})}\ . \tag{4.13}$$

Using the proportionality relation for $f(\underline{\psi}_{\ k})$ (Eq. 4.12), the expression for the Favre-average below is identical to that in Eq. 4.11:

$$\widetilde{Q(\underline{x},t)} \approx \frac{\sum_{ip=1}^{N_p} \rho(\underline{\psi}_{\ ip})Q(\underline{\psi}_{\ ip})\frac{m_{ip}}{\rho(\underline{\psi}_{\ ip})}}{\sum_{ip=1}^{N_p} \rho(\underline{\psi}_{\ ip})\frac{m_{ip}}{\rho(\underline{\psi}_{\ ip})}} = \frac{\sum_{ip=1}^{N_p} m_{ip}Q(\underline{\psi}_{\ ip})}{\sum_{ip=1}^{N_p} m_{ip}}\ . \tag{4.14}$$

The proportionality expression for probability of occurrence of the scalar set represented by particle ip in cell ic (given by $m_{ip}/\rho(\underline{\psi}_{\ ip})$) also corresponds to the volume of an identical mass of homogeneous fluid with composition $\underline{\psi}_{\ ip}$. However, in the context of notional particles, it is better to interpret $m_{ip}/\rho(\underline{\psi}_{\ ip})$ as a probabilistic measure of the occurrence of a particle realization, rather than giving it such a specific physical attribute.

To summarize, one-point statistics in turbulent flows can be captured accurately in transported PDF methods where a modeled transport equation for a mass-density function is solved using a stochastically-equivalent Lagrangian particle Monte Carlo procedure. In this approach, notional point-particles that carry mass and composition scalars evolve in physical and compositional space to yield the same MDF as the real fluid system. Notional particles are stochastic in nature, and each particle can be thought of as one possible realization of the instantaneous properties in the cell that they reside in. The mass carried by particles has dual implications: (1) the spatial mass distribution of notional particles must remain consistent with the mean fluid mass, since notional particles mimic the evolution of the MDF; and (2) the probability of occurrence of a particle's realization in its host cell in a turbulent flow is proportional to particle's mass divided by its thermochemical density. The ratio of notional particle mass and thermochemical density should be interpreted as a probabilistic measure of the occurrence of particle realization, and should not be assigned further physical attributes. With these concepts in mind, a new PMC/PDF algorithm is proposed to account for radiative

heat transfer in participating medium, with particular attention to representing absorption and absorption TRI.

4.2.1.2 Model Formulation

A photon Monte Carlo (PMC) method [128] has been developed and implemented in the hybrid FV/PDF (and FV/FDF) computational module to solve the radiation transfer equation in turbulent flow fields characterized by stochastic notional PDF (and FDF) particles. In this model, photon-particle interaction schemes have been devised that are consistent with the notional particle representation in PDF (and FDF) methods. This is an advancement compared to the previously proposed PMC schemes [153] for treating radiation in PDF particle fields. A brief description of the scheme is presented below.

The method is based on the probability of occurrence of notional particle realizations in their host finite-volume cells (Eq. (4.12)). For a finite-volume cell ic that contains N_p stochastic particles, the probability of occurrence of the scalar set represented by particle ip in cell ic is given by

$$f(\underline{\psi}_{ip}) \;=\; \frac{\frac{m_{ip}}{\rho(\underline{\psi}_{ip})}}{\sum_{ip=1}^{N_p} \frac{m_{ip}}{\rho(\underline{\psi}_{ip})}} \;. \tag{4.15}$$

The ip^{th} particle realization contribution to radiative emission from a finite-volume cell is given by total emission from the cell for scalar set $\underline{\psi}_{ip}$ times the probability of occurrence of that set. That is,

$$E_{emiip} = 4\sigma\kappa(\underline{\psi}_{ip})T^4(\underline{\psi}_{ip})V_{cell}f(\underline{\psi}_{ip}) \;. \tag{4.16}$$

The total emission from a finite-volume cell is the sum total of emission for all particle realizations, as follows:

$$E_{emi} = \sum_{ip=1}^{N_p} 4\sigma\kappa(\underline{\psi}_{ip})T^4(\underline{\psi}_{ip})V_{cell}f(\underline{\psi}_{ip}) = 4\sigma \;\frac{\sum_{ip=1}^{N_p} \kappa(\underline{\psi}_{ip})T^4(\underline{\psi}_{ip})\frac{m_{ip}}{\rho(\underline{\psi}_{ip})}}{\sum_{ip=1}^{N_p} \frac{m_{ip}}{\rho(\underline{\psi}_{ip})}}\; V_{cell} \;. \tag{4.17}$$

Radiative emission from a finite-volume cell is treated by launching representa-

tive photon bundles for every PDF particle realization present in that cell, using an adaptive emission technique [185]. The emitted photon bundles (rays) are traced through the computational domain. The energy associated with these bundles is attenuated due to radiative absorption as they travel through finite-volume cells.

Radiative absorption is modeled using a stochastic scheme. Here, a cumulative probability function (P_{CDF}) is constructed for each finite-volume cell by summing up the individual probabilities (Eq. (4.15)) for all PDF particles present in that cell. The cummulative probability corresponding to particle ip is given by,

$$P_{CDF}(\underline{\psi}_{ip}) = \sum_{i=1}^{ip} f(\underline{\psi}_i) = \frac{\sum_{i=1}^{ip} \frac{m_i}{\rho(\underline{\psi}_i)}}{\sum_{i=1}^{N_p} \frac{m_i}{\rho(\underline{\psi}_i)}} \ . \tag{4.18}$$

Each particle realization holds a certain probability band in the cumulative probability distribution. The probability band for particle ip is as follows:

$$\text{Probability Band}_{ip} = \left[P_{CDF}(\underline{\psi}_{ip-1}), P_{CDF}(\underline{\psi}_{ip}) \right] \ . \tag{4.19}$$

There is a one-to-one mapping between probability values from zero to one and the particle realization that corresponds to that probability value. Using this mapping (Eq. 4.19), the scalar composition (or notional particle) in a finite-volume cell that is selected to interact with the traversing photon bundle is determined stochastically by drawing a random number between zero and one.

Multiple interactions, where a photon bundle interacts with multiple PDF particles, can be accommodated by drawing multiple random numbers. In that case, the length traversed by the photon bundle inside the finite-volume cell is split equally among all interacting particles to compute the total attenuation of the ray.

This method is unbiased, since the interaction scheme is independent of the order of particles and their locations within a cell. That is, for multiple interactions within a cell, since the selection order is based on the outcome of the uniform random number generator, the local particle ordering within a cell has no bearing on the radiative absorption inside a cell.

This new stochastic PMC method is consistent with the notional particle representation in PDF methods. In contrast to earlier PMC/PDF schemes [153], no new physical attributes are assigned to the notional particles to treat radiative

	Cone-PPM	Line-CDS	Stochastic
Assumptions about notional particle field	Yes (particles as point masses; spheres for emission purposes)	Yes (particles modeled as constant-density spheres)	No (retains stochastic nature of particles)
Ray-particle interaction	Deterministic selection of particles		Random selection (based on probability of occurrence)
Reduction to cell-based PMC	No (volume of influence is not equal to physical volume)	No (length traversed not equal to physical length)	Yes
Ray topology	Cone (higher-order representation)	Line	Line
Computational cost	High	Moderate	Low

Table 4.1. A comparison of different PDF/PMC schemes.

processes. Also, this method reduces to cell-based PMC in the limit of no TRI; here the optical thickness that a ray experiences in a FV cell is equal to the absorption coefficient times the distance traversed. Table 4.1 presents a comparison of the new PMC method with the previous schemes.

4.2.1.3 Coupling PMC with FV/PDF Routines

The PMC schemes described above need information about particle compositions and the particle-cell mapping to model radiative emission and absorption in a turbulent flow field. They also require information about the grid (mesh cells and their connectivity) to track photon bundles through the computational domain. In this work, the PMC module is coupled with the FV/PDF code such that it only communicates with the PDF code to access the necessary data structures. This design allows for the portability of the PDF/PMC code to any FV code.

At every time step, the mesh and particle information is passed from the PDF code to the PMC code. The PMC routines for releasing and tracing photon bundles are invoked in the PDF code while advancing the notional particles in the composition space. The radiative emission and absorption experienced by the notional particles is fed back into the PDF code by updating the particle enthalpy.

4.3 Underlying Finite-Volume Solver

OpenFOAM, an open source, unstructured, colocated, finite-volume CFD software written in C++, is used as the underlying CFD solver for RAS/PDF and LES/FDF simulations. OpenFOAM provides both pressure- and density-based segregated solvers with various options for pressure-velocity coupling. In this work, a compressible, pressure-based segregated solver with the PISO algorithm for pressure-velocity coupling is used for RAS and LES simulations. To obtain the solution for PDE's and ODE's, OpenFOAM integrates the governing equations and utilizes Gauss' theorem to convert volume integrals into surface integrals for divergence and Laplacian terms in the equations. This leads to the presence of face-centered quantities in addition to the cell-centered quantities. Various schemes are available in OpenFOAM to interpolate the data from cell-centers to face-centers, ranging from simple upwind and linear interpolation to more sophisticated TVD schemes [127]. In this work, a linear scheme (central differencing) is used for cell-face interpolation, and second-order TVD schemes (for RAS) and filtered schemes (for LES) are employed for treatment of convection terms. The filtered scheme for LES is a modified central differencing scheme that removes staggering caused by pressure-velocity decoupling by adding small amounts of upwind. OpenFOAM offers Euler, Crank-Nicholson, and backward schemes for time derivatives. Crank-Nicholson is used in this research work. OpenFOAM supports domain-decomposed parallel computations via MPI (Message Passing Interface), where the computational domain is divided into several parts that are distributed over the compute nodes of a multiprocessor/multicore machine or a cluster.

4.4 Parallelization Strategies

The coupled FV/PDF/PMC (and FV/FDF/PMC) computational module poses a great challenge in terms of finding an optimum strategy for efficient parallelization of the fully coupled system for domain-decomposed parallel simulations. The chemistry computations exhibit locality and independence. That is, the cost of the chemistry computations in a given finite-volume cell is only dependent on the scalar compositions of the particles in that cell. The computational expense for

mixing in PDF routines is also local to a finite-volume cell. However, PMC ray tracing is nonlocal and requires information about the entire mesh. In domain-decomposed parallel runs, the computational domain is broken up and distributed among participating processors. This makes it difficult to efficiently parallelize the PMC solver, since rays traveling long distances would require communication across multiple processors. Furthermore, since ray tracing is a nonlocal process, the time spent in ray tracking is nonuniform in the domain since some parts of the computational domain would encounter more rays than other parts. The advection of PDF particles is also nonlocal, but typically a particle would traverse only a small number of cells in one timestep, in contrast to a PMC photon bundle that can pass through an arbitrary number of cells. The parallelization characteristics of the various components of the coupled FV/PDF/PMC code are summarized in Table 4.2.

It is nontrivial to devise a single parallelization strategy that performs efficiently for this heterogeneous (FV + PDF + PMC) code. In general, a different strategy is most effective for each individual component, and different aspects of the simulation may dominate the computational effort, depending on the choice of models.

An efficient parallelization scheme for the coupled FV/PDF/PMC module is developed in this work. The scheme is generic in nature, and can be used for different combinations of models. The main idea of this scheme is to generate an initial estimate of the computational cost of various components, and to utilize that knowledge to decompose the computational domain. The scheme is presented in detail below.

4.4.1 Local-Computation-Time-Map-Based Domain-Decomposition + Deferred Ray Tracking Scheme

In this scheme, the total computational cost of each component (e.g., chemistry, PMC ray tracing) is assessed first for all finite-volume cells. Then the entire computational domain is decomposed such that each processor is responsible for approximately the same aggregated computational effort. This was found to be more effective than approaches that attempted to optimize the parallelization of

Component	Sub-Component	Computational Expense and Remark	Parallelizability	Parallelization Technique
FV	Flow solution	Global in nature; System of linear equations solved simultaneously for entire domain	Highly parallel	Domain-decomposition
PDF	Chemistry	Usually most expensive; Local in nature	Almost perfectly parallel	*a priori* measure: customized domain-decomposition; *a posteriori* measure: Particle redistribution across processors for chemistry
	Mixing	Low to medium computational load; Local in nature	Highly parallel	Basic domain-decomposition (for most mixing models)
	Advection	Low to medium cost; Nonlocal in nature	Difficult to parallelize effectively	Basic or customized domain-decomposition
PMC	Ray tracing + radiative properties evaluation	Medium to high cost; Highly nonlocal in nature	Extremely difficult for domain-decomposed parallel runs	Customized domain-decomposition and deferred tracing; Distribute rays across processors for non-domain-decomposed parallel runs

Table 4.2. Parallelization characteristics of the various components of the coupled FV/PDF/PMC code.

each component (e.g., chemistry or radiation) separately.

The assessment of computational cost for chemistry calculations in a finite-volume cell is straightforward because of its inherently local nature. However, in assessing the cost for PMC calculations for a finite-volume cell, there are several options. For example, one could base the analysis on (i) time spent in tracing rays

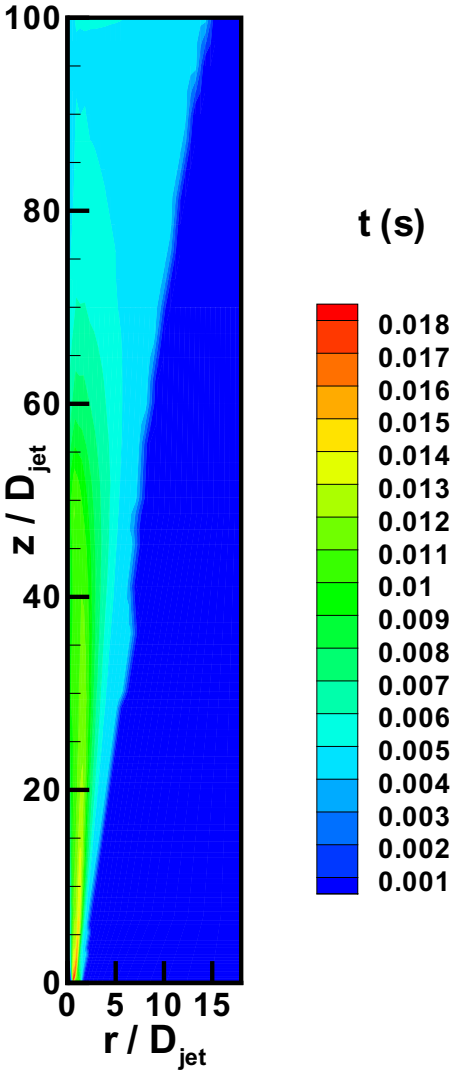

Figure 4.2. Computational time map for RAS/PDF/PMC of a modified Sandia flame. The plot represents average CPU time spent (in s) per time-step for chemistry calculations.

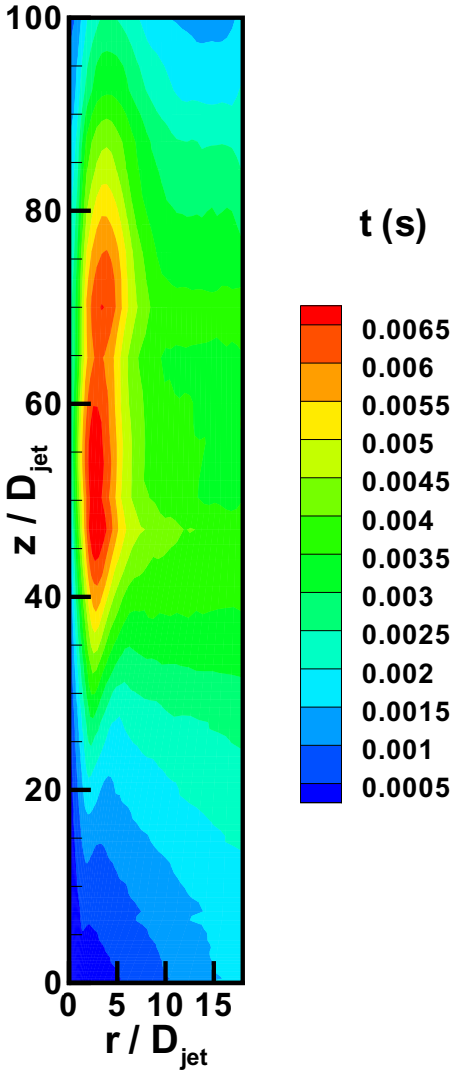

Figure 4.3. Computational time map for RAS/PDF/PMC of a modified Sandia flame. The plot represents average CPU time spent (in s) per time-step for PMC calculations.

emitted from that cell, or (ii) total time spent in performing tracking operations (ray-particle interactions and search for the next cell) for all rays passing through that cell. With the former option, load balancing would imply that tracing of rays should be done on the parent processor at each time step. This would require the entire mesh and all PDF particle information to be available on that processor, which is not possible for large mesh sizes. With the latter option, if the ray's

tracking is continued at the next time step once it hits the processor boundary, eventually a state is attained where all processors see rays that originated from the entire computational domain (which would take maximum of $N-1$ time steps if a run is made on N processors) and the computational load is completely balanced. After $N-1$ time steps, each processor will have rays that originated from everywhere in the domain, although rays from further away will have originated on earlier time steps. The inherent assumption is that the collective nature of the rays emitted from any processor will not vary significantly over N time steps. Here the latter option is chosen for the assessment of PMC cost for a finite-volume cell.

With the latter option for characterizing PMC cost as discussed above, the computational cost-maps for chemistry and PMC calculations for RAS/PDF/PMC simulation of a modified Sandia Flame D (introduced in Section 5.4) are shown in Figs. 4.2 and 4.3, respectively. The RAS/PDF/PMC simulation employed approximately 80000 notional particles and as many photon bundles. The contour plots in these figures represent the time spent per time-step in FV cells for chemistry and radiation computations. The difference in the cost-map for chemistry and PMC computations is quite evident; the cost-map for chemistry exhibits locality and is concentrated in the flame region, whereas PMC costs are dependent on the number of rays passing through a FV cell, and therefore regions with high view factors from emission-dominated zones exhibit significant PMC costs. The aggregated cost-map for PMC and chemistry calculations is shown in Fig. 4.4.

For efficient parallelization of FV/PDF/PMC runs, once the time spent on chemistry and PMC calculations has been recorded for each finite-volume cell for a short run (as demonstrated above by Fig. 4.4), the next step is to decompose the computational domain into several parts such that each part bears the same computational cost. For this purpose, the computational costs are aggregated for all cells to get the global computational cost. Based on the number of domains, computational cost per processor is estimated. Then cells are clustered in the computational domain to form blocks with computational cost equal to the estimated computational cost per processor. At this point, the clustering operation is essentially manual and care needs to be taken to ensure the spatial locality of the cells within the cluster. The cells might be nonlocal in space in the default mesh representation, and therefore reordering of cells might be helpful before the clustering

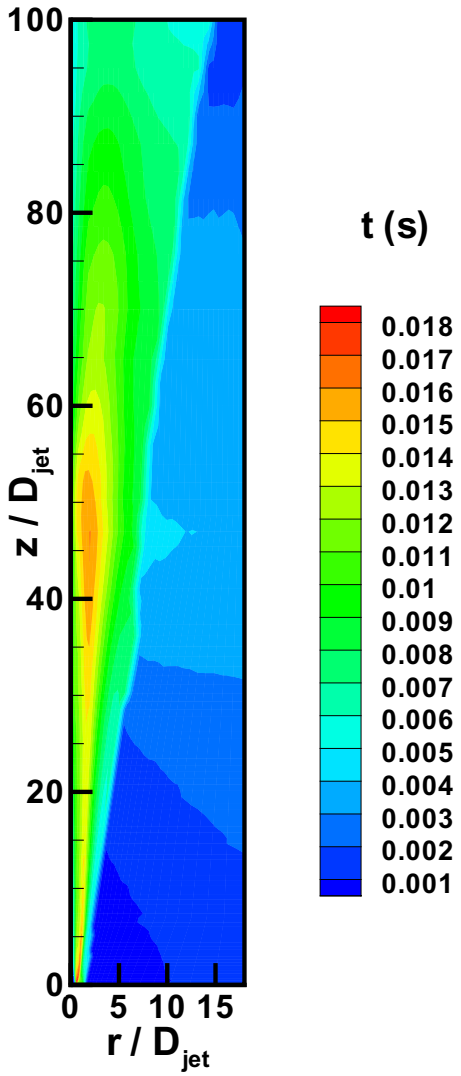

Figure 4.4. Computational time map for RAS/PDF/PMC of a modified Sandia flame. The plot represents average CPU time spent (in s) per time-step for chemistry and PMC calculations.

operation. This is illustrated in Fig. 4.5 that shows the ordering of cells in the FV mesh for RAS/PDF of an axisymmetric modified Sandia flame case (Section 5.4). Before clustering is performed, the cells are reordered (temporarily) to get a monotone distribution, as shown in Fig. 4.6. Then, the reordered cells are clustered to form blocks such that each block has the same computational cost. Fig. 4.7 shows the clustering of cells into 16 blocks for the reordered cells of Fig. 4.6.

Note that the computational cost can vary significantly from cell to cell, and cells with high computational cost might be confined to one region in the compu-

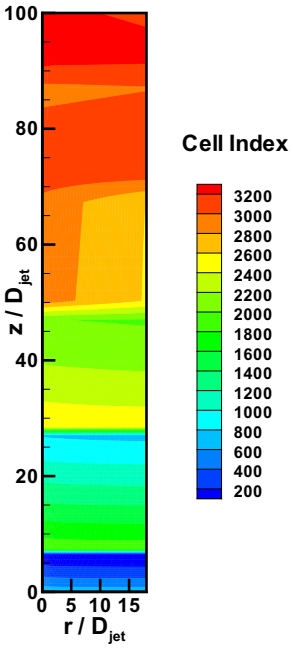

Figure 4.5. Default cell ordering in the FV mesh of a modified Sandia flame. The plot represents indices of cells.

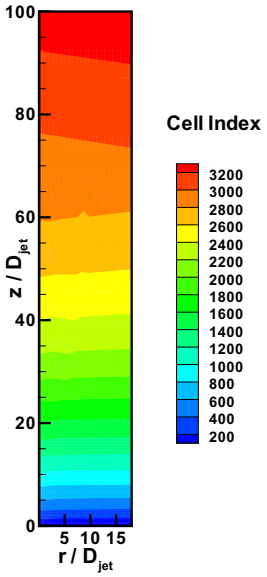

Figure 4.6. Reordered cell indices in a modified Sandia flame.

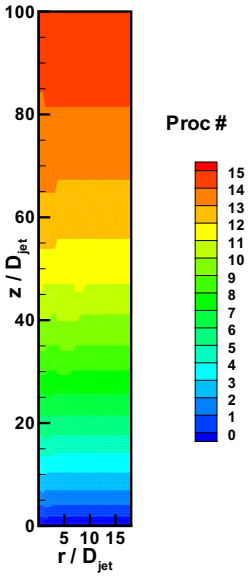

Figure 4.7. Clustering of cells for the reordered cell indices.

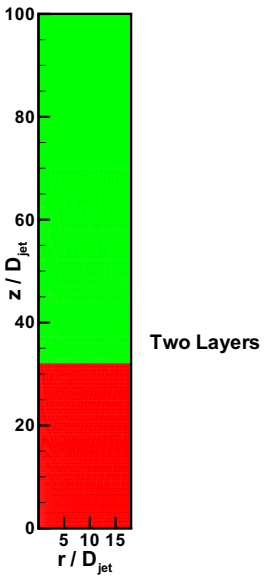

Figure 4.8. Double layer approach for cell reordering. The plot represents two layers for reordering of cells

.

tational domain. This could result in mesh decompositions with large unevenness in the number of cells across processors. Therefore, a custom reordering and clustering strategy needs to be adopted for each reacting flow system to ensure good spatial locality of cells on a processor and a reasonably uniform cell count across processors.

To this end, reordering and clustering operations are revisited for the configuration discussed above (cost-map of Fig. 4.4). In the aggregated cost-map, the computational cost is high in regions close to the axis ($r/D_{jet} = 0$) and in the vicinity of $y/D_{jet} = 40$ in the axial direction. Therefore, instead of a single layer reordering (of Fig. 4.6), the computational domain is divided into two zones axially (as illustrated in Fig. 4.8) and reordering is done in a local manner in each of the two zones. This double-layer reordering is shown in Fig. 4.9. For this reordering, the clustering is performed within each layer (zone) and is illustrated in Fig. 4.10. The main purpose of this double-layer reordering is to divide the region with high computational cost and assign it uniformly over multiple processors. With the double-layer ordering, the uniformity in the cell count across processors improves by a significant margin, as can be seen in Fig. 4.11. The single-layer reordering

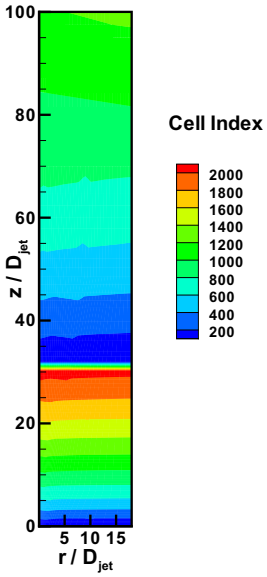

Figure 4.9. Reordered cell indices for a double layer in a modified Sandia flame.

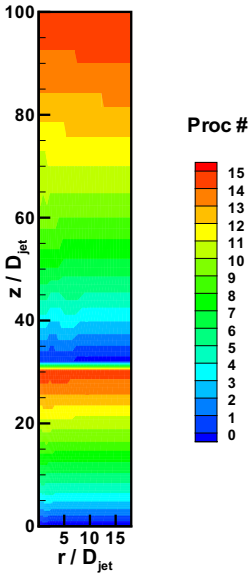

Figure 4.10. Clustering of cells for a double layer reordered cell indices in a modified Sandia flame.

leads to significant differences in the cell counts between processors due to the large local variations in computational costs for RAS/PDF/PMC simulation of the modified Sandia flame. For LES/FDF/PMC simulations, the computational costs and cell-sizes vary in the computational domain more than RAS-based runs, and single-layer ordering can lead to large differences in the cell counts across processors. For the parallelization studies presented in Section 5.6, double-layer reordering is performed for both RAS/PDF/PMC and LES/FDF/PMC computations.

4.5 Modular Code Structure

Significant effort has been invested to consolidate the several individual component modules (FV/FDF, PMC for thermal radiation, soot models - see Chapters 5 and 6) into a comprehensive and modular code that can be used for RAS/PDF and LES/FDF simulations of nonsooting and sooting turbulent reacting systems. The structure and connections among modules are illustrated in Fig. 4.12. The goal is to provide a comprehensive package that will allow a user to specify the desired level

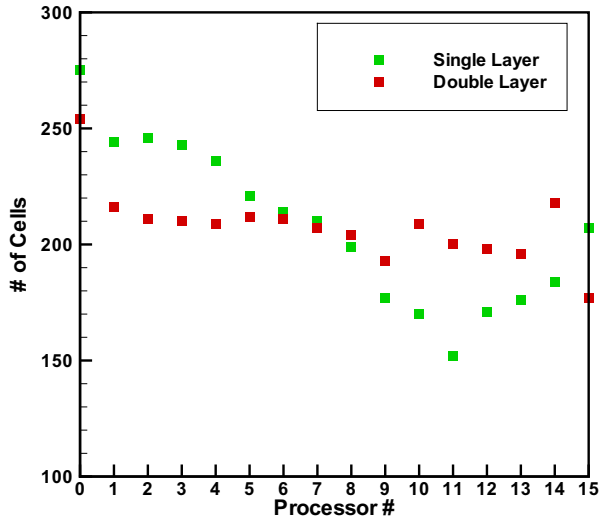

Figure 4.11. Comparison of processor cell counts for single-layer and double-layer reordering.

of turbulence closure, gas-phase thermochemical properties and chemical kinetics mechanism, soot model, and level of radiation modeling (e.g., including versus excluding TRI). A similar structure is being designed for spherical-harmonics-based RTE solvers. In this study, the focus is on the detailed RAS and LES simulations of nonsooting systems and analyzing radiation characteristics of both sooting and sooting systems.

4.6 Summary of Key Equations for RAS/PDF and LES/FDF Simulations

The set of equations and model constants employed in this research for RAS/PDF and LES/FDF simulations are summarized in this section. These equations invoke standard simplifications such as high-Reynolds-number, low-Mach-number, reacting ideal-gas mixture where the thermochemical state of the system can be determined from mixture specific enthalpy, species mass-fractions, and pressure. A hybrid FV/Lagrangian-particle approach is used in this work, where mean/filtered equations for mass, momentum and energy are solved on the FV side and a mod-

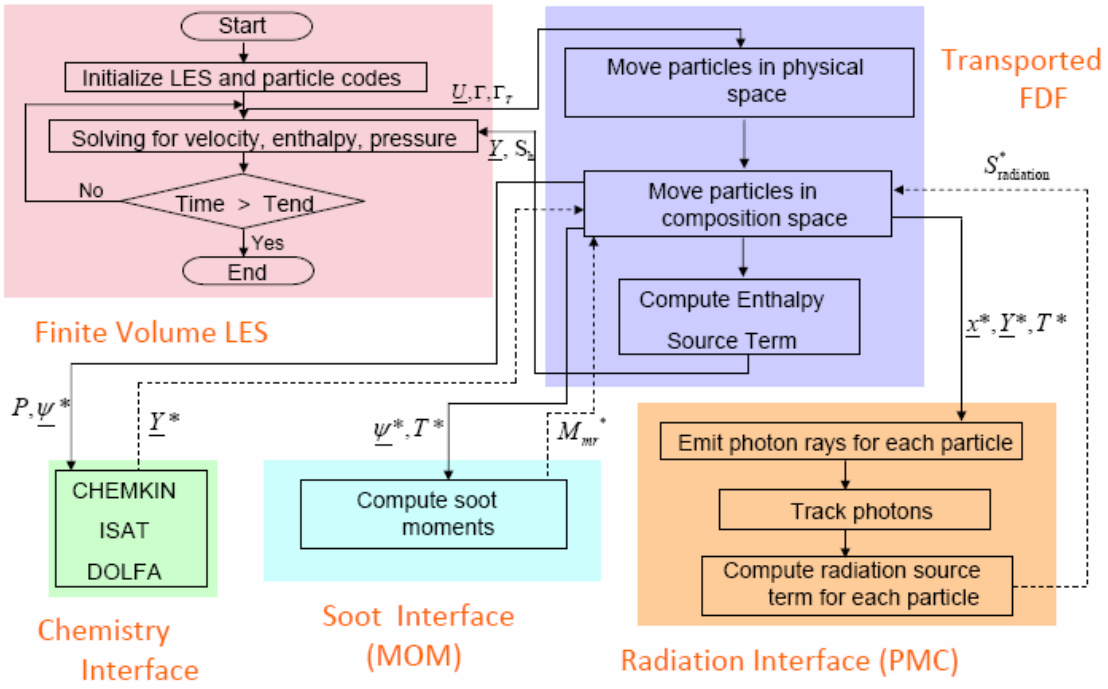

Figure 4.12. Schematic illustration of the LES/FDF/PMC/MOM-based computational module.

eled equation for a one-point, one-time joint-PDF (or joint-FDF for LES/FDF) of species mass-fractions and mixture specific enthalpy is solved using a Lagrangian particle Monte Carlo procedure. For RAS/PDF simulations, a standard two-equation $k-\epsilon$ model is used and equations for turbulence kinetic energy (k) and eddy dissipation rate (ϵ) are solved on the FV side. The SFS stress tensor in the filtered momentum equations is modeled using a constant-coefficient Smagorinsky eddy-viscosity model for LES/FDF computations.

The equations being solved for mass, momentum, and energy are

- Mass

$$\frac{\partial \bar{\rho}}{\partial t} + \frac{\partial}{\partial x_i}\left[\bar{\rho}\widetilde{u}_i\right] = 0 \ , \tag{4.20}$$

- Momentum $(j = 1, 2, 3)$

$$\frac{\partial}{\partial t}\left[\bar{\rho}\widetilde{u}_j\right] + \frac{\partial}{\partial x_i}\left[\bar{\rho}\widetilde{u}_i\widetilde{u}_j\right] = -\frac{\partial}{\partial x_i}\left[\bar{\rho}\left(\widetilde{u_i u_j} - \widetilde{u}_i\widetilde{u}_j\right)\right] + \frac{\partial \overline{\tau_{ij}}}{\partial x_i} - \frac{\partial \bar{p}}{\partial x_j} + \overline{\rho g_j} \ , \quad (4.21)$$

- Equivalent enthalpy (a sensible energy representation; refer to Section 4.1.6)

$$\frac{\partial \overline{\rho}\widetilde{h}_{eq}}{\partial t} + \frac{\partial \overline{\rho}\widetilde{h}_{eq}\widetilde{u}_i}{\partial x_i} = -\frac{\partial}{\partial x_i}\left[\bar{\rho}(\widetilde{h_{eq}u_i} - \widetilde{h}_{eq}\widetilde{u}_i)\right] - \frac{\partial \overline{J_i^{h_{eq}}}}{\partial x_i} + \overline{\rho}\widetilde{S}_{h_{eq}-\text{from}-\text{FDF}} \ . \quad (4.22)$$

The above equations hold true for both RAS/PDF and LES/FDF computations, though with different meanings for operators $\bar{}$ and $\widetilde{}$. The operator $\bar{}$ represents mean quantities for RAS/PDF computations and filtered quantities (Eq. 2.8) for LES/FDF computations. Likewise, operator $\widetilde{}$ denotes Favre-mean and Favre-filtered (Eq. 2.9) quantities for RAS/PDF and LES/FDF, respectively.

The stress tensor $[\bar{\rho}\left(\widetilde{u_i u_j} - \widetilde{u}_i\widetilde{u}_j\right)]$ in the momentum equation above (Eq. 4.21) represents the effect of all turbulent fluctuations on the mean flow in RAS computations and is denoted as Reynolds stress tensor. For LES, it can be interpreted as the effect of subfilter fluctuations on resolved scales and is termed as the SFS stress tensor.

The flux of equivalent enthalpy $[\bar{\rho}(\widetilde{h_{eq}u_i} - \widetilde{h}_{eq}\widetilde{u}_i)]$ in the energy equation (Eq. 4.22) needs to be closed and is referred to as the flux of equivalent enthalpy due to turbulent fluctuations in RAS. For LES, it is termed as the SFS flux of equivalent enthalpy due to unresolved turbulent fluctuations.

The RAS Reynolds stress tensor is determined using a Boussinesq approximation, and is represented as

$$\bar{\rho}\left(\widetilde{u_i u_j} - \widetilde{u}_i\widetilde{u}_j\right) = -\mu_T\left(\frac{\partial \widetilde{u}_i}{\partial x_j} + \frac{\partial \widetilde{u}_j}{\partial x_i} - \frac{2}{3}\delta_{ij}\frac{\partial \widetilde{u}_k}{\partial x_k}\right) + \frac{2}{3}\bar{\rho}k\delta_{ij} \ . \quad (4.23)$$

Here μ_T is the apparent turbulent viscosity that is given by

$$\mu_T = \bar{\rho}C_\mu\frac{k^2}{\epsilon} \ . \quad (4.24)$$

The k and ϵ in the above expression for μ_T are obtained by solving the following equations in a standard two-equation $k - \epsilon$ model:

C_μ	$C_{\epsilon 1}$	$C_{\epsilon 2}$	$C_{\epsilon 3}$	σ_k	σ_ϵ
0.09	1.44	1.92	-0.33	1.0	1.22

Table 4.3. Values of model coefficients for a standard $k-\epsilon$ model.

$$\frac{\partial}{\partial t}\left[\bar{\rho}k\right] + \frac{\partial}{\partial x_i}\left[\bar{\rho}\widetilde{u}_i k\right] = \frac{\partial}{\partial x_i}\left[\left(\mu + \frac{\mu_T}{\sigma_k}\right)\frac{\partial k}{\partial x_i}\right] + \tau_{T_{ij}}\frac{\partial \widetilde{u}_j}{\partial x_i} - \bar{\rho}\epsilon \ , \tag{4.25}$$

and

$$\frac{\partial}{\partial t}\left[\bar{\rho}\epsilon\right] + \frac{\partial}{\partial x_i}\left[\bar{\rho}\widetilde{u}_i \epsilon\right] = \frac{\partial}{\partial x_i}\left[\left(\mu + \frac{\mu_T}{\sigma_\epsilon}\right)\frac{\partial \epsilon}{\partial x_i}\right] + C_{\epsilon 1}\frac{\epsilon}{k}\tau_{T_{ij}}\frac{\partial \widetilde{u}_j}{\partial x_i} - C_{\epsilon 2}\bar{\rho}\frac{\epsilon^2}{k} + C_{\epsilon 3}\bar{\rho}\epsilon\frac{\partial \widetilde{u}_k}{\partial x_k} \ . \tag{4.26}$$

Here μ is the molecular viscosity and $\tau_{T_{ij}}$ is the Reynolds stress tensor (Eq. 4.23). C_μ, $C_{\epsilon 1}$, $C_{\epsilon 2}$, $C_{\epsilon 3}$ and the apparent turbulent Schmidt numbers σ_k and σ_ϵ are model coefficients for the standard $k-\epsilon$ model. Standard values for these coefficients are given in Table 4.3.

In LES, the SFS stress tensor in the filtered momentum equation needs to be closed, and is modeled here using a constant-coefficient Smagorinsky eddy-viscosity model [81]:

$$\bar{\rho}\left(\widetilde{u_i u_j} - \widetilde{u}_i\widetilde{u}_j\right) = -2\mu_{T,SFS}\left(\widetilde{S}_{ij} - \frac{1}{3}\delta_{ij}\widetilde{S}_{kk}\right) + \frac{2}{3}\bar{\rho}k_{SFS}\delta_{ij} \ , \tag{4.27}$$

$$k_{SFS} = 2C_I\bar{\rho}\Delta^2\left|\widetilde{S}\right|^2 \ , \tag{4.28}$$

$$\mu_{T,SFS} = \left(C_S\Delta\right)^2\bar{\rho}\left|\widetilde{S}\right| \ . \tag{4.29}$$

Here k_{SFS} is the SFS kinetic energy and is modeled through Eq. (4.28), $\mu_{T,SFS}$ is the eddy-viscosity, and $\left|\widetilde{S}\right| = \sqrt{\widetilde{S}_{ij}\widetilde{S}_{ij}}$ where $\widetilde{S}_{ij}$ is the resolved rate-of-strain tensor. C_S and C_I are model constants and their standard values are 0.16 and 0.09, respectively.

The turbulent flux of equivalent enthalpy is closed using a gradient diffusion hypothesis for both RAS and LES computations:

$$\bar{\rho}\left(\widetilde{h_{eq}u_i} - \widetilde{h}_{eq}\widetilde{u}_i\right) = -\frac{\mu_T}{Pr_T}\frac{\partial \widetilde{h}_{eq}}{\partial x_i} \ , \tag{4.30}$$

where Pr_T is the turbulent Prandtl number ($Pr_T = 0.7$), and μ_T is given by Eq. (4.24) and Eq. (4.29) for RAS and LES, respectively.

For RAS/PDF simulations, in addition to the FV equations described above, a one-point, one-time joint-PDF of species mass-fractions and mixture specific enthalpy is computed by solving the following modeled transport equation for the mass density function ($\mathcal{F}$) [108, 111, 113]:

$$\frac{\partial \mathcal{F}}{\partial t} + \frac{\partial}{\partial x_i}\left[\widetilde{u}_i \ \mathcal{F}\right] + \frac{\partial}{\partial \psi_\alpha}[\widehat{S}_\alpha(\underline{\psi})\mathcal{F}] = \frac{\partial}{\partial x_i}\left[\overline{\rho}\Gamma_{\text{eff}}\frac{\partial\left(\mathcal{F}/\overline{\rho}\right)}{\partial x_i}\right] + F_{\text{mix}} \ . \tag{4.31}$$

Here Γ_{eff} ($= \Gamma_t = \mu_T/(\bar{\rho}\sigma_\phi)$) is the apparent diffusivity, σ_ϕ is the turbulent Prandtl or Schmidt number, and F_{mix} is the flux in the composition space due to molecular mixing and is obtained from a mixing model. Here σ_ϕ is set to 0.7 for simulations performed in this research.

The above equation for $\mathcal{F}$ (Eq. 4.31) is solved using a Lagrangian particle Monte Carlo method [108, 113] where the MDF is represented by a large number of notional particles that evolve in physical and composition spaces according to the following stochastic equations [108]:

$$d\underline{\mathbf{x}}^*(t) = \left[\widetilde{\underline{u}} + \nabla\left(\Gamma_{\text{eff}}\right)/\overline{\rho}\right]_{\underline{\mathbf{x}}^*(t)}dt + \left[2\left(\Gamma_{\text{eff}}\right)/\overline{\rho}\right]^{1/2}_{\underline{\mathbf{x}}^*(t)}d\underline{W} \ , \tag{4.32}$$

$$d\phi^*_\alpha(t) = S^*_{\alpha,\text{reaction}}dt + F^*_{\text{mix}} + \delta_{\alpha s}\frac{S^*_{\text{radiation}}}{\rho^*}dt, \alpha = 1,\ldots,s \ . \tag{4.33}$$

In the above equations, the number of species is varied from $\alpha = 1,\ldots,s-1$ and the s^{th} scalar is the enthalpy; the radiation source term only affects the s^{th} scalar. Variables with an asterisk refer to the values of a Lagrangian particle, and $\underline{W}$ is an isotropic vector Wiener process. In this work, F^*_{mix} (the change in species composition due to molecular mixing) is computed using the CD model [192, 193] with model coefficient $C_\phi = 4$ for RAS/PDF simulations.

For LES/FDF simulations in this work, a modeled transport equation is solved

for the filtered mass density function (Section 2.5.2.1) via a Lagrangian particle Monte Carlo method along with a FV solver for hydrodynamics and equivalent enthalpy. The modeled transport equation for the FMDF and the stochastic equations for particles in the LES/FDF method are almost identical to the corresponding equations (Eqs. 4.31, 4.32, and 4.33) in the RAS/PDF method. The only differences are:

- The operator $\bar{}$ represents mean quantities for RAS/PDF computations and filtered quantities for LES/FDF computations.
- The operator $\tilde{}$ denotes Favre-mean and Favre-filtered quantities for RAS/PDF and LES/FDF, respectively.
- The apparent diffusivity Γ_{eff} includes both molecular and turbulent component in LES/FDF versus only a turbulent component in RAS/PDF.
- For the mixing model, the time scale in RAS/PDF is set to k/ϵ. In LES/FDF, the time scale is computed as $\Delta^2/(\Gamma + \Gamma_t)$.
- The mixing model constant, C_ϕ is not a universal constant and wide range of values have been reported in the literature depending on the choice of mixing model, flow regime (nonreacting/reacting), and turbulence closure (RAS/LES) [111]. Here, the mixing model constant is set to 6 in LES/FDF and to 4 in RAS/PDF.

Chapter 5

Development and Validation Studies

A comprehensive computational module has been developed in this work for simulating turbulent reacting flows in both LES and RAS frameworks. In this module, a transported composition FDF (PDF) method and a spectral photon Monte Carlo (PMC) radiation solver that completely account for turbulence/chemistry and turbulence/radiation interactions are used in conjunction with a finite-volume LES (RAS) solver. The development of the computational module has been carried out in several stages. At each stage, the updated module has been tested and validated (where possible) against data available from experimental measurements or previous computational studies.

The finite-volume, variable-density LES solver in the OpenFOAM CFD code [127] forms the basic building block of this computational module. To establish the suitability of the finite-volume solver for LES, LES of a co-axial annular jet [194] has been conducted, and the results obtained have been compared with experimental data. Details are presented in Section 5.1.

The Lagrangian particle Monte-Carlo PDF code originally developed by Zhang and Haworth [139] has been taken as the starting point for this study. Here it is coupled with OpenFOAM. OpenFOAM–PDF coupling requires significant data passing from the finite-volume side to the PDF side; data to be passed include the FV mesh, turbulence scales, and velocities. The coupling is tested for an incompressible lid-driven cavity flow case, which was originally employed by Zhang

and Haworth [139] to evaluate the performance of mass-consistency schemes implemented in their hybrid FV/PDF code. Section 5.2 presents results obtained from coupled OpenFOAM/PDF runs for a lid-driven cavity configuration.

The implementation of the Lagrangian composition FDF module is similar to that for a PDF module, a key difference being in the specification of length and time scales in the particle Monte Carlo PDF code. Therefore, the coupled OpenFOAM/PDF module is first tested for a canonical nonpremixed turbulent jet flame (Sandia Flame D [124, 125]) in the RAS framework, since the original PDF code by Zhang and Haworth was developed for RAS/PDF. The indirect feedback procedure (equivalent enthalpy approach - Section 4.1.6) is also implemented in the RAS solver in the OpenFOAM code, and is tested for Sandia Flame D. Results for coupled OpenFOAM-RAS/PDF runs are discussed in Section 5.3.

Emission and absorption schemes consistent with the notional particle representation in FDF and PDF methods have been developed for the PMC thermal radiation solver. Section 5.4 compares the performance of these new schemes with the previous schemes for treating radiation in a notional particle field.

With the various components of the computational module appropriately tested and validated, the LES/FDF/PMC solver is then applied to simulate Sandia Flame D. A detailed description of the simulation study is provided in Section 5.5.4, where comparisons between computed and measured quantities are presented. The inflow turbulence generation, grid adequacy, and consistency of mass representations in LES/FDF are also discussed.

The coupled FV–LES/FDF/PMC simulations are computationally highly expensive and necessitate the use of parallel simulations. A generic, efficient parallelization scheme has been developed in this work to ensure faster turn-around times for computationally intensive simulations. The scaling performance of the parallelization scheme is presented in Section 5.6.

5.1 Variable-Density LES Solver: A Co-axial Annular Jet

As a first step toward building the LES/FDF computational module, the selected LES code, which serves as the basic building block for the module, is validated for nonreacting variable-density flows. To this end, a low-Mach-number annular jet flow configuration [194] is simulated using the compressible LES code in OpenFOAM [127]. The computational grid consists of approximately $1.4M$ hexahedral cell elements, created in a semi-structured fashion. A parabolic velocity-profile is used at the inlet and a zero-gradient boundary condition is employed at the outlet. The temperature at the inlet is set to a fixed value (373 K) and zero-gradient is specified at all other boundaries. For pressure, a wave-transmissive boundary condition [195] is used at the outlet that is a simple reconstruction of the non-reflective scheme proposed by Lele et al. [196] to allow the acoustic waves to escape the domain; all other boundaries are set to zero-gradient. Computations are carried out on 16 processors and METIS [197] (already available in OpenFOAM) is used to decompose the computational domain for parallel runs. The time-step used ($1.6e^{-5}s$) is sufficiently low to ensure that the maximum material Courant number is less than 0.5 for all cells in the computational domain.

The instantaneous resolved axial velocity on a cut-plane along axis through the computational domain for the annular jet flow is shown in Fig. 5.1. This configuration is studied for a number of subfilter-scale (SFS) models, namely a k-equation eddy-viscosity model, a constant-coefficient Smagorinsky model and the MILES approach (no explicit SFS model). Comparisons between computed and measured mean and rms axial velocity profiles at several axial locations are presented in Figs. 5.2 and 5.3.

The computed mean and rms velocity profiles in OpenFOAM are obtained by time-averaging the instantaneous resolved velocity data for roughly 14 flow-through times. The computed data are further averaged in the azimuthal direction. The comparison between the experimental and computed mean axial velocities is shown in Fig. 5.2. Here, OF_1eqn_k represents the LES calculations with a k-equation eddy-viscosity model, OF_noSFS represents LES with no explicit SFS model, and OF_Smag represents LES with a constant-coefficient Smagorinsky model. The

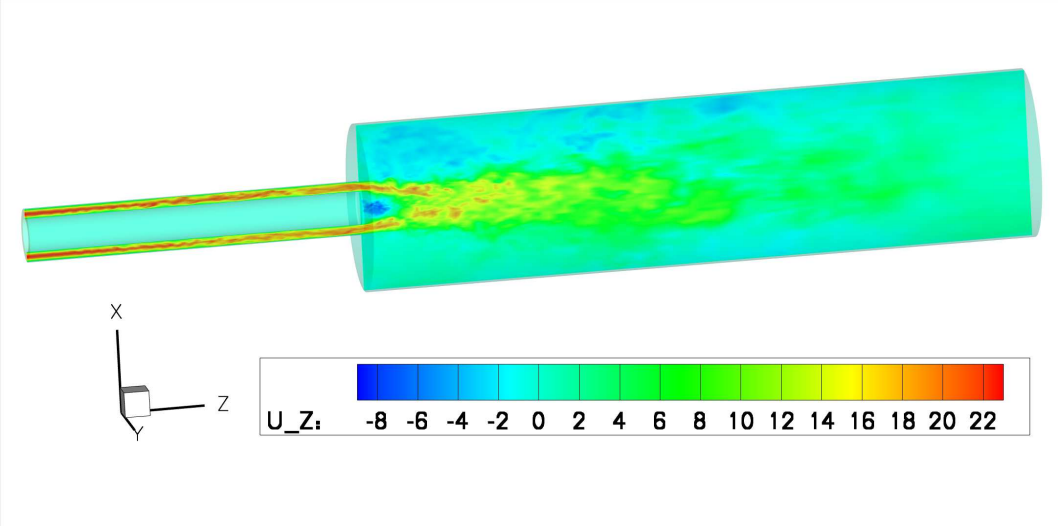

Figure 5.1. Instantaneous axial velocity component on a cutting plane for the annular jet flow.

computed mean velocities for all the SFS models are in close agreement with the experimental data for all axial locations. The same trend is observed in the comparison plots for the rms of axial velocity at downstream locations, as seen in Fig. 5.3. Here only the resolved-scale contribution to the rms velocity is included (no contribution from the subfilter-scale model). At upstream locations, the computed rms velocities deviate somewhat from the measured values in predicting the peaks/valleys in the region enveloped by the annular jet, but still maintain the same qualitative structure as the experimental data. The deviation is attributed to insufficient mesh density in that region, and results are expected to improve with finer mesh resolution. Previous LES studies [198] for this flow configuration have shown a similar level of agreement between computed and measured mean and rms velocities for similar computational grids. Therefore, the results obtained here suffice to establish the accuracy of the LES solver in OpenFOAM, and lay the foundation for the development of the LES/FDF/PMC module.

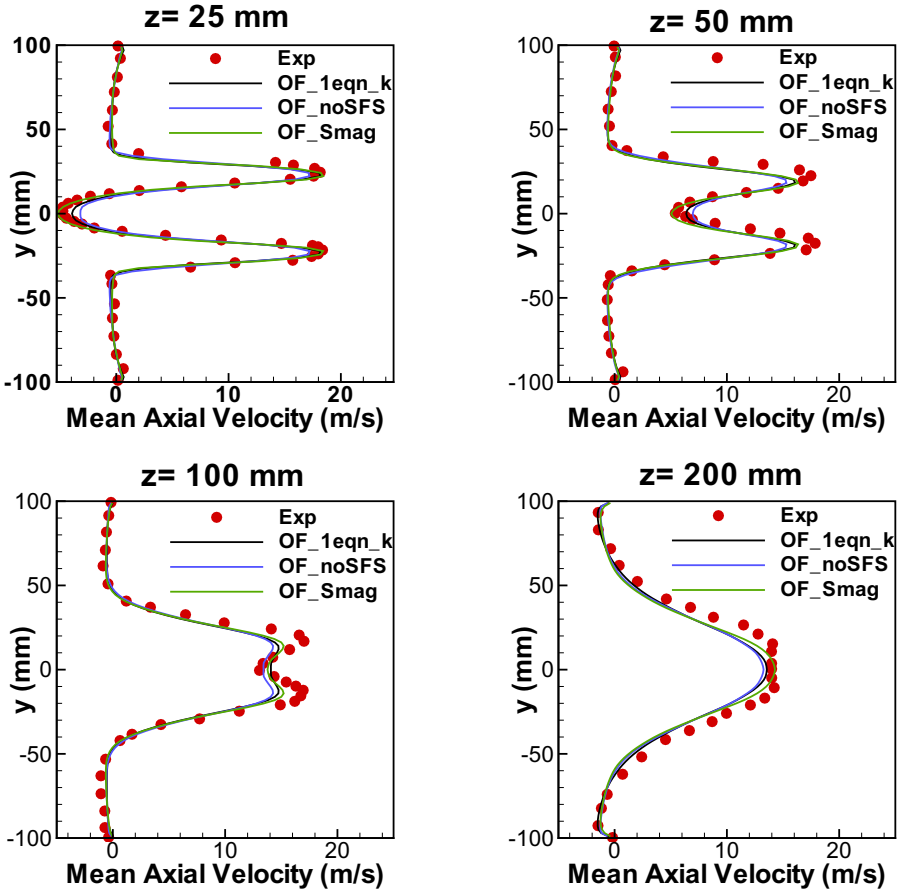

Figure 5.2. Computed and measured mean axial velocity profiles for the annular jet flow.

5.2 OpenFOAM/PDF Coupling: Lid-driven Cavity

The purpose of analyzing the lid-driven cavity case is to ascertain the correctness of the coupling between the CFD code (OpenFOAM) and the Lagrangian particle code, and to demonstrate mass-consistency between the FV side and the PDF side. The PDF code needs information about the mesh connectivity and topology from the FV solver. Furthermore, the PDF code is not self-contained, and demands information about the velocity field, cell-face-fluxes, and turbulence length and time scales from the FV CFD code. Also, since particles on the PDF side carry mass with them, and they move through the computational domain due to convection

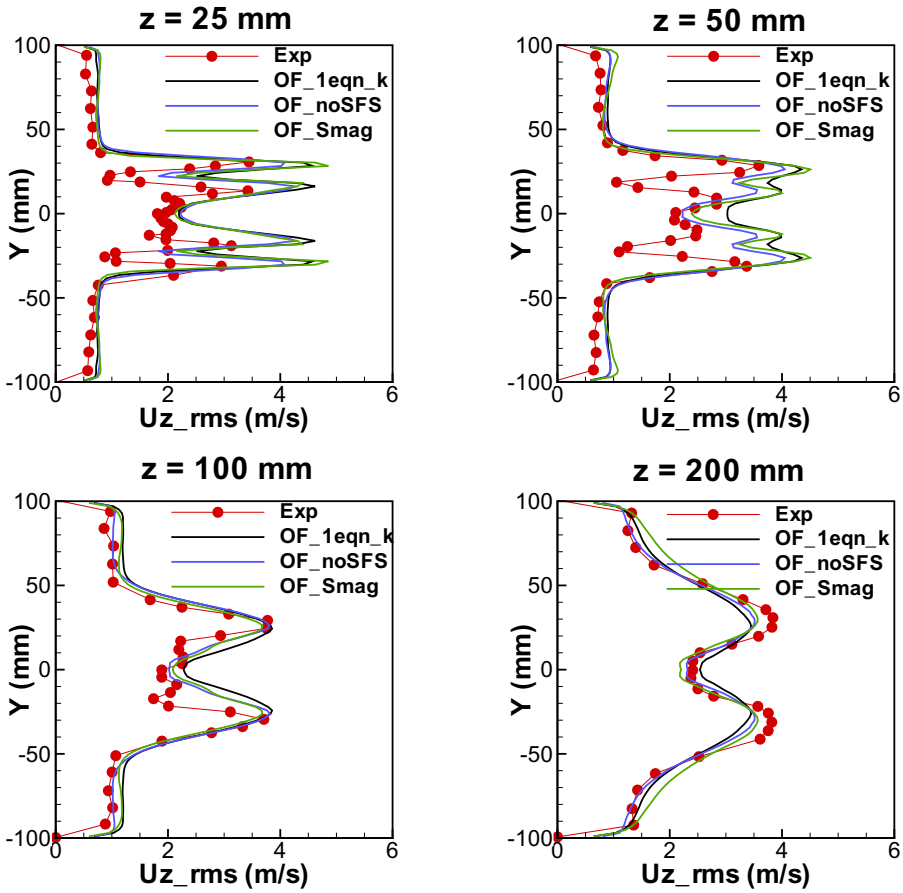

Figure 5.3. Computed and measured rms axial velocity profiles for the annular jet flow.

and diffusion, the particle mass distribution is dynamic. A key requirement is that the PDF algorithm maintains a mean particle mass distribution that is consistent with that on the FV side.

A laminar, incompressible (constant-property), two-dimensional, steady lid-driven cavity configuration is chosen to investigate coupling and mass-consistency. This configuration has long served as a benchmark validation case for CFD. The lid-driven cavity may seem to be quite straightforward for any Lagrangian particle method to handle, but in reality this is a deceptively challenging and revealing configuration. The flow is marked by steep velocity gradients, no-slip walls, recirculation, and ambiguity in the specification of the velocity at the intersections of the fixed and driven walls. In this test, given the steady nature of the flow and the constant density specification, the PDF algorithm should yield a stationary

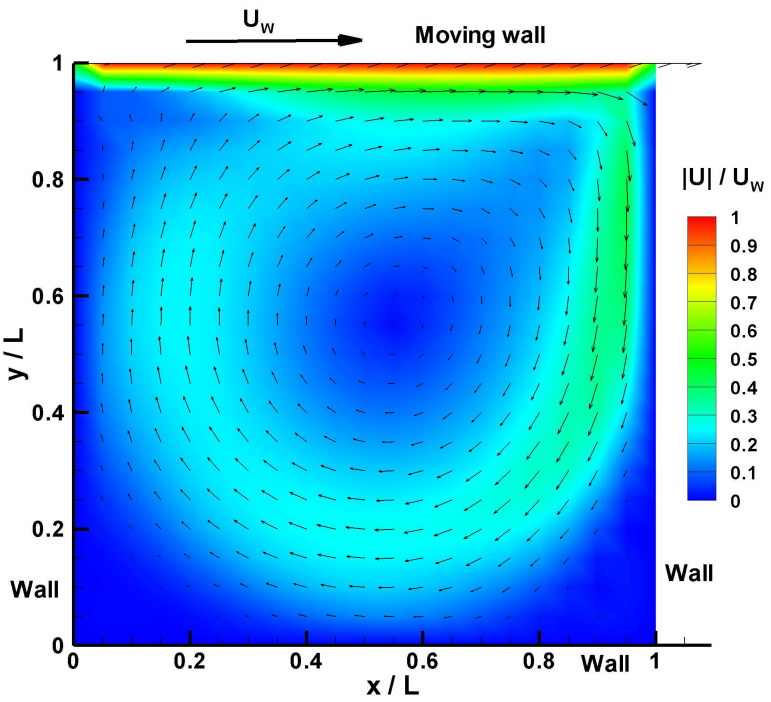

Figure 5.4. The steady-state velocity field for the lid-driven cavity configuration. Arrows are used to depict the direction of the local velocity vectors.

and uniform particle mass distribution. Verification of this will also serve to establish that the coupling procedure between OpenFOAM and particle code is correct. There is no feedback of PDF-based quantities to the FV side for this configuration, hence the FV solution does not change once steady-state is reached.

The computational domain considered is an $L\times L\times 1$ cube with $20\times 20\times 1$ finite-volume cells in x, y, and z directions, respectively. The bottom ($y/L = 0$) and side ($x/L = 0, x/L = 1$) walls are no-slip (zero-velocity) walls, whereas the top wall ($y/L = 1$) moves tangentially to the right at a constant speed of U_W. Reynolds number $Re_W \equiv U_W L/\nu$ is the key parameter here; ν is the constant kinematic fluid viscosity. The values for L, U, and ν are chosen such that $Re_W = 1000$, representing a laminar case. At the start of the run, a converged steady-state solution (Fig. 5.4) is obtained on the FV side, and time is reset to $t = 0$. Then computational particles, with approximately uniform particle number density, are initialized in physical space such that the total mass of particles in each finite-

volume cell is equal to the finite-volume cell mass. Particle locations and velocities are then advanced in time according to the equations listed in [54]. In this case, there is no random component corresponding to turbulent diffusion.

As the particles move, the particle mass distribution should remain the same as the initial uniform mass distribution. The principal quantity of interest, then, is the deviation between the cell-level particle mass density ρ_P^k (total particle mass in cell k, divided by the cell volume) and the finite-volume mass density ρ_{FV}^k (here $\rho_{FV}^k \equiv \rho_O$, $k = 1, \cdots, N_c$, where ρ_O is the fluid density and N_c is the total number of cells):

$$d\rho^k \equiv \frac{\rho_P^k - \rho_{FV}^k}{\rho_{FV}^k} \ . \tag{5.1}$$

The root-mean-square value of $d\rho^k$, denoted by ${\rho'}_{rms}$, over the entire computational domain is monitored as a global indicator of the deviation between the particle and finite-volume mass distributions. Here ${\rho'}_{rms}$ is given by

$${\rho'}_{rms} \equiv \left[\frac{\sum_{k=1}^{N_c} \left(d\rho^k\right)^2}{N_c} \right]^{1/2} \ . \tag{5.2}$$

${\rho'}_{rms}$ is plotted as a function of normalized time, $t^+ \equiv tU_W/L$, in Fig 5.5. The plot in Fig 5.5 presents the result for two specifications of the particle advection velocity: no correction (Stage 1 only [139]) and first-level velocity correction (Stages 1 and 2 [139]). Stage 1 refers to a case where discrete values of velocity at mesh vertices and linear interpolation functions are employed to establish a continuous approximation to the mean velocity field. In Stage 2, the velocities at mesh vertices are corrected to enforce consistency between FV cell-face mass flow-rates and the cell-face mass flow-rates implied by the Stage 1 velocity field. Details of Stages 1 and 2 are available in [139]. Zhang and Haworth [139] also presented a Stage 3 algorithm where the deviation between FV mass and mean particle mass in each cell is monitored, and a second correction velocity field is computed that redistributes the particles in physical space to drive the deviation towards zero. Stage 3 is not implemented here for the coupled OpenFOAM/PDF analyses.

As seen in Fig. 5.5, the rms mass density deviation increases continuously in time in the absence of any correction (Stage 1), whereas with a first-level correction

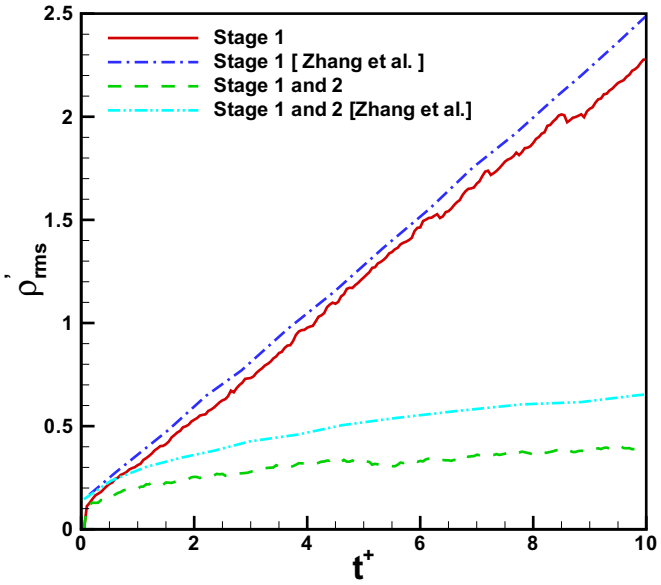

Figure 5.5. Time evolution of instantaneous rms mass density deviation (ρ'_{rms}) over the computational domain for the lid-driven cavity. Results are compared with data obtained by Zhang and Haworth [139].

(Stages 1 and 2) the deviation levels decrease by an order of magnitude. The agreement with previously obtained results [139] serves to establish the correctness of the coupling procedure, and emphasizes the importance of correction schemes to ensure mass-consistency.

5.3 OpenFOAM-RAS/PDF Module: Sandia Flame D

The modeled transport equations for composition FDF and composition PDF methods are very similar; the particle evolution equations (SDEs) for the two differ only in their specification of particle advection velocities and turbulence length and time scales [19, 108]. Therefore, it is appropriate to perform a RAS/PDF validation before moving to LES/FDF. Here, the coupled OpenFOAM-RAS/PDF code is used to simulate Sandia Flame D [124, 125].

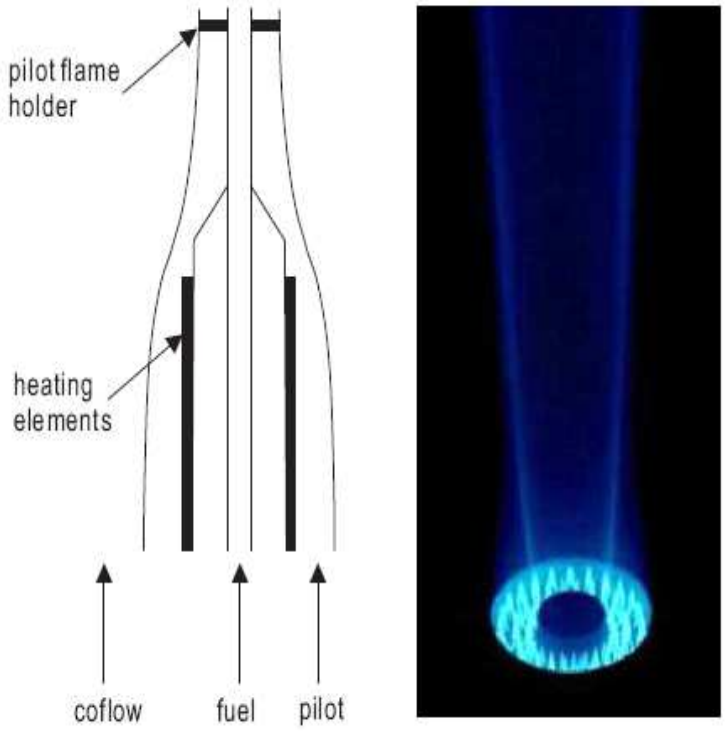

Figure 5.6. Schematic of the piloted-jet burner and a flame image [190].

Sandia Flame D is one of several nonpremixed flames investigated experimentally as part of the "International Workshop on Measurement and Computation of Turbulent Nonpremixed Flames" [199]. Because of the availability of extensive high-quality experimental data [200], Sandia Flame D has been widely simulated in the literature. It is a nonluminous piloted-jet methane flame, in which radiative heat transfer is mainly due to the emission and absorption by major combustion gases, especially water vapor and carbon dioxide. Figure 5.6 shows a schematic of the piloted-jet burner and a time-averaged flame image. The central jet, with a diameter $D_{jet} = 7.2$ mm, issues a methane/air mixture with a volume ratio of 1 : 3. The annular pilot that surrounds the central jet has an outer diameter of $D_{pilot} = 2.62\ D_{jet}$. The pilot composition is equivalent to the products of a burnt methane/air mixture with an equivalence ratio of 0.77. The pilot is surrounded by co-flowing air. The inlet boundary conditions for temperature, velocity, and species mass fractions are listed in Table 5.1.

The computational mesh employed in this study is a 10-degree axisymmetric

	jet	pilot	coflow
T(K)	294	1880	291
u(m/s)	49.6	10.57	0.90
Y_{CH_4}	0.15605	0.0	0.0
Y_{O_2}	0.1962	0.054	0.23113
Y_{H_2O}	0.0	0.0942	0.00581
Y_{CO_2}	0.00045	0.1098	0.00055
Y_{N_2}	0.6473	0.7377	0.76251
Y_{CO}	0.0	0.00407	0.0
Y_{H_2}	0.0	0.000129	0.0
Y_H	0.0	0.0000248	0.0

Table 5.1. Inlet boundary conditions for Sandia Flame D [191].

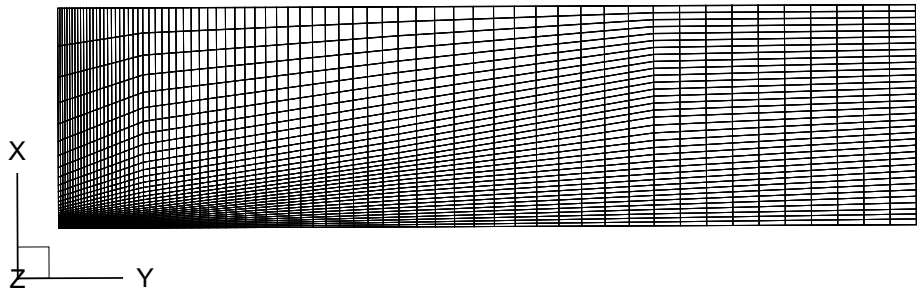

Figure 5.7. Computational mesh for RAS/PDF simulation of Sandia Flame D.

wedge consisting of 2520 hexahedral cells with a domain size of $70D_{jet}$ and $18D_{jet}$ in the axial and radial directions, respectively. The wedge-like 3D grid, shown in Fig. 5.7, is one-cell thick in the azimuthal direction. Such a grid has often been used in the literature [36, 37, 54] to simulate 2D axisymmetric flames. The grid is designed to be very fine in the fuel jet and mixing regions near the inlet to resolve the large local gradients, and coarser in the air coflow and downstream to save computational time. The wedge-like grid is truncated close to the axis (centerline) for the creation of a hexahedral mesh without any singularities. A fixed-pressure boundary condition and zero-gradients for all other quantities are applied at the outlet and at the outer peripheral boundary. Symmetry conditions are applied at the inner peripheral boundary and the two lateral faces.

In the particle Monte Carlo method, approximately 27 particles per cell are used for a total of approximately 70,000 particles. A simple coalescence-dispersion (CD) mixing model [192, 193] is used to model micromixing, and the mixing model constant is set to $C_\phi = 4$. A 16-species, 41-reaction methane/air skeletal mechanism is used to account for chemical reaction [201]. Thermal radiation is not considered in this study, since the main focus here is on validating the RAS/PDF code.

Updates in species mass-fractions and density from the particle Monte Carlo side are fed to the FV side at every time-step. For this statistically stationary flow, time-blending is performed to reduce the statistical noise in the fields being passed to the FV side (Section 4.1.6). The value of the blending factor k (Eq. 4.4) is increased toward unity as run progresses toward a statistically stationary state.

Results obtained using time-blending for feedback of mean density to the FV side are compared with those obtained using the equivalent enthalpy approach (Section 4.1.6). Mean temperatures obtained with the two approaches (equivalent enthalpy versus time-blending) also are compared.

Figure 5.8 presents the comparison of computed mean temperatures with experimentally measured data at three axial locations for the two density-coupling schemes and for different values of C_ϕ; a value of 3 or higher has been suggested [202] for the mixing models usually employed in the simulation of Sandia Flame D. Mean temperature profiles for $C_\phi = 4$ show a better match with the experimental data than those for $C_\phi = 6$, and results obtained using the equivalent enthalpy approach with $C_\phi = 4$ are essentially the same as those obtained using the time-blending approach.

In the literature, the k-ϵ model constants usually are modified to better match the spreading rate in axisymmetric flames. Therefore, another run has been made with $C_\phi = 4$ and one modified k-ϵ constant ($c_{\epsilon 1}$ in the modeled ϵ equation set to 1.55 instead of 1.44). Results with the modified model constant are in better agreement with the experimental data. Further improvement can be obtained with the consideration of thermal radiation, which will reduce the overpredicted mean temperatures towards the experimentally recorded values. Also, the methane/air chemical mechanism used here is a skeletal mechanism, and using a better chemical mechanism will improve the computed results [203].

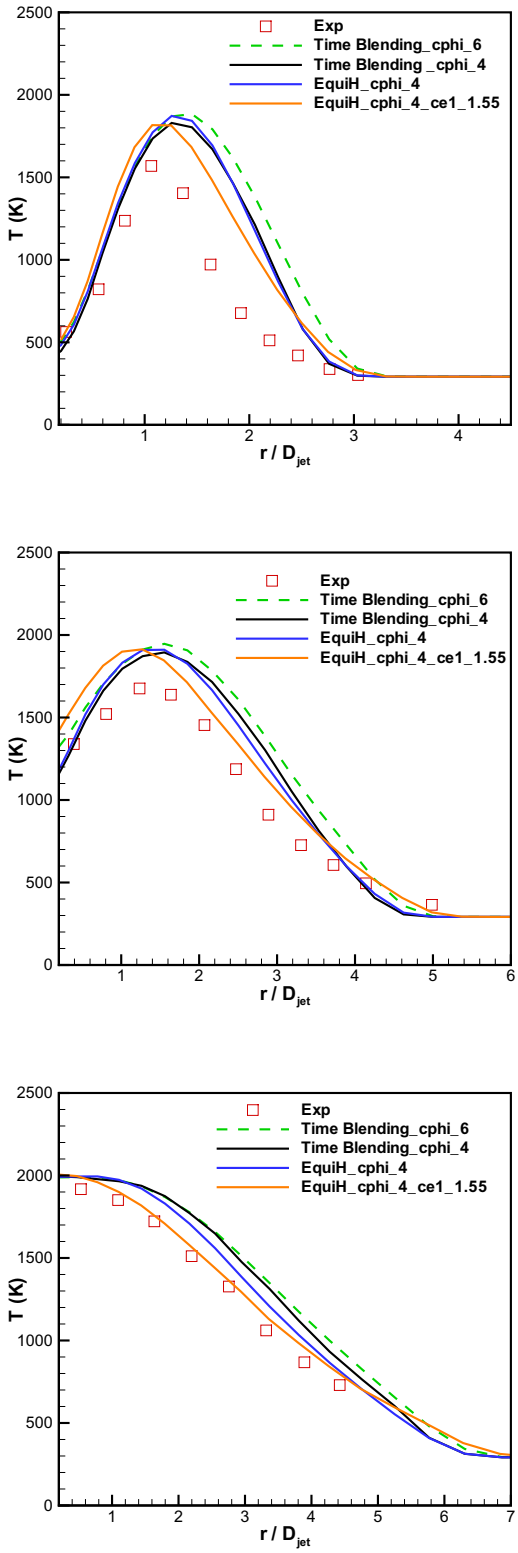

Figure 5.8. Computed Favre-mean temperatures at three axial locations ($x/D_{jet} = 15$, $x/D_{jet} = 30$, and $x/D_{jet} = 45$) for Sandia Flame D.

5.4 Comparison of Stochastic PMC Scheme with Previous Schemes

Stochastic schemes for radiative emission and absorption have been developed for incorporating the photon Monte Carlo treatment of thermal radiation in FV/PDF (FV/FDF) frameworks. These schemes (discussed in detail in Section 4.2.1) have been constructed in a manner that is more consistent with the PDF particle formulation, compared to earlier approaches [153].

A RAS/PDF/PMC simulation of a scaled-up Sandia Flame D is conducted as a validation exercise for the stochastic PMC schemes developed in this work. Sandia Flame D is a small optically thin flame that does not exhibit appreciable thermal radiation. For this validation study, Sandia Flame D was scaled up four times (keeping the jet Reynolds number fixed, thereby reducing jet velocity by a factor of four) [37] to enhance the effect of radiation. The line-by-line (LBL) model [37] is used for spectral modeling of thermal radiation, with H_2O and CO_2 as the participating species. Computed steady-state mean temperature contours for the scaled-up flame are shown in Fig. 5.9.

Radial profiles of the mean temperature at three axial locations for five different PMC schemes are shown in Fig. 5.10. In the line-legend, "Cone-PPM" and "Line-CDS" refer to the previous PMC schemes [153] where rays are modeled as cones or lines, PDF particles are modeled as point particle masses or constant density spheres, respectively, and radiation is solved on the particle field. "Stochastic-all particles" denotes a generalization of the proposed stochastic scheme in which a ray when passing through a finite-volume cell interacts with all particle realizations of that cell. In this scheme, the length that a ray traverses while traveling through a cell is divided among all particle realizations based on the probability of their occurrence. "Stochastic-1 particle" is the proposed scheme in which the ray passing through a cell interacts with only one realization, and that is determined stochastically using the probability of occurrences of all realizations of that cell. "Stochastic-15 particle" refers to a generalized case of the proposed scheme in which the ray interacts with approximately half of the realizations of the cell, that are selected stochastically based on their probability of occurrence. All three stochastic PMC schemes are consistent with the stochastic nature of notional PDF

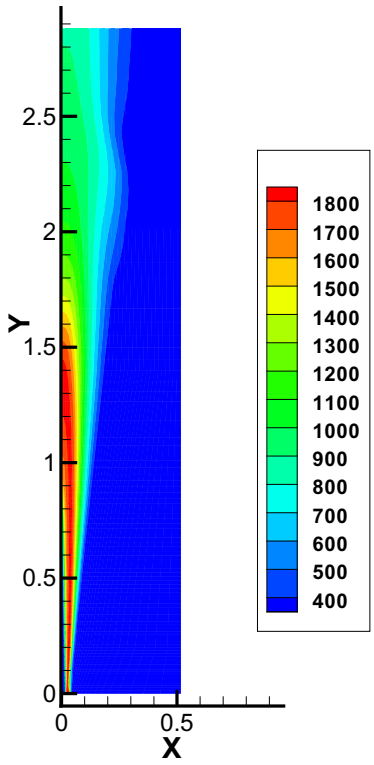

Figure 5.9. Computed mean temperature field for the scaled-up Sandia Flame D.

particles.

The plots in Fig. 5.10 show that the computed mean temperatures for stochastic schemes are in good agreement with the earlier cone-PPM and line-CDS schemes. The cone-PPM scheme predicts lower mean temperatures than other schemes on the outer boundaries of the flame front (in the radially outward direction). This is because the emitted rays are represented as cones, and absorption is computed by accounting for the point particles lying within the cone. As the mesh size increases with increasing radial distance, it is possible for a cone-ray to traverse uninterruptedly (or with less interference) through a finite-volume cell due to the presence of large void spaces between point particles. This leads to lower radiative absorption and, consequently, lower temperatures. The line-CDS scheme also allows for the possibility of void spaces, but the effect is not evident in the computed mean temperatures since the spherical representation of notional particles make it less likely to occur.

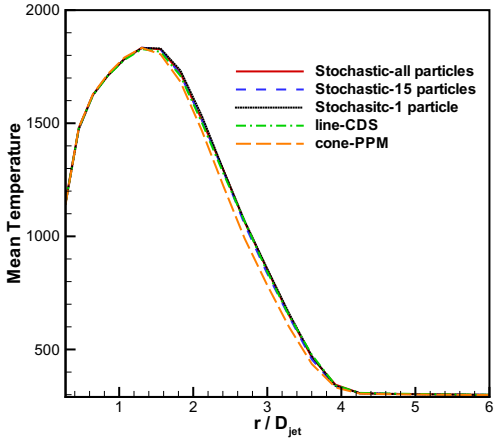

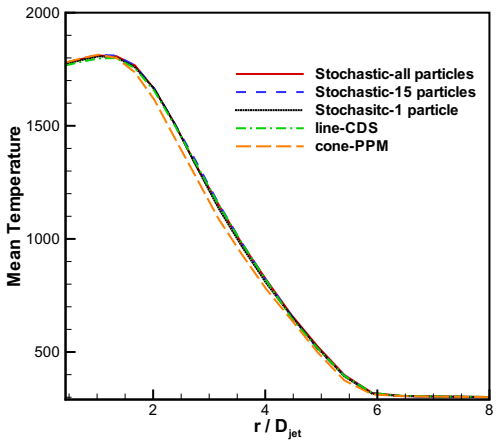

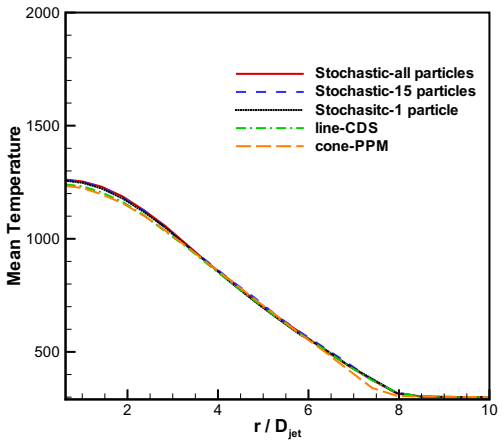

Figure 5.10. Computed Favre-mean temperatures at different axial locations ($x/D_{jet} = 15$, $x/D_{jet} = 30$, and $x/D_{jet} = 45$) for scaled-up Sandia Flame D.

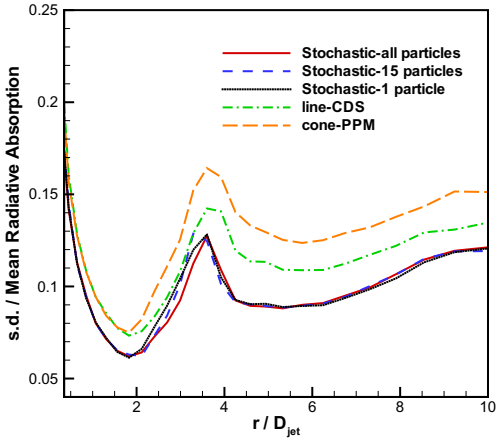

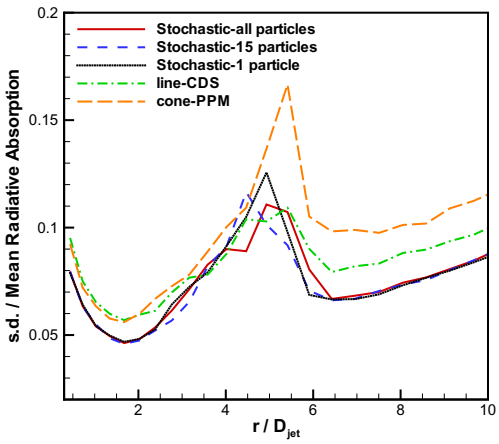

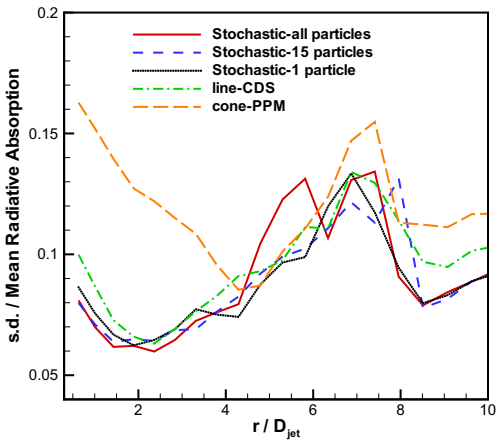

Figure 5.11. Ratio of standard deviation and mean absorption at different axial locations ($x/D_{jet} = 15$, $x/D_{jet} = 30$, and $x/D_{jet} = 45$) for scaled-up Sandia Flame D.

PMC Scheme	$(\sum s.d./\sum(\text{Mean absorption}))$ in %
Stochastic-1 particle	8.27
Stochastic-15 particles	8.23
Stochastic-all particles	8.16
Line-CDS	9.20
Cone-PPM	10.37

Table 5.2. Assessment of a global metric (summation of standard deviation over the entire computational domain divided by the total absorption) for various PDF/PMC schemes.

The standard deviation of volumetric radiative absorption in every FV cell in the computational domain is computed from statistics collected for approximately six flow-through times. Figure 5.11 shows the radial profiles of the ratio of standard deviation of radiative absorption and its mean at three axial locations for various schemes. The ratios (i.e., relative standard deviations) for all stochastic schemes are in good agreement with each other, and are less than 10% in all cases. Note that the actual statistical error in the simulation is much lower than 10%, since time averaging is used to estimate the mean quantities. The relative standard deviations for cone-PPM and line-CDS schemes are higher than for the stochastic schemes, due to the possibility of rays traveling uninterruptedly through the particles present in a finite-volume cell. The cone-PPM scheme presents higher possibility for rays escaping because of the point-mass representation of notional particles, thereby leading to higher relative standard deviation than the line-CDS scheme. Since the relative standard deviations in the radial profiles are quite close to each other for different stochastic schemes, a global metric is considered to assess the relative performance for the various schemes. Table 5.2 lists the ratio of the sum of the standard deviations of radiative absorption and the total absorption in the computational domain for various schemes. The global metric is highest for the cone-PPM scheme for the reasons explained above. For the various stochastic schemes, the global metric decreases as more number of particle realizations interact with the traversing rays. This is expected, since more particle interactions lead to less variation in absorption at different time steps. However, the benefits of using more than a single particle are small.

The computational cost of the proposed stochastic scheme ("Stochastic-1 particle") is approximately 16% of the cone-PPM scheme and 75% of the line-CDS

scheme. This, together with the observations that the accuracy is comparable to that of the earlier approaches and the standard deviations are lower, establishes its suitability for PDF/PMC computations.

5.5 LES/FDF Module

The coupled OpenFOAM/PDF code has been validated for RAS/PDF simulations (details in Section 5.3). Next it is implemented in the LES/FDF context. As noted earlier, the evolution equations of notional particles are very similar for RAS and LES; they only differ in the definition of the advection velocities and turbulence time and length scales used in the Lagrangian Monte Carlo code for evolution of notional particles. For LES/FDF simulations, appropriate turbulence length and time scales are computed and used in the particle Monte Carlo code. The PMC schemes for treatment of thermal radiation work directly with the particle Monte Carlo code, and are therefore immediately applicable in the LES/FDF simulations without any modification.

The coupled LES/FDF/PMC code is used to simulate a laboratory-scale non-luminous turbulent flame (Sandia Flame D). For this simulation, an unstructured mesh of approximately $1.2M$ hexahedral cells is created in a cylindrical computational domain that extends 70 D_{jet} and 18 D_{jet} in the axial and radial directions, respectively. There are approximately 196, 90, and 64 cells in the axial, radial, and azimuthal directions, respectively. The grid points are clustered near the shear layers to resolve the large local gradients. The adequacy of the grid used here is discussed in detail in Section 5.5.1. A nonreflecting pressure boundary condition and zero-gradient boundary conditions for all other quantities are applied at the downstream outlet and at the outer radial boundary. At the inlet, zero-gradient is applied for pressure. Fixed species mass-fractions and temperature are specified at the inlet. The velocity field at the inlet is created using a digital-filter-based turbulence synthesis technique [204] that is discussed in detail in Section 5.5.2.

Approximately 15 particles are used per cell (18M particles total) for FDF analysis. A simple coalescence-dispersion (CD) mixing model [192, 193] is used to mimic micromixing, and the mixing model constant is set to $C_\phi = 6$. The lower value of $C_\phi = 4$ that was used in RAS/PDF simulations for the CD model

was found to be inadequate for LES/FDF. The higher value of the mixing model constant required for LES/FDF compared to RAS/PDF is consistent with other LES/FDF simulations reported in the literature [7, 205]. The use of higher values is mostly attributed to the inaccuracy in computing the hydrodynamic time scale (or dissipation rate).

For LES/FDF simulations, duplicate representations of mass are present in the solution and it is desired to have consistency across FV and FDF representations. The mass-consistency algorithms [139] and the equivalent enthalpy procedure are employed in this work for maintaining consistent Eulerian and Lagrangian density fields and for density feedback, respectively. An assessment of the mass consistency and density feedback is presented in Section 5.5.3.

A 16-species/41-reactions skeletal methane/air chemical mechanism [201] is used to model chemical kinetics in the LES/FDF analysis. Thermal radiation and TRI are accounted for via PMC, where a LBL model is employed for spectral modeling (water vapor and carbon dioxide are the two participating species), and approximately $2M$ photon-bundles are traced in the computational domain at every time-step. The computed mean and rms temperature and species mass fractions for the LES/FDF/PMC analysis are compared with the experimental data in Section 5.5.4.

5.5.1 Computational Grid

Grid quality is known to have a strong influence on accuracy in LES. LES is based on the premise that the large, energy-containing scales are explicitly resolved, while effects of the small scales are modeled. This dictates that the grid should be fine enough to resolve the large scales of turbulence. In this work, information about the turbulence length scales is derived from the RAS/PDF study of Sandia Flame D (Section 5.3); this is used to ensure sufficient grid resolution in the LES mesh. From scaling arguments, the turbulence length scale can be computed from the turbulent kinetic energy k and the dissipation rate ϵ as

$$l_{\mathrm{T}} = {C_\mu}^{0.75} \frac{k^2}{\epsilon} \ , \tag{5.3}$$

where l_{T} is the turbulence integral length scale and C_μ is a $k-\epsilon$ model constant

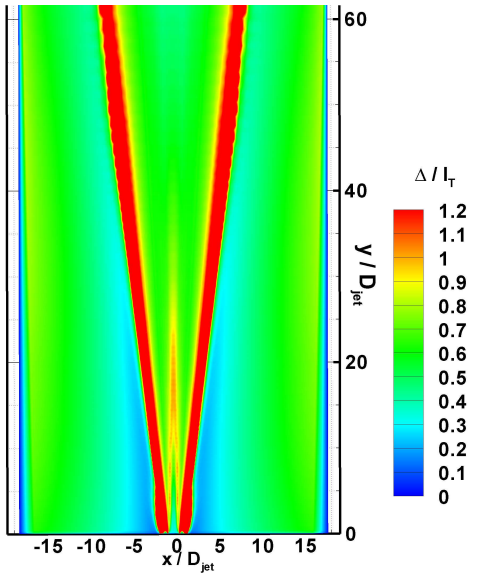

Figure 5.12. Ratio of filter width to turbulence length scale in the computational domain for LES of Sandia Flame D.

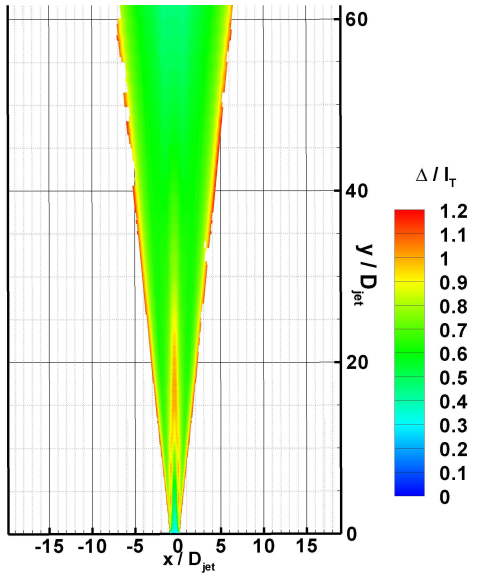

Figure 5.13. Ratio of filter width to turbulence length scale plotted over only those regions in the computational domain where the temperature is above 292 K and the rms axial velocity is greater than 0.5 m/s.

(0.09).

Figure 5.12 shows the ratio of the LES filter width to the turbulence integral length scale from RAS on a cutting plane that contains the axis of symmetry in the LES grid. The ratio is less than unity in most of the region of interest. This can be seen in Fig. 5.13, which is same as the previous figure, but here the grid is blanked out where the temperature is below 292 K and the rms axial velocity is less than 0.5 m/s. The small values of the ratio indicate that the filter width is sufficiently fine to resolve the large scales of turbulence. The procedure used here is an *a priori* measure to investigate the suitability of a mesh for LES simulations, and to make modifications if needed. The mesh is iteratively refined to ensure that the local filter widths are smaller than the estimated turbulence length scale. Once a satisfactory mesh is obtained, an LES/FDF analysis is performed. *A posteriori* analysis of the LES/FDF results indicated that the subfilter-scale (unresolved) turbulent kinetic energy is approximately 16% of the total turbulence kinetic energy (resolved + subfilter-scale).

5.5.2 Turbulent Inflow

Turbulence specification at inflow boundaries plays an important role in determining how the flow evolves downstream in the computational domain, especially in cases where the inlet turbulence governs or significantly influences the turbulence production mechanism (free shear layer or wall-shear) inside the domain. In the RAS approach, the inlet turbulence is relatively easy to handle, and is generally specified in terms of turbulence kinetic energy and eddy dissipation rate or via a turbulence length scale and turbulent intensity, in addition to the mean velocities. For LES, the inlet specification is not as straight forward, and requires specifying fluctuating spatially-varying velocities that mimic the unsteady turbulent flow at the inlet. Several methods have been proposed in the literature for specifying turbulent velocity profiles at inlets for LES computations.

The most basic method is to superimpose random fluctuations (white noise, based on the magnitude of the rms velocity fluctuations) on the mean inlet profile. The disadvantage with this method is that there are no physical structures of turbulence in the inflow, and the fluctuations tend to damp out quickly in the computational domain. Another method is to pre-compute the flow upstream of the computational domain and use the pre-computed flow solution to impose inlet conditions at the plane of the fuel-nozzle exit. This is potentially a good method for specifying inlet velocities, but is dependent on the availability of accurate information about upstream flow conditions that is not readily available in many cases. A mapped-inlet boundary condition is available in OpenFOAM, where velocity profiles from an interior plane are mapped onto the inlet. This specification allows for structures in the inflow, but is only applicable when the interior plane is topologically identical to the inlet. That is, if the inlet consists of a circular jet surrounded by an annular jet, the interior plane should also have a circular jet and an annular jet. Both mapped-inlet and pre-computed methods do not necessarily give the correct level of turbulent fluctuations, if that is known experimentally for a particular configuration. Another method is to synthesize turbulence at the inlet using algebraic procedures to reconstruct structures with approximately the right statistics. This method is similar to the first approach described above, in the sense that fluctuations are superposed on mean velocities; the difference lies in the fact that the fluctuations have well-defined spatial and temporal correlations.

The inflow created in this case exhibits artificial turbulent structures, and allows for the accurate representation of the experimentally measured means and rms of turbulent fluctuations.

In this LES study, a digital-filter based turbulent synthesis technique [204] based on measured mean and rms velocities is used to create turbulent inflow at the inlet boundary for Sandia Flame D. It is observed that in the absence of a valid turbulent inflow (i.e., when random fluctuations or just flow mean velocities are specified), the numerical solution does not generate sufficient turbulence in the computational domain, and the flame blows out. The ineffectiveness of white-noise random fluctuations is attributed to the fact that the fluctuations damp out rapidly due to the lack of energy in the low wavenumber range. An accurate turbulent inflow specification is found to be critical for the spreading and mixing of the fuel jet and, consequently, the stabilization of the flame. The digital filter method used in this study consists of two steps:

1. In the first step, a three-dimensional signal U_i is generated for each velocity component with prescribed two-point statistics (two-point correlation). The statistics can be experimentally derived or estimated heuristically. Digital filtering of the random data set then is performed, where filter coefficients are tuned to capture the desired two-point statistics. The details are available in [204].

2. To account for the one-point statistics (means; self- and cross-correlation between different velocity components), the 3-D velocity signal with two-point statistics obtained in the first step is transformed by a method proposed by Lund et al. [206]. In this method the velocity signal is modified via $u_i = \bar{u}_i + a_{ij}U_j$, where $\bar{u}_i$ is the mean velocity and u_i is the final velocity signal with the desired one-point and two-point statistics. The tensor a_{ij} is given by

$$(a_{ij}) = \begin{pmatrix} (R_{11})^{1/2} & 0 & 0 \\ \mathrm{R}_{21}/a_{11} & (R_{22} - a_{21}^2)^{1/2} & 0 \\ \mathrm{R}_{31}/a_{11} & (R_{32} - a_{21}a_{31})/a_{22} & (R_{33} - a_{31}^2 - a_{32}^2)^{1/2} \end{pmatrix}. \qquad (5.4)$$

In the above expression, R_{ij} represents the correlation tensor, which may be known from the experimental data.

Figure 5.14 shows instantaneous contours of x-, y-, and z-velocities (y-axis de-

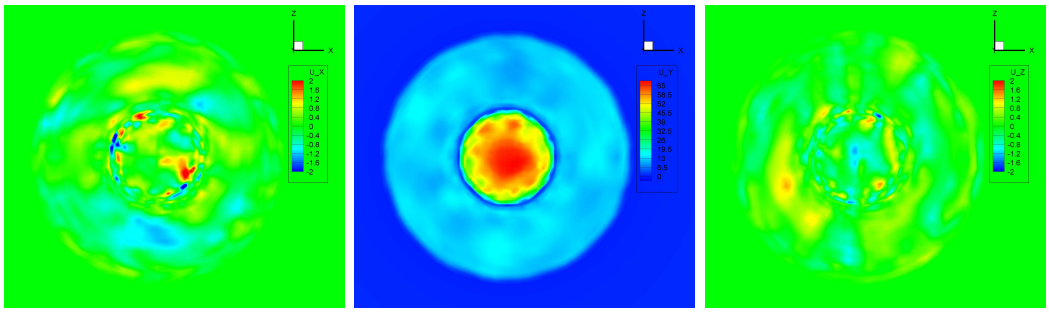

Figure 5.14. Instantaneous x-, y-, and z-velocities (in m/s) at the inlet constructed using the turbulence synthesis approach. The inner-most circle (as seen in the middle contour plot) is the fuel jet and the surrounding annulus is hot pilot.

notes the axial direction, and z-x plane represents the cross-section) constructed using the above method on the inlet boundaries for Sandia Flame D. The presence of structures is evident from the velocity contours. The method used here reproduces the prescribed one-point statistics and autocorrelation functions.

5.5.3 Assessment of Mass Consistency and Density Feedback

In hybrid FV/particle-Monte-Carlo solution procedures for LES/FDF simulations, the notional particles representing fluid mass are initialized in the computational domain and evolve in physical and composition spaces via the FDF equations. This method requires that the Eulerian density field remain consistent with the density field implied by the particle masses. The numerical implementation of the hybrid FV/Monte-Carlo method requires special treatment to satisfy this criterion. In this work, the mass consistency algorithms by Zhang and Haworth [139] are employed to ensure that the Lagrangian density field remains consistent with the FV Eulerian density field. Furthermore, the equivalent enthalpy procedure has been implemented in this work to evolve the FV density, since direct feedback of particle thermochemical density (density based on particle composition) is not stable due to the inherent statistical noise. Thus, three density representations are available here: the Eulerian FV density field, the Lagrangian density implied by the particle mass, and the Lagrangian density obtained from particles' compositions.

Figure 5.15 shows the comparison of the three mean density fields at different axial locations for LES/FDF analysis of Sandia Flame D. The three representations

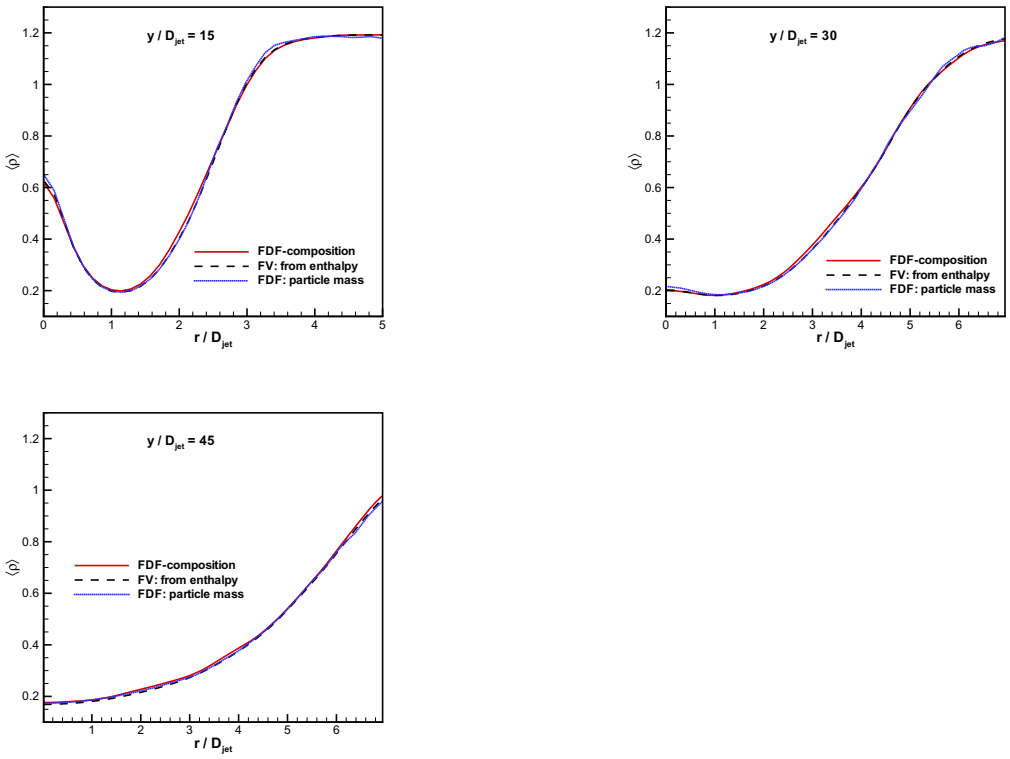

Figure 5.15. Comparison of radial profiles of mean density at three axial locations for different density representations.

are in excellent agreement with each other at all axial locations. This demonstrates that the Eulerian and the Lagrangian density fields remain consistent in the mean, and therefore establishes the accuracy of the underlying numerical implementation and the density feedback algorithm.

5.5.4 Results

The LES/FDF simulation is carried out in several stages. A FV chemistry solution (chemical source terms are computed directly using the filtered quantities with no consideration of subfilter-scale TCI) is obtained first where the fuel jet, hot pilot and co-flowing air issue into the computational domain with quiescent, ambient air as the initial condition. The FV chemistry computations are performed for approximately 20 flow-through times. Next, the FV solution is used as the starting point for the LES/FDF computations. LES/FDF computations are run for

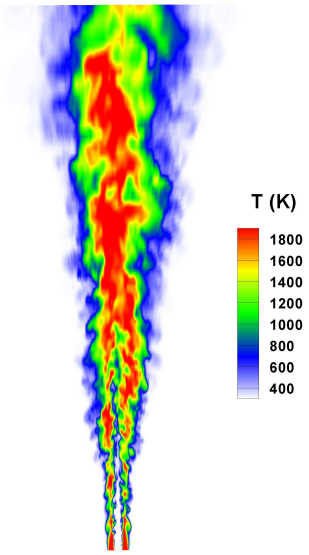

Figure 5.16. Computed instantaneous temperatures on a plane along the jet centerline for Sandia Flame D.

approximately seven flow-through times before time-averaged statistics are accumulated, so that the turbulence dynamics are fully equilibrated and a statistically stationary state is reached. Here the flow-through time is based on the mean fuel jet inlet velocity and the axial length of the computational domain. Time-averaged statistics then are collected for approximately 1.5 flow-through times. They are further averaged in the azimuthal direction to take advantage of the statistical homogeneity in that direction. The computed instantaneous resolved temperatures on a plane along the jet centerline for LES/FDF of Sandia Flame D are shown in Fig. 5.16.

Figure 5.17 presents comparisons of computed and measured mean temperatures at three axial locations for four models: (1) LES with FV chemistry (i.e., no subfilter-scale TCI) for a one-step methane/air global mechanism; (2) LES/FDF calculations for the one-step global mechanism; (3) LES with FV chemistry for a 16-species/41-reactions skeletal mechanism; and (4) LES/FDF/PMC for the 16-species/41-reactions skeletal mechanism. As expected, for all three axial locations, computed mean temperatures from LES/FDF calculations are in better agreement with the experimental data than the LES/FV-chemistry results. Differences between LES/FDF and LES/FV are manifestations of subfilter-scale TCI. For axial locations $x/D_{jet} = 15$ and $x/D_{jet} = 30$, the LES/FDF results for the global mech-

anism deviate significantly from the experimentally measured mean temperatures, whereas computed mean temperatures are in reasonable agreement with experimental data at the $x/D_{jet} = 45$ location. This behavior is attributed to the global methane/air chemistry that has been used here to model chemical reactions. The global mechanism does not provide an accurate prediction of the chemical reaction rates, and tends to overpredict the reaction rates at upstream locations. At downstream locations (say, $x/D_{jet} = 45$), the effect of inaccuracies in the modeled chemical mechanism is diminished since most of the chemical reactions have gone to completion by that time. The 16-species/41-reactions mechanism represents finite-rate chemical kinetics appreciably better than the global mechanism and, therefore, the computed results for both FV and LES/FDF calculations with this skeletal mechanism are in better agreement with the experimental data than the results for global mechanism at all three axial locations. The LES/FDF calculations predict burning of fuel somewhat further upstream in the computational domain compared to the FV calculations for the 16-species mechanism, as evident from the higher centerline temperatures at $x/D_{jet} = 15$ and $x/D_{jet} = 30$ axial locations. This is due to the use of a simple mixing model along with a fixed model constant. A higher value of the model constant is employed for LES/FDF than that used for RAS/PDF simulations, and no attempt has been made here to optimize its value. Nevertheless, mean temperatures computed here from LES/FDF with a fixed mixing model constant are in reasonably good agreement with the experimental data. The main focus of this work is to demonstrate the accuracy of the LES/FDF method and to validate the code, and to that end, additional computed mean and rms quantities from LES/FDF/PMC calculations are compared with the experimental data below.

Figure 5.18 presents a comparison of computed (resolved contributions only) and measured rms of temperature fluctuations at three axial locations for two models: (1) LES/FDF/PMC for the 16-species mechanism and (2) LES with FV chemistry with the same mechanism. The rms temperatures from LES/FDF computations are in excellent agreement with the experimentally measured values at $x/D_{jet} = 30$ and $x/D_{jet} = 45$ locations. The LES/FDF results are off at the $x/D_{jet} = 15$ location and this is attributed to the deficiencies in the mixing model and chemical mechanism employed in this study.

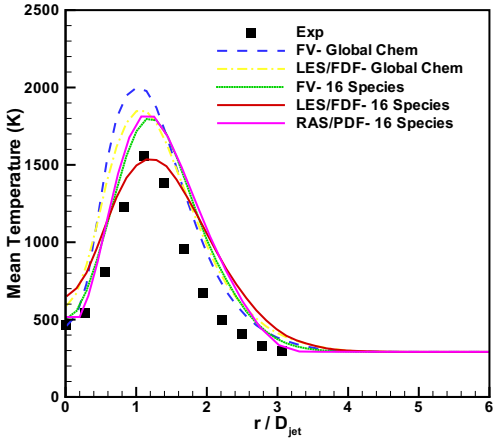

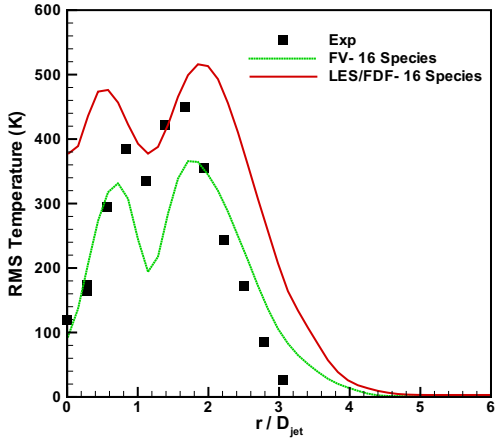

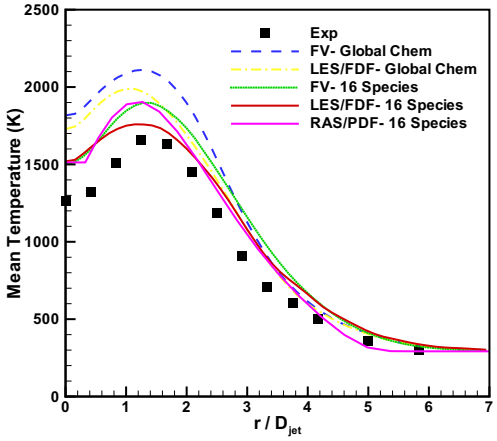

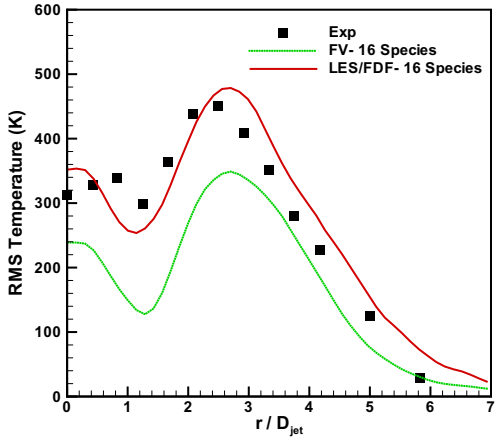

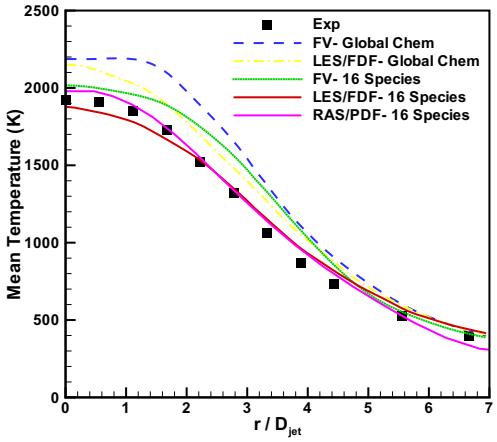

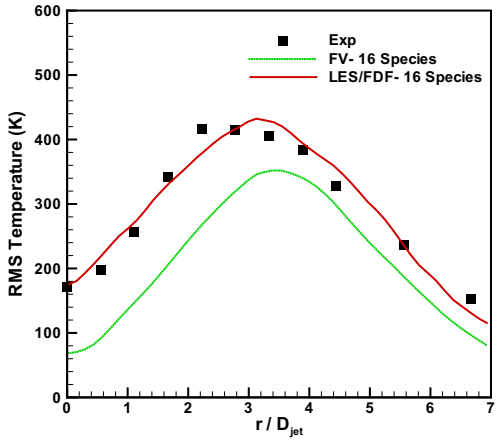

Figure 5.17. Radial profiles of mean temperature at three axial locations (x/D_{jet} = 15, x/D_{jet} = 30, and x/D_{jet} = 45) for Sandia Flame D.

Figure 5.18. Radial profiles of rms temperature at three axial locations (x/D_{jet} = 15, x/D_{jet} = 30, and x/D_{jet} = 45) for Sandia Flame D.

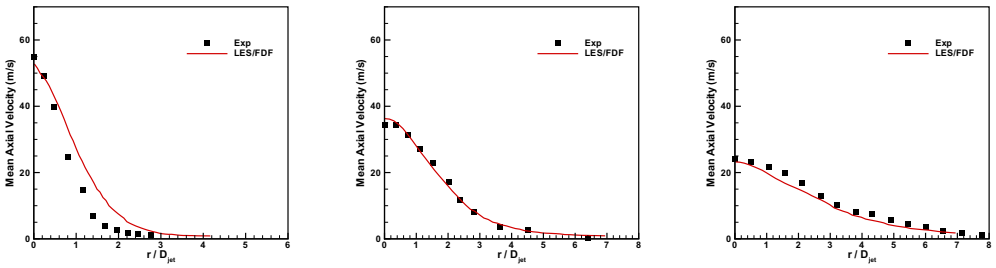

Figure 5.19. Radial profiles of mean axial velocity at three axial locations ($x/D_{jet} = 15$, $x/D_{jet} = 30$, and $x/D_{jet} = 45$) for Sandia Flame D.

Figure 5.19 presents a comparison of computed and measured mean velocity profiles at three axial locations for the LES/FDF/PMC calculations for the 16-species mechanism. The computed mean velocities are in good agreement with the experimentally measured velocities at all three axial locations.

The plots in Figs. 5.20 and 5.21 compare the computed mean and resolved rms mass-fractions of CO_2 with the experimental data at $x/D_{jet} = 15$ and $x/D_{jet} = 30$ axial locations for LES/FDF/PMC calculations with the 16-species mechanism. The computed mean and rms mass-fractions of CO_2 are in good agreement with the measured data. The computed mean and rms mass-fractions of OH at $x/D_{jet} = 15$ and $x/D_{jet} = 30$ axial locations are plotted and compared with the measured values in Figs. 5.22 and 5.23, respectively. The computed quantities for OH capture the trends seen in the experimental data quite well. Quantitatively, the computed values are slightly to moderately off from the experimental data, which is mainly due to the simple skeletal chemical mechanism used here for methane/air chemistry.

The LES/FDF/PMC simulation conducted in this study employs a skeletal chemical mechanism and a simple mixing model. The level of agreement with the experimental data can be readily improved by incorporating a detailed chemical mechanism [203, 207] and a better mixing model [202]. Using a detailed chemical mechanism that captures chemical kinetics much more accurately than the skeletal mechanism is computationally prohibitive for LES/FDF calculations due to the enormous costs involved, and necessitates the use of ISAT [208] or similar chemistry acceleration procedure. Nonetheless, the accuracy achieved in the results shown here demonstrates the promise of the LES/FDF/PMC method.

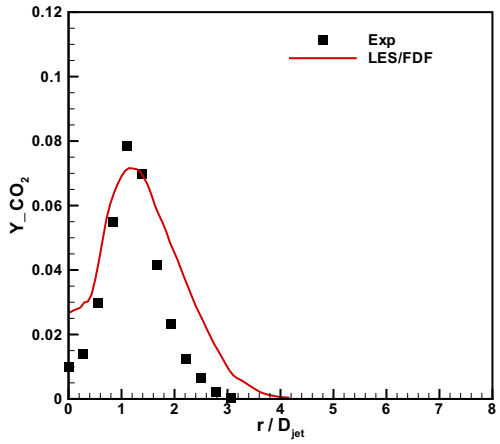

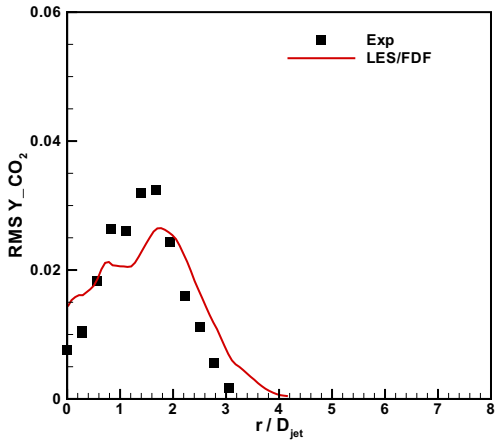

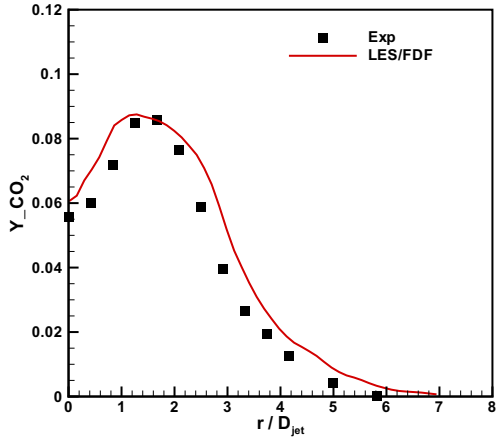

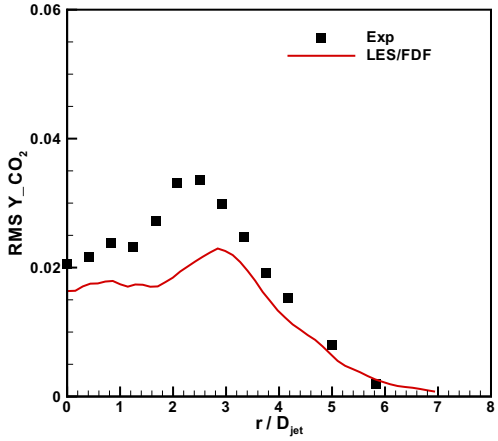

Figure 5.20. Radial profiles of mean mass-fraction of CO_2 at two axial locations ($x/D_{jet} = 15$ and $x/D_{jet} = 30$) for Sandia Flame D.

Figure 5.21. Radial profiles of rms mass-fraction of CO_2 at two axial locations ($x/D_{jet} = 15$ and $x/D_{jet} = 30$) for Sandia Flame D.

5.6 Parallelization Studies

The computational-time-map-based parallelization scheme proposed in Section 4.4.1 is evaluated here for two test cases. In this scheme, the time spent in chemistry and PMC calculations is recorded for each finite-volume cell, and that information is used to decompose the domain. For more details, see Section 4.4.1.

The first test case is the RAS/PDF/PMC simulation of the scaled-up Sandia Flame D using a 16-species/41-reactions methane/air mechanism. For the

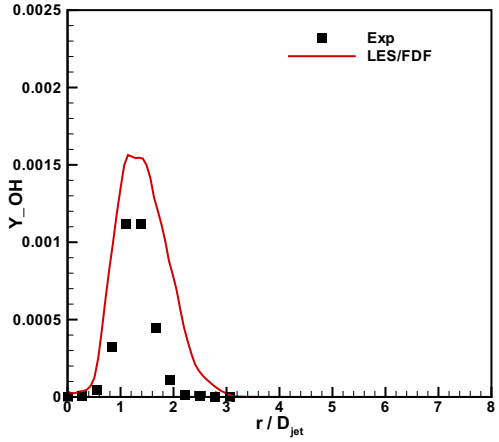

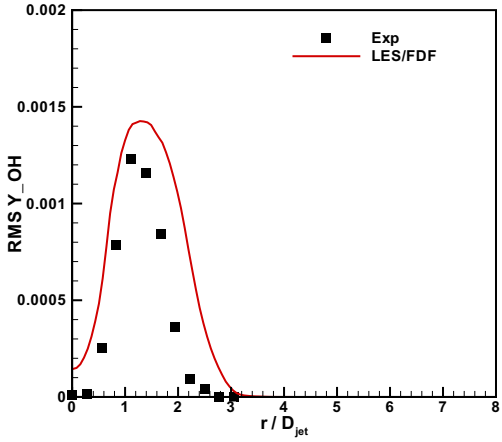

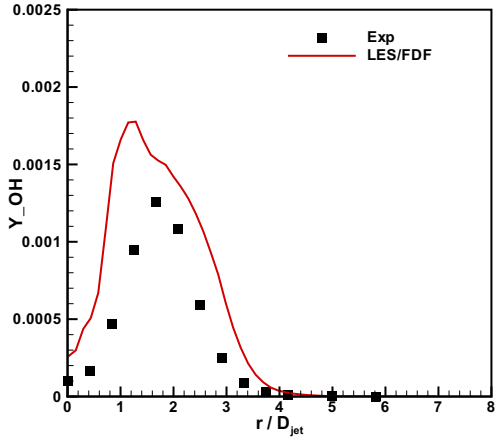

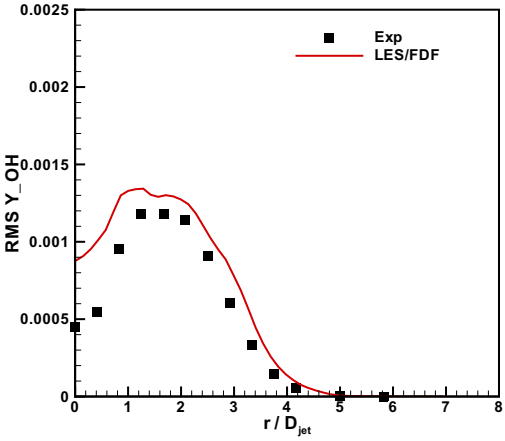

Figure 5.22. Radial profiles of mean mass-fraction of OH at two axial locations ($x/D_{jet} = 15$ and $x/D_{jet} = 30$) for Sandia Flame D.

Figure 5.23. Radial profiles of rms mass-fraction of OH at two axial locations ($x/D_{jet} = 15$ and $x/D_{jet} = 30$) for Sandia Flame D.

proposed scheme, the contours of average CPU time spent in each finite-volume cell at each time-step for chemistry, PMC calculations and their aggregate for RAS/PDF/PMC simulation of the scaled-up Sandia Flame D are shown in Figs. 4.2, 4.3, and 4.4, respectively. The computational domain is then distributed among processors to balance the overall load.

To analyze the parallelization efficiency of this scheme, RAS/PDF/PMC analyses of scaled-up Sandia Flame D are performed on 1 and 16 processors for approximately four flow-through times. The speed-up resulting from parallelization

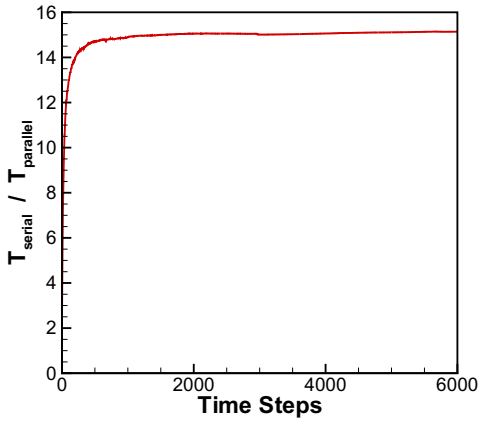

Figure 5.24. Speed-up for a 16-processor run for RAS/PDF/PMC of scaled-up Sandia Flame D.

for these runs is shown in Fig. 5.24. As seen in the figure, a speed-up of approximately 15 is obtained for the 16 processor run. Better results could be obtained with further iteration on the domain decomposition.

A LES/FDF/PMC test case is considered next. This is a simulation of Sandia Flame D using a global methane/air mechanism. The cost of the chemistry computations for this test case is approximately eight times lower than the PMC cost (in contrast to RAS/PDF/PMC, where the chemistry cost is five times that of PMC), thereby allowing us to effectively isolate the PMC component of the LES/FDF/PMC module and assess the performance of the scheme. The computational time-maps for the cost of chemistry and PMC calculations on an axial plane passing through the centerline are shown in Figs. 5.25 and 5.26, respectively. The time-maps for PMC and chemistry computations are quite different from each other, with PMC being the dominant contributor to the total cost. The total cost, i.e., the average CPU time spent in each finite-volume cell at each time-step for PMC and chemistry calculations, is shown in Fig. 5.27.

In the strong scaling limit*, the LES/FDF/PMC simulation of the above flame is carried out on 16, 32, 64, and 128 processors, for which the computational domain has been decomposed using the total cost time-map shown in Fig. 5.27. A double-layer reordering (for details, see Section 4.4.1) is employed and clus-

*Total computational cost (problem size) is kept constant, thereby the computational load per processor decreases with the increase in number of processors.

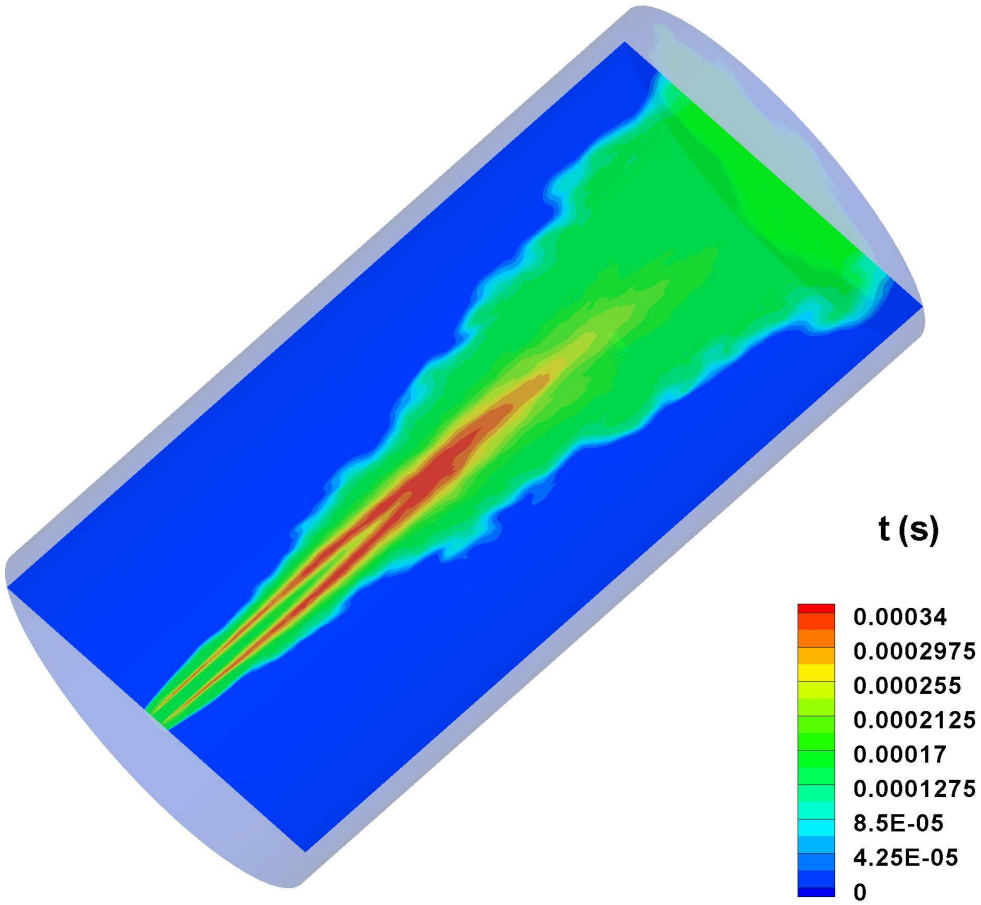

Figure 5.25. Computational time-map for LES/FDF/PMC of Sandia Flame D. The plot represents average CPU time spent (in s) per time-step for chemistry calculations.

tering is performed within each layer. The decomposed domains are plotted in Figs. 5.28 and 5.29 for 16-processor and 32-processor runs, respectively. The domain-decomposition for 64 and 128 processors uses the identical double-layer reordering as that for 16 and 32 processors. The differences arise from the clustering operation, where more clusters are created within each layer to meet the specified number of processors. The parallel efficiency for these runs is presented in Fig. 5.30. The plot demonstrates that the proposed parallelization scheme scales reasonably well even for this stringent scenario. For the 128-processor run, a speed-up of approximately 6.6 is obtained with respect to 16-processor computa-

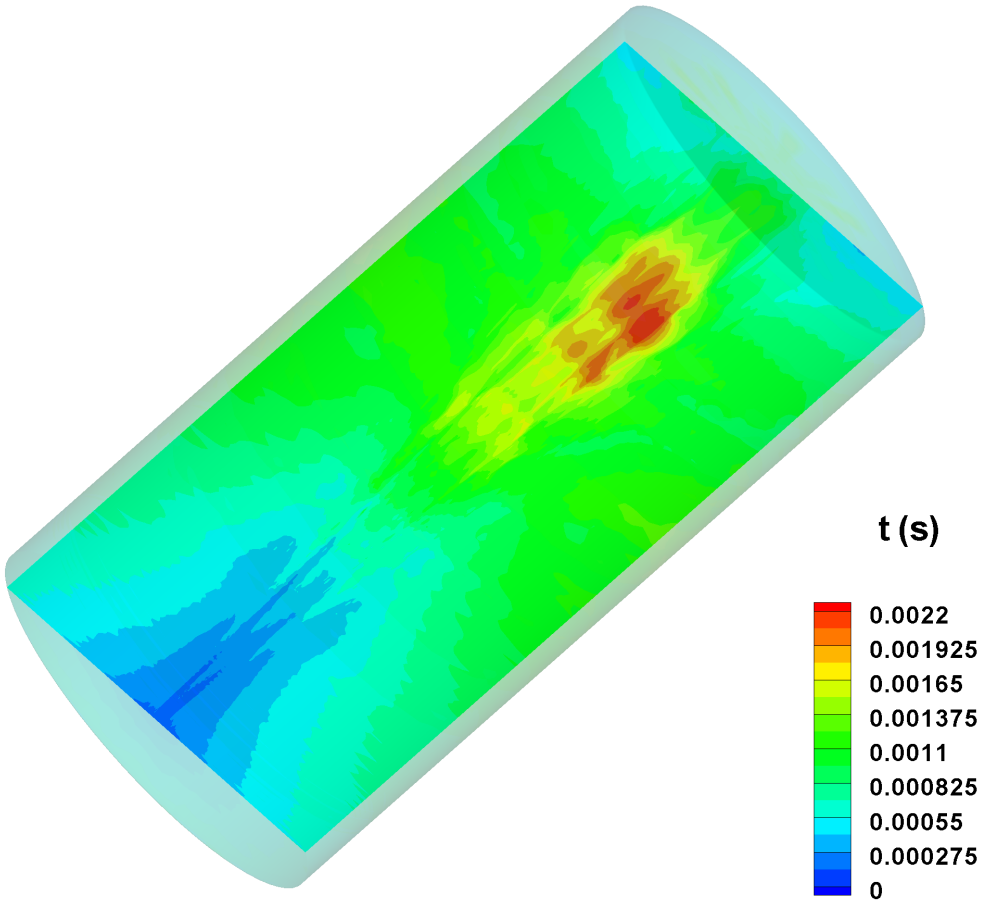

Figure 5.26. Computational time-map for LES/FDF/PMC of Sandia Flame D. The plot represents average CPU time spent (in s) per time-step for PMC calculations.

tions, thereby achieving a parallel efficiency of 83% in this configuration where the PMC cost (nonlocal in nature) dominates the chemistry cost. Further iterations on the domain decomposition based on these CPU time mappings can be expected to yield better scalability.

5.7 Summary

Various development and validation studies have been performed toward the construction of a comprehensive computational module for simulation of turbulent reacting flows. The module consists of a finite-volume LES solver to treat turbulence,

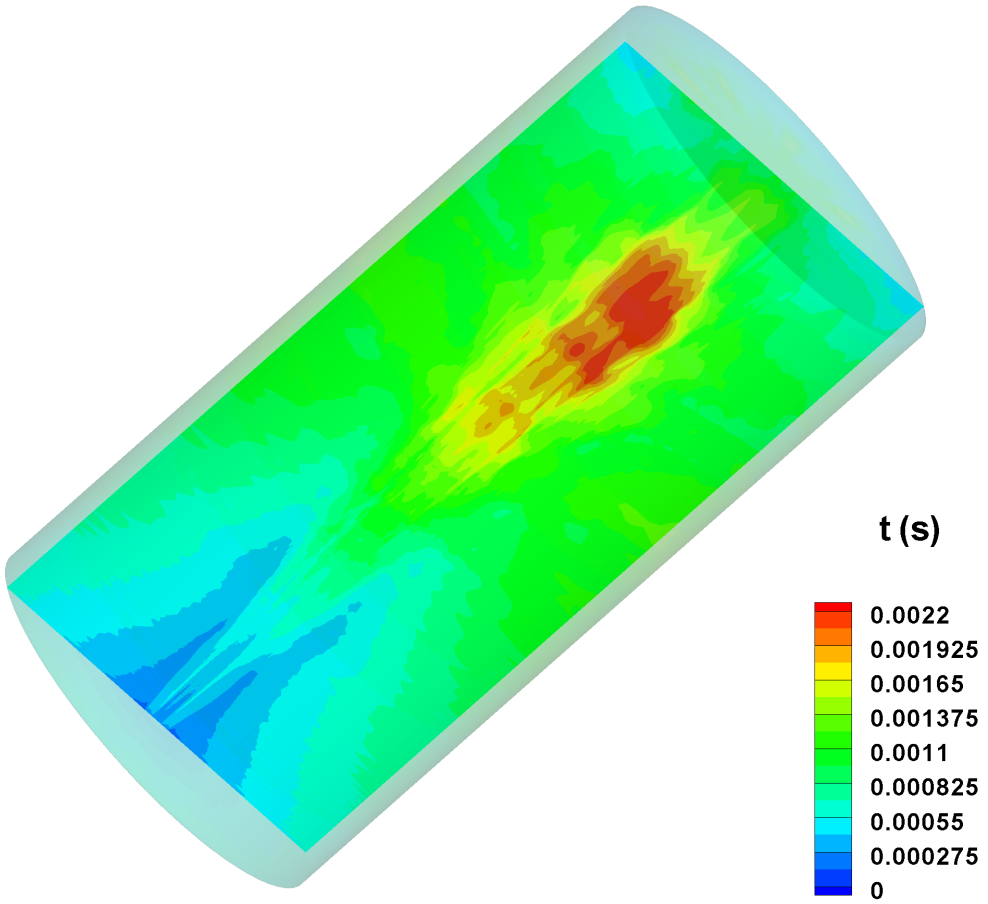

Figure 5.27. Computational time-map for LES/FDF/PMC of Sandia Flame D. The plot represents average CPU time spent (in s) per time-step for chemistry and PMC calculations.

a Lagrangian particle Monte Carlo solver to model chemistry and turbulence–chemistry interactions, and another Monte Carlo solver to account for thermal radiation and turbulence–radiation interactions. The developed module has been exercised to simulate a piloted jet diffusion flame (Sandia Flame D), and the computed mean and rms quantities from LES/FDF/PMC calculations have been compared with experimental data. The parallel efficiency of the computational module has also been assessed for a test configuration, and the results are used to perform the TRI studies that are reported in the next chapter.

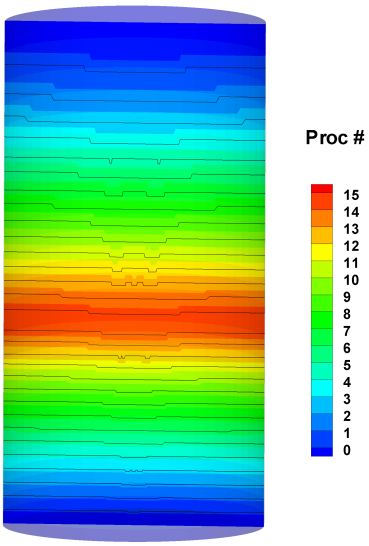

Figure 5.28. Decomposed domain using a double-layer clustering approach for a 16-processor simulation of LES/FDF/PMC of Sandia Flame D.

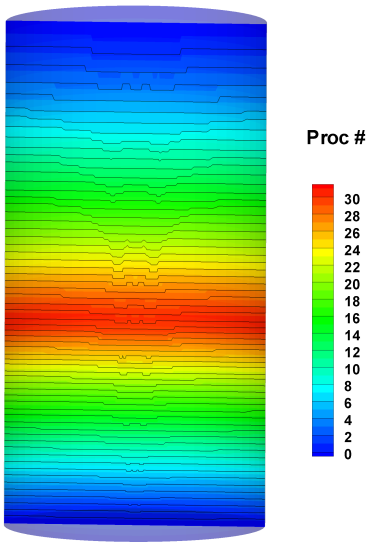

Figure 5.29. Decomposed domain using a double-layer clustering approach for a 32-processor simulation of LES/FDF/PMC of Sandia Flame D.

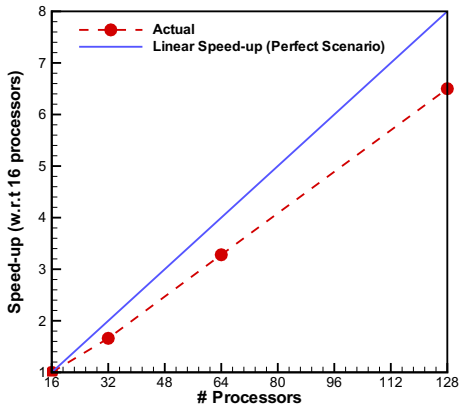

Figure 5.30. Scalability (strong scaling limit) for LES/FDF/PMC of Sandia Flame D.

Chapter 6

Treating Thermal Radiation in LES of Reacting Flows

Thermal radiation is known to be important for accurate simulation of combustion systems. The gaseous species and particulate media (such as soot) in a combustion system emit significant energy at high temperatures, part of which is re-absorbed within the system. Detailed analysis of emission, absorption, and other radiative processes is necessary for accurate predictions of flame temperatures and pollutant emissions. A photon Monte Carlo method has been presented in Section 4.2.1 to account for radiation in turbulent flow fields characterized by notional particles in PDF and FDF methods. The performance of the PMC method is dependent on the number of photon bundles considered; previous studies have shown that approximately one photon bundle per notional particle in the RAS/PDF method is sufficient to resolve the time-averaged solution with reasonable accuracy [37]. In the RAS/PDF approach, only the time-averaged mean solution is of concern; the PMC solution does not need to be time-resolved at every time step. In contrast, for LES/FDF simulations, radiation needs to be considered in a manner that is consistent with the time-dependent nature of LES. This imposes more strict requirements on the use of a PMC method for radiation treatment in LES/FDF simulations, and the PMC method needs to be revisited to estimate the optimum number of photon bundles required for transient treatment of radiation and accurate prediction of means. For that reason, a scoping study is conducted here to quantify the statistical uncertainties in the instantaneous PMC solution for various

photon bundle sizes, and to address the photon bundle requirement for accurate prediction of means in the LES context. Details of the analysis being performed are presented in Section 6.1.

An important physical modeling issue pertaining to thermal radiation in the LES context is the relative importance of subfilter-scale emission and absorption TRI. In LES, since the large-scales are explicitly resolved, the contributions of large-scale fluctuations to emission and absorption TRI are automatically captured. Models still are needed for the contributions of subfilter-scale fluctuations to emission and absorption TRI (hereby referred to as SFS emission and absorption TRI). SFS emission TRI, a one-point statistic, is completely accounted for in a LES/FDF framework. The PMC scheme discussed in Section 4.2.1 provides a closure for SFS absorption TRI. In this work, investigations are made to assess the importance of SFS emission and absorption TRI (Section 6.2).

6.1 PMC Requirements in LES

PMC methods have been used successfully in RAS/PDF simulations of both non-luminous and luminous flames [37, 188, 209]. These methods are statistical in nature and require sampling of a reasonable number of photon bundles to have confidence in the predicted statistics. The degree of confidence is generally evaluated by comparing the standard deviation with the mean. For RAS/PDF simulations, previous studies have concluded that on the order of one photon bundle per notional particle is needed for acceptable accuracy in the time-averaged solution. For LES/FDF simulations, PMC requirements are two-fold: (1) LES is time-dependent and, therefore, a sufficiently large number of photon bundles at each time step needs to be traced to achieve a PMC solution that captures the transient nature of the LES/FDF simulation and has low levels of statistical uncertainty; and (2) an adequate number of photon bundles needs to be considered for accurate prediction of mean quantities. In this work, we investigate the statistical uncertainties in the PMC solution for various photon bundle sizes for instantaneous LES/FDF snapshots of four flame configurations, and establish the number of photon bundles required for accurate means in the LES context. The flames considered are:

flame (i): Sandia Flame D

flame (ii): Sandia Flame D-like flame with soot based on a state-relationship

flame (iii): Scaled-up Sandia Flame D (Sandia Flame D is scaled four times. See Section 5.4)

flame (iv): Scaled-up Sandia Flame D with soot based on a state-relationship

The reasoning behind choosing these flames is to cover a wide range of flames for PMC analysis. Sandia Flame D is an optically thin laboratory-scale flame and contains a negligible amount of soot. In flame (ii), soot is added through a model based on a state-relationship to represent luminous sooting flames similar in size to Sandia Flame D. Flames (iii) and (iv) mimic nonsooting and sooting flames, respectively, that are about four times larger than Sandia Flame D. Flames (i)-(iv) range from small optically thin flames to several-meters-long optically thick flames. The relative importance of spectral molecular gas radiation versus broadband soot radiation is also varied by considering nonsooting versus sooting flames.

A one-step global reaction mechanism for methane/air combustion is considered to model chemical reactions in the above flames, where methane reacts with oxygen to form water vapor and carbon dioxide:

$$CH_4 + 2O_2 \rightarrow CO_2 + 2H_2O \ . \tag{6.1}$$

Soot is modeled in flames (ii) and (iv) using a state relationship where an algebraic function is considered for soot volume fraction as a function of mixture-fraction. The state relationship assumed here is based on the experimental work of [210]. The quantitative accuracy of soot prediction is not central to the present study, since the main focus is on thermal radiation characteristics. A qualitative representation of the soot volume fraction that yields reasonable soot levels at appropriate locations in the flame is sufficient here. The state relationship for soot volume fraction employed in this study is plotted in Fig. 6.1. Here the stoichiometric value of the mixture fraction is 0.37.

The flames considered in this study (Sandia Flame D and scaled-up Sandia Flame D) have been described in detail in Sections 5.3 and 5.4, respectively. The computational domain for these flames for LES/FDF/PMC simulations consists of a cylindrical block with a radius of 18 D_{jet} and an axial length of 70 D_{jet}, where D_{jet} is the fuel-jet diameter. A block-structured hexahedral mesh is created; the

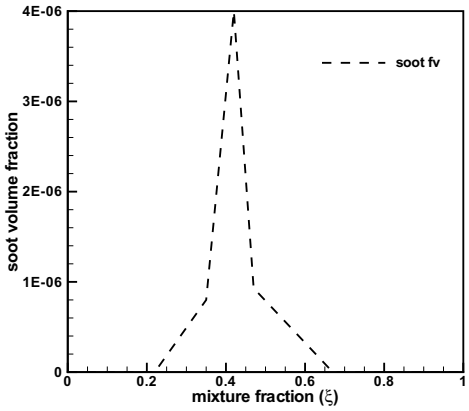

Figure 6.1. Soot volume fraction as a function of the mixture-fraction; state-relationship for soot employed in this study.

computational domain is divided into several blocks and a structured mesh is created within each block. The mesh consists of approximately $1.2M$ hexahedral cells. The digital filter technique described in Section 5.5.2 is used to generate turbulent inflow. The Smagorinsky model is used for the SFS stress tensor in the filtered Navier-Stokes equations. Approximately 84% of the turbulent kinetic energy is resolved by the grid. A nominal particle density of 15 particles per cell is used for the LES/FDF analysis. Examples of computed instantaneous temperatures and soot volume-fractions (from the state relationship) on a plane along the jet centerline for LES/FDF/PMC of flame (iv) [scaled-up Sandia Flame D with soot] are shown in Figs. 6.2 and 6.3, respectively.

An instantaneous snapshot of the LES/FDF particle field for the above flames is considered, and a frozen-field analysis is performed to investigate the transient resolution of the PMC method in LES simulations. For the frozen LES/FDF particle field, PMC ray tracing is conducted 600 times for a given number (N) of photon bundles, and statistics (averages and standard deviation based on the outcome of 600 tracings) are computed for radiative absorption and radiative heat flux in each finite-volume cell. The averages computed here represent the "exact" radiation solution for the LES/FDF snapshot. The PMC emission scheme is (by construction) such that the emission from each finite-volume cell is always exact irrespective of the number of photon bundles considered and, therefore, there is

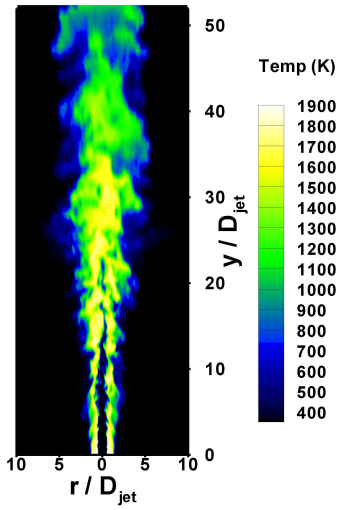

Figure 6.2. Computed instantaneous resolved temperatures on a plane along the jet centerline for flame (iv) [scaled-up Sandia Flame D with soot].

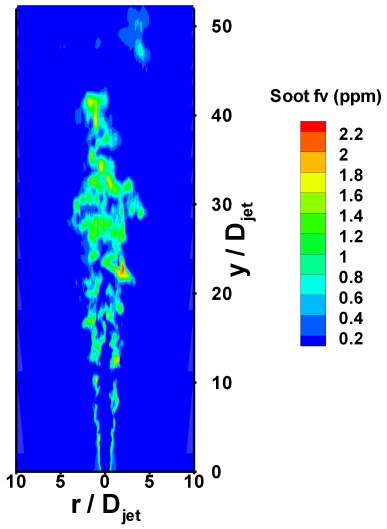

Figure 6.3. Computed instantaneous resolved soot volume-fractions (from state-relationship) on a plane along the jet centerline for flame (iv) [scaled-up Sandia Flame D with soot].

no statistical variation in radiative emission from one instance to the other. The exact volumetric absorption (or radiative heat source) for the LES/FDF snapshot in any arbitrary FV cell ic is given by

$$Q_{\text{exact,ic}} = \frac{\sum_{i=1}^{600} Q_{i,ic}}{600} \ , \tag{6.2}$$

where Q_i represent the volumetric absorption (or radiative heat source) in cell ic due to the i^{th} tracing of N photon bundles.

The standard deviation in volumetric absorption (or radiative heat source) in any arbitrary cell ic is computed as follows:

$$\sigma_{abs,ic} = \sqrt{\frac{\sum_{i=1}^{600} \left(Q_{abs,i,ic} - Q_{\text{abs,exact,ic}}\right)^2}{600-1}} \ . \tag{6.3}$$

In the above expression, σ_{abs} is the standard deviation in volumetric absorption, $Q_{\text{abs,exact,ic}}$ is the exact volumetric absorption in cell ic, and $Q_{abs,i,ic}$ is the volumetric absorption at the i^{th} instance of the tracing of N photon bundles.

The ratio of the standard deviation in the radiative absorption (σ_{abs}) to the

exact radiative absorption ($Q_{\text{abs,exact}}$) gives an indication of the statistical error in the predicted radiative absorption with respect to the exact value when a single history of photon bundle tracing is considered (that is, when N photon bundles are traced only once as opposed to 600 times).

Figure 6.4 presents the ratio of standard deviation to exact radiative absorption in the radial direction at three axial locations ($15D_{jet}$, $30D_{jet}$, and $45D_{jet}$) for scaled-up Sandia Flame D (flame iii) for different values of N. The radiative absorption along these lines is shown in Fig. 6.5; the plots compare the radiative absorption (for only $4M$ photon bundles) with the exact absorption. The standard deviation is also included in the plots in the form of upper- and lower-bound curves on the exact absorption profiles. The plots in Figs. 6.4 and 6.5 indicate that the spread in the predicted radiative absorption for a single tracing of photon bundles decreases with the increase in photon bundles (N) and attains a level of approximately 10% for $N = 4$ million. As a result of 10% standard deviation, the absorption profiles for an arbitrary tracing of $4M$ photon bundles well represent the profiles for exact absorption (see Fig. 6.5) in a qualitative manner.

The above results indicate that even with $4M$ photon bundles, the statistical uncertainty in local absorption is approximately 10% of the exact value, and more bundles are needed to reduce the uncertainty in the local absorption. Global estimates for tracing of $4M$ photon bundles are presented in Table 6.1 where, based on 600 samples of $4M$ photon bundles each for a frozen LES/FDF particle field, the radiative absorption and radiative heat source are aggregated over only those finite-volume cells where the computed standard deviation is within a specified fraction (namely, 10%, 15%, and 20%) of the exact volumetric absorption and radiative heat source, respectively. The aggregated absorption and radiative heat source are then expressed as a fraction of the total absorption and radiative heat source in the computational domain.

In this analysis, the cut-offs are an indicator of statistical uncertainty and can be thought of as the error margins (in the outcome of a single tracing of $4M$ bundles) about the exact values, and the fractions presented in Table 6.1 indicate the percentages of total absorption and radiative heat source in the computational domain that would be predicted within the error margins for a single tracing of $4M$ photon bundles. That is, the finite-volume cells for which the absorption and ra-

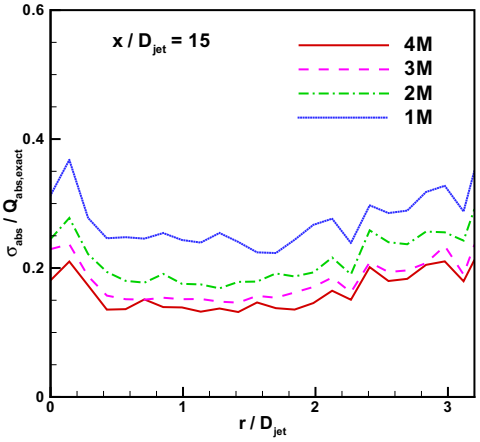

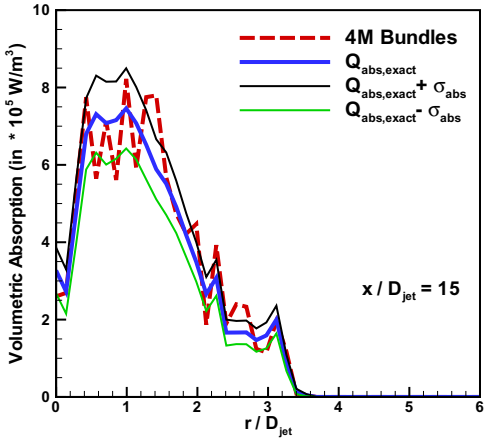

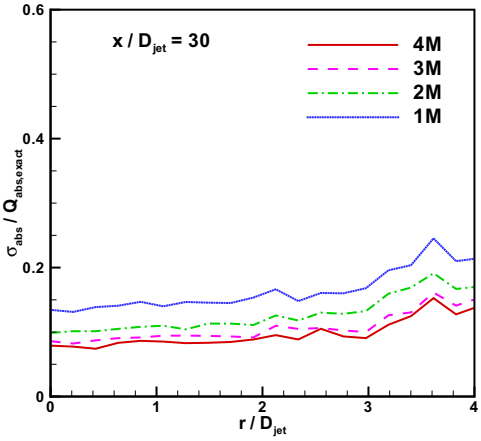

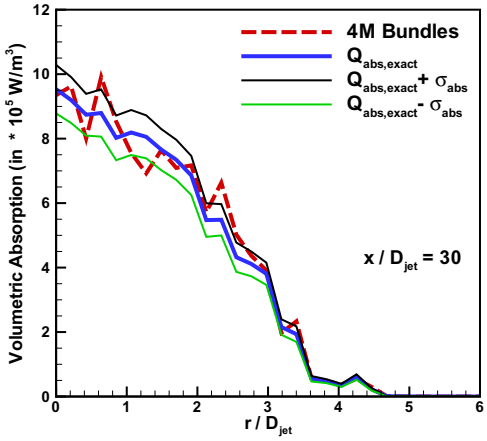

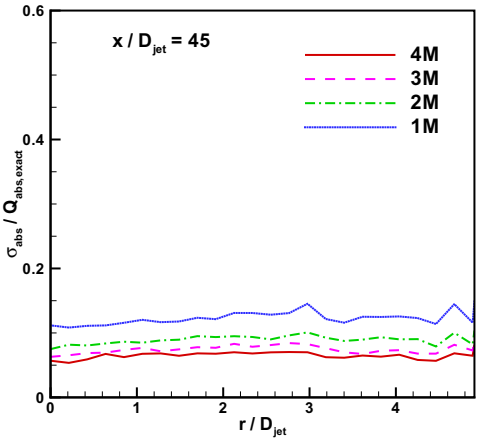

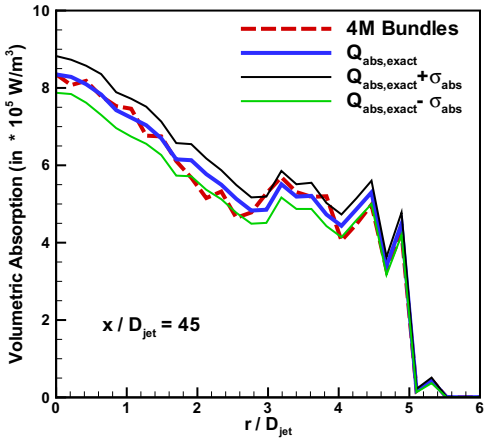

Figure 6.4. Radial profiles of the ratio of standard deviation in the volumetric absorption and its exact value at three axial locations ($x/D_{jet} = 15$, $x/D_{jet} = 30$, and $x/D_{jet} = 45$) for LES/FDF snapshot of scaled-up Sandia Flame D.

Figure 6.5. Radial profiles of exact volumetric absorption at three axial locations ($x/D_{jet} = 15$, $x/D_{jet} = 30$, and $x/D_{jet} = 45$) for LES/FDF snapshot of scaled-up Sandia Flame D.

$\frac{\sigma}{Q_{\text{exact}}}$ cutoff [based on 600 samples;$N = 4M$] (in %)	Fraction of total absorption	Fraction of total radiative heat source
10	0.803	0.936
15	0.936	0.991
20	0.971	0.995

Table 6.1. The aggregate absorption and radiative heat source expressed as a fraction of the total absorption and total radiative heat source, respectively, in the computational domain for flame (iii). The aggregation is conducted over FV cells where $\frac{\sigma}{Q_{\text{exact}}}$ is within a specified cutoff; here Q_{exact} refers to the exact volumetric absorption (or exact radiative heat source) for the LES/FDF snapshot, and σ corresponds to the standard deviation in the exact quantity.

diative heat source would be predicted within the error margins for a single tracing of $4M$ photon bundles contribute to x% of the total absorption and radiative heat source in the computational domain, where x is reported in Table 6.1. It can be seen that more than 90% of the total radiative heat source in the computational domain would be predicted within 10% deviation from the actual cell-level, exact values. Approximately 80% of the total radiative absorption is resolved within 10% uncertainty for $4M$ photon bundles.

For an instantaneous snapshot of scaled-up Sandia Flame D with soot based on a state-relationship (flame iv), the ratios of standard deviation to exact radiative absorption (for 600 samples) along a line in the radial direction at three axial locations ($15D_{jet}$, $30D_{jet}$, and $45D_{jet}$) are presented in Fig. 6.6. The ratios are plotted for different values of N, where N is the number of photon bundles considered in each sample. The trends observed for this flame configuration are similar to those for the previous flame. The standard deviation in the computed quantities decreases as the sample size (N) increases and attains a level of approximately 10% at $4M$ photon bundles per sample. Likewise, the computed radiative absorption for a single tracing of $4M$ photon bundles is a good qualitative indicator of the exact radiative absorption and stays for the most part within the one standard deviation band, as shown in Fig. 6.7.

Table 6.2 presents the fraction of the total radiative absorption and total radiative heat sources predicted within the error margins (statistical uncertainty; namely, 10%, 15%, and 20%) for a single tracing of $4M$ photon bundles. As dis-

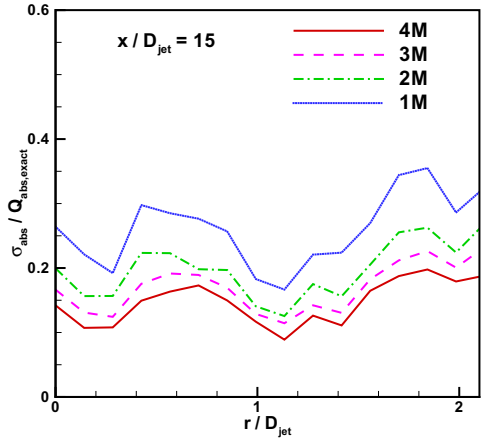

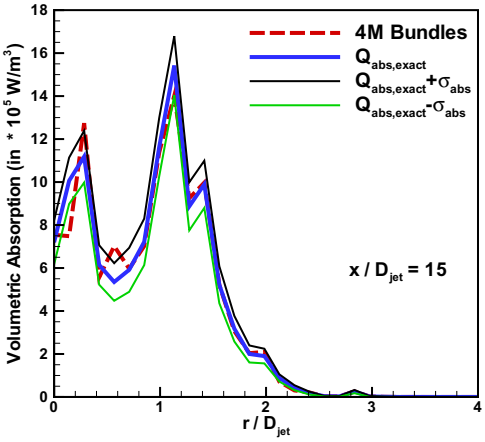

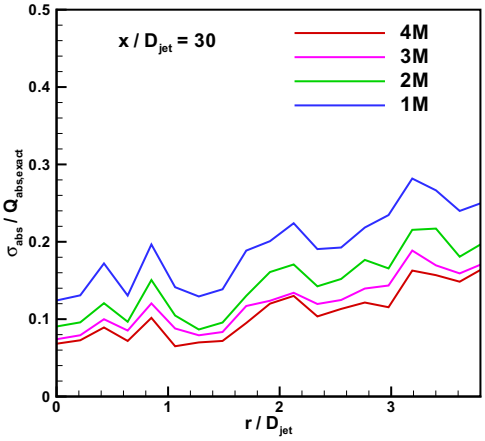

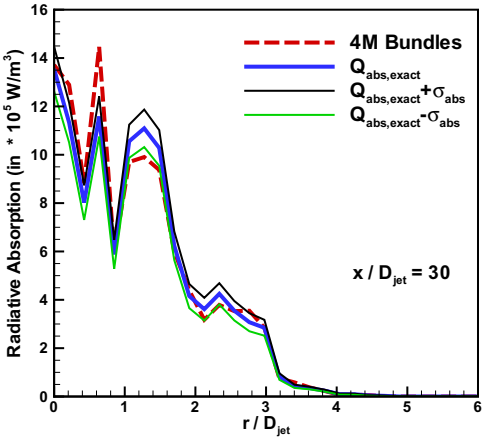

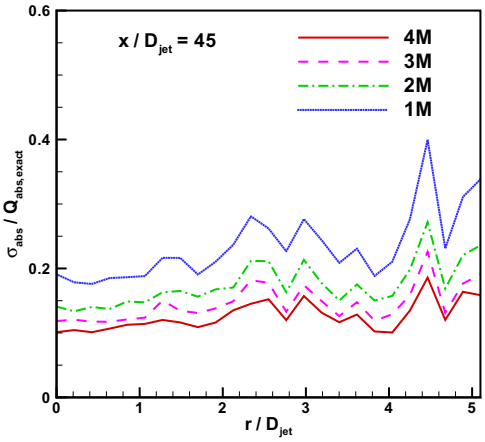

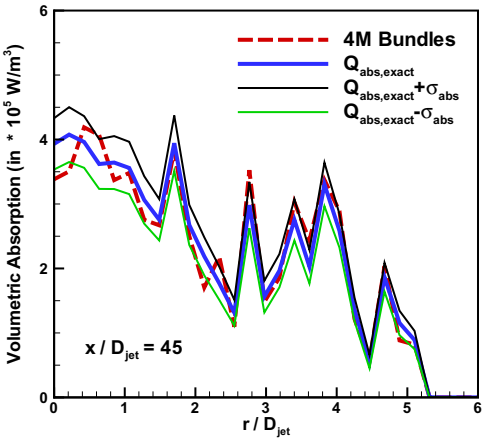

Figure 6.6. Radial profiles of the ratio of standard deviation in the volumetric absorption to its exact value at three axial locations ($x/D_{jet} = 15$, $x/D_{jet} = 30$, and $x/D_{jet} = 45$) for LES/FDF snapshot of scaled-up Sandia Flame D with artificial soot.

Figure 6.7. Radial profiles of exact volumetric absorption at three axial locations ($x/D_{jet} = 15$, $x/D_{jet} = 30$, and $x/D_{jet} = 45$) for LES/FDF snapshot of scaled-up Sandia Flame D with artificial soot.

$\frac{\sigma}{Q_{\text{exact}}}$ cutoff [based on 600 samples] (in %)	Fraction of total absorption	Fraction of total radiative heat source
10	0.547	0.895
15	0.875	0.954
20	0.949	0.977

Table 6.2. The aggregated absorption and radiative heat source expressed as a fraction of the total absorption and total radiative heat source, respectively, in the computational domain for flame (iv).

cussed before, these fractions are computed by aggregating the radiative absorption and heat source for the finite-volume cells where the ratio of the standard deviation and the average quantity is less than the tolerance set by the error margin (0.1, 0.15, and 0.2 for 10%, 15%, and 20%, respectively). The fractions are computed as the ratio of the aggregate obtained above (conditional aggregate based on the ratio of σ and Q_{exact} value) to the unconditional aggregate (aggregate over all cells). As reported in the table, 90% of the total radiative heat source is predicted within 10% error margin for a single tracing of $4M$ photon bundles. The contribution of cells with predicted radiative heat source within 15% error margin increases to 95% of the total radiative heat source. The absorption in the cells within 10% error margin contributes to only 55% of the total absorption in the computational domain. The contribution jumps to 88% for 15% error margin. In this analysis, the effect on cell-level emission is not considered since it has no statistical error. This is because the emission schemes implemented here represent emission exactly, irrespective of the number of photon bundles.

The exact radiative absorption, radiative heat source and their standard deviation were also analyzed for Sandia Flame D (flame i) where 600 samples of $1M$ and $4M$ photon bundles are traced in the computational domain for an instantaneous snapshot of the LES/FDF notional particle field. The ratio of standard deviation to exact absorption (obtained via averaging over 600 samples) is plotted along a line in the radial direction at three axial locations in Fig. 6.8. As seen earlier for the scaled-up flames, this flame also exhibits standard deviation that is approximately 10% of the averaged (i.e., exact radiation solution) value for most of the computational domain when a sample size of $4M$ photon bundles is used. Figure 6.9 compares the radiative absorption for a single tracing of $4M$ bundles

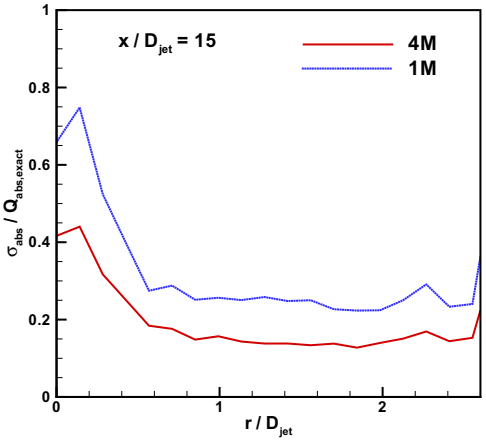

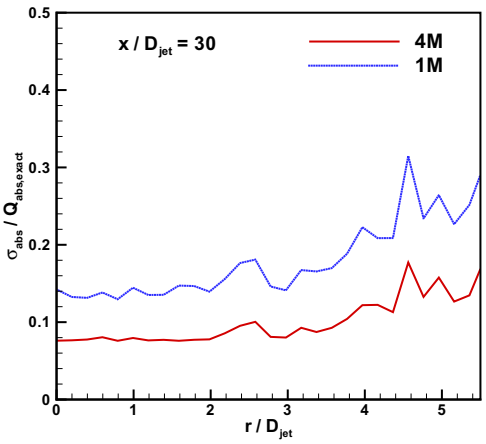

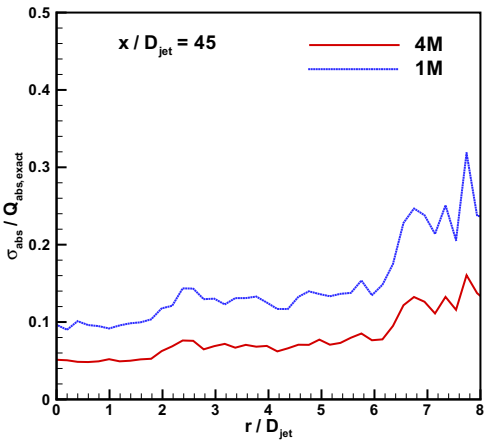

Figure 6.8. Radial profiles of the ratio of standard deviation in the volumetric absorption to its exact value at three axial locations ($x/D_{jet} = 15$, $x/D_{jet} = 30$, and $x/D_{jet} = 45$) for LES/FDF snapshot of Sandia Flame D.

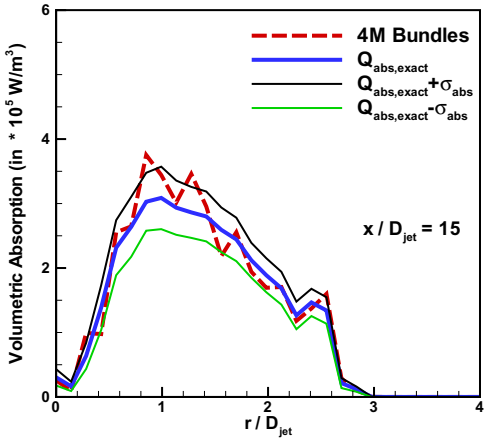

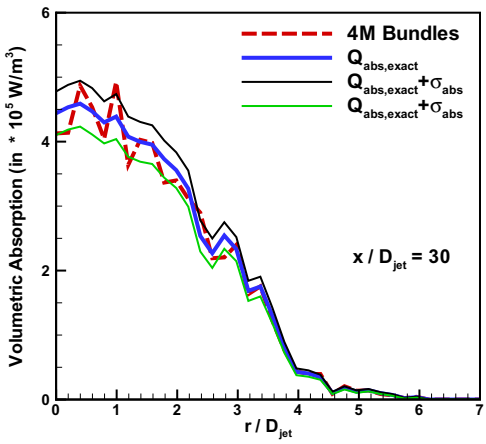

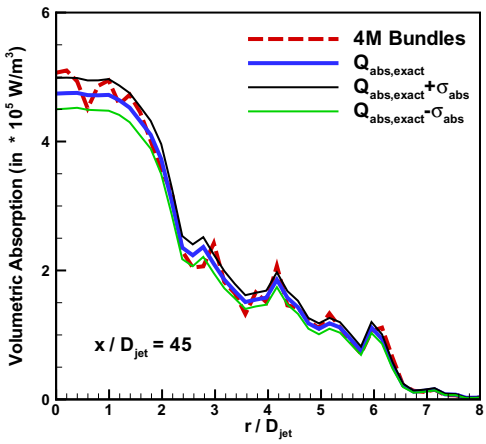

Figure 6.9. Radial profiles of exact volumetric absorption at three axial locations ($x/D_{jet} = 15$, $x/D_{jet} = 30$, and $x/D_{jet} = 45$) for LES/FDF snapshot of Sandia Flame D.

$\frac{\sigma}{Q_{\text{exact}}}$ cutoff [based on 600 samples] (in %)	Fraction of total absorption	Fraction of total radiative heat source
10	0.1	0.949
15	0.679	0.995
20	0.9	0.999

Table 6.3. The aggregated absorption and radiative heat source expressed as a fraction of the total absorption and total radiative heat source, respectively, in the computational domain for flame (i).

with the exact absorption profiles along the radial lines. The predicted radiative absorption for a single tracing of $4M$ bundles agrees qualitatively with the exact absorption.

As seen in Table 6.3, approximately 95% of the heat loss in the computational domain stays below a standard deviation of 10%, but only 10% of the absorption is within the statistical uncertainty of 10%. This is because Sandia Flame D is an optically thin flame with weak absorption, and more photon bundles per sample are required to lower the standard deviation in the absorption. Nevertheless, most of the radiative heat loss is within the 10% error margin.

Because other flame configurations have shown reasonable qualitative comparison with the exact solution and standard deviation to be approximately 10% for $4M$ bundles, flame ii (Sandia D-like flame with soot based on a state relationship) is analyzed for only one sample size ($N = 4M$ photon bundles), with 600 samples considered to compute the exact absorption, radiative heat loss, and their standard deviation for an instantaneous LES/FDF snapshot. The profiles of the radiative absorption for a single tracing of $4M$ bundles are compared with the exact absorption in Fig. 6.11, for radial lines at three axial locations. The tracing of only $4M$ bundles leads to absorption profiles that qualitatively well represent the exact absorption profiles. The ratio of the standard deviation to the exact absorption along the radial lines (lines as in Fig. 6.10) are plotted in Fig. 6.10. As shown in Table 6.4, the aggregate of exact radiative heat loss over cells with statistical uncertainty less than 10% (i.e., where the standard deviation is within 10% of the exact value) is approximately 98% of the total radiative heat loss.

Only 51% of the absorption is contributed from cells where the standard deviation is less than 10% of the absorption in the cell. For a cut-off of 15% for the

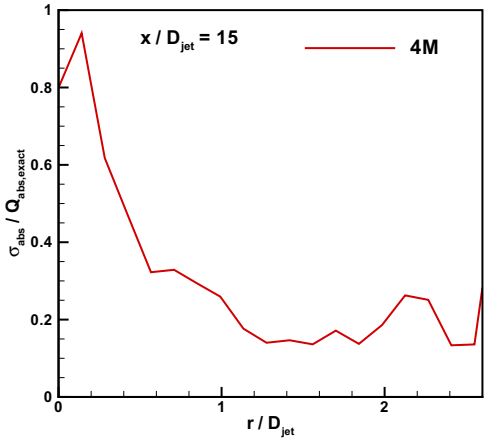

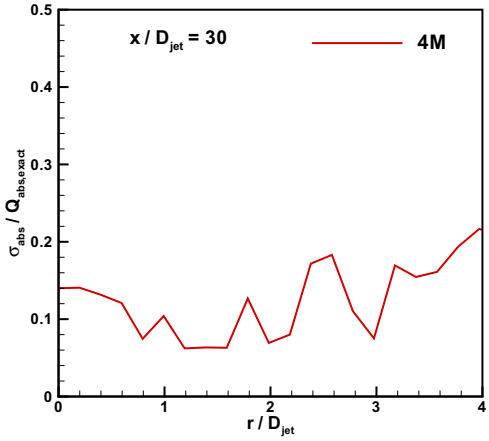

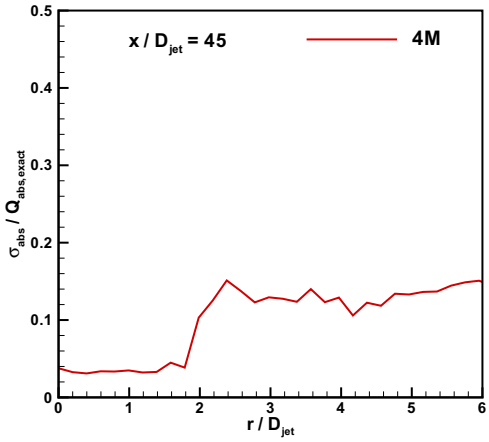

Figure 6.10. Radial profiles of the ratio of standard deviation in the volumetric absorption to its exact value at three axial locations ($x/D_{jet} = 15$, $x/D_{jet} = 30$, and $x/D_{jet} = 45$) for LES/FDF snapshot of Sandia Flame D with artificial soot.

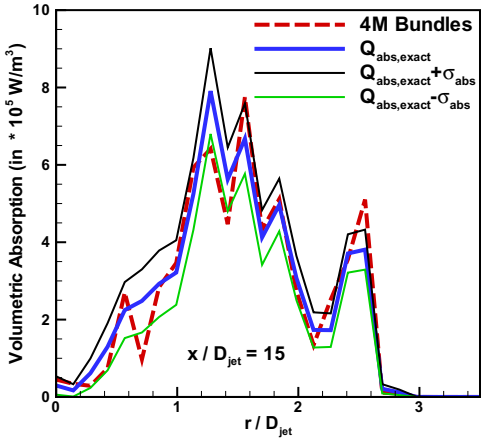

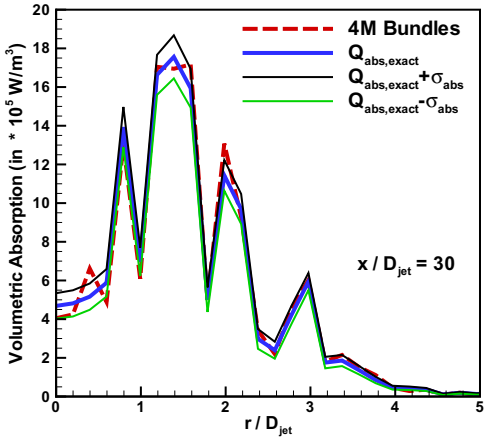

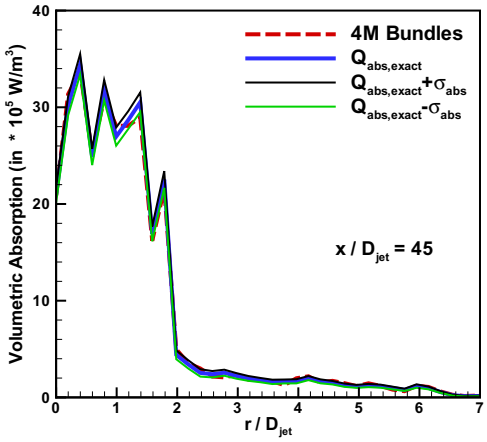

Figure 6.11. Radial profiles of exact volumetric absorption at three axial locations ($x/D_{jet} = 15$, $x/D_{jet} = 30$, and $x/D_{jet} = 45$) for LES/FDF snapshot of Sandia Flame D with artificial soot.

$\frac{\sigma}{Q_{\text{exact}}}$ cutoff [based on 600 samples] (in %)	Fraction of total absorption	Fraction of total radiative heat source
10	0.507	0.983
15	0.807	0.991
20	0.936	0.993

Table 6.4. The aggregated absorption and radiative heat source expressed as a fraction of the total absorption and total radiative heat source, respectively, in the computational domain for flame (ii).

standard deviation, the selected cells contribute 81% of the total absorption. The high standard deviation in the radiative absorption is attributed to the low optical thickness of the flame which, in spite of the presence of soot, remains optically thin and exhibits weak absorption. There are rapid variations in radiative intensities in the computational domain that require higher numbers of photon bundles to resolve the variation in intensities and the absorption. Soot is a strong absorber of thermal radiation, which aids in reducing variation in the intensities and predicts radiative absorption with lower standard deviation than flame (i) for a sample size of $4M$ photon bundles.

The snapshot analysis for various flame configurations presented above shows that approximately $4M$ photon bundles (i.e., ~ 4 bundles per FV cell) in the PMC method lead to a statistical uncertainty of about $10-15\%$ in the predictions of local radiative quantities (volumetric absorption and radiative heat loss). Due to this level of statistical uncertainty, the volumetric absorption profiles are in reasonable qualitative agreement with the exact profiles. However, the impact of statistical uncertainty (for $4M$ bundles) in PMC predictions on coupled LES/FDF/PMC simulations is not known and is investigated below.

Fully-coupled LES/FDF/PMC analyses are conducted next for flame (iv) with $4M$ and $8M$ photon bundles to investigate the effects of statistical uncertainty, and results are presented here. Figure 6.12 shows the variation of instantaneous resolved temperature with time at two locations ($y/D_{jet} = -1.75, z/D_{jet} = -1.75, x/D_{jet} = 35.0$; and $y/D_{jet} = 1.4, z/D_{jet} = 1.4, x/D_{jet} = 20.0$) in the computational domain. As seen in the plots, the time evolution of the local temperature for $4M$ and $8M$ photon bundles is different due to the statistical uncertainties in the PMC solution, however the trend is consistent in most of the regions, which suggests the suitability

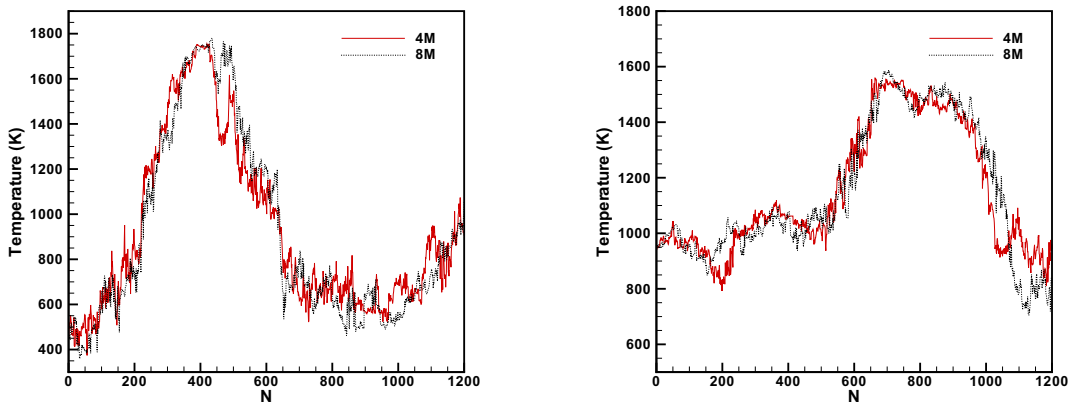

Figure 6.12. The variation in resolved temperature with time at two locations in scaled-up Sandia Flame D with artificial soot for different number of photon bundles in the PMC analysis.

of $4M$ photon bundles for accurate prediction of means and higher-order statistics. The time-averaged plots of mean temperature and radiative heat source along radial lines are shown in Figs. 6.13 and 6.14 at three axial locations. The computed mean profiles for different numbers of photon bundles are almost coincident with each other, thereby establishing the sufficiency of $4M$ photon bundles for accurate prediction of mean quantities.

Figures 6.15 and 6.16 show the radial profiles of mean temperature and mean radiative heat source, respectively, at three axial locations for flame (iii) for a fully-coupled LES/FDF/PMC analysis. The computed mean quantities are in excellent agreement for different number of photon bundles, thereby demonstrating that $4M$ photon bundles is adequate for accurate predictions of means in LES simulations of statistically-stationary systems.

Various flames have been investigated in this study to assess the statistical uncertainty in the instantaneous PMC solution (of a LES/FDF snapshot) for different photon bundle sizes, and results presented above indicate that $4M$ photon bundles lead to approximately $10-15\%$ uncertainty levels. It is shown that this level of uncertainty has no effect on mean quantities and $4M$ bundles (i.e., approximately four photon bundles per FV cell) suffice for accurate means. The effect on the higher-order statistics is still unclear, and quantities such as variances, two-point correlations, etc., need to be studied.

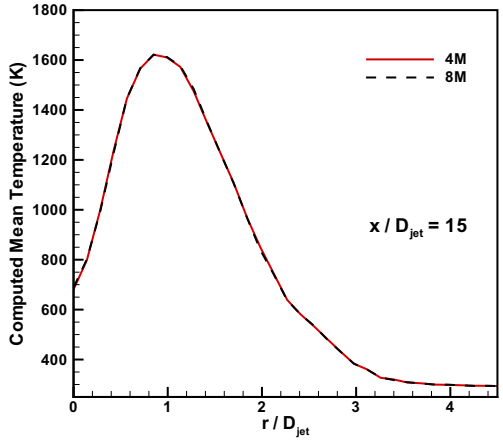

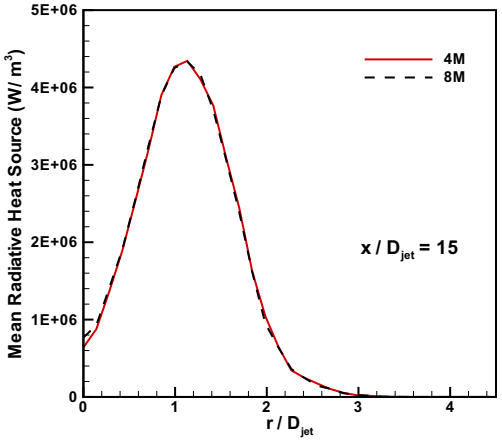

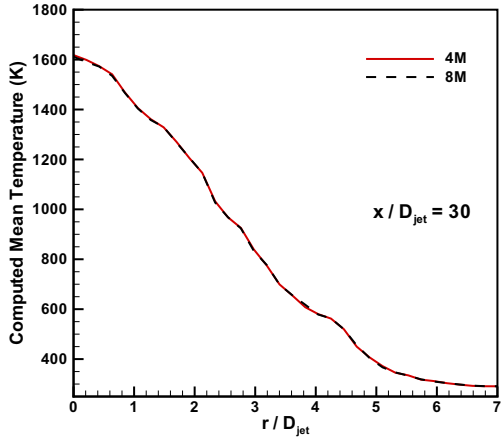

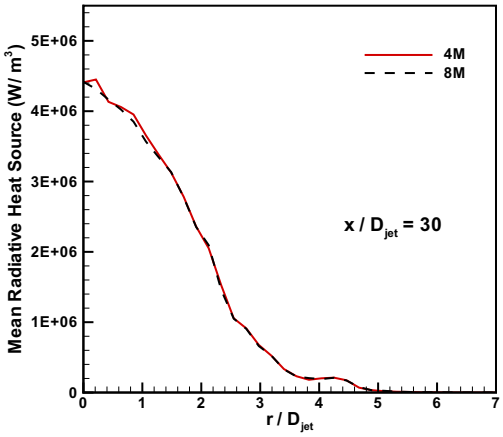

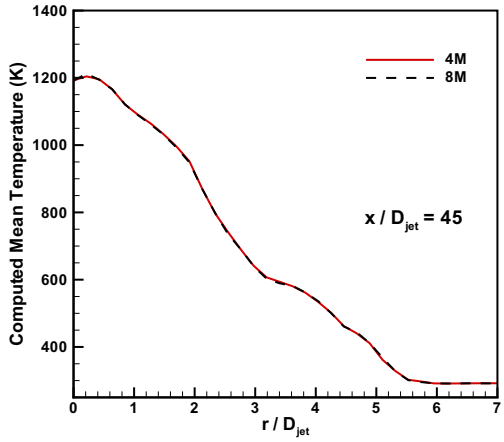

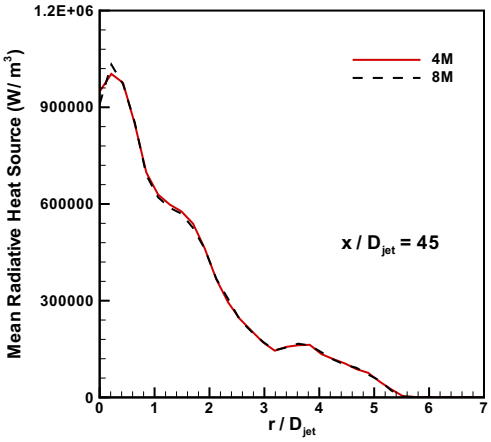

Figure 6.13. Comparison of radial profiles of mean temperature at three axial locations ($x/D_{jet} = 15$, $x/D_{jet} = 30$, and $x/D_{jet} = 45$) for scaled-up Sandia Flame D with artificial soot for different numbers of photon bundles.

Figure 6.14. Comparison of radial profiles of mean radiative heat source at three axial locations ($x/D_{jet} = 15$, $x/D_{jet} = 30$, and $x/D_{jet} = 45$) for scaled-up Sandia Flame D with artificial soot for different numbers of photon bundles.

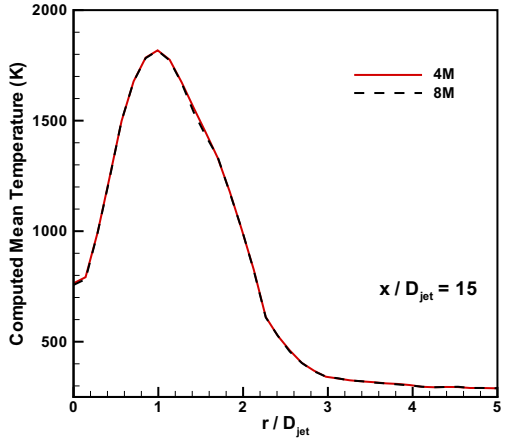

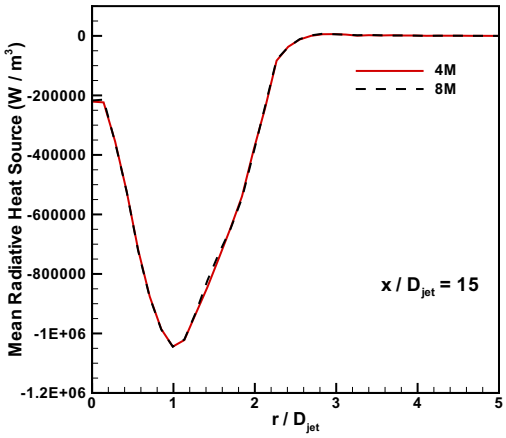

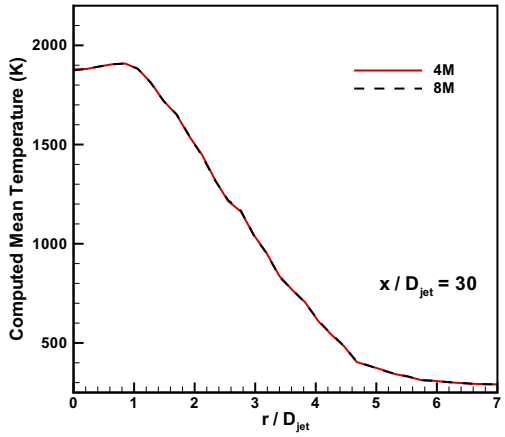

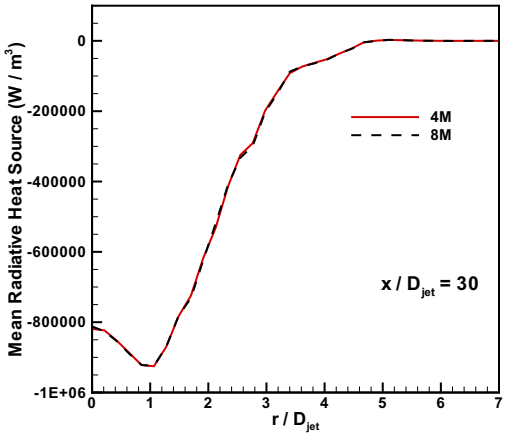

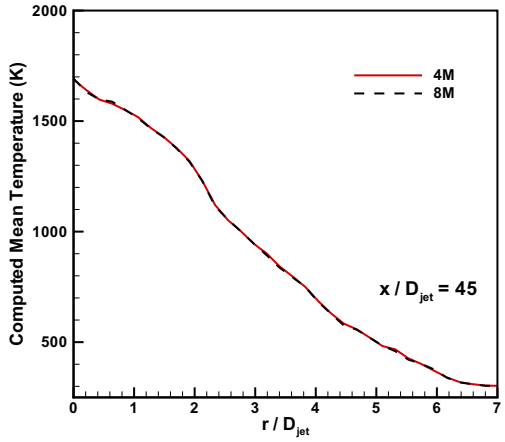

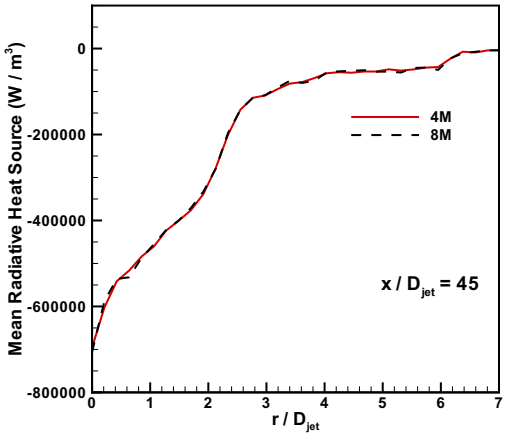

Figure 6.15. Comparison of radial profiles of mean temperature at three axial locations ($x/D_{jet} = 15$, $x/D_{jet} = 30$, and $x/D_{jet} = 45$) for scaled-up Sandia Flame D for different numbers of photon bundles.

Figure 6.16. Comparison of radial profiles of mean radiative heat source at three axial locations ($x/D_{jet} = 15$, $x/D_{jet} = 30$, and $x/D_{jet} = 45$) for scaled-up Sandia Flame D for different numbers of photon bundles.

6.2 TRI at Subfilter-Scale Level

A large number of experimental, theoretical and computational studies [27–36, 188, 211] have demonstrated the importance of TRI in reacting flows. Computational investigations of reacting systems using RAS approaches require explicit models to account for TRI. However, for LES, since the large scales are explicitly resolved, the large-scale contributions to TRI (henceforth referred to as resolved TRI) are explicitly captured in the solution procedure. The effect of subfilter-scale fluctuations on radiative emission and absorption (henceforth denoted by SFS TRI) still needs to be modeled in LES. Theoretical analysis of LES suggests that most of the TRI should be present as resolved TRI, since the large-scale fluctuations are significantly larger than the subfilter-scale fluctuations. However, for engineering meshes (where the filter cut-off is somewhere close to the energy-containing scales, rather than in the sub-inertial range) and in the presence of large turbulent fluctuations (as seen in reacting systems), it is anticipated that the SFS TRI could be an important contributor to TRI.

In this study, the contributions of SFS TRI are estimated for the flame configurations (flames i, ii, iii, and iv) introduced in Section 6.1. An instantaneous snapshot of the LES/FDF simulation is considered for each of the above flames. The snapshot consists of filtered (resolved) quantities available at the finite-volume cell level and notional particles representing the SFS fluctuations. PMC analysis is carried out (with approximately $220M$ photon bundles) for the frozen LES/FDF fields for three scenarios:

1. No SFS TRI: Emission and absorption are computed based on filtered quantities (denoted as "TRI-1" scenario).

2. Only Emission SFS TRI: Absorption is based on the filtered quantities while emission is based on particle values (denoted by "TRI-2").

3. Full SFS TRI: Both emission and absorption are based on particle quantities (denoted by "TRI-3").

Comparison of radiative emission for scenarios 1 and 3 is indicative of the importance of SFS emission TRI. The significance of SFS absorption TRI can be estimated by comparing scenarios 2 and 3.

For the frozen LES/FDF field of flame (iii) (scaled-up Sandia Flame D), the

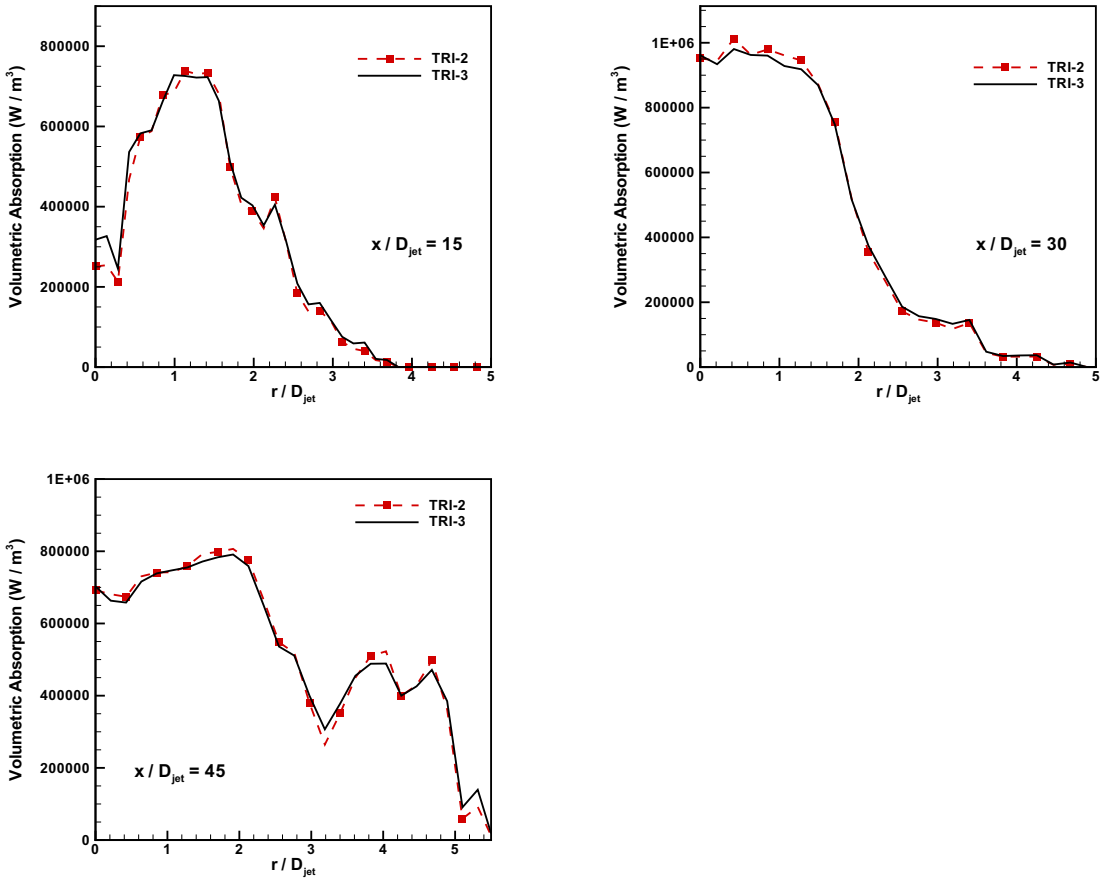

Figure 6.17. Radial profiles of instantaneous volumetric absorption at three axial locations ($x/D_{jet} = 15$, $x/D_{jet} = 30$, and $x/D_{jet} = 45$) for a LES/FDF snapshot of scaled-up Sandia Flame D for different treatments of SFS absorption TRI.

profiles of volumetric radiative absorption along a line in the radial direction at three axial locations are plotted in Fig. 6.17. The plot presents the volumetric absorption for PMC treatment with full SFS TRI (scenario 3) and in the absence of SFS absorption TRI (scenario 2). As seen in the figure, the radiative absorption in the absence of SFS absorption TRI is in excellent agreement with absorption for full SFS TRI, demonstrating that SFS absorption TRI is negligible and can be ignored.

Figure 6.18 presents the variation of volumetric absorption along radial lines at three axial locations for flame (iv) for different treatments of SFS absorption TRI. The radiative absorption in the absence of SFS absorption TRI (TRI-2) is

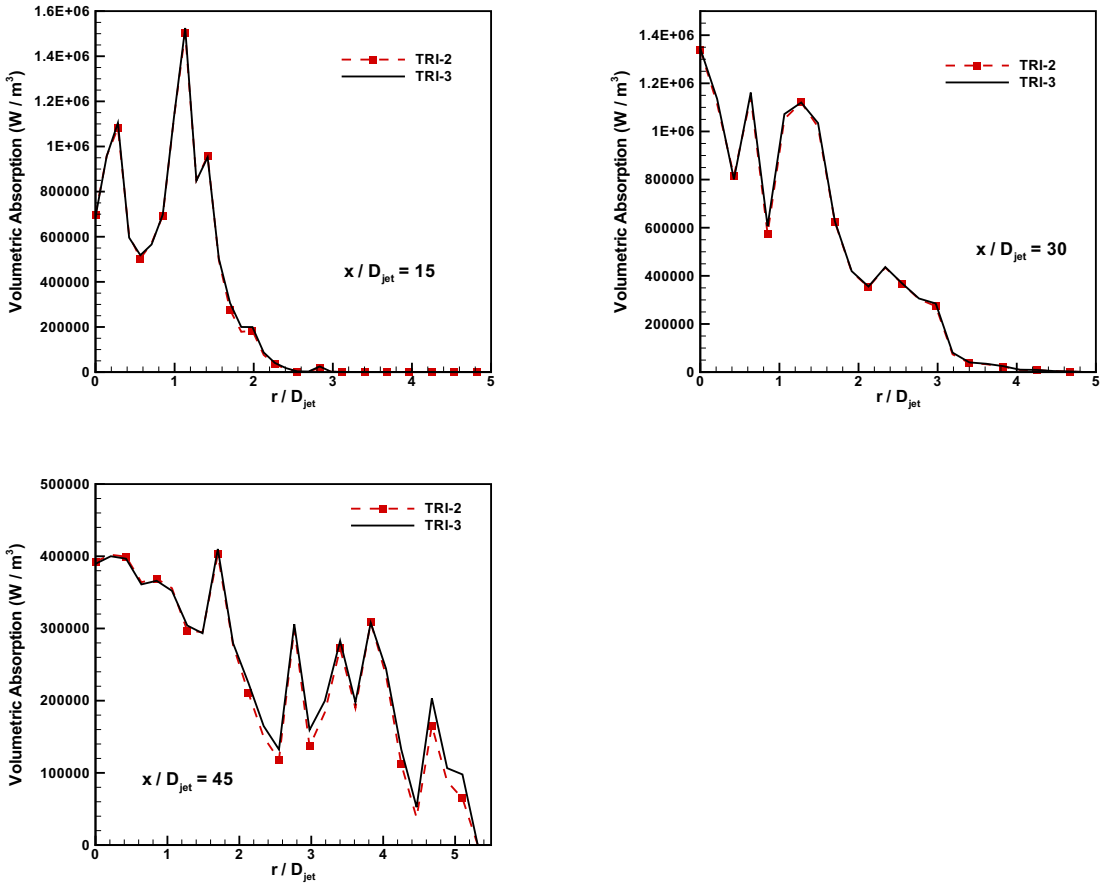

Figure 6.18. Radial profiles of instantaneous volumetric absorption at three axial locations ($x/D_{jet} = 15$, $x/D_{jet} = 30$, and $x/D_{jet} = 45$) for a LES/FDF snapshot of scaled-up Sandia Flame D with artificial soot for different treatments of SFS absorption TRI.

in almost exact agreement with absorption in the presence of SFS absorption TRI (TRI-3) at all three radial locations, thereby indicating the negligible influence of SFS absorption TRI.

To analyze the importance of SFS emission TRI, the volumetric emission for the LES/FDF snapshot is plotted along radial lines (same as the previous plots) in Figs. 6.19 and 6.20. These plots are for flames (iii) and (iv), respectively, where TRI-3 refers to emission in presence of SFS emission TRI and TRI-1 represents emission in the absence of SFS emission TRI. The plots clearly demonstrate that the local radiative emission is underpredicted when SFS fluctuations are neglected (TRI-1), thereby highlighting the importance of SFS emission TRI. The effect of

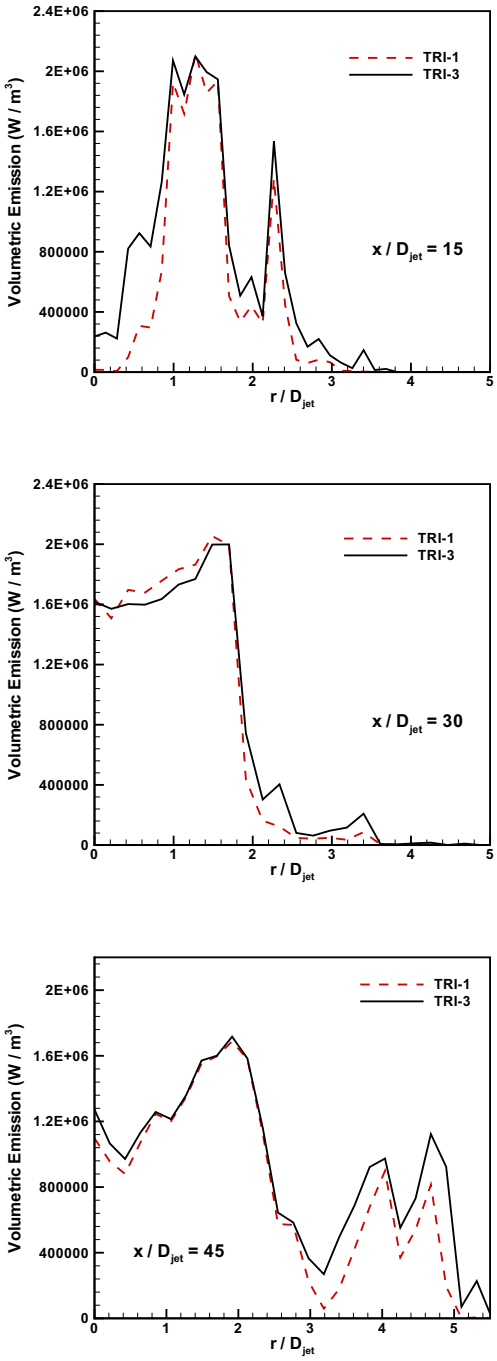

Figure 6.19. Radial profiles of instantaneous volumetric emission at three axial locations (x/D_{jet} = 15, x/D_{jet} = 30, and x/D_{jet} = 45) for a LES/FDF snapshot of scaled-up Sandia Flame D for different treatments of SFS emission TRI.

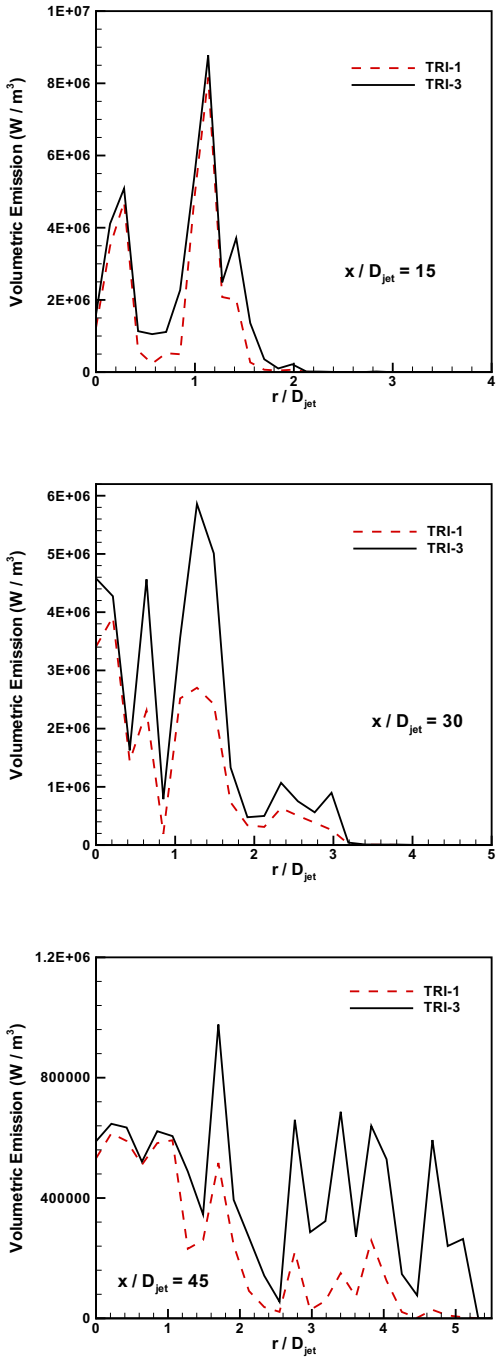

Figure 6.20. Radial profiles of instantaneous volumetric emission at three axial locations (x/D_{jet} = 15, x/D_{jet} = 30, and x/D_{jet} = 45) for a LES/FDF snapshot of scaled-up Sandia Flame D with artificial soot for different treatments of emission SFS TRI.

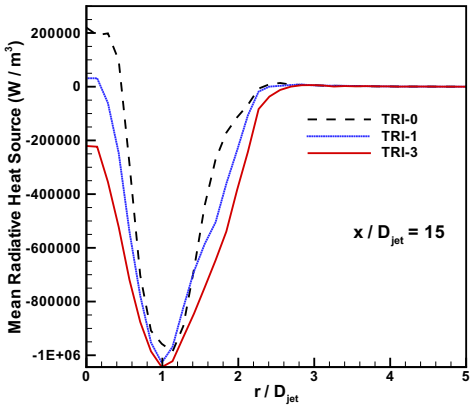

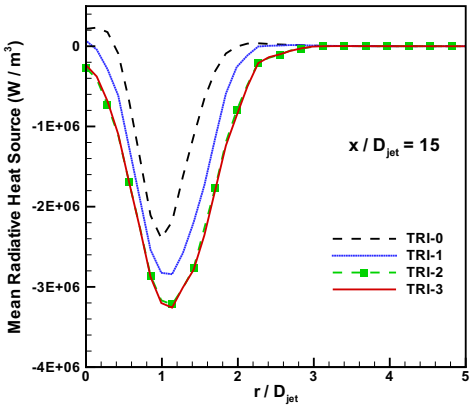

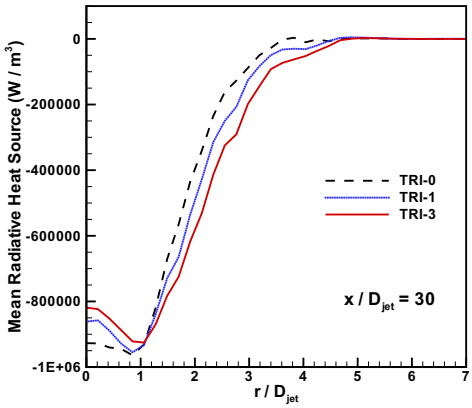

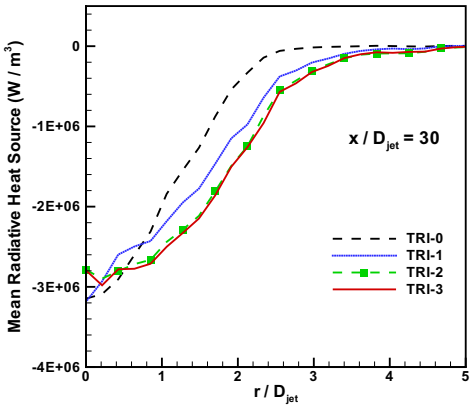

Figure 6.21. Radial profiles of mean radiative heat source at two axial locations (x/D_{jet} = 15 and x/D_{jet} = 30) for scaled-up Sandia Flame D for different treatments of SFS emission TRI.

Figure 6.22. Radial profiles of mean radiative heat source at two axial locations (x/D_{jet} = 15 and x/D_{jet} = 30) for scaled-up Sandia Flame D with artificial soot for different treatments of SFS emission TRI.

SFS emission TRI is more pronounced in flame (iv) due to the presence of soot.

At some locations in the computational domain, local emission in the absence of SFS emission TRI somewhat exceeds the radiative emission for the TRI-3 case. This is possibly due to the opposite effects of fluctuations in temperature and species mass fractions on absorption coefficient as shown in previous studies [41, 212], which might result in lower emission when considering SFS fluctuations (i.e., TRI-3) than computing emission based on filtered values (TRI-1).

Fully-coupled LES/FDF/PMC studies with radiation feedback are carried out next for flames (iii) and (iv) with and without the inclusion of SFS emission TRI

(i.e., TRI-3 and TRI-1 scenarios). To analyze the effect of SFS absorption TRI, a coupled LES/FDF/PMC analysis in the absence of SFS absorption TRI (TRI-2 scenario) is also carried out for flame (iv), which is the most optically thick among all flames considered here. The plots in Figs. 6.21 and 6.22 present the computed mean radiative heat source for flames (iii) and (iv), respectively, for coupled analyses. Here, mean quantities are computed by averaging over time and over the azimuthal direction. The plots also present the mean radiative heat source in the absence of TRI (denoted by "TRI-0"; here radiation calculations are based on mean temperature and mean species concentrations/mass fractions fields) to indicate the relative importance of filter-scale TRI. In accord with our previous observations, these plots also demonstrate the importance of SFS emission TRI and negligible effect of absorption SFS TRI.

The mean temperatures and the differences in the mean temperatures (for different SFS TRI treatments) are shown in Figs. 6.23 and 6.24 for flames (iii) and (iv), respectively. The total radiative heat loss in flame (iii) is underpredicted by approximately 20% when SFS TRI is neglected, resulting in a deviation (albeit small) in mean temperatures, as seen in Fig. 6.23. SFS emission TRI is found to be more important in flame (iv) due to the presence of soot, which leads to overprediction of mean flame temperatures by as much as 60 K, as evident from Fig. 6.24.

Table 6.5 presents the total emission in the computational domain for flames (iii) and (iv) for different treatments of emission TRI. The significant underprediction of emission in the absence of SFS emission TRI is evident from the table, and strongly suggests that it is important to consider SFS emission TRI in LES studies of reacting flows, especially for engineering meshes. This is due to the presence of appreciable SFS fluctuations on engineering meshes, leading to significant SFS emission TRI. This is evident from Fig. 6.25, where mean emission with and without SFS TRI in the computational domain are reordered as a function of local fraction of unresolved turbulence kinetic energy ($\equiv$ SFS turbulent kinetic energy divided by total turbulent kinetic energy). For this purpose, the finite-volume cells in the computational domain are sorted into bins according to the local fraction of the unresolved turbulence kinetic energy, and mean emissions are aggregated over the computational cells in each bin. The mean emission is clearly

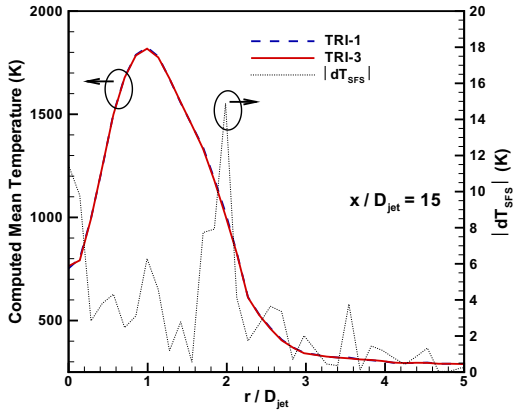

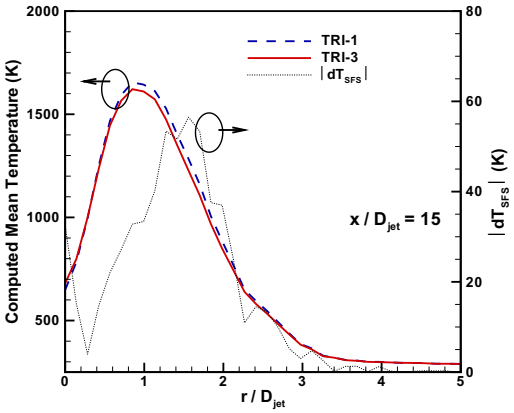

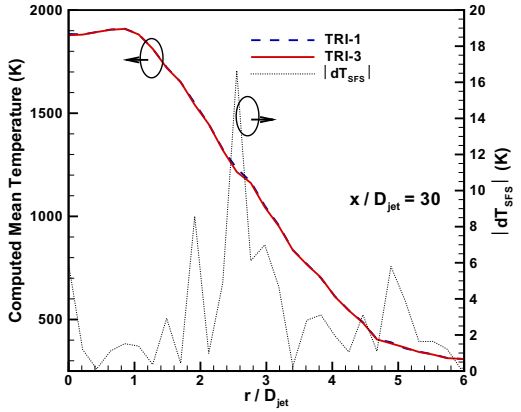

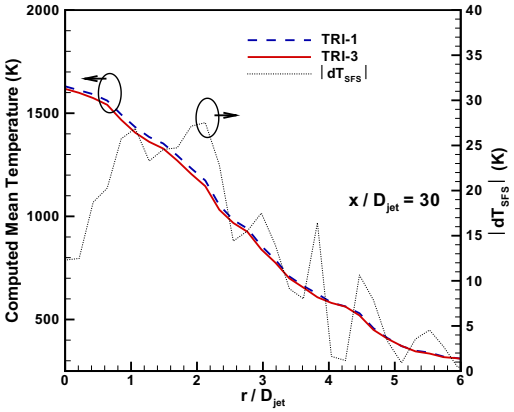

Figure 6.23. Radial profiles of mean temperature at two axial locations ($x/D_{jet} = 15$ and $x/D_{jet} = 30$) for scaled-up Sandia Flame D for different treatments of SFS emission TRI.

Figure 6.24. Radial profiles of mean temperature at two axial locations ($x/D_{jet} = 15$ and $x/D_{jet} = 30$) for scaled-up Sandia Flame D with artificial soot for different treatments of SFS emission TRI.

underpredicted for unresolved turbulence kinetic energy that is 8% and greater of the total turbulence kinetic energy, and the underprediction increases with the increase in the fraction of unresolved turbulence kinetic energy, as demonstrated by the correlation for SFS emission TRI (≡ SFS emission divided by total emission) in Fig. 6.25.

Another important inference from Table 6.5 is that, for "engineering" grids as used here, the contribution of SFS emission TRI is greater than the resolved emission TRI. To investigate this behavior, various correlations ($\kappa_P - T^4$ correlation, κ_P self-correlation, and temperature self-correlation; see Section 3.4.2) that

SFS TRI treatment	scaled-up Sandia Flame D		scaled-up Sandia Flame D with soot	
	Total emission, $\dot{Q}_{emm}$ (kW)	$\frac{\dot{Q}_{emm}}{\dot{Q}_{emm,TRI-3}}$	Total emission, $\dot{Q}_{emm}$ (kW)	$\frac{\dot{Q}_{emm}}{\dot{Q}_{emm,TRI-3}}$
TRI-3	51.68	1	53.61	1
TRI-1	41.49	0.81	39.23	0.73
TRI-0	36.08	0.70	29.06	0.54

Table 6.5. Total radiative emission in the computational domain for different treatments of SFS emission TRI. Here, "TRI-3" denotes emission with SFS TRI and "TRI-1" refers to emission without SFS TRI. "TRI-0" refers to emission based on mean temperature and mean mass fractions (no TRI).

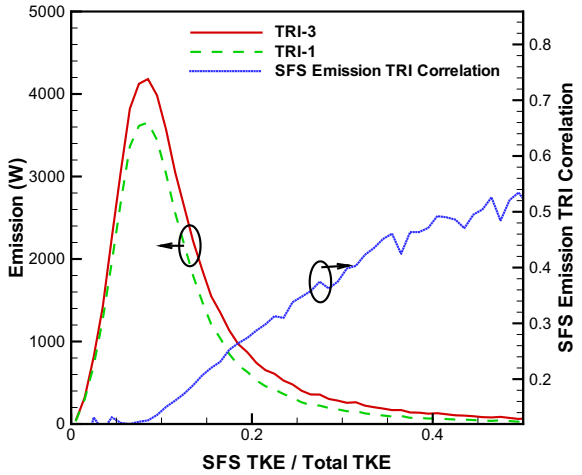

Figure 6.25. Mean emission reordered as a function of the unresolved turbulence kinetic energy for scaled-up Sandia Flame D with and without the consideration of SFS emission TRI.

contribute to resolved-scale and SFS emission TRI are computed for flame (iv) to facilitate better understanding of relative contribution of resolved-scale fluctuations and SFS fluctuations. These correlations are computed via a coupled LES/FDF/PMC analysis of flame (iv) where $4M$ photon bundles are considered at every time step.

Figure 6.26(a) shows the comparison between the resolved-scale and SFS contributions to the $\kappa_P - T^4$ correlation, where radial profiles of the correlation are plotted at the $15D_{jet}$ axial location. The SFS contribution to this correlation exceeds the resolved-scale contribution. This is attributed to the combined effect of two factors: (a) fluctuations in temperature and product mass-fractions are known

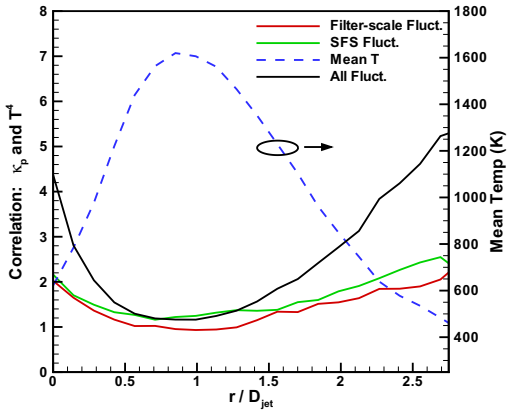

(a) $\kappa_P - T^4$ correlation. This is given by $\left(\frac{\langle\kappa_P(\tilde{T},\tilde{Y})\tilde{T}^4\rangle}{\langle\kappa_P(\tilde{T},\underline{\tilde{Y}})\rangle\langle\tilde{T}^4\rangle}\right)$ for resolved fluctuations, $\left(\frac{\widetilde{\langle\kappa_P T^4\rangle}}{\langle\widetilde{\kappa_P}\rangle\langle\widetilde{T^4}\rangle} * \frac{\langle\kappa_P(\tilde{T},\tilde{Y})\rangle\langle\tilde{T}^4\rangle}{\langle\kappa_P(\tilde{T},\underline{\tilde{Y}})\tilde{T}^4\rangle}\right)$ for SFS fluctuations, and $\frac{\widetilde{\langle\kappa_P T^4\rangle}}{\langle\widetilde{\kappa_P}\rangle\langle\widetilde{T^4}\rangle}$ for all fluctuations. See Table 3.2.

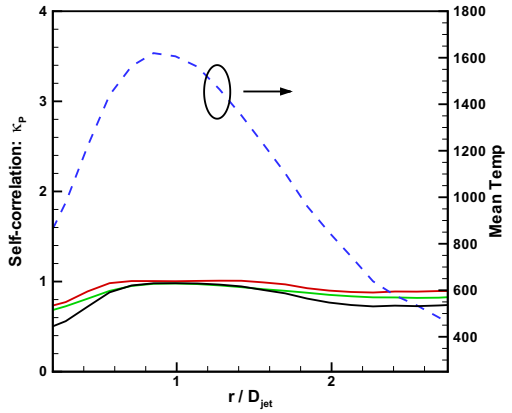

(b) κ_P self-correlation. This is given by $\left(\frac{\langle\kappa_P(\tilde{T},\tilde{Y})\rangle}{\kappa_P(\langle\tilde{T}\rangle,\langle\tilde{Y}\rangle)}\right)$ for resolved fluctuations, $\left(\frac{\langle\widetilde{\kappa_P}\rangle}{\langle\kappa_P(\tilde{T},\underline{\tilde{Y}})\rangle}\right)$ for SFS fluctuations, and $\frac{\langle\widetilde{\kappa_P}\rangle}{\kappa_P(\langle\tilde{T}\rangle,\langle\tilde{Y}\rangle)}$ for all fluctuations. See Table 3.2.

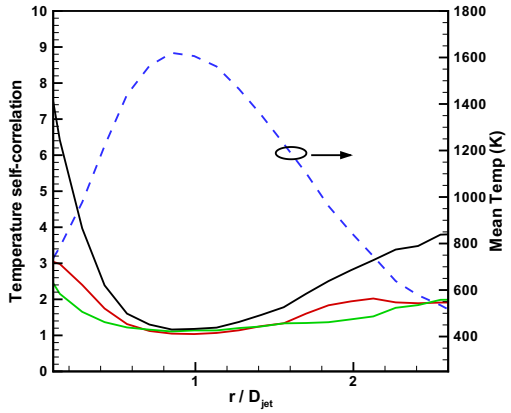

(c) Temperature self-correlation. This is given by $\left(\frac{\langle\tilde{T}^4\rangle}{\langle\tilde{T}\rangle^4}\right)$ for resolved fluctuations, $\left(\frac{\langle\widetilde{T^4}\rangle}{\langle\tilde{T}^4\rangle}\right)$ for SFS fluctuations, and $\frac{\langle\widetilde{T^4}\rangle}{\langle\tilde{T}\rangle^4}$ for all fluctuations. See Table 3.2.

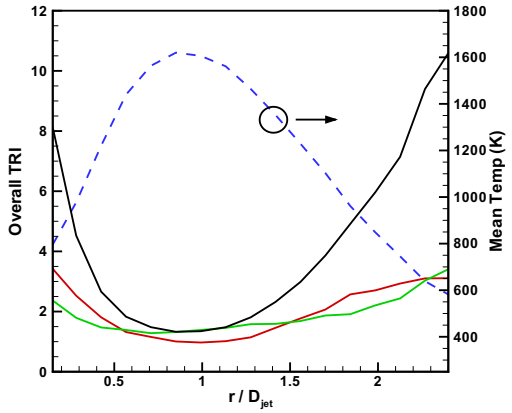

(d) Over-all TRI: (a)*(b)*(c). This is given by $\frac{\langle\kappa_P(\tilde{T},\tilde{Y})\tilde{T}^4\rangle}{\kappa_P(\langle\tilde{T}\rangle,\langle\tilde{Y}\rangle)\langle\tilde{T}\rangle^4}$ for resolved fluctuations, $\frac{\widetilde{\langle\kappa_P T^4\rangle}}{\langle\kappa_P(\tilde{T},\underline{\tilde{Y}})\tilde{T}^4\rangle}$ for SFS fluctuations, and $\frac{\widetilde{\langle\kappa_P T^4\rangle}}{\kappa_P(\langle\tilde{T}\rangle,\langle\tilde{Y}\rangle)\langle\tilde{T}\rangle^4}$ for all fluctuations. See Table 3.2.

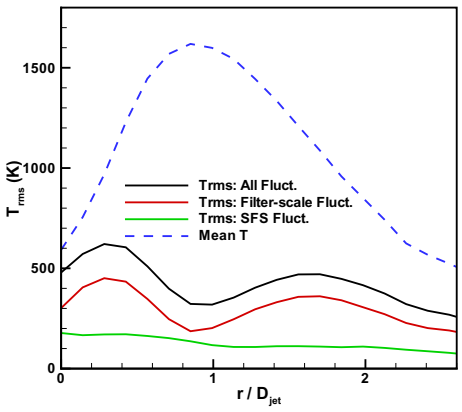

(e) RMS Temperature.

Figure 6.26. Comparison between resolved and SFS components for various contributions to TRI at $x/D_{jet} = 15$ axial location for scaled-up Sandia Flame D with artificial soot. Correlations plotted in this figure are summarized in Table 3.2.

to have an opposite effect on the $\kappa_P - T^4$ correlation, leading to relatively weak resolved-scale correlation even though the resolved-scale fluctuations are strong; and (b) the SFS fluctuations are appreciable in engineering meshes especially at upstream locations for jet flames where significant turbulence exists in shear layers and the jet-core.

The comparison between resolved-scale and SFS contributions to κ_P self-correlation at the $15D_{jet}$ axial location is shown in Fig. 6.26(b). This correlation is less than unity for both resolved-scale and SFS fluctuations, due to the inverse dependence of κ_P on temperature. Also, this correlation for resolved-scale fluctuations is very similar to that for SFS fluctuations.

The radial profiles of temperature self-correlation due to resolved and SFS fluctuations at the $15D_{jet}$ axial location are shown in Fig. 6.26(c). The presence of higher levels of fluctuation at resolved-scale (see Fig. 6.26(e)) leads to higher contribution of resolved-scale fluctuations to the temperature self-correlation.

Figure 6.26(d) compares the overall contribution to TRI for the resolved-scale and SFS fluctuations. Here, the cummulative effect of $\kappa_P - T^4$ correlation, κ_P self-correlation, and temperature self-correlation are plotted for both resolved-scale fluctuations and SFS fluctuations. The SFS contribution to TRI seems to be stronger than the resolved-scale contribution to TRI, for engineering grids used in this research work.

The three correlations and the overall TRI due to resolved-scale and SFS fluctuations are plotted in Figs. 6.27 and 6.28 for axial locations $x/D_{jet} = 30$ and $x/D_{jet} = 45$, respectively. At these axial locations, the turbulent fluctuations are small near the jet centerline (Figs. 6.27(e) and 6.28(e)), leading to relatively low levels of $\kappa_P - T^4$ correlation and temperature self-correlation for both resolved and SFS fluctuations in that region. At locations away from the centerline, the turbulent fluctuations are stronger, leading to significant levels of $\kappa_P - T^4$ self-correlation and temperature self-correlation for both resolved scale and SFS fluctuations (Figs. 6.27(a) and 6.28(a)). The temperature self-correlation for resolved-scale fluctuations is mostly stronger than the correlation for SFS fluctuations as expected since the resolved-scale fluctuations in temperature are stronger than the SFS temperature fluctuations (Figs. 6.27(e) and 6.28(e)). For $\kappa_P - T^4$ correlation, since fluctuations in temperature and product mass fractions have competing

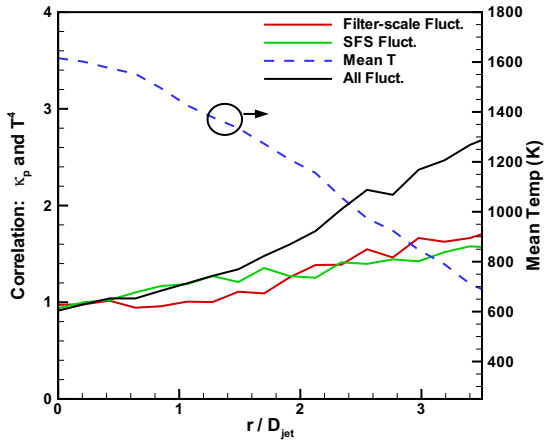

(a) $\kappa_P - T^4$ correlation

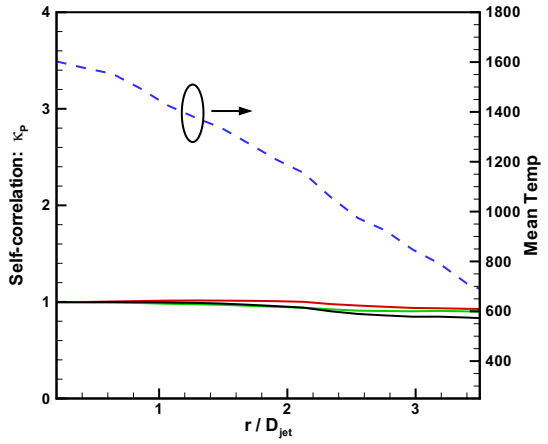

(b) κ_P self-correlation

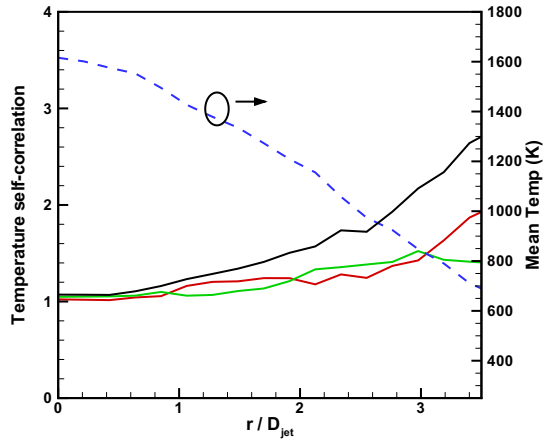

(c) Temperature self-correlation.

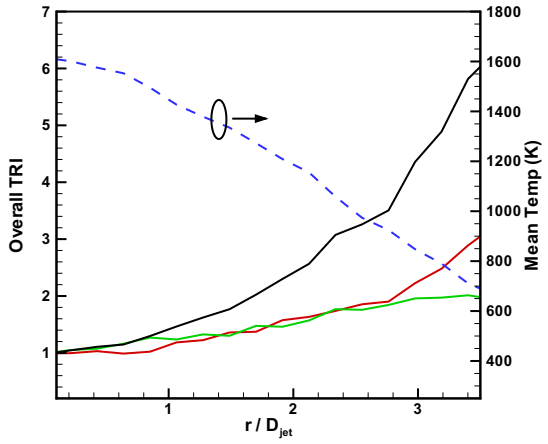

(d) Over-all TRI: (a)*(b)*(c)

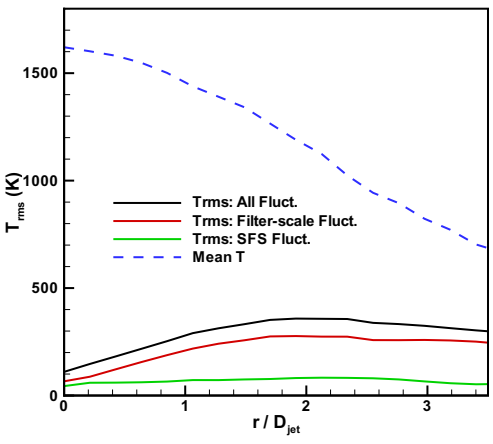

(e) RMS Temperature.

Figure 6.27. Comparison between resolved and SFS components for various contributions to TRI at $x/D_{jet} = 30$ axial location for scaled-up Sandia Flame D with artificial soot. Correlations plotted in this figure are same as Fig. 6.26 and are also summarized in Table 3.2.

effects, the overall effect depends on the relative levels of fluctuations in temperature and product mass fraction and their effect on κ_P. The $\kappa_P - T^4$ correlation due to SFS fluctuations is stronger than the resolved-scale correlation in most of the region, as seen in Figs. 6.27(a) and 6.28(a). The κ_P self-correlation stays in the proximity of unity for both resolved-scale and SFS fluctuations (Figs. 6.27(b) and 6.28(b)).

Overall, the SFS contribution to TRI is greater than the contribution from resolved fluctuations. That is because the overall correlations (plotted in Figs. 6.26(d), 6.27(d), and 6.28(d)) are of about the same magnitude for resolved and SFS fluctuations (red vs. green curves). Since the SFS correlation is with respect to TRI-1 (emission with the effect of resolved fluctuations) and the resolved correlation is with respect to TRI-0 (emission based on mean quantities), the same value of correlation for resolved and SFS fluctuations leads to higher contribution of SFS fluctuations toward emission TRI. Alternatively, the comparison of black (correlation due to both SFS and filter-scale fluctuations) and red (correlation due to filter-scale fluctuations) curves that are with respect to the same reference emission (TRI-0), clearly indicate that the SFS fluctuations have a greater contribution to emission TRI than resolved fluctuations.

SFS emission and absorption TRI are also investigated for flames (i) and (ii). For an instantaneous LES/FDF snapshot of these flames, the radial profiles of volumetric absorption at three axial locations are shown in Figs. 6.29 and 6.30. The trends seen in these plots are consistent with the findings for the other flames discussed above. The SFS absorption TRI is negligible for both the flames.

The ratios of total absorption in the computational domain in the absence of SFS absorption TRI to the total absorption in the presence of SFS TRI for four flames are presented in Table 6.6. The ratio is close to unity for all flames, which further demonstrates the negligible effect of SFS absorption TRI for all flames considered.

Figure 6.31 presents radial profiles of the radiative emission at three axial locations for an instantaneous LES/FDF field for flame (i). Radiative emission computed in the absence of SFS TRI (TRI-1) is compared with the emission with SFS TRI (TRI-3) in these plots. As seen here, the energy emitted in the absence of SFS TRI is significantly underpredicted locally, which again highlights the impor-

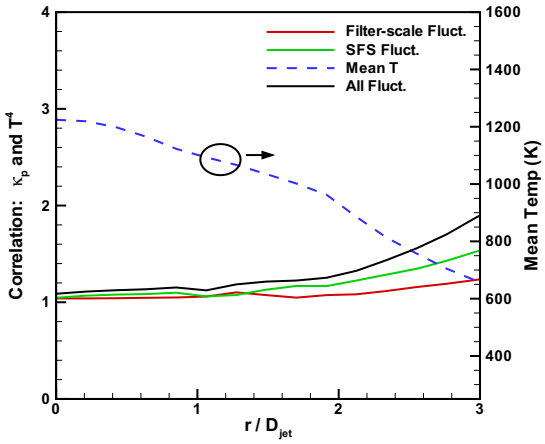

(a) $\kappa_P - T^4$ correlation

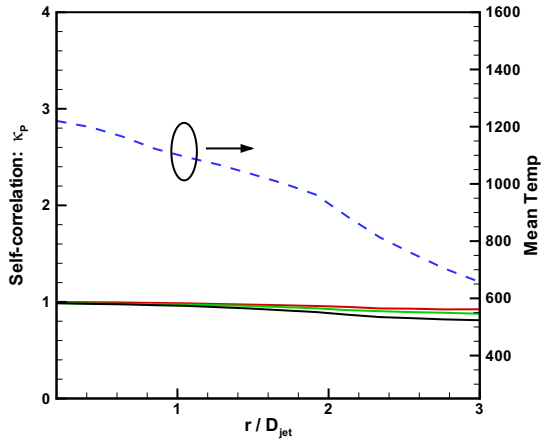

(b) κ_P self-correlation

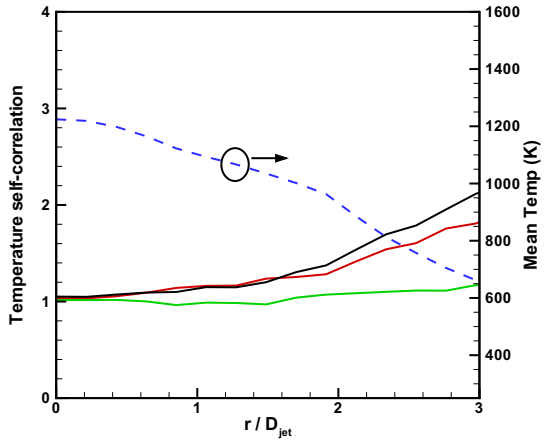

(c) Temperature self-correlation.

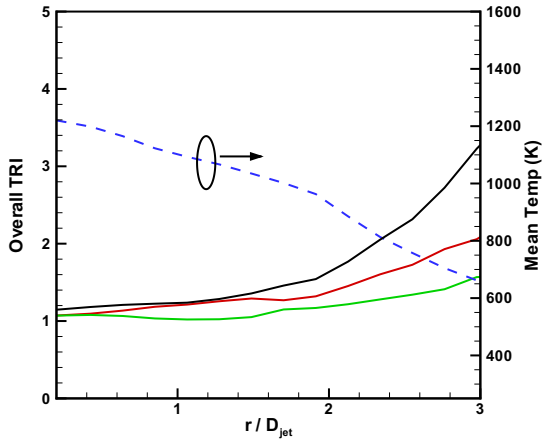

(d) Over-all TRI: (a)*(b)*(c)

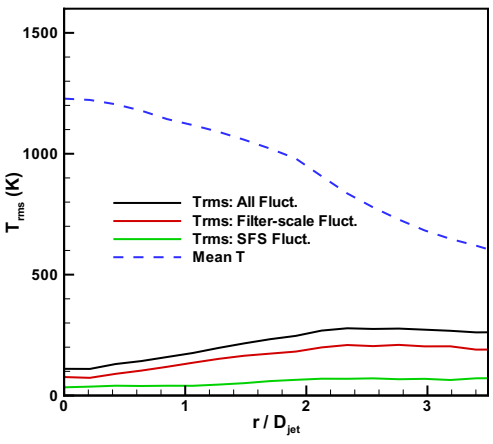

(e) RMS Temperature.

Figure 6.28. Comparison between resolved and SFS components for various contributions to TRI at $x/D_{jet} = 45$ axial location for scaled-up Sandia Flame D with artificial soot. Correlations plotted in this figure are same as Fig. 6.26 and are also summarized in Table 3.2.

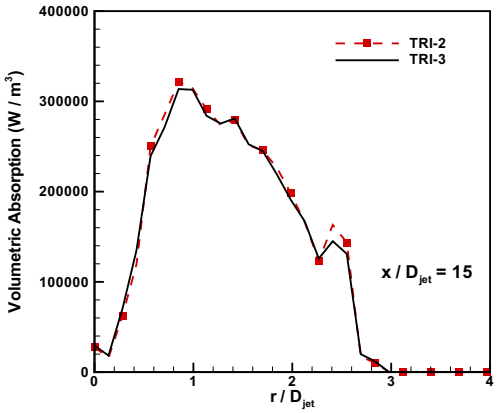

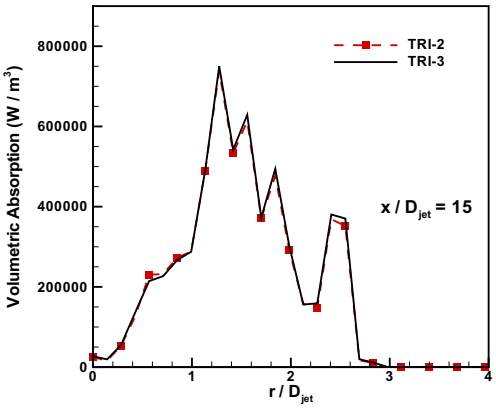

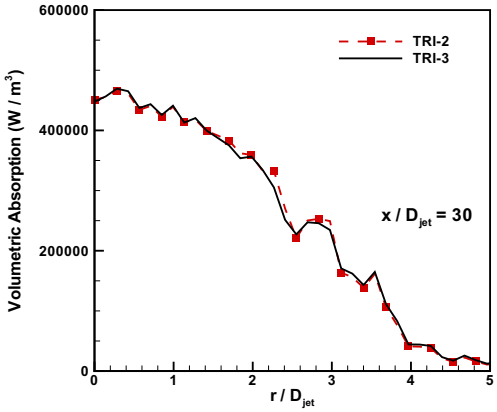

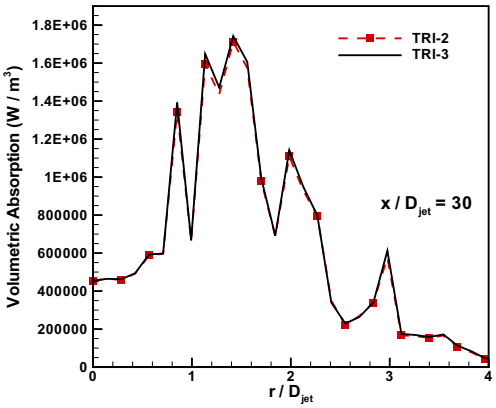

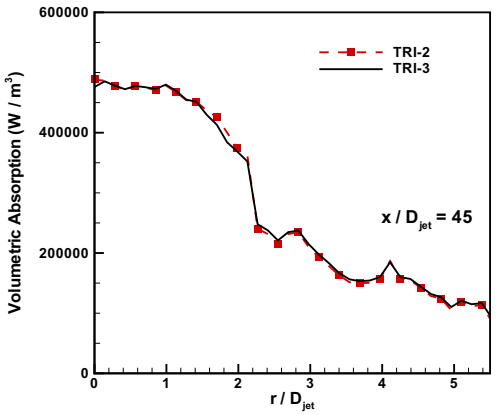

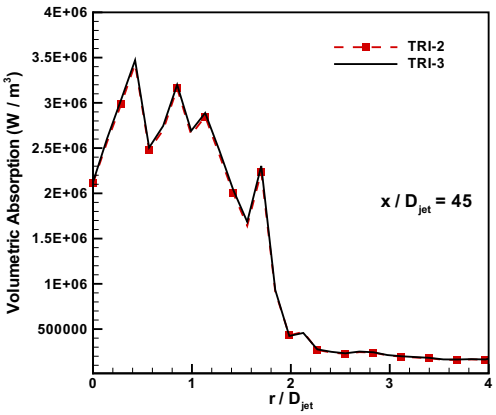

Figure 6.29. Radial profiles of instantaneous volumetric absorption at three axial locations (x/D_{jet} = 15, x/D_{jet} = 30, and x/D_{jet} = 45) for a LES/FDF snapshot of Sandia Flame D for different treatments of SFS absorption TRI.

Figure 6.30. Radial profiles of instantaneous volumetric absorption at three axial locations (x/D_{jet} = 15, x/D_{jet} = 30, and x/D_{jet} = 45) for a LES/FDF snapshot of Sandia Flame D with artificial soot for different treatments of SFS absorption TRI.

Ratio of absorption in the absence of SFS TRI to absorption in the presence of SFS TRI (TRI-2/TRI-3)			
flame (i)	flame (ii)	flame (iii)	flame (iv)
0.989	0.981	0.981	0.978

Table 6.6. Total absorption in the computational domain in the absence of absorption SFS TRI expressed as a fraction of the total absorption in the presence of SFS TRI.

SFS TRI treatment	Sandia Flame D	
	Total emission, Q_{emm} (kW)	$\frac{Q_{emm}}{Q_{emm,TRI-3}}$
TRI-3	1.041	1
TRI-1	0.836	0.80
TRI-0	0.752	0.72

Table 6.7. Total radiative emission in the computational domain for different treatments of SFS TRI. Here, "TRI-3" denotes emission with SFS TRI and "TRI-1" refers to emission without SFS TRI. "TRI-0" refers to emission based on mean temperature and mean mass fractions (no TRI).

tance of considering SFS TRI in computing radiative emission for these engineering meshes. This is further corroborated by the approximately 20% underprediction in the mean total energy emitted in the absence of SFS emission TRI, as reported in Table 6.7. As stated earlier for flames (iii) and (iv), these findings further stress the need to model SFS emission TRI for accurate predictions of radiative emission in engineering LES studies of reacting flows. The total emission based on mean fields (TRI-0) is also presented in Table 6.7. The difference between TRI-1 emission and TRI-0 emission indicates the effect of filter-scale emission TRI. The SFS emission TRI exceeds the resolved-scale emission TRI for flame (i), as noticed earlier for flames (iii) and (iv). The computed radiant fraction (radiative heat loss expressed as a fraction of the heat of combustion of fuel entering the domain) for TRI-3 the scenario is approximately 0.041, which compares well with the experimental value of 0.051 [213], given that the experimental data are for a domain $120D_{jet}$ long whereas the computational domain used in this work is only $70D_{jet}$ long.

For flame (ii), the SFS TRI analysis reveals similar findings as the other flames. The SFS emission TRI is found to be important, leading to an underprediction of approximately 30% in the total emission in its absence. The increase in the underprediction with respect to flame (i) is due to the presence of soot. Soot is

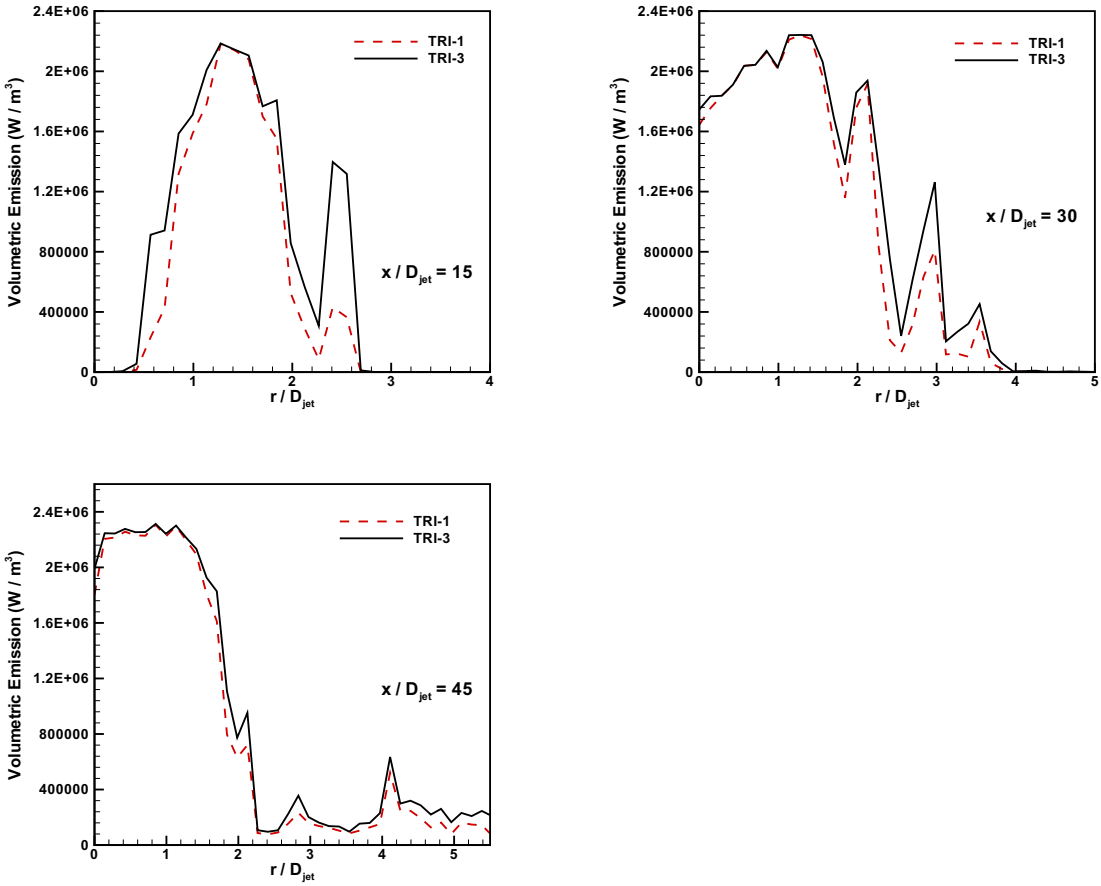

Figure 6.31. Radial profiles of instantaneous volumetric emission at three axial locations ($x/D_{jet} = 15$, $x/D_{jet} = 30$, and $x/D_{jet} = 45$) for a LES/FDF snapshot of Sandia Flame D for different treatments of SFS emission TRI.

a strong emitter of radiation, and neglecting the local SFS fluctuations in soot volume fraction severely underpredicts emission when SFS TRI is not considered.

The investigation presented above to analyze the importance of SFS TRI leads to the conclusion that SFS emission is important for all flame configurations (with and without soot, and optically thin and thick) considered in this study. On the other hand, the SFS absorption is negligible for all flames. The effect of SFS fluctuations on emission is seen to be stronger than the effect of resolved-scale fluctuations for all flames, primarily due to the use of engineering meshes (consequently, significant SFS fluctuations) and the competing effects of temperature fluctuations and product mass fraction fluctuations on absorption coefficient.

6.3 Summary

The statistical uncertainty in the PMC solution in LES/FDF/PMC simulation of statistically stationary systems has been investigated. Four different flame configurations ranging from small, optically thin to large, optically thick were considered. For each configuration, PMC analysis was carried out for different numbers of photon bundles for an instantaneous snapshot of the LES/FDF field. It was found that approximately four photon bundles per finite-volume cell provide radiative solution within $10-15\%$ statistical uncertainty. Fully coupled LES/FDF/PMC analyses were also conducted for two flame configurations, where each configuration was modeled with approximately 4 and 7 photon bundles per cell. For both flames, mean temperature and radiative heat sources are in excellent agreement for different numbers of photon bundles. These findings suggest that statistical uncertainties associated with as few as four photon bundles per finite-volume cell do not affect means and suffice for accurate time-averaged solutions.

The effects of subfilter-scale fluctuations on radiative emission and absorption (i.e., subfilter-scale TRI) also have been investigated for several flame configurations. For each of these flames, radiative emission and absorption were computed in the absence of SFS TRI for an instantaneous LES/FDF field. The SFS absorption TRI was found to be negligible for all flames, whereas the SFS emission TRI was found to be highly important, more so for sooting flames. The SFS fluctuations were responsible for 20% or more of the total emission. In contrast, the resolved-scale fluctuations only contribute to approximately $10-15\%$ of the total emission. This is due to the combined effect of the significant level of SFS fluctuations (mesh resolution used here is representative of engineering meshes) and opposing effects of fluctuations in temperature and product mass fractions on absorption coefficient. The SFS absorption TRI is negligible here. However, since the current model (stochastic-1 particle) for radiative absorption does not incur significant extra cost to model SFS absorption TRI, it is recommended to include the effect of SFS fluctuations on absorption for increased accuracy.

Chapter 7

Summary and Conclusion

Large-eddy simulation is being applied increasingly to address key issues for next-generation combustion systems. In turbulent combustion systems, processes including chemical kinetics, thermal radiation, and turbulence interact closely with each other in highly nonlinear and challenging ways, and these interactions are known to significantly affect the flame structure and pollutant formation. It is important to completely account for TCI, thermal radiation, and TRI for accurate modeling of turbulent combustion. To this end, a hybrid FV-LES/Lagrangian-particle (LES/FDF/PMC) based computational solver has been developed in this work for the analysis of turbulent flames. The formulation completely accounts for TCI and TRI; thermal radiation, absorption TRI and spectral radiation properties are incorporated through a PMC method. Transported FDF methods are one of the most promising methods for treating TCI, and are easily extended to account for emission TRI. Previously proposed PMC schemes that account for absorption TRI assigned additional physical attributes to the notional PDF particles. In this work, a stochastic PMC scheme has been introduced for treating radiation in a turbulent flow field characterized by notional particles. This scheme more strictly adheres to the information that is available in the PDF framework to construct emission and absorption routines. This scheme is simpler to implement, has the same level of accuracy, and is significantly faster than previous schemes.

Validation studies have been conducted for underlying components of the comprehensive LES/FDF/PMC computational solver. The finite-volume LES solver has been validated for cold flow through a canonical co-axial annular-flow combus-

tor. The coupling of the Lagrangian particle solver and the FV solver has been tested in a RAS framework for Sandia Flame D, where the computed mean quantities are in good agreement with experimental data. The computational costs associated with LES/FDF simulations are quite high, and this is exacerbated by the presence of PMC schemes for radiation treatment; effective parallelization strategies are needed. The chemistry calculations can be parallelized quite effectively, but the PMC radiation solver poses a significant challenge for parallelization. In this work, an efficient scheme has been developed for effective parallelization of the LES/FDF/PMC code. The parallel performance of the code has been tested for a challenging configuration where PMC computations dominate the total computational cost. The code demonstrated a speed-up of approximately 85% for a 128-processor run compared to a 16-processor run in the strong scaling limit for this configuration. In the presence of chemistry acceleration routines, the computational cost for chemistry for even detailed chemical mechanisms would be significantly reduced, and the resulting proportions of chemistry and radiation costs should be similar to the configuration considered here for testing the parallel performance of the LES/FDF/PMC code. The accuracy of the LES/FDF/PMC-based computational solver has been demonstrated for Sandia Flame D. The computed mean and rms temperature and species profiles agree well with the experimental data, and show higher fidelity than the computed quantities for FV-LES and RAS/PDF/PMC calculations.

Unlike RAS/PDF/PMC analysis of stationary systems where the PMC solution for thermal radiation at every time-step/iteration need not be highly indicative of the associated RAS/PDF field, the PMC solution needs to well represent the LES/FDF field in the LES/FDF/PMC framework to maintain the transient nature and spatial resolution of the LES solution. This demands that the statistical uncertainty be kept low in the PMC analysis, which in turn requires considering an adequate number of photon bundles. Investigations have been made to assess the statistical uncertainty for various photon bundle sizes for a broad range of flame configurations, ranging from small, optically thin flames to large, sooting flames. Findings from this exercise indicate that approximately four photon bundles per FV cell lead to an uncertainty level of $10-15\%$ and are sufficient to predict accurate means for the configurations considered here. This result is encouraging, since

the PMC solver used in this study is among the most accurate radiation solvers available to date, and the computational cost associated with this PMC analysis with four photon bundles per FV cell is a small fraction of the chemistry cost for a semi-detailed chemical mechanism. The low cost of this PMC method is a result of careful consideration of the emission, absorption, and tracing schemes together with analysis of the optimum number of photon bundles and parallelization strategies. Further investigations need to be made to analyze the effect of statistical uncertainty on higher-order statistics.

In LES, since large scales are explicitly modeled, the large-scale contributions to the emission and absorption TRI are captured in the solution. The effects of subfilter-scale fluctuations and their interactions with resolved scales need to be modeled in the filtered emission and absorption terms. The SFS emission TRI can be completely accounted for through a transported FDF, or can be closed in a manner similar to those that have been used for the filtered chemical source terms. The SFS absorption TRI is usually neglected via the OTFA assumption. Here SFS absorption TRI has been modeled through a PMC solver. The importance of SFS emission and absorption TRI has been assessed in this study for a wide range of flames. Soot is artificially introduced through a state relationship. For the several flames considered in this study, the SFS emission TRI was found to be significantly important. The importance of SFS emission TRI has been attributed to the fact that unresolved (subfilter) velocity fluctuations contribute to approximately 15% of the total turbulent kinetic energy in the computational domain for these flames, leading to appreciable levels of SFS emission. This level of contribution of unresolved fluctuations toward the total turbulent kinetic energy is typical of engineering and research meshes that have been used for LES, and therefore the findings from this study show the need to model SFS emission. The effect of SFS emission is more pronounced in the presence of soot, since soot is a strong emitter and estimation based on the filtered quantities (i.e., in the absence of SFS TRI) significantly underpredicts the emission due to ignoring the strong subfilter-scale soot fluctuations. The SFS absorption TRI is found to be negligible for all flames and, therefore, establishes the validity of OTFA for LES simulations. Nevertheless, with the algorithms that have been developed here, SFS absorption TRI can be included with little increase in overall simulation cost.

7.1 Recommendations for Future Work

The LES/FDF studies conducted in this work have exhibited sensitivity to the mixing model coefficient used in the Lagrangian FDF procedure to model molecular mixing. Also, a relatively high value of the coefficient has been used; the mixing model coefficient has been set to 6 for LES/FDF versus 4 for RAS/PDF simulations. Other LES/FDF studies reported in the literature have also used a high value of the coefficient for a similar mixing model. These mixing models do not account for particles' (un)proximity in the composition space, leading to the unphysical occurrence of mixing of particles across flame sheet. It is recommended to incorporate a better model for molecular mixing such as EMST [137] that mixes particles based on their distance in composition space. Furthermore, to address the sensitivity of the mixing model coefficient, a dynamic procedure [214] can be implemented to calculate the local value of the coefficient rather than prescribing it directly.

Combustion systems often produce soot particles, and it is important to account for soot in a detailed manner for accurate numerical predictions of these systems. Soot formation/destruction is governed by complex physical and chemical processes, and these processes are tightly coupled with gas-phase chemical kinetics. Soot is also a strong emitter and absorber of thermal radiation and plays an important role in thermal radiation and TRI [36]. Therefore, detailed models for soot need to be considered for accurate representation of chemical kinetics and thermal radiation. The method of moments [215, 216] is one such model that has already been implemented in the context of RAS/PDF methods [36, 217–219], and will be extended to LES/FDF framework presented here to accurately account for soot. The detailed soot model can also be utilized to confirm that the strong SFS fluctuations in soot, as seen in this work, are physical and not an artifact of the simple state-relationship-based soot model.

In LES/FDF/PMC and RAS/PDF/PMC simulations, it is extremely expensive computationally to incorporate detailed chemical mechanisms to model chemical kinetics since a large number of stiff ODE's corresponding to reaction rates for chemical species have to be integrated for each notional particle at each time step. Detailed models for soot require detailed gas-phase chemistry which makes

LES/FDF/PMC computationally expensive for sooting systems. This issue can be addressed via chemistry acceleration algorithms such as ISAT [208] and DOLFA [52], which are based on storage/retrieval concepts. Implementation of such a procedure is highly recommended for LES/FDF/PMC analysis of nonsooting and sooting systems, and constitutes a key improvement for the future.

Another suggested modification is to extend the existing LES/FDF/PMC solver [10, 111, 140, 220, 221] to account for combustion of liquid fuel sprays. That requires Lagrangian tracking of liquid fuel droplets with a size distribution that evolves in the computational domain as a result of atomization, droplet evaporation, secondary break-up, and wall-droplet interaction. Spray modeling has been an active area of research for quite some time, and a large number of models has been proposed for various physical processes encountered in sprays. Spray models are already available in OpenFOAM and the LES/FDF/PMC code needs to be modified appropriately to account for the interaction of gas-phase species with liquid droplets.

To fully understand the effect of statistical uncertainties in the PMC solution in LES/FDF/PMC simulations, higher-order statistics (one-point and two-point correlations in space/time) need to be investigated. This will help determine the optimum number of photon bundles required for LES/FDF/PMC simulations.

The parallelization strategy devised here is implemented in a semi-automated manner, where precomputations are conducted for a short period of time to obtain the computational cost map in the domain, which is then used for domain-decomposition. It is recommended that this process be automated and implemented as an adaptive strategy to perform domain-decomposition on-the-fly based on the evolving computational cost map in the domain.

With SFS absorption TRI shown to be negligible and SFS emission TRI modeled via FDF, it is recommended to incorporate deterministic RTE solvers such as spherical harmonics or discrete ordinates method in the LES/FDF framework, which promises to offer similar computational accuracy as PMC but at a lower computational cost.

Bibliography

[1] U.S. Environmental Protection Agency, July 2011. EPA and NHTSA, in Coordination with California, Announce Plans to Propose Greenhouse Gas and Fuel Economy Standards for Passenger Cars and Light Trucks. EPA-420-F-11-027. Available at http://www.epa.gov/otaq/climate/420f11027.pdf.

[2] U.S. Environmental Protection Agency, July 2011. EPA Proposed NOx Emission Standards for Aircraft Gas Turbine Engines. EPA420-F-11-019. Available at http://www.epa.gov/otaq/regs/nonroad/aviation/420f11019.pdf.

[3] Euro 5 and Euro 6 Standards: Reduction of Pollutant Emissions From Light Vehicles. Available at http://europa.eu/legislation_summaries/environment/air_pollution/l28186_en.htm.

[4] U.S. Environmental Protection Agency. Regulation and Standards. Availble at http://www.epa.gov/otaq/climate/regulations.htm#prez and http://www.epa.gov/otaq/aviation.htm.

[5] H. Pitsch, Improved Pollutant Predictions in Large-Eddy Simulations of Turbulent Non-Premixed Combustion by Considering Scalar Dissipation Rate Fluctuations, *Proc. Combust. Inst.* 29, 1971–1978 (2002).

[6] V. Raman, H. Pitsch and R. O. Fox, Hybrid Large Eddy Simulation/Lagrangian Filtered Density Function Approach for Simulating Turbulent Combustion, *Comb. Flame* 143, 56–58 (2005).

[7] M. R. H. Sheikhi, T. G. Drozda, P. Givi, F. A. Jaberi and S. B. Pope, Large

Eddy Simulation of a Turbulent Nonpremixed Piloted Methane Jet Flame (Sandia Flame D), *Proc. Combust. Inst.* 30, 549–556 (2005).

[8] L. Selle, G. Lartigue, T. Poinsot, R. Koch, K.-U. Schildmacher, W. Krebs, B. Prade, P. Kaufmann and D. Veynante, Compressible Large-Eddy Simulation of Turbulent Combustion in Complex Geometry on Unstructured Meshes, *Comb. Flame* 137, 489–505 (2004).

[9] P. Moin and S. V. Apte, Large-Eddy Simulation of Realistic Gas Turbine Combustors, *AIAA Paper No. AIAA-2004-330*, (2004).

[10] S. James, J. Zhu and M. S. Anand, Large-Eddy Simulations of Gas Turbine Combustors, *AIAA Paper no. 2005-0552*, (2005).

[11] P. Flohr, CFD Modeling for Gas Turbine Combustors, In *Turbulent Combustion* (Edited by L. Vervisch, D. Veynante and J. P. A. J. Van Beeck), von Karman Institute for Fluid Dynamics Lecture Series 2005-02, Rhode-Saint-Genèse, Belgium (March 2005).

[12] I. Celik, I. Yavuz and A. Smirnov, Large-Eddy Simulations of In-Cylinder Turbulence for IC Engines: A Review, *Internl. J. Engine Res.* 2, 119–148 (2001).

[13] D. C. Haworth, A Review of Turbulent Combustion Modeling for Multidimensional In-Cylinder CFD, *SAE Transactions, Journal of Engines*, 899–928 (2005).

[14] S. Richard, O. Colin, O. Vermorel, A. Benkenida, A. Angelberger and D. Veynante, Towards Large-Eddy Simulation of Combustion in Spark-Ignition Engines, *Proc. Combust. Inst.* 31, 3059–3066 (2007).

[15] D. Veynante and L. Vervisch, Turbulent Combustion Modeling, *Progr. Energy Combust. Sci.* 28 (3), 193–266 (2002).

[16] R. O. Fox, *Computational Models for Turbulent Reacting Flows*, Cambridge University Press, Cambridge (2003).

[17] T. Poinsot and D. Veynante, *Theoretical and Numerical Combustion* (2nd Edn), R.T. Edwards, Inc., (2005).

[18] P. J. Colucci, F. A. Jaberi, P. Givi and S. B Pope, Filtered Density Function for Large Eddy Simulation of Turbulent Reacting Flows, *Phys. Fluids* 10, 499–515 (1998).

[19] F. A. Jaberi, P. J. Colucci, S. James, P. Givi and S. B. Pope, Filtered Mass Density Function for Large-Eddy Simulation of Turbulent Flows, *J. Fluid Mech.* 401, 85–122 (1999).

[20] M. R. H. Sheikhi, T. G. Drozda, P. Givi and S. B. Pope, Velocity-Scalar Filtered Density Function for Large Eddy Simulation of Turbulent Flows, *Phys. Fluids* 15, 2321–2337 (2003).

[21] V. Raman, H. Pitsch and R. O. Fox, Eulerian Transported Probability Density Function Sub-Filter Model for Large-Eddy Simulations of Turbulent Combustion, *Combustion Theory and Modelling* 10, 439–458 (2006).

[22] V. Raman and H. Pitsch, A Consistent LES/Filtered-Density Function Formulation for the Simulation of Turbulent Flames with Detailed Chemistry, *Proc. Combust. Inst.* 31(2), 1711–1719 (2007).

[23] S. James, J. Zhu and M. S. Anand, Large Eddy Simulations of Turbulent Flames Using the Filtered Density Function Model, *Proc. Combust. Inst.* 31(2), 1737–1745 (2007).

[24] A. A. Townsend, The Effects of Radiative Transfer on Turbulent Flow of a Stratified Fluid, *J. Fluid Mech.* 4, 361–375 (1958).

[25] T.H. Song and R. Viskanta, Interaction of Radiation with Turbulence: Application to a Combustion System, *J. Thermoph. Heat Transfer* 1, 56–62 (1987).

[26] A. Soufiani, P. Mignon and J. Taine, Radiation–Turbulence Interaction in Channel Flows of Infrared Active Gases, In *Proceedings of the International Heat Transfer Conference*, Vol. 6, pp. 403–408, ASME (1990).

[27] J. P. Gore and G. M. Faeth, Structure and Spectral Radiation Properties of Turbulent Ethylene/Air Diffusion Flames, In *Twenty-First Symposium (International) on Combustion*, pp. 1521–1531, The Combustion Institute (1986).

[28] J. P. Gore and G. M. Faeth, Structure and Spectral Radiation Properties of Luminous Acetylene/Air Diffusion Flames, *J. Heat Transfer* 110, 173–181 (1988).

[29] M. E. Kounalakis, J. P. Gore and G. M. Faeth, Turbulence/Radiation Interactions in Nonpremixed Hydrogen/Air Flames, In *Twenty-Second Symposium (International) on Combustion*, pp. 1281–1290, The Combustion Institute (1988).

[30] M. E. Kounalakis, Y. R. Sivathanu and G. M. Faeth, Infrared Radiation Statistics of Nonluminous Turbulent Diffusion Flames, *J. Heat Transfer* 113(2), 437–445 (1991).

[31] G. M. Faeth, J. P. Gore, S. G. Shuech and S. M. Jeng, Radiation from Turbulent Diffusion Flames, *Ann. Rev. Numer. Fluid Mech. Heat Trans.* 2, 1–38 (1989).

[32] P. J. Coelho, Detailed Numerical Simulation of Radiative Transfer in a Nonluminous Turbulent Jet Diffusion Flame, *Comb. Flame* 136, 481–492 (2004).

[33] L. Tessé, F. Dupoirieux and J. Taine, Monte Carlo Modeling of Radiative Transfer in a Turbulent Sooty Flame, *Int. J. Heat Mass Transfer* 47, 555–572 (2004).

[34] S. Mazumder and M. F. Modest, A PDF Approach to Modeling Turbulence–Radiation Interactions in Nonluminous Flames, *Int. J. Heat Mass Transfer* 42, 971–991 (1999).

[35] G. Li and M. F. Modest, Application of Composition PDF Methods in the Investigation of Turbulence–Radiation Interactions, *J. Quant. Spectrosc. Radiat. Transfer* 73(2–5), 461–472 (2002).

[36] R. S. Mehta, *Modeling of Soot Formation and Turbulence–Radiation Interactions in Turbulent Jet Flames*, PhD thesis, The Pennsylvania State University, (2008).

[37] A. Wang, *Investigation of Turbulence–Radiation Interactions in Turbulent Flames Using a Hybrid FVM/Particle-Photon Monte Carlo Approach*, PhD thesis, The Pennsylvania State University, University Park, PA, (2007).

[38] A. Wang, Modest. M. F., Haworth. D. C. and L. Wang, Monte Carlo Simulation of Radiative Heat Transfer and Turbulence Interactions in Methane/Air Jet Flames, *J. Quant. Spectrosc. Radiat. Transfer* 109(2), 269–279 (2008).

[39] R. S. Mehta, A. Wang, M. F. Modest and D. C. Haworth, Modeling of a Turbulent Ethylene/Air Flame Using Hybrid Finite Volume/Monte Carlo Methods, Proceedings of CHT-08, ICHMT International Symposium on Advances in Computational Heat Transfer,May 11–16, 2008, Marrakech, Morocco, (2008).

[40] A. J. Chandy, D. J. Glaze and S. H. Frankel, Mixing Models and Turbulence–Radiation Interactions in Non-Premixed Jet Flames via the LES/FMDF Approach, In *5th US Combustion Meeting, San Diego, CA, March 25–28*, (2007).

[41] A. Gupta, M. F. Modest and D. C. Haworth, Large-Eddy Simulation of Turbulence–Radiation Interactions in a Turbulent Planar Channel Flow, *J. Heat Transfer* 131 (6), 061704–1–8 (2009).

[42] M. Roger, C. B. Da Silva and P. J. Coelho, Analysis of the Turbulence-Radiation Interactions for Large Eddy Simulations of Turbulent Flows, *Int. J. Heat Mass Transfer* 52, 2243–2254 (2009).

[43] M. Roger, P. J. Coelho and C. B. Da Silva, The Influence of the Non-Resolved Scales of Thermal Radiation in Large Eddy Simulation of Turbulent Flows: A Fundamental Study, *Int. J. Heat Mass Transfer* 53, 2897–2907 (2010).

[44] M. Roger, P. J. Coelho and C. B. Da Silva, Relevance of the Subgrid-Scales for Large Eddy Simulations of Turbulence-Radiation Interactions in a Turbulent Plane Jet, *J. Quant. Spectrosc. Radiat. Transfer* 112, 1250–1256 (2011).

[45] S. R. Turns, *An Introduction to Combustion: Concepts and Applications* (2nd Edn), McGraw-Hill, (2000).

[46] G. P. Smith, D. M. Golden, M. Frenklach, N. W. Moriarty, B. Eiteneer, M. Goldenberg, C. T. Bowman, R. Hanson, S. Song, W. C. Gardiner, V. Lissianski and Z. Qin, GRI-Mech 3.0, (1999), Available at http://www.me.berkeley.edu/gri_mech.

[47] Reduced Kinetic Mechanisms and Asymptotic for Methane-Air Flames, In *Lecture Notes in Physics 384* M. D. Smooke (Editors), Springer-Verlag, Berlin (1991).

[48] N. Peters and B. Rogg, Reduced Kinetic Mechanisms for Application in Combustion, In *Lecture Notes in Physics Monograph 15*, Springer-Verlag, Berlin (1993).

[49] J. Y. Chen, Development of Reduced Mechanisms for Numerical Simulation of Turbulent Combustion, In *Workshop on Numerical Aspects of Reduction in Chemical Kinetics*, Center d'Enseignement et de Recherche en Mathematiques, Informatique et Calcul Scientifique, Ecole Nationale des Ponts et Chaussees (September 1997).

[50] J. Y. Chen, K. Kollmann and R. W. Dibble, PDF Modeling of Turbulent Nonpremixed Methane Jet Flames, *Comb. Sci. T.* 64, 315–346 (1989).

[51] S. B. Pope, Computationally Efficient Implementation of Combustion Chemistry Using in situ Adaptive Tabulation, *Combust. Theory& Modeling* 1, 41–63 (1997).

[52] I. Veljkovic, P. Plassmann and D. C. Haworth, A Scientific On-Line Database for Efficient Function Approximation, In *Computational Science and Its Applications—ICCSA 2003, The Springer Verlag Lecture Notes in Computer Science (LNCS 2667), Part I*, (2003).

[53] G. Li and M. F. Modest, Investigation of Turbulence–Radiation Interactions in Reacting Flows Using a Hybrid FV/PDF Monte Carlo Method, In *Proceedings of the ICHMT 3rd International Symposium on Radiative Transfer* (Edited by M. P. Mengüç and N. Selçuk), Antalya, Turkey (2001).

[54] Y. Z. Zhang, *Hybrid particle/finite-volume PDF methods for three-dimensional time-dependent flows in complex geometries*, PhD thesis, The Pennsylvania State University, University Park, PA, (2004).

[55] J. Appel, H. Bockhorn and M. Frenklach, Kinetic Moldeing of Soot Formation with Detailed Chemistry and Physics: Laminar Premixed Flames of C_2 Hydrocarbons, *Comb. Flame* 121, 122–136 (2000).

[56] S. B. Pope, *Turbulent Flows*, Cambridge University Press, Cambridge (2000).

[57] R. D. Moser, J. Kim and N. N. Mansour, Direct Numerical Simulation of Turbulent Channel Flow up to Re_τ=590, *Phys. Fluids* 11 (4), 943–945 (1999).

[58] B. Debusschere and C. J. Rutland, Turbulent Scalar Transport Mechanisms in Plane Channel and Couette Flows, *Int. J. Heat Mass Transfer* 47, 1771–1781 (2004).

[59] B. Bedat, F. N. Egolfopoulos and T. Poinsot, Direct Numerical Simulation of Heat Release and NOx Formation in Turbulent Nonpremixed Flames, *Comb. Flame* 119 (1), 69–83 (1999).

[60] E. R. Hawkes, R. Sankaran, J. C. Sutherland and J. H. Chen, Scalar Mixing in Direct Numerical Simulations of Temporally Evolving Plane Jet Flames with Skeletal CO/H_2 Kinetics, *Proc. Combust. Inst.* 31 (1), 1633–1640 (2007).

[61] A. Juneja and S. B. Pope, A DNS Study of Turbulent Mixing of Two Passive Scalars, *Phys. Fluids* 8, 2161–2184 (1996).

[62] D. C. Haworth and T. J. Poinsot, Numerical Simulations of Lewis Number Effects in Turbulent Premixed Flames, *Comb. Flame* 104, 111–137 (1996).

[63] M. Ulitsky, C. Ghenaï, I. Gökalp, L. P. Wang and L. R. Collins, Comparison of a Spectral Model for Premixed Turbulent Flame Propagation to DNS and Experiments, *Combust. Theory and Modelling* 4, 241–264 (2000).

[64] B. E. Launder and D. B. Spalding (Editors), *Lectures in Mathematical Models of Turbulence*, Academic Press, London, England (1972).

[65] P. Spalart and S. Allmaras, A One-Equation Turbulence Model for Aerodynamic Flows, Technical Report AIAA92-0439, American Institute of Aeronautics and Astronautics, (1992).

[66] D. C. Wilcox, *Turbulence Modeling for CFD*, DCW Industries, Inc., La Canada, California (1998).

[67] B. E. Launder, G. J. Reece and W. Rodi, Progress in the Development of a Reynolds-Stress Turbulence Closure, *J. Fluid Mech.* 68 (3), 537–566 (1975).

[68] B. E. Launder, Second Moment Closure: Present... and Future?, *Int. J. Heat Fluid Flow* 10 (4), 282–300 (1989).

[69] B. E. Launder and M. M. Gibson, Ground Effects on Pressure Fluctuations in the Atmospheric Boundary Layer, *J. Fluid Mech.* 86, 491–511 (1978).

[70] D. A. Johnson, F. R. Menter and Rumsey C. L., The Status of Turbulence Modelling for External Aerodynamics, Technical Report AIAA94-2226, American Institute of Aeronautics and Astronautics, (1994).

[71] I. P. Castro and E. Epik, Boundary Layer Development After a Separated Region, *J. Fluid Mech.* 374, 91–116 (1998).

[72] S. Obi, K. Aoki and S. Masuda, Experimental and Computational Study of Turbulent Separating Flow in an Asymmetric Plane Diffuser, In *9th Symposium on Turbulent Shear Flows, vol. 3, Kyoto, Japan, August 16-19*, (1993).

[73] C. U. Buice and J. K. Eaton, Experimental Investigation of Flow Through an Asymmetric Plane Diffuser, Technical Report Report No. TSD-107, Dept of Mech. Eng, Stanford University, USA, (1997).

[74] A. Hellsten and P. Rautaheimo, In *8th ERCOFTAC/IAHC/COST Workshop on Refined Turbulence Modelling, Report 127*, (1999).

[75] W. Rodi, Comparison of LES and RANS Calculations of the Flow Around Bluff Bodies, *J. Wind Engg. Industrial Aero.* 69-71, 55–75 (1997).

[76] K. R. Mcmanus, T. Poinsot and S. M. Candel, A Review of Active Control of Combustion Instabilities, *Progr. Energy Combust. Sci.* 19(1), 1–29 (1993).

[77] S. Koshigoe, T. Komatsuzaki and V. Yang, Adaptive Control of Combustion Instability with On-Line System Identification, *J. Propul. Power* 15(3), 383–389 (1999).

[78] B. Vreman, B. Geurts and H. Kuerten, Subgrid-Modelling in LES of Compressible Flow, *Applied Scientific Research* 54(3), 191–203 (1995).

[79] W. Sutherland, The Viscosity of Gases and Molecular Force, *Philosophical Magazine* S. 5(36), 507–531 (1893).

[80] J. Smagorinsky, General Circulation Experiments With the Primitive Equations. I. The Basic Experiment, *Mon. Weather Review* 91 (3), 99–164 (1963).

[81] A. Yoshizawa, Statistical Theory for Compressible Turbulent Shear Flows, with the Application to Subgrid Modeling, *Phys. Fluids* 29(7), 2152–2164 (1986).

[82] L. Y. M. Gicquel, P. Givi, F. A. Jaberi and S. B. Pope, Velocity Filtered Density Function for Large Eddy Simulation of Turbulent Flows, *Phys. Fluids* 14, 1196–1213 (2002).

[83] J. W. Deardorff, Three-Dimensional Numerical Study of the Height and Mean Structure of a Heated Planetary Boundary Layer, *Boundary-Layer Meteorology* 7, 81–106 (1974).

[84] J. W. Deardorff, Stratocumulus-Capped Mixed Layers derived From a Three-Dimensional Model, *Boundary-Layer Meteorology* 18, 495–527 (1980).

[85] S. Ghosal, T. S. Lund, P. Moin and K. Akselvoll, A Dynamic Localization Model For Large-Eddy Simulation of Turbulent Flows, *J. Fluid Mech.* 286, 229–255 (1995).

[86] J. P. Boris, F. F. Grinstein, E. S. Oran and R. J. Kolbe, New Insights Into Large Eddy Simulation, *Fluid Dynamics Res.* 10, 199–228 (1992).

[87] M. Germano, U. Piomelli, P. Moin and W. H. Cabot, A Dynamic Subgrid-Scale Eddy Viscosity Model, *Phys. Fluids A* 3 (7), 1760–1765 (1991).

[88] F. Sarghini, U. Piomelli and E. Balaras, Scale-Similar Models for Large-Eddy Simulation, *Phys. Fluids* 11 (6), 1596–1607 (1999).

[89] X. Wu and K. D. Squires, Large Eddy Simulation of an Equilibrium Three-Dimensional Turbulent Boundary Layer, *AIAA Jl* 35 (1), 67–74 (1997).

[90] M. P. Martn, U. Piomelli and G. V. Candler, Subgrid-Scale Models for Compressible Large-Eddy Simulations, *Theoretical and Computational Fluid Dynamics* 13(5), 361–376 (2000).

[91] C. Meneveau, T. S. Lund and W. Cabot, A Lagrangian Dynamic Subgrid-Scale Model of Turbulence, *J. Fluid Mech.* 319, 353–385 (1996).

[92] D. C. Haworth and K. Jansen, Large-Eddy Simulation on Unstructured Deforming Meshes: Towards Reciprocating IC Engines, *Comp. Fluids* 29 (5), 493–524 (2000).

[93] C. G. Speziale, G. Erlebacher, T. A. Zang and M. Y. Hussaini, The Subgrid-Scale Modeling of Compressible Turbulence, *Phys. Fluids* 31(4), 940–942 (1988).

[94] H. Pitsch, Large-Eddy Simulation of Turbulent Combustion, *Annual Review of Fluid Mechanics* 38, 453–482 (2006).

[95] J. Janicka and A. Sadiki, Large Eddy Simulation of Turbulent Combustion Systems, *Proc. Combust. Inst.* 30(1), 537–547 (2005).

[96] J. J. Riley, Review of Large-Eddy Simulation of Non-Premixed Turbulent Combustion, *J. Fluids Engg.* 128(2), 209–215 (2006).

[97] P. Givi, Subgrid Scale Modeling in Turbulent Combustion: A Review, AIAA Paper no. 2003-5081, (2003).

[98] D. B. Spalding, Mixing and Chemical Reaction in Steady Confined Turbulent Flames, *Proc. Combust. Inst.* 13, 649–657 (1971).

[99] H. Pitsch and H. Steiner, Large-Eddy Simulation of a Turbulent Piloted Methane/Air Diffusion Flame (Sandia Flame D), *Phys. Fluids* 12(10), 2541–2554 (2000).

[100] W. K. Bushe and H. Steiner, Conditional Moment Closure for Large Eddy Simulation of Nonpremixed Turbulent Reacting Flows, *Phys. Fluids* 11(7), 1896–1906 (1999).

[101] H. Steiner and W. K. Bushe, Large Eddy Simulation of a Turbulent Reacting Jet with Conditional Source-Term Estimation, *Phys. Fluids* 13(3), 754–769 (2001).

[102] A. Y. Klimenko and R. W. Bilger, Conditional Moment closure for Turbulent Combustion, *Progr. Energy Combust. Sci.* 25, 595–687 (1999).

[103] T. G. Drozda, M. R. H. Sheikhi, C. K. Madnia and P. Givi, Developments in Formulation and Application of the Filtered Density Function, *Flow Turb. Combust.* 78(1), 35–67 (2007).

[104] W. H. Calhoon and S. Menon, Linear-Eddy Subgrid Model for Reacting Large-Eddy Simulations - Heat Release Effects, *AIAA paper 1997-368*, (2000).

[105] R. Borghi, Turbulent Combustion Modeling, *Progr. Energy Combust. Sci.* 14(4), 245–292 (1988).

[106] K. K. Kuo, *Principles of Combustion*, Wiley Interscience, New York (1986).

[107] P. Givi, Model-Free Simulations of Turbulent Reactive Flows, *Progr. Energy Combust. Sci.* 15, 1–107 (1989).

[108] S. B. Pope, PDF Methods for Turbulent Reactive Flows, *Progr. Energy Combust. Sci.* 11, 119–192 (1985).

[109] W. Kollmann, The PDF Approach to Turbulent Flow, *Theor. Compt. Fluid Dyn.* 1, 249–285 (1990).

[110] C. Dopazo, Recent Developments in PDF Methods, In *Turbulent Reacting Flows*, pp. 375–474. Academic Press, (1994).

[111] D. C. Haworth, Progress in Probability Density Function Methods for Turbulent Reacting Flows, *Progr. Energy Combust. Sci.* 36 (2), 168–259 (2010).

[112] S. Heinz, *Statistical Mechanics of Turbulent Flows*, Springer, Berlin Heidelberg New York (2003).

[113] D. C. Haworth and S. B. Pope, Transported Probability Density Function Methods for Reynolds-Averaged and Large-Eddy Simulations, In *Turbulent Combustion Modeling* (Edited by Tarek Echekki and Epaminondas Mastorakos), Vol. 95 of *Fluid Mechanics and Its Applications*, pp. 119–142. Springer Netherlands, (2011).

[114] P. Givi, Model-Free Simulations of Turbulent Reactive Flows, *Progr. Energy Combust. Sci.* 15, 1–107 (1989).

[115] S. B. Pope, Computations of Turbulent Combustion: Progress and challenges, *Proc. Combust. Inst.* 23, 591–612 (1990).

[116] C. K. Madnia and P. Givi, In *Large Eddy Simulations of Complex Engineering and Geophysical Flows* (Edited by Boris Galperin and Steven A. Orszag), Ch. Direct Numerical Simulation and Large Eddy Simulation of Reacting Homogeneous Turbulence. Cambridge University Press, 315–346 (1993).

[117] A. W. Cook and J. J. Riley, A Subgrid Model for Equilibrium Chemistry in Turbulent Flows, *Phys. Fluids* 6(8), 2868–2870 (1994).

[118] J. Jiminez, A. Linan, M. M. Rogers and F. J. Higuera, A Priori Testing of Subgrid Models for Chemically Reacting Non-Premixed Turbulent Shear Flows, *J. Fluid Mech.* 349, 149–171 (1997).

[119] C. Wall, B. J. Boersma and P. Moin, An Evaluation of the Assumed Beta Probability Density Function Subgrid-Scale Model for Large Eddy Simulation of Nonpremixed, Turbulent Combustion with Heat Release, *Phys. Fluids* 12(10), 2522–2529 (2000).

[120] C. Tong, Measurements of Conserved Scalar Filtered Density Function in a Turbulent Jet, *Phys. Fluids* 13(10), 2923–2937 (2001).

[121] D. Wang, C. Tong, R. S. Barlow and A. N. Karpetis, Experimental Study of Scalar Filtered Mass Density Function in Turbulent Partially Premixed Flames, *Proc. Combust. Inst.* 31(1), 1533 – 1541 (2007).

[122] F. A. Jaberi, R. S. Miller, C. K. Madnia and P. Givi, Non-Gaussian Scalar Statistics in Homogeneous Turbulence, *J. Fluid Mech.* 313, 241–282 (1996).

[123] R. Sheikhi, P. Givi and S. B. Pope, Joint Frequency-Velocity-Scalar Filtered Mass Density Function for Large Eddy Simulation of Turbulent Reacting Flows, In *59th Annual Meeting of the American Physical Society Division of Fluid Dynamics*, Tampa Bay, FL (19-21 November 2006).

[124] Sandia National Laboratories Combustion Research Facility, *Intern'l. Workshop on Measurement and Computation of Turbulent Nonpremixed Flames* (2002).

[125] R. S. Barlow and J. H. Frank, Effects of Turbulence on Species Mass Fractions in Methane/Air Jet Flames, *Proc. Combust. Inst.* 27, 1087–1095 (1998).

[126] B. B. Dally, A. R. Masri, R. S. Barlow and G. J. Fiechtner, Instantaneous and Mean Compositional Structure of Bluff-Body Stabilized Nonpremixed Flames, *Comb. Flame* 114(1-2), 119–148 (1998).

[127] OpenFoam Website, http://www.opencfd.co.uk/openfoam/.

[128] A. Gupta, D. C. Haworth and M. F. Modest, A Stochastic Photon Monte Carlo Scheme for RAS/PDF and LES/FDF-based Simulations of Turbulent Reacting Flows, *In Preparation*.

[129] C. Dopazo, Relaxation of Initial Probability Density Function in the Turbulent Cconvection of Scalar Fields, *Phys. Fluids* 22, (1979).

[130] L. Valiño and C. Dopazo, A Binomial Langevin Model for Turbulent Mixing, *Physics of Fluids A* 3, 3034 (1991).

[131] T. Vaithiananthan, *Multiscale Mixing Model for Turbulent Reacting Flows*, PhD thesis, The Pennsylvania State University, (2004).

[132] C. Dopazo and E. E. O'Brien, Functional Formulation of Non-isothermal Turbulent Reactive Flows, *Phys. Fluids* 17, 1968–1975 (1974).

[133] R. Borghi, Turbulent Combustion Modelling, *Progr. Energy Combust. Sci.* 14, 245–292 (1988).

[134] J. Janicka, W. Kolbe and W. Kollmann, The Solution of a PDF-Transport Equation for Turbulent Diffusion Flames, In *Proceedings of 1978 Heat Trans. Fluid Mech. Inst., Stanford University*, (1978).

[135] S. B. Pope, Monte Carlo Method for the PDF Equations of Turbulent Reactive FLow, *Comb. Sci. T.* 25, 159–174 (1981).

[136] Saxena V. and S. B. Pope, PDF Calculations of Major and Minor Species in a Turbulent Piloted Jet Flames, 1081–1086 (1998).

[137] S. Subramaniam and S. B. Pope, A Mixing Model for Turbulent Reactive Flows based on Euclidean Minimum Spanning Trees, *Comb. Flame* 115, 487–514 (1998).

[138] S. V. Subramaniam and D. C. Haworth, A PDF Method for Turbulent Mixing and Combustion on Three-Dimensional Unstructured Deforming Meshes, *Intern'l. J. Engine Research* 1, 171–190 (2000).

[139] Y. Z. Zhang and D. C. Haworth, A General Mass Consistency Algorithm for Hybrid Particle/Finite-Volume PDF Methods, *J. Comp. Phys.* 194, 156–193 (2004).

[140] Y. Z. Zhang, E. H. Kung and D. C. Haworth, A PDF Method for Multidimensional Modeling of HCCI Engine Combustion: Effects of Turbulence/Chemistry Interactions on Ignition Timing and Emissions, *Proc. Combust. Inst.* 30, 2763–2771 (2005).

[141] P. Jenny, S. B. Pope, M. Muradoglu and D. A. Caughey, A Hybrid Algorithm for the Joint PDF Equation of Turbulent Reactive Flows, *J. Comp. Phys.* 166, 218–252 (2001).

[142] M. Muradoglu, P. Jenny, S. B. Pope and D. A. Caughey, A Consistent Hybrid Finite Volume/Particle Method for the PDF Equations of Turbulent Reactive Flows,, *J. Comp. Phys.* 154, 342–371 (1999).

[143] M. Muradoglu, S. B. Pope and D.A. Caughey, The Hybrid Method for the PDF Equations of Turbulent Reactive Flows: Consistency Conditions and Correction Algorithm, *J. Comp. Phys.* 172, 841–878 (2001).

[144] M. Muradoglu, K. Liu and S. B. Pope, PDF Modeling of a Bluff-Body Stabilized Turbulent Flame, *Comb. Flame* 132(1-2), 115–137 (2003).

[145] G. Li, *Investigation of Turbulence–Radiation Interactions By a Hybrid FV/PDF Monte Carlo Method*, PhD thesis, The Pennsylvania State University, University Park, PA, (2002).

[146] G. Li and M. F. Modest, An Effective Particle Tracing Scheme on Structured/Unstructured Grids in Hybrid Finite Volume/PDF Monte Carlo Methods, *J. Comp. Phys.* 173, 187–207 (2001).

[147] S. B. Pope, On the Relationship Between Stochastic Lagrangian Models of Turbulence and Second-Moment Closures, *Phys. Fluids* 6, 973–985 (1994).

[148] S. B. Pope, Lagrangian PDF methods for turbulent flows, *Annual Review of Fluid Mechanics* 26, 23 (1994).

[149] M. F. Modest, *Radiative Heat Transfer* (2nd Edn), Academic Press, New York (2003).

[150] D. V. Walters and R. O. Buckius, Monte Carlo Methods of Radiative Heat Transfer in Scattering Media, In *Ann. Review Heat Transfer (5)*, Hemisphere, New York (1992).

[151] M. F. Modest and S. C. Poon, Determination of Three-Dimensional Radiative Exchange Factors for the Space Shuttle by Monte Carlo, ASME paper no. 77-HT-49, (1977).

[152] M. F. Modest, Determination of Radiative Exchange Factors for Three Dimensional Geometries with Nonideal Surface Properties, *Numer. Heat Transfer* 1, 403–416 (1978).

[153] A. Wang and M. F. Modest, Photon Monte Carlo Simulation for Radiative Transfer in Gaseous Media Represented by Discrete Particle Fields, *J. Heat Transfer* 128, 1041–1049 (2006).

[154] L. Wang, D. C. Haworth, S. R. Turns and M. F. Modest, Interactions Among Soot, Thermal Radiation, and NOx Emissions in Oxygen-Enriched Turbulent Nonpremixed Flames: a CFD Modeling Study, *Comb. Flame* 141(1-2), (2005), 170–179.

[155] L. Wang, M. F. Modest, D. C. Haworth and S. R. Turns, Modeling Nongray Soot and Gas-Phase Radiation in Luminous Turbulent Nonpremixed Jet Flames, *Combustion Theory and Modelling* 9(3), 479–498 (2005).

[156] S. Mazumder and M. F. Modest, A PDF Approach to Modeling Turbulence–Radiation Interactions in Nonluminous Flames, *Int. J. Heat Mass Transfer* 42, 971–991 (1999).

[157] Y. Ju, G. Masuya and P. D. Ronney, Effects Of Radiative Emission And Absorption On The Propagation And Extinction Of Premixed Gas Flames, In *Proceedings of the Twenty-Seventh Symposium (International) on Combustion*, Vol. 2, pp. 2619–2626, (1998).

[158] Y. Ju, G. Masuya and F. Liu, Asymptotic Analysis Of Radiation Extinction Of Stretched Premixed Flames, *Int. J. Heat Mass Transfer* 43(2), 231–239 (2000).

[159] S. Mazumder and M. F. Modest, Application of the Full Spectrum Correlated-k Distribution Approach to Modeling Non-Gray Radiation in Combustion Gases, *Comb. Flame* 129(4), 416–438 (2002).

[160] L. S. Rothman, R. R. Gamache, R. H. Tipping, C. P. Rinsland, M. A. H. Smith, D. C. Benner, V. M. Devi, J.-M. Flaud, C. Camy-Peyret, A. Perrin, A. Goldman, S. T. Massie, L. R. Brown and R. A. Toth, The HITRAN Molecular Database: Editions of 1991 and 1992, *J. Quant. Spectrosc. Radiat. Transfer* 48(5/6), 469–507 (1992).

[161] L. S. Rothman, R. B. Wattson, R. R. Gamache, J. Schroeder and A. McCann, HITRAN, HAWKS and HITEMP High Temperature Database, *Proceedings of SPIE* 2471, 105–111 (1995).

[162] L. S. Rothman, C. P. Rinsland, A. Goldman, S. T. Massie, D. P. Edwards, J.-M. Flaud, A. Perrin, C. Camy-Peyret, V. Dana, J.-Y. Mandin, J. Schroeder, A. McCann, R. R. Gamache, R. B. Wattson, K. Yoshino, K. V. Chance, K. W. Jucks, L. R. Brown, V. Nemtchinov and P. Varanasi, The HITRAN Molecular Spectroscopic Database and HAWKS (HITRAN Atmospheric Workstation): 1996 Edition, *J. Quant. Spectrosc. Radiat. Transfer* 60, 665–710 (1998).

[163] S. A. Tashkun, V. I. Perevalov, J.-L. Teffo, A. D. Bykov and N. N. Lavrentieva, CDSD-1000, the High-Temperature Carbon Dioxide Spectroscopic Databank, *J. Quant. Spectrosc. Radiat. Transfer* 82(1–4), 165–196 (2003), available from ftp://ftp.iao.ru/pub/CDSD-1000.

[164] M. F. Modest, The Weighted-Sum-of-Gray-Gases Model for Arbitrary Solution Methods in Radiative Transfer, *J. Heat Transfer* 113(3), 650–656 (1991).

[165] M. K. Denison and B. W. Webb, A Spectral Line Based Weighted-Sum-of-Gray-gases Model for Arbitrary RTE Solvers, *J. Heat Transfer* 115, 1004–1012 (1993).

[166] M. K. Denison and B. W. Webb, The Spectral-Line-Based Weighted-Sum-of-Gray-Gases Model in Nonisothermal Nonhomogeneous Media, *J. Heat Transfer* 117, 359–365 (1995).

[167] M. F. Modest and H. Zhang, The Full-Spectrum Correlated-k Distribution For Thermal Radiation from Molecular Gas–Particulate Mixtures, *J. Heat Transfer* 124(1), 30–38 (2002).

[168] H. Zhang and M. F. Modest, A Multi-Scale Full-Spectrum Correlated-k Distribution For Radiative Heat Transfer in Inhomogeneous Gas Mixtures, *J. Quant. Spectrosc. Radiat. Transfer* 73(2–5), 349–360 (2002).

[169] H. Zhang and M. F. Modest, Scalable Multi-Group Full-Spectrum Correlated-k Distributions For Radiative Heat Transfer, *J. Heat Transfer* 125(3), 454–461 (2003).

[170] H. Chang and T. T. Charalampopoulos, Determination of the Wavelength Dependence of Refractive Indices of Flame Soot, *Proceedings of the Royal Society (London) A* 430(1880), 577–591 (1990).

[171] V. P. Kabashnikov and G. I. Myasnikova, Thermal Radiation in Turbulent Flows—Temperature and Concentration Fluctuations, *Heat Transfer-Soviet Research* 17(6), 116–125 (1985).

[172] J. W. Hartick, M. Tacke, G. Fruchtel, E. P. Hassel and J. Janicka, Interaction of Turbulence and Radiation in Confined Diffusion Flames, In *Twenty-Sixth Symposium (International) on Combustion*, pp. 75–82, The Combustion Institute (1996).

[173] R. Mehta, Modeling Absorption Coefficient-Intensity Correlations for Optically Thick Eddies in Turbulent Reacting Flows Using Hybrid Finite Volume/PDF Monte Carlo Methods, Master's thesis, The Pennsylvania State University, University Park, PA (2006).

[174] P. J. Foster, The Relation of Time-Mean Transmission of Turbulent Flames to Optical Depth, *Journal of the Institute of Fuel* 42, 179–182 (1969).

[175] S. Mazumder and M. F. Modest, Turbulence–Radiation Interactions in Nonreactive Flow of Combustion Gases, *J. Heat Transfer* 121, 726–729 (1999).

[176] S. H. Chan and X. C. Pan, A General Semicausal Stochastic Model for Turbulence / Radiation Interactions in Flames, *J. Heat Transfer* 119 (3), 509–516 (1997).

[177] P. J. Coelho, Numerical Simulation of the Interaction between Turbulence and Radiation in Reactive Flows, *Progr. Energy Combust. Sci.* 33, 311–383 (2007).

[178] H. A. Becker, Effect of Concentration Fluctuations in Turbulent Diffusion Flames, *Proc. Combust. Institute* 15, 601–615 (1975).

[179] G. Cox, On Radiant Heat Transfer from Turbulent Flames, *Comb. Sci. T.* 17, 75–78 (1977).

[180] V. P. Kabashnikov and G. I. Kmit, Influence of Turbulent Fluctuations on Thermal Radiation, *J. Appl. Spectr.* 31 (2), 963–967 (1979).

[181] J.-F. Ripoll, An Averaged Formulation of the M_1 Radiation Model with Mean Absorption Coefficients and Presumed Probability Density Functions for Turbulent Flows, *J. Quant. Spectrosc. Radiat. Transfer* 83, 493–517 (2004).

[182] P. J. Coelho, O. J. Teerling and D. Roekaerts, Spectral Radiative Effects and Turbulence/Radiation Interaction in a Non-Luminous Turbulent Jet Diffusion Flame, *Comb. Flame* 133, 75–91 (2003).

[183] Y. Wu, D. C. Haworth., M. F. Modest and B. Cuenot, Direct Numerical Simulation of Turbulence/Radiation Interaction in Premixed Combustion Systems, *Proc. Combust. Inst.* 30, 639–646 (2005).

[184] K. V. Deshmukh, D. C. Haworth and M. F. Modest, Direct Numerical Simulation of Turbulence/Radiation Interactions in Nonpremixed Combustion Systems, *Proc. Combust. Inst.* 31, 1641–1648 (2007).

[185] A. Wang and M. F. Modest, An Adaptive Emission model for Monte Carlo Ray-Tracing in Participating Media Represented by Statistical Particle Fields, *J. Quant. Spectrosc. Radiat. Transfer* 104(2), 288–296 (2007).

[186] A. Wang and M. F. Modest, Spectral Monte Carlo Models for Nongray Radiation Analyses in Inhomogeneous Participating Media, *Int. J. Heat Mass Transfer* 50, 3877–3889 (2007).

[187] A. Wang and M. F. Modest, Photon Monte Carlo Simulation of Radiative Heat Transfer in Turbulent Sooty Flames, In *ASME-JSME Thermal Engineering and Summer Heat Transfer Conference*, Vancouver, Canada (2007).

[188] R. S. Mehta, M. F. Modest and D. C. Haworth, Radiation Characteristics and Turbulence-Radiation Interactions in Sooting Turbulent Jet Flames, *Combust. Theory Modelling* 14 (1), 105–124 (2010).

[189] http://chasm-interop.sourceforge.net.

[190] R. S. Barlow, website:http://www.ca.sandia.gov/tdf/Workshop.html.

[191] S. Subramaniam and D. C. Haworth, A PDF Method for Turbulent Mixing and Combustion on Three-Dimensional Unstructured Deforming Meshes, *Journal of Engine Research* 1, 171–190 (2000).

[192] R. L. Curl, Dispersed Phase Mixing: I. Theory and Effects of Simple Reactors, *AIChE Jl* 9, 175–181 (1963).

[193] L. A. Spielman and O. Levenspiel, A Monte Carlo Treatment for Reacting and Coalescing Dispersed Phase Systems, *Chem. Engg. Sci.* 20, 247–254 (1965).

[194] M. Sommerfeld and H. Qiu, Experimental Studies of Spray Evaporation in Turbulent Flow, *Int. J. Heat Fluid Flow* 19, 10–22 (1998).

[195] OpenFOAM waveTransmissive BC, *http://www.openfoamwiki.net/index.php/HowTo_Using_the_WaveTransmissive_Boundary_condition.*

[196] T. J. Poinsot and S. K. Lele, Boundary Conditions for Direct Simulations of Compressible Viscous Flows, 101 (1), 104–129 (1992).

[197] METIS Website, http://www.cs.umn.edu/ metis.

[198] S. James, J. Zhu and M. S. Anand, Large-Eddy Simulations as a Design Tool for Gas Turbine Combustion Systems, *AIAA Jl* 44 (4), 674–686 (2006).

[199] See www.sandia.gov/TNF/.

[200] R. S. Barlow and A. Dreizler, Sandia/TUD Piloted CH4/Air Jet Flames, (2003), Data available at http:www.sandia.govTNFDataArchFlameD.html.

[201] CH4/air Skeletal Mechanism by Sanjay M. Correa.

[202] R. R. Cao, H. Wang and S. B. Pope, The Effect of Mixing Models in PDF Calculations of Piloted Jet Flames, *Proc. Combust. Inst.* 31, 1543–1550 (2007).

[203] R. R. Cao and S. B. Pope, The Influence of Chemical Mechanisms on PDF Calculations of Nonpremixed Piloted Jet Flames, *Comb. Flame* 143, 450–470 (2005).

[204] M. Klein, A. Sadiki and J. Janicka, A Digital Filter based Generation of Inflow Data for Spatially Developing Direct Numerical or Large Eddy Simulations, *J. Comp. Phys.* 186, 652–665 (2003).

[205] S. James, J. Zhu and M. S. Anand, Large Eddy Simulations of Turbulent Flames Using the Filtered Density Function Model, *Proc. Combust. Inst.* 31, 1737–1745 (2007).

[206] T. Lund, X. Wu and D. Squires, Generation of Turbulent Inflow Data for Spatially-Developing Boundary layer Simulations, *J. Comp. Phys.* 140, 233–258 (1998).

[207] J. Jaishree and D. C. Haworth, Comparisons of Lagrangian and Eulerian PDF Methods in Simulations of Nonpremixed Turbulent Jet Flames with Moderate-to-Strong Turbulence/Chemistry Interactions, *Combust. Theory Modelling*.

[208] S. B. Pope, Computationally Efficient Implementation of Combustion Chemistry using In Situ Adaptive Tabulation, *Combust. Theory Modelling* 1 (1), 41–63 (1997).

[209] A. Wang and M. F. Modest, Monte Carlo Simulation of Radiative Heat Transfer and Turbulence Interactions in Methane/Air Jet Flames, In *Radiative Transfer 2007 — The Fifth International Symposium on Radiative Transfer* (Edited by M. P. Mengüç and N. Selçuk), Begell House, Bodrum, Turkey (2007).

[210] J. P. Gore, *A Theoretical and Experimental Study of Turbulent Flame Radiation*, PhD thesis, The Pennsylvania State University, University Park, PA, (1986).

[211] G. Pal, A. Gupta, D. C. Haworth and M. F. Modest, The Influences of Spectral Modeling of Radiative Properties and Solution Method of the Radiative Transfer Equation in Simulations of Nonpremixed Turbulent Jet Flames, *ICHMT Digital Library Online*, (2010).

[212] A. Gupta, Large-Eddy Simulation of Turbulence/Chemistry/Radiation Interactions in Planar Channel Flow, Master's thesis, The Pennsylvania State University, University Park, PA (2007).

[213] J. H. Frank, R. S. Barlow and C. Lundquist, Radiation and Nitric Oxide Formation in Turbulent Non-Premixed Jet Flames, *Proc. Combust. Inst.* 28, 447–454 (2000).

[214] V. Raman and H. Pitsch, A Consistent LES/Filtered-Density Function Formulation for the Simulation of Turbulent Flames with Detailed Chemistry, *Proc. Combust. Inst.* 31, 1711–1719 (2007).

[215] M. Frenklach and S. J. Harris, Aerosol Dynamics Modeling Using the Method of Moments, *Journal of Colloid and Interface Science* 118(1), 252–261 (1987).

[216] M. Frenklach and H. Wang, Detailed Mechanism and Modeling of Soot Particle Formation, In *Soot Formation in Combustion: Mechanisms and Models* (Edited by H. Bockhorn), Springer-Verlag, New York (1994).

[217] M. Balthasar, F. Mauss, A. Knobel and M. Kraft, Detailed Modeling of Soot Formation in a Partially Stirred Plug Flow Reactor, *Comb. Flame* 128, 395–409 (2002).

[218] R. P. Lindstedt and S. A. Louloudi, Joint-Scalar Transported PDF Modeling of Soot Formation and Oxidation, *Proc. Combust. Inst.* 30, 775–783 (2005).

[219] R. Mehta, *Detailed Modeling of Soot Formation and Turbulence–Radiation Interactions in Turbulent Jet Flames*, PhD thesis, The Pennsylvania State University, University Park, PA, (2008).

[220] H. W. Ge and E. Gutheil, Simulation of a Turbulent Spray Flame Using Coupled PDF Gas Phase and Spray Flamelet Modeling, *Comb. Flame* 153, 173–185 (2008).

[221] E. H. Kung, *PDF-Based Modeling of Autoignition and Emissions for Advanced Direct-Injection Engines*, PhD thesis, The Pennsylvania State University, University Park, PA, (2008).

Vita

Ankur Gupta

Ankur Gupta was born in Kota, India on June 22, 1981. He received his Bachelor of Technology (B. Tech) degree in Mechanical Engineering from Indian Institute of Technology Bombay, India in 2002. He worked at Fluent India (now ANSYS India) as an Applications Engineer for two years before joining the graduate program in the Department of Mechanical and Nuclear engineering at The Pennsylvania State University in Fall 2004. He was also employed as a research assistant during this time, and received his Masters degree in Mechanical Engineering in Summer 2007. Ankur worked with COMSOL Inc. as an Applications Engineer for about a year, and is currently working with Rolls-Royce Corporation, USA as a Combustion Methods Specialist.